

NO-A104 037

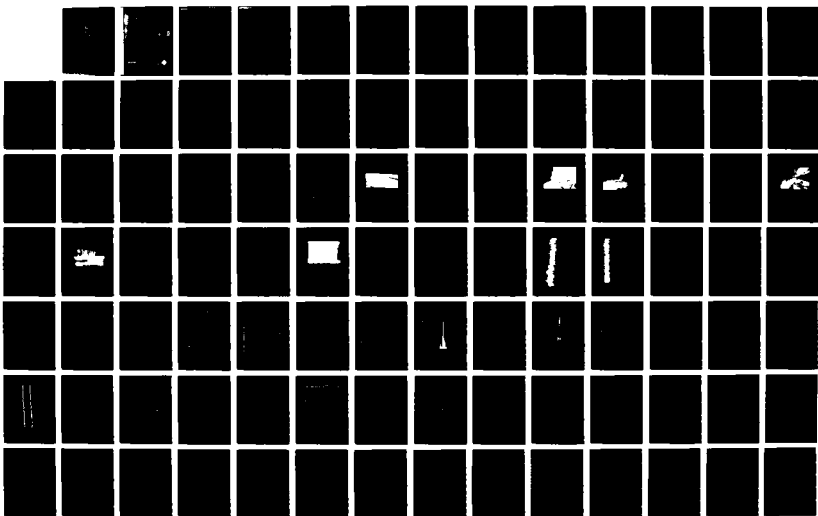
AN INVESTIGATION OF MILLIMETER WAVE PROPAGATION IN THE  
ATMOSPHERE: MEASUR. (U) GEORGIA TECH RESEARCH INST  
ATLANTA R W MCILLAN ET AL. 17 JUN 87 ARO-10457.12-05  
DAGG29-01-K-0173

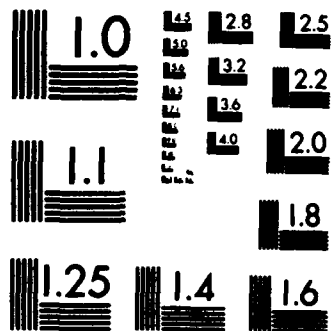
1/3

UNCLASSIFIED

F/G 20/14

NL





MICROCOPY RESOLUTION TEST CHART  
NATIONAL BUREAU OF STANDARDS-1963-A

DTIC FILE COPY

ARO 18457.12-65

Final Report

AD-A184837

(2)

**AN INVESTIGATION OF MILLIMETER WAVE  
PROPAGATION IN THE ATMOSPHERE:  
MEASUREMENT PROGRAM**

By

**R.W. McMillan and R.A. Bohlander  
Georgia Tech Research Institute**

Prepared for

**U.S. ARMY RESEARCH OFFICE  
P.O. Box 12211  
Research Triangle Park, NC 27709-2211**

**DTIC  
ELECTE  
SEP 17 1987  
S D**

Under

**Contract Number DAAG29-81-K-0173**

**June 17, 1987**

**Approved for Public Release  
Distribution Unlimited**

**GEORGIA INSTITUTE OF TECHNOLOGY**

**A Unit of the University System of Georgia  
Atlanta, Georgia 30332**

**GTRI**  
GEORGIA TECH RESEARCH INSTITUTE



87 9 9 162

## REPORT DOCUMENTATION PAGE

1a. REPORT SECURITY CLASSIFICATION <b>Unclassified</b>		1b. RESTRICTIVE MARKINGS	
2a. SECURITY CLASSIFICATION AUTHORITY		3. DISTRIBUTION/AVAILABILITY OF REPORT Approved for public release; distribution unlimited.	
2b. DECLASSIFICATION/DOWNGRADING SCHEDULE			
4. PERFORMING ORGANIZATION REPORT NUMBER(S)		5. MONITORING ORGANIZATION REPORT NUMBER(S) <b>ARO 18457.12-65</b>	
6a. NAME OF PERFORMING ORGANIZATION Georgia Institute of Technology Georgia Tech Research Institute	6b. OFFICE SYMBOL (If applicable)	7a. NAME OF MONITORING ORGANIZATION U. S. Army Research Office	
6c. ADDRESS (City, State, and ZIP Code) Atlanta, Georgia 30332		7b. ADDRESS (City, State, and ZIP Code) P. O. Box 12211 Research Triangle Park, NC 27709-2211	
8a. NAME OF FUNDING/SPONSORING ORGANIZATION U. S. Army Research Office	8b. OFFICE SYMBOL (If applicable)	9. PROCUREMENT INSTRUMENT IDENTIFICATION NUMBER <b>DAAG29-81-K-0173</b>	
8c. ADDRESS (City, State, and ZIP Code) P. O. Box 12211 Research Triangle Park, NC 27709-2211		10. SOURCE OF FUNDING NUMBERS	
		PROGRAM ELEMENT NO.	PROJECT NO.
		TASK NO.	WORK UNIT ACCESSION NO.
11. TITLE (Include Security Classification) An investigation of Millimeter Wave Propagation in the Atmosphere: Measurement Program			
12. PERSONAL AUTHOR(S) R. W. McMillan and R. A. Bohlander			
13a. TYPE OF REPORT Final	13b. TIME COVERED FROM 9/21/81 TO 3/31/87	14. DATE OF REPORT (Year, Month, Day) 1987, June 17	15. PAGE COUNT 187
16. SUPPLEMENTARY NOTATION The view, opinions and/or findings contained in this report are those of the author(s) and should not be construed as an official Department of the Army position, policy, or decision, unless so designated by other documentation.			
17. COSATI CODES		18. SUBJECT TERMS (Continue on reverse if necessary and identify by block number)	
FIELD	GROUP	SUB-GROUP	
		Millimeter Wave Turbulence, Millimeter Wave Propagation Millimeter Wave Atmospheric Effects.	
19. ABSTRACT (Continue on reverse if necessary and identify by block number) <p>This report describes work done on Contract DAAG29-81-K-0173, "An Investigation of Millimeter Wave Propagation in the Atmosphere: Measurement Program," conducted by the Georgia Tech Research Institute during the period September 1981 through May 1987. The objective of this program was to measure the effects of atmospheric turbulence on the propagation of millimeter wave radiation, with emphasis on inclement weather effects. Five separate measurement sessions were conducted at a site near Urbana, Illinois, and these measurements were made jointly with personnel from the National Oceanic and Atmospheric Administration, who furnished meteorological instrumentation and information on experiment design. Personnel from the Atmospheric Sciences Laboratory at White Sands Missile Range also contributed to this program.</p> <p>(Continued on next page)</p>			
20. DISTRIBUTION/AVAILABILITY OF ABSTRACT <input type="checkbox"/> UNCLASSIFIED/UNLIMITED <input type="checkbox"/> SAME AS RPT. <input type="checkbox"/> DTIC USERS		21. ABSTRACT SECURITY CLASSIFICATION Unclassified	
22a. NAME OF RESPONSIBLE INDIVIDUAL		22b. TELEPHONE (Include Area Code)	22c. OFFICE SYMBOL

Measurements were made at frequencies near 118, 142, 173, and 230 GHz to cover all of the major atmospheric features in the millimeter wave spectral range, and were made during clear air, rain, fog, and snow. The equipment comprised a small step-van transmitter truck, and an array of four receivers, pumped by a common local oscillator, mounted in a semi-trailer. This arrangement provided the means for measuring fluctuations in both intensity and phase of the MMW signal.

It is concluded in this report that atmospheric turbulence has a marginal effect on the performance of Army MMW systems. For example, a system with a tracking accuracy of 100 microradians might have its accuracy degraded by 15-20% by turbulence. It is also concluded, perhaps surprisingly, that the worst-case MMW effects of turbulence occur during clear air under conditions of high temperature and humidity.

Accession For	
NTIS CRA&I	<input checked="checked" type="checkbox"/>
DTIC TAB	<input type="checkbox"/>
Unannounced	<input type="checkbox"/>
Justification	
By	
Distribution/	
Availability Codes	
Dist	Avail and/or Special
A-1	

QUALITY  
INSPECTED  
2

## TABLE OF CONTENTS

Section	Title	Page
	List of Figures	iii
	List of Tables	vii
	Abstract	viii
1.	Introduction	1
1.1	General Atmospheric Effects on Millimeter Wave Systems	2
1.2	Summary of the Effects of Atmospheric Turbulence on MMW Systems	4
2.	Millimeter Wave Turbulence Theories	7
2.1	Soviet Theories	7
2.1.1	General Approach	7
2.1.2	Determination of the Magnitude of Intensity Fluctuations	8
2.1.3	Determination of the Magnitude of Angle-of-Arrival Fluctuations	9
2.2	The Theory of Hill, Clifford, and Lawrence	12
3.	Results of Measurements of Turbulence Effects at Millimeter Wave Frequencies	16
3.1	Results Obtained at Burlington, Vermont	16
3.2	Experiments Conducted at Flatville, Illinois	20
3.2.1	Description of Experiments	20
3.2.2.1	Transmitter Subsystem	20
3.2.1.2	Receiver Subsystem	23
3.2.1.3	Signal Combiner	32

## TABLE OF CONTENTS

Section	Title	Page
3.2.1.4	Meteorological Instrumentation	33
3.2.1.5	Data Collection/Processing Subsystem	36
3.2.2	Results	36
3.2.2.1	Clear Air Results	37
3.2.2.2	Results Obtained in Rain	45
3.2.2.3	Fog Results	51
3.2.2.4	Results Obtained in Snow	56
3.2.2.5	Summary of Results Obtained	56
4.	Conclusions	63
	Acknowledgements	68
	References	69
	Bibliography	71
	Appendix A Reprints of Articles Published Under the Contract	74

## LIST OF FIGURES

<u>Section</u>	<u>List of Figures</u>	<u>Page</u>
Figure 2-1.	Angle-of-Arrival Geometry.	10
Figure 3-1.	Layout of the measurement system used for evaluating turbulence effects at the Snow-One site near Burlington, VT.	17
Figure 3-2.	Log amplitude variance for MMW propagation in turbulence as a function of frequency and range, showing that the scaling relations are valid.	18
Figure 3-3.	Diagram of the Flatville experiment showing transmitter, receiver, and meteorological instrumentation.	21
Figure 3-4.	Photograph of the propagation range at Flatville, viewed looking South. The receiver trailer is in the foreground, and some of the ASL met instrumentation can be seen to the left.	22
Figure 3-5.	Block diagram of the transmitter subsystem showing phase-lock loop.	24
Figure 3-6.	Photograph of the 230 GHz extended interaction oscillator source used in Session 5.	25
Figure 3-7.	Photograph of transmitter truck. This truck was placed on a mound of earth so that transmitter and receiver were at the same height.	26
Figure 3-8.	Diagram of beam waveguide system used for local oscillator distribution.	27
Figure 3-9.	Photograph of the interior of the receiver trailer showing beam waveguide lenses. The local oscillator is at the far end of the beam and one of the receiver lenses can be seen near the top of the picture.	29

## LIST OF FIGURES

<u>Section</u>	<u>List of Figures</u>	<u>Page</u>
Figure 3-10.	Block diagram of the double-conversion receiver showing relationship to beam waveguide.	30
Figure 3-11.	Photograph of the receiver trailer showing steel/ concrete I-beam supports and aperture awnings.	31
Figure 3-12.	Block diagram of one channel of the signal combiner.	34
Figure 3-13.	Photograph of one of the met stations, showing left to right: a Lyman- $\alpha$ hygrometer, a sonic anemometer and a prop-vane anemometer. The Lyman- $\alpha$ and sonic anemometer have a fine-wire temperature probe at their centers. On the lower level are two psychrometers and a Vaisala humidiometer.	
Figure 3-14.	Copy of a chart recorder trace showing fluctuations observed at 142 GHz on a hot humid sunny day.	38
Figure 3-15.	Copy of a recorder trace show showing phase shift measured between antennas 1 and 4 at 142 GHz. This trace corresponds to the intensity measurement shown in Figure 3-14.	39
Figure 3-16.	Intensity (upper) and phase (lower) fluctuations observed for all four antennas and six antenna pairs at 173 GHz on a hot, humid summer day.	40
Figure 3-17.	Intensity probability distribution function corresponding to Figure 3-16. Note that the log normal distribution is a better fit to the data.	42

## LIST OF FIGURES

<u>Section</u>	<u>List of Figures</u>	<u>Page</u>
Figure 3-18.	Phase probability distribution function for the antenna pair with 10 m spacing, corresponding to Figures 3-16 and 3-17.	43
Figure 3-19.	Phase structure function for six different runs on the same day. The solid curve is the result of a calculation based on an assumed outer scale dimension of 14 m.	44
Figure 3-20.	Measured and calculated values of the mutual coherence function corresponding to several different runs at 173 GHz. Each curve or series of points corresponds to a different observed value of $C_n^2$ .	46
Figure 3-21.	Intensity changes observed in rain at 173 GHz for two of the four channels.	47
Figure 3-22.	Weighing bucket rain gauge chart corresponding to Figure 3-21. The slope of this curve is proportional to rain rate.	48
Figure 3-23.	Optical rain gauge output for a data run at 230 GHz.	49
Figure 3-24.	Intensity probability distribution function measured at 230 GHz corresponding to the rain gauge trace of Figure 3-23. Note the width of this PDF as compared to Figure 3-17.	50
Figure 3-25.	Phase probability distribution function corresponding to Figures 3-23 and 3-24. Apparently the gaussian profile is maintained independent of rain rate.	52

## LIST OF FIGURES

<u>Section</u>	<u>List of Figures</u>	<u>Page</u>
Figure 3-26.	Intensity power spectra corresponding to Figures 3-23 through 3-25. The two curves are derived by different averaging methods as described in the text.	53
Figure 3-27.	Phase difference power spectra corresponding to Figure 3-26.	54
Figure 3-28.	Copy of a chart recorder trace of relative power measured in a heavy fog at 142 GHz.	55
Figure 3-29.	Copy of a chart recorder trace of intensity fluctuations measured in snow at 116 GHz.	57
Figure 3-30.	Intensity power spectra observed in snow at 230 GHz.	58
Figure 3-31.	Phase difference power spectra observed in snow at 230 GHz for three different antenna spacings.	59
Figure 3-32.	Comparison of phase difference variances observed in snow at 116 GHz and 230 GHz to clear-air variances observed at 116 GHz.	61
Figure 4-1.	Comparison of calculations of $C_n^2$ using the inertial range formula to measured values.	64
Figure 4-2.	Schematic of unattended MMW system for continuous measurement of $C_n^2$ , relative phase, and cross wind.	

## LIST OF TABLES

<u>Section</u>	<u>List of Tables</u>	<u>Page</u>
Table 3-I.	Angle-of-Arrival Geometry.	41
Table 3-II.	Typical Fluctuation Levels in Millimeter Wave Propagation	62

## ABSTRACT

This report describes work done on Contract DAAG29-81-K-0173, "An Investigation of Millimeter Wave Propagation in the Atmosphere: Measurement Program," conducted by the Georgia Tech Research Institute during the period September 1981 through May 1987. The objective of this program was to measure the effects of atmospheric turbulence on the propagation of millimeter wave radiation, with emphasis on inclement weather effects. Five separate measurement sessions were conducted at a site near Urbana, Illinois, and these measurements were made jointly with personnel from the National Oceanic and Atmospheric Administration, who furnished meteorological instrumentation and information on experiment design. Personnel from the Atmospheric Sciences Laboratory at White Sands Missile Range also contributed to this program.

Measurements were made at frequencies near 118, 142, 173, and 230 GHz to cover all of the major atmospheric features in the millimeter wave spectral range, and were made during clear air, rain, fog, and snow. The equipment comprised a small step-van transmitter truck and an array of four receivers, pumped by a common local oscillator, mounted in a semi-trailer. This arrangement provided the means for measuring fluctuations in both intensity and phase of the MMW signal.

It is concluded in this report that atmospheric turbulence has a marginal effect on the performance of Army MMW systems. For example, a system with a tracking accuracy of 100 microradians might have its accuracy degraded by 15-20% by turbulence. It is also concluded, perhaps surprisingly, that the worst-case MMW effects of turbulence occur during clear air under conditions of high temperature and humidity.

## FINAL REPORT ON ARO MMW TURBULENCE PROJECT

### 1. Introduction

This document is the final report on Contract DAAG29-81-K-0173, "Study of Millimeter-Wave Propagation in the Atmosphere", a program supported by the U. S. Army Research Office and conducted jointly by the Georgia Tech Research Institute (GTRI) and the National Oceanic and Atmospheric Administration (NOAA), supported by separate grants. The major responsibility of Georgia Tech during this program was to design and construct hardware for measuring the effects of atmospheric turbulence on millimeter wave (MMW) propagation, at several different wavelengths of current and potential interest to the Army, under a variety of weather conditions. NOAA's responsibility was to design the experiment, provide meteorological instrumentation support, and analyze the data, although Georgia Tech has also participated to some extent in this latter activity. The frequencies chosen for this experiment were 116, 118, 143, 173, and 230 GHz, and measurements were made under conditions of clear air, rain, fog, and snow; although time and circumstances did not permit the acquisition of data at all of these frequencies under all of these atmospheric conditions.

The frequencies listed above were chosen to lie on or near prominent atmospheric transmission features in the MMW bands, namely the broad window near 95 GHz, the 118 GHz oxygen absorption, the 140 GHz window, the 183 GHz water vapor absorption, and the 230 GHz window. Frequencies near absorption lines were chosen to assess the observation of Soviet workers of damping of turbulence-induced fluctuations on these lines. Damping has not yet been observed, but not all of the data are analyzed to the extent necessary to make this assessment.

The experiment was conducted at a site near Flatville,

Illinois, chosen for its exceptional flatness and "fetch" which is the distance to large man-made or terrain features measured transversely to the propagation path. Flatness and fetch are necessary to ensure that the atmospheric features are not disturbed by objects near the path; otherwise, it would be necessary to use several meteorological instrumentation stations to adequately characterize the atmosphere.

### 1.1 General Atmospheric Effects on Millimeter Wave Systems

The atmosphere has traditionally been a paradox when regarded from the point of view of the millimeter wave (MMW) system designer. On the one hand, MMW systems are considered as solutions to the problems inherent in optical and near infrared systems due to poor weather, especially fog, because such systems retain at least a part of the resolution capability of the shorter wavelengths while having the ability to penetrate the turbid atmosphere. On the other hand, the ability of millimeter wavelengths to penetrate rain, fog, and snow is not as good as that of microwaves, and many workers in the field consider these longer wavelengths to be superior both because of this better transmission and because of the highly-developed state of component technology at these longer wavelengths. It thus appears that the choice of MMW technology represents a compromise between the higher resolution of the optical systems and the better weather penetration and advanced componentry of microwaves. In summary, one would always choose the shorter wavelengths if the weather were always good, and one would choose the longer wavelengths if the resolution were good enough, and there would be no applications for millimeter waves, if these were the only criteria. Unfortunately, the weather is not always clear enough for optical systems, and microwaves do not always provide sufficient resolution, so that the potential niche for

millimeter waves is fairly wide, and has not as yet been filled by operational systems.

The major atmospheric effect on the performance of MMW systems is attenuation, but other effects such as forward- and back-scattering, atmospheric ducting, and of course atmospheric turbulence are also of some importance. With regard to attenuation, MMW radiation shows excellent capability for penetrating fog and generally good transmission through snow, but is no better than the visible/near IR wavelengths in penetrating rain, depending of course to some extent on the frequencies chosen. Atmospheric ducting is not considered a serious problem for MMW systems because it is generally a long range phenomenon, and most tactical MMW systems are designed for the shorter ranges. Ducting has been observed at 35 GHz by workers at Bell Laboratories [1], but the propagation path lengths studied were several tens of kilometers in length.

The effects of atmospheric turbulence on MMW systems are the same as those which occur in the optical wavelength spectrum, except that they are generally less severe at the longer wavelengths. These effects are power (intensity) fluctuations, phase shifts which give rise to angle-of-arrival fluctuations, depolarization, frequency shift, and thermal blooming. These latter three effects are thought to be negligible for MMW systems.

The balance of this introductory section summarizes the effects of atmospheric turbulence on MMW systems. Section 2 treats the theories of MMW turbulence including a brief reference to the Soviet theory, but emphasizing the theory of Hill, et al. [2]; and qualitatively assesses the agreement between these theories and experiment. Section 3 discusses the results of measurements of turbulence effects made during the series of experiments conducted at the site near Flatville, Illinois.

These results represent perhaps the most carefully made and carefully instrumented measurements of this type ever made. Section 4 gives some conclusions and compares the results of the measurements described above to available theory, and the agreement is found to be generally good. The report concludes with a bibliography of publications by Georgia Tech authors supported by this program and published during its course.

## 1.2 Summary of the Effects of Atmospheric Turbulence on MMW Systems

Scintillation of electromagnetic energy traversing the turbulent atmosphere is caused by refractive index inhomogeneities in the propagation path that cause phase shifts, giving rise to selective reinforcement or degradation of the energy across the wavefront. These refractive index inhomogeneities are caused by varying optical densities in the path, which are in turn caused by variations in temperature and absolute humidity in cells of various sizes within the path. These cells are called scales, and the smallest cell that has effect on propagation is called the inner scale and the largest is called the outer scale. The resulting energy distribution of electromagnetic radiation within the beam is log normal [3], and is characterized by a variance  $\sigma_E^2$  that is a function of the degree of atmospheric turbulence. The distribution of phase shifts between any two points in the wavefront is normal, and its variance is taken to be  $\sigma_\phi^2$ . Intensity fluctuations in the propagated signal cause rapid fades in signal, which may cause problems if large enough, but which probably are too small to be of consequence. Perhaps the major potential problem caused by atmospheric turbulence is angle-of-arrival fluctuations, which are related to phase shifts by the relation  $\theta = \beta/kr$ , where  $\theta$  is angle-of-arrival,  $\beta$  is phase shift,  $k$  is wavenumber  $2\pi/\lambda$ , and  $r$

is the separation between points in the wavefront. These fluctuations cause a potential target to be detected at an angle different from its actual angle, and thus give rise to aimpoint wander and decreased accuracy. Depolarization, frequency shift, and thermal blooming are other turbulence effects that can sometimes be observed at optical wavelengths, but whose effects may be shown to be negligible at MMW.

Most of the original work on atmospheric turbulence was done in the Soviet Union by Chernov [4] and Tatarski [3], and in this country by Clifford [5]. These workers treated optical fluctuations and neglected the effects of absorption on the fluctuation intensity. This approach has worked well for optical wavelengths, as attested by the large number of turbulence measurements which show good agreement with theory. More recently, several other Soviet workers have examined the problem of millimeter and submillimeter wave fluctuations; which requires that absorption by atmospheric constituents, mainly water vapor, be considered. This approach was apparently first taken by Izyumov [6,7,8] who solved the wave equation using a complex index of refraction to account for absorption, and thus obtained expressions for amplitude and phase fluctuations valid for MMW propagation. This work was further refined by Gurvich [9] and later by Armand, et al. [10]. Recent work on MMW atmospheric turbulence theory in this country has been done by Hill, et al. [2] who used the existing optical solutions for the turbulence equations and accounted for the absorption by water vapor. They derived a new index of refraction structure parameter  $C_n^2$  by considering the effects of absorption and using this result in the optical solutions. This approach will be discussed in later sections of this report.

To summarize this section, it appears that the effects of atmospheric turbulence on the performance of MMW systems are

probably small - almost negligible. It will be seen that intensity fluctuations are about 1-2 dB and angle-of-arrival fluctuations are about 300 microradians peak-to-peak under worst-case conditions. Automatic gain control circuitry should easily take care of this level of intensity change, while the 50 microradian standard deviation of angle fluctuations should be almost negligible for a system with a tracking accuracy of 100 microradians standard deviation. These conclusions are based on the measurements made at Flatville, and may not necessarily hold for extreme climatic conditions, such as those encountered in the tropics. It will also be seen that the worst case for atmospheric fluctuations occurs in clear, hot, humid weather, and not in rain or snow as one might expect. The smallest fluctuations in both intensity and phase occur during a dense fog.

Although the measurements described in this report were made at wavelengths that may not be of immediate interest to designers of Army systems, it will be shown that the results scale in a very predictable way, and may therefore be used with confidence at almost any frequency in the MMW range. The appropriate scaling law is predicted by theory and confirmed by experiment, as will be shown later in the report.

## 2. Millimeter-Wave Turbulence Theories

### 2.1 Soviet Theories

The Soviets were the first to study the problems of millimeter-wave propagation through turbulence, just as they were first to study optical propagation, and they have made important contributions in both areas. This section gives a very brief sketch of the approach taken by the Soviets in developing this MMW theory, and attempts to detail its shortcomings, if any. The treatment is necessarily brief; for a more detailed analysis, the interested reader should see the paper by Armand [10] and the references cited therein.

#### 2.1.1 General Approach

In general, the method used by workers in the Soviet Union for solving the problems of determining the magnitudes of the amplitude and phase variations of an electromagnetic wave propagating through the turbulent atmosphere consists of solving the scalar wave equation by using a complex index of refraction and thus arriving at the autocorrelation functions  $R_\chi$  and  $R_\phi$  of the fluctuations of amplitude and phase. The scalar wave equation

$$\nabla^2 u + k^2 N^2 u = 0 \quad (2-1)$$

is solved under the conditions

$$n = n_0 + u \quad (2-2)$$

$$m = m_0 + v$$

where  $u$  is the wave function,  $k$  is wave number, and  $N$  is the

index of refraction. To account for index fluctuations, the form of this index is taken to be that of equations (2-2), where  $n$  and  $m$  are the real and imaginary parts of the refractive index,  $n_0$  and  $m_0$  are the mean values of these parts, and  $u$  and  $v$  are the fluctuating parts which give rise to fluctuations in intensity and phase of the propagated MMW signal.

Equation (2-1) is solved by the method of smooth perturbations which is discussed in detail in Tatarski [3]. As mentioned above, the results of solving this equation are the autocorrelation functions  $R_\chi$  and  $R_\phi$  of the fluctuations of the amplitude and phase of the propagated signal. The  $R_\chi$  and  $R_\phi$  are functions of the spectra of the real and imaginary parts of the refractive index  $\phi_u$  and  $\phi_v$  and their cross-correlation  $\phi_{uv}$  which are in turn related in a complicated but straightforward way to the spectra of the temperature and humidity fluctuations. These can be derived from deterministic atmospheric parameters, if an appropriate form for the spectral distributions of the temperature and humidity are assumed. Such a distribution is the von Karman distribution [9], which satisfies the necessary condition of obeying the Kolmogorov  $f^{-5/3}$  law [3], where  $f$  is fluctuation frequency, for the range of atmospheric scale sizes between the inner and outer scales.

### 2.1.2 Determination of the Magnitude of Intensity Fluctuations

The log amplitude variance of the intensity fluctuations is related to the autocorrelation function  $R_\chi(a, L)$  by the equation [9]

$$\sigma_\chi^2 = R_\chi(0, L), \quad (2-3)$$

where  $a$  is correlation distance and  $L$  is transmission path length. Substitutions are made for the spectral distributions in

$R_X$  and a tractable expression for  $\sigma_X^2$  results, although it is necessary to evaluate the integrals numerically. This variance is a function of the atmospheric temperature and humidity structure parameters  $C_T^2$  and  $C_Q^2$ , respectively, the spectra of these fluctuations, and the cross-correlation of the spectra. A possible shortcoming of this theory is evident here, because this expression for log amplitude variance is not a function of the cross-correlation of the temperature and humidity structure parameters  $C_{TQ}$ , which will be seen later to be an important parameter; however, this expression for log amplitude variance gives reasonably good agreement with theory.

### 2.1.3 Determination of the Magnitude of Angle-of-Arrival Fluctuations

The angle-of-arrival of an electromagnetic wave propagating through the atmosphere at any point may be defined as the angle between the normal to the wavefront and the line-of-sight to the transmitter at that point. Fluctuations in angle-of-arrival are caused by refractive index inhomogeneities that cause phase shifts resulting in constructive and destructive interference across the wavefront which in turn cause the localized angle of the wavefront normal to change relative to the line-of-sight to the transmitter. It should be noted that the angle-of-arrival for a wavefront may not be well defined, because it will change in accordance with its correlation function, sometimes over very small distances. This parameter also changes rapidly with time, with a spectral density similar to that of the fluctuations in intensity.

The parameter which determines the angle-of-arrival is the phase as shown in Figure 2-1, which shows two receivers separated by a distance  $a$ , which is assumed to be small enough that the wavefront angle does not change appreciably if measured at each

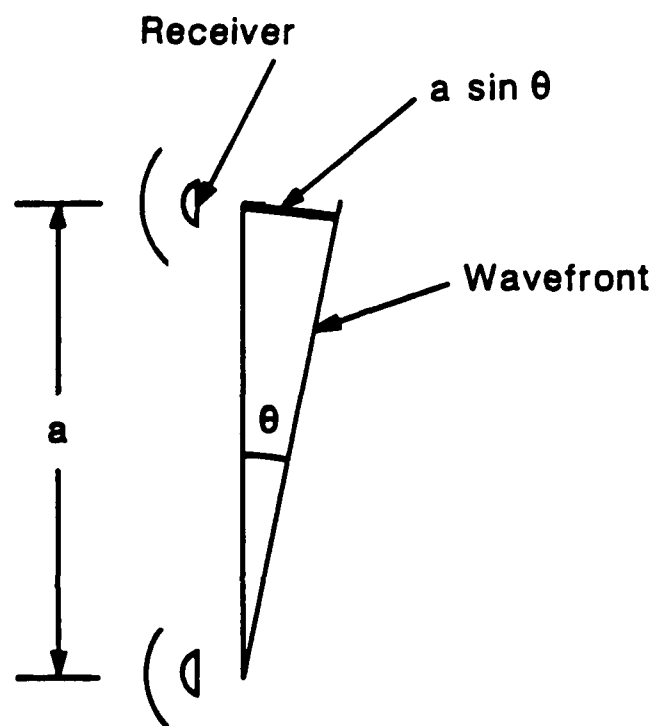


Figure 2-1. Angle-of-Arrival Geometry.

receiver. The phase difference of the signal between the two points is then

$$\beta = 2\pi/\lambda a \sin \theta \approx ka\theta, \quad (2-4)$$

since  $\theta$  is small. Using this equation, the angle-of-arrival can be determined if the phase difference is known. More particularly, the variance of the angle fluctuations can be determined from the variance of the phase fluctuations, since both are statistical quantities.

The variance of the phase fluctuations may be determined in the same way as the variance of the log amplitude fluctuations was derived, by calculating the phase autocorrelation function for zero spacing:

$$\sigma_{\phi}^2 = R_{\phi}(0, L). \quad (2-5)$$

Note that the concept of phase is not meaningful unless it is specified over some distance or time; i.e., phase is a relative parameter. The result of determining the phase autocorrelation function for zero spacing must therefore be regarded as the variance of phase fluctuations when measured as a function of time. This parameter is calculated in much the same way as the log amplitude variance, i.e. by numerical integration of the correlation integrals as discussed in Reference [10]; in fact, the integrals are the same except for sign changes. In spite of the fact that the derivation of Armand, et al. apparently does not adequately treat the cross-correlation between the temperature and humidity structure parameters, calculations using

these results give plausible agreement with experiment.

## 2.2 The Theory of Hill, Clifford, and Lawrence

In this country, the group at the National Oceanic and Atmospheric Administration (NOAA) in Boulder, Colorado, including Hill, Clifford, and Lawrence [2], has taken the lead in developing theories appropriate for the propagation of MMW radiation through the turbulent atmosphere. Perhaps a more accurate way of assessing their work is to state that they have adapted the earlier theories of optical propagation to MMW propagation by modifying the index of refraction structure parameter  $C_n^2$  to include the effects of fluctuations in humidity, characterized by the humidity structure parameter  $C_Q^2$  in addition to those of the temperature structure parameter  $C_T^2$  and their cross-correlation  $C_{TQ}$ . This approach gives perhaps a more satisfying result than that obtained by the Soviets, despite the fact that the Soviet result is based more nearly on first principles, because the NOAA work has an explicit dependence on the cross-correlation term. The treatment of this approach is necessarily brief, but again the interested reader may find more detail in the original paper of Hill, et al. [2] or in the paper by McMillan, et al. [11].

Hill, Clifford, and Lawrence [2] have derived an expression for the log amplitude variance of the fluctuations of electromagnetic radiation propagating through the turbulent atmosphere which holds for microwave through optical frequencies and maintains the proper dependence on  $C_T^2$ ,  $C_Q^2$ , and  $C_{TQ}$ . This equation comprises separate contributions from the real and imaginary parts and from the cross-correlation of these parts, as follows:

$$\sigma_{\chi}^2 = \sigma_R^2 + \sigma_I^2 + \sigma_{IR} \quad (2-6)$$

where R, I, and IR refer to the real, imaginary, and cross-correlation contributions, respectively. For spherical wave propagation, the real part of  $\sigma_{\chi}^2$  is given by

$$\sigma_R^2 = 0.124 k^{7/6} L^{11/6} \left[ 1 - 2.73 \left( \frac{L_0}{L/k} \right)^{-7/3} \right] \quad (2-7)$$

$$\cdot \left( A_I^2 \frac{C_I^2}{\langle T \rangle^2} + A_Q^2 \frac{C_Q^2}{\langle Q \rangle^2} + 2 A_Q A_T \frac{C_{TQ}}{\langle T \rangle \langle Q \rangle} \right)$$

where k is the wave number  $2\pi/\lambda$ ,  $\langle T \rangle$  is the mean value of temperature,  $\langle Q \rangle$  is the mean value of absolute humidity, and  $L_0$  is the outer scale dimension. The dimensionless parameters  $A_T$  and  $A_Q$  are functions of the refractivity of the atmosphere, which is in turn a function of the absolute temperature, humidity, and pressure of the atmosphere. Details of the determination of values for  $A_T$  and  $A_Q$  are given in References [2] and [11].

Fortunately, the contributions of the parameters  $\sigma_I^2$  and  $\sigma_{IR}$  are considered negligible because they contain a parameter  $B_Q$  which is a function of the atmospheric absorption coefficient. In the low-frequency window regions which are of interest to this study, this parameter is considered negligible, as is borne out by calculations displayed graphically in References [2] and [12].

To complete the derivation of  $\sigma_{\chi}^2$ , it is necessary to devise a value for the cross-correlation term in Equation (2-7). Hill, et al. suggest that an order-of-magnitude estimate for  $C_{TQ}$  is

$$\frac{C_{TQ}}{\langle T \rangle \langle Q \rangle} = \pm \left( \frac{C_Q^2}{\langle Q \rangle^2} \frac{C_T^2}{\langle T \rangle^2} \right)^{1/2} \quad (2-8)$$

assuming a correlation coefficient of  $\pm 1$ . That this assumption is valid is borne out by numerous experiments conducted at Flatville, IL, which will be described in some detail later. During the daytime, especially on clear, sunny days when the sun is warming the ground, temperature and humidity fluctuations were observed to have a correlation coefficient of unity, and in the morning and evening, when the earth is warmer than the air, the correlation coefficient is  $-1$ . The transition between these two states occurs in the morning and evening over a time span of a very few minutes. It is therefore valid to take the correlation coefficient in Equation (2-9) to be exactly  $\pm 1$ .

Since  $\sigma_X^2 = \sigma_R^2$  the log amplitude variance for MMW propagation in the window regions is given by Equation (2-7). By comparison of this equation to similar expressions derived for propagation in the optical portion of the spectrum, one may conclude that  $C_n^2$  for MMW propagation in the window regions is given by the portion of Equation (2-7) enclosed in large parentheses. In addition, Tatarski [3] has shown that the variance of the angle-of-arrival fluctuations of a spherical wave is given approximately by

$$\sigma_A^2 = 0.54 LC_n^2 r^{-1/3}, \quad (2-9)$$

where  $\sigma_A$  is measured in radians, and where  $r$  may be interpreted as the spacing between antennas in an array or the width of a large antenna. Note that Equation (2-9) predicts, perhaps surprisingly, that the magnitude of angle-of-arrival fluctuations is independent of frequency.

Equations (2-7) and (2-9) contain essentially all that needs to be known, in fairly simple form, to calculate the effects of turbulence on MMW propagation, provided the structure parameters

of temperature and humidity, together with basic information about temperature, humidity, and atmospheric pressure are known. In later sections the results of calculations using these expressions will be compared to experimental results obtained.

### 3. Results of Measurements of Turbulence Effects at Millimeter-Wave Frequencies

#### 3.1 Results Obtained at Burlington, Vermont

The Snow-One measurement effort was conducted at Fort Ethan Allen near Burlington, Vermont during the winter of 1981-82. This series of tests was concerned with the measurement of propagation through snow and other types of winter weather by several different wavelengths, including 35, 94, 140, and 217 GHz, and with measurements of such phenomena as snow backscatter. Meteorological support for these tests did not include turbulence instrumentation, and on the day that turbulence measurements were made, essentially all of the met instrumentation had been damaged by a storm on the night before. These handicaps did not preclude the acquisition of some data which turned out to be among the most important obtained to date, because they verify the scaling laws relative to frequency and range. The Burlington tests were unique in this regard, because they provided the means to make simultaneous measurements at four different frequencies and two different ranges.

The measurements of turbulence fluctuations at the wavelengths mentioned above were made by D.G. Bauerle of the U.S. Army Ballistic Research Laboratory at Aberdeen Proving Ground, MD, and the data were analyzed by G.R. Ochs of NOAA. Figure 3-1 is a diagram of the experiment, in which radiation from four radar transmitters at each of the above frequencies is propagated simultaneously down range to reflect from corner reflectors at two different ranges. This experiment was originally designed to measure absolute atmospheric attenuation by comparing the returns from the two corner cubes at known ranges. The signal is perturbed by the atmosphere in both directions and finally collected by a receiver, detected, and output to four strip-chart

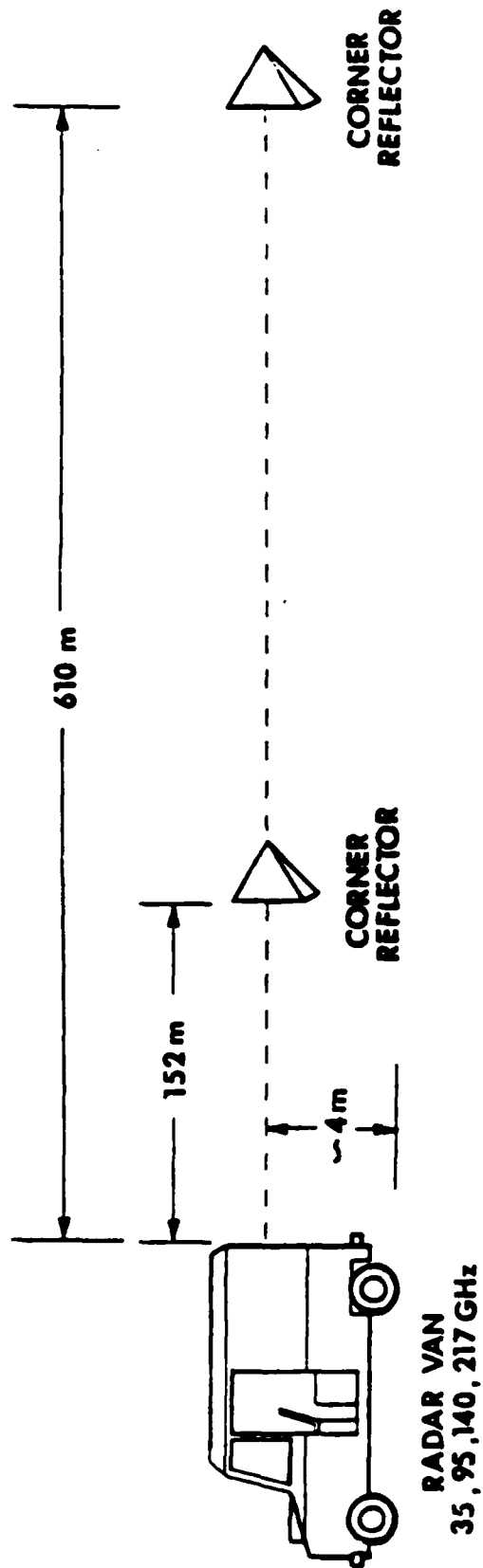


Figure 3-1. Layout of the measurement system used for evaluating turbulence effects at the Snow-One site near Burlington, VT.

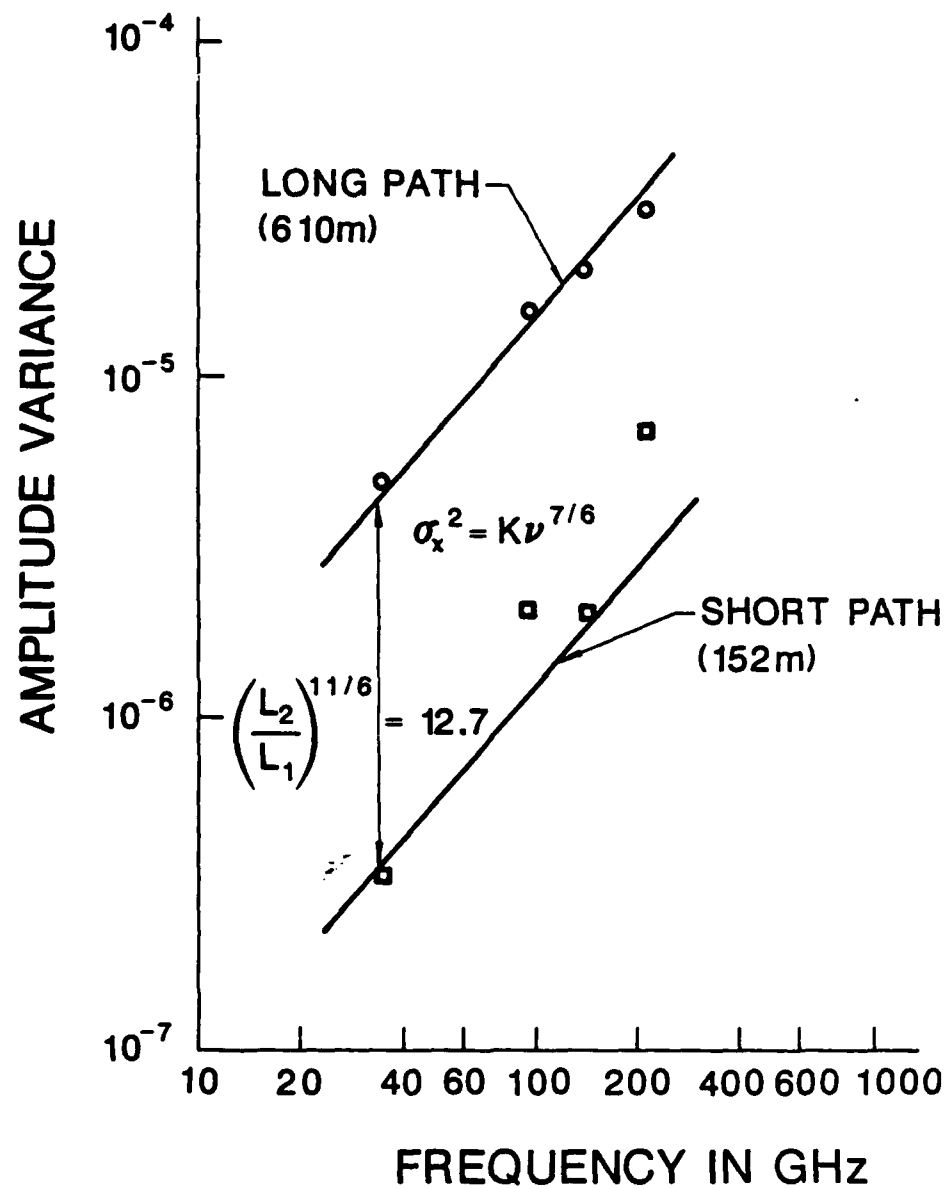


Figure 3-2. Log amplitude variance for MMW propagation in turbulence as a function of frequency and range, showing that the scaling relations are valid.

recorders. The resulting data were then analyzed to determine the log amplitude variance as a function of both frequency and range. The results of this analysis are shown in Figure 3-2. The log amplitude variance was first plotted as a function of frequency for the long (610m) path, and the best straight line was drawn through the points. This line was found to have a slope essentially equal to the  $k^{7/6}$  slope predicted by theory. This line was then moved downward by a factor of 12.7, which corresponds to  $(L_2/L_1)^{11/6}$ , and a line parallel to the first was drawn. The log amplitude variance data from the shorter (152m) path was then plotted, with the result shown in the figure. These results show that the frequency scaling law  $\nu^{7/6}$  is very well verified for the longer range and less well verified for the shorter range, although the agreement with theory of the short-range measurements is quite good when compared to other measurements of this type, which typically have quite a bit of scatter. The range scaling law  $(L_2/L_1)^{11/6}$  is also fairly well verified. The poorer agreement obtained for the shorter range may be due in part to the fact that the corner cubes were in the near field of the antennas, at least for the higher frequencies.

These results are significant because they show that the large number of measurements made at the Flatville, IL site at frequencies in the range 116-230 GHz may be scaled to frequencies of greater interest to the Army in the near term, notably 94 GHz. Although the Burlington results were obtained with essentially no met support, they are still very important for this reason. As far as is known, no other measurements of turbulence phenomena have been made at more than one frequency at a time or at more than one range. Fortunately, the fairly unique measurement system developed by the Ballistic Research Laboratory was available at the proper time to make these measurements.

## 3.2 Experiments Conducted at Flatville, Illinois

### 3.2.1 Description of Experiments

Since the summer of 1983, Georgia Tech, NOAA, and the U.S. Army Atmospheric Sciences Laboratory (ASL), with Army Research Office (ARO) support, have been engaged in a program whose purpose is to measure the effects of atmospheric turbulence on the propagation of millimeter waves [12,13]. Five different measurement sessions have been conducted, and observations have been made in clear air, rain, fog, and snow at frequencies of 116, 118, 142, 173, and 230 GHz, so that results have been obtained on or near all atmospheric features of interest in this range, including the 118 GHz oxygen line, the 140 GHz window, the 183 GHz water vapor line, and the 230 GHz window. These measurements have been made over a 1.4 km path at a site near Flatville, Illinois, chosen for its exceptional flatness. Figure 3-3 is a diagram of the layout of the experiment site and Figure 3-4 is a photograph of the propagation path looking from transmitter toward receiver. In making measurements of this type, it is important that the path and surrounding terrain be flat, homogeneous, and free of trees or other obstructions, to avoid perturbation of the atmospheric fields. The following paragraphs discuss the equipment used to make these measurements, and the next section presents some results obtained under each of the types of atmospheric conditions under which measurements were made.

#### 3.2.1.1 Transmitter Subsystem

Phase-locked reflex klystron oscillators were used as both transmitters and receiver local oscillators in this experiment, with the exception of the 230 GHz system which used a phase-locked cw extended interaction oscillator as transmitter [14,15].

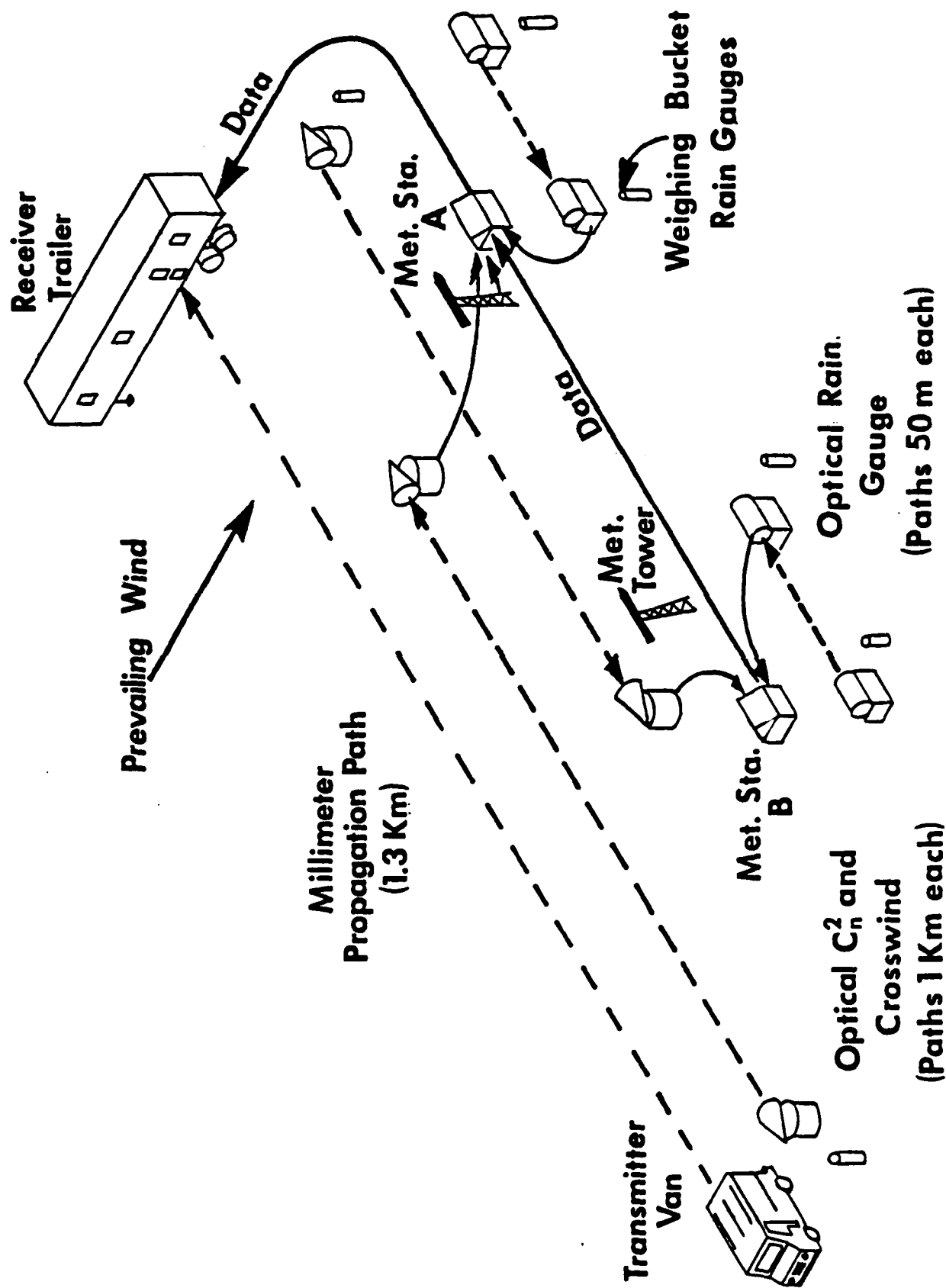


Figure 3-3. Diagram of the Flatville experiment showing transmitter, receiver, and meteorological instrumentation.



Figure 3-4. Photograph of the propagation range at Flatville, viewed looking South. The receiver trailer is in the foreground, and some of the ASL met instrumentation can be seen to the left.

Phase-locking of the sources is necessary in this experiment for three reasons: (1) it improves amplitude stability of the source so that the transmitter power variations are less than the smallest atmospherically induced fluctuations, (2) it narrows the bandwidth and therefore improves the detection signal-to-noise ratio, (3) phase-locking aids in system calibration because the receiver second intermediate frequency (IF) output is a very stable sine wave. Figure 3-5 is a block diagram of the transmitter and Figure 3-6 is a photograph of the 230 GHz EIO transmitter showing the horn antenna and phase-lock mixer. The primary antenna, fed by the horn antenna shown in Figure 3-6, was an offset paraboloid with an elliptical shape, resulting in an elliptical beam pattern with long axis horizontal. This arrangement gives a beam shape which roughly conforms to the extent of the horizontally distributed receiver array.

The transmitter was housed in a small step-van truck, and was mounted on a steel pedestal which was, in turn, mounted to a concrete pad in the ground, thus mechanically isolating the transmitter from the truck suspension. The truck was supported off its wheels and fixed to the ground with screw anchors. A high-density polyethylene transmission window was placed in the rear door, and this window was protected by a plywood and canvas awning. Figure 3-7 is a photograph of this transmitter truck.

#### 3.2.1.2 Receiver Subsystem

The receiver comprises four apertures with individual mixers and with separations varying from 1.4 to 10 meters, so that a wide range of atmospheric scale sizes can be considered in the determination of the millimeter wave mutual coherence function. Local oscillator (LO) power was distributed to the mixers via a low-loss optical beam waveguide system [16]. Figure 3-8 is a diagram of the beam waveguide system, and Figure

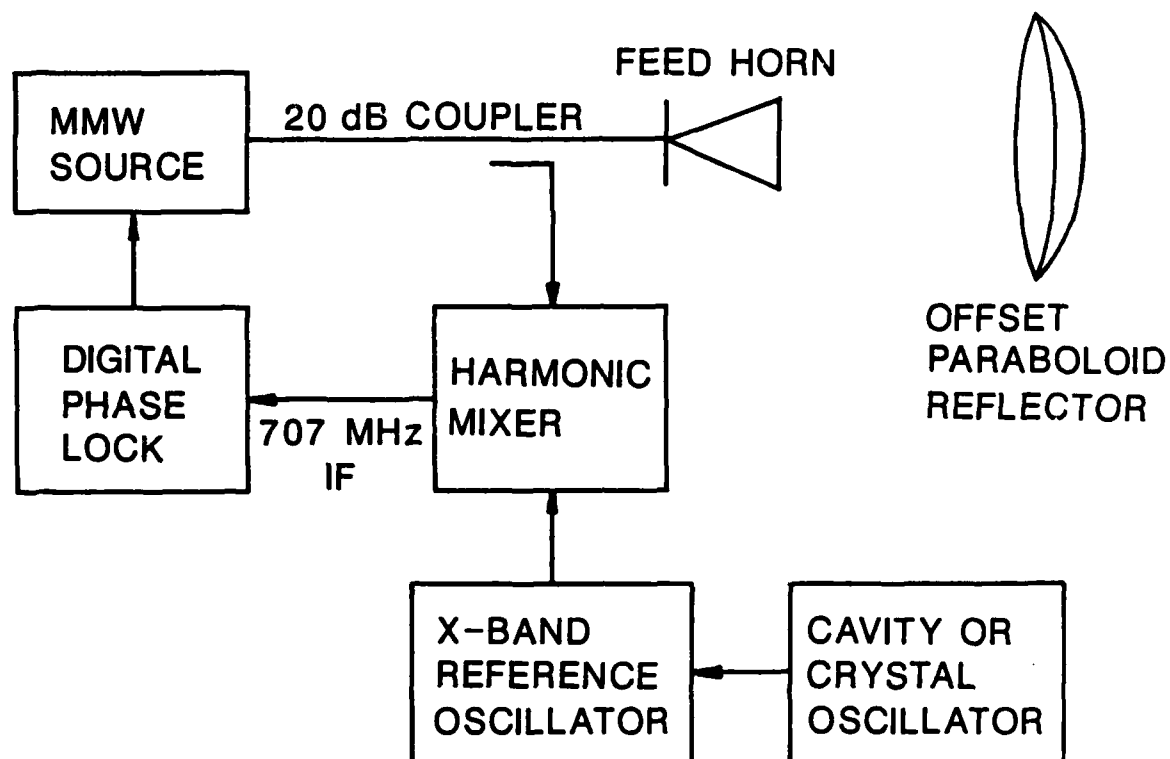


Figure 3-5. Block diagram of the transmitter subsystem showing phase-lock loop.



Figure 3-6. Photograph of the 230 GHz extended interaction oscillator source used in Session 5.



Figure 3-7. Photograph of transmitter truck. This truck was placed on a mound of earth so that transmitter and receiver were at the same height.

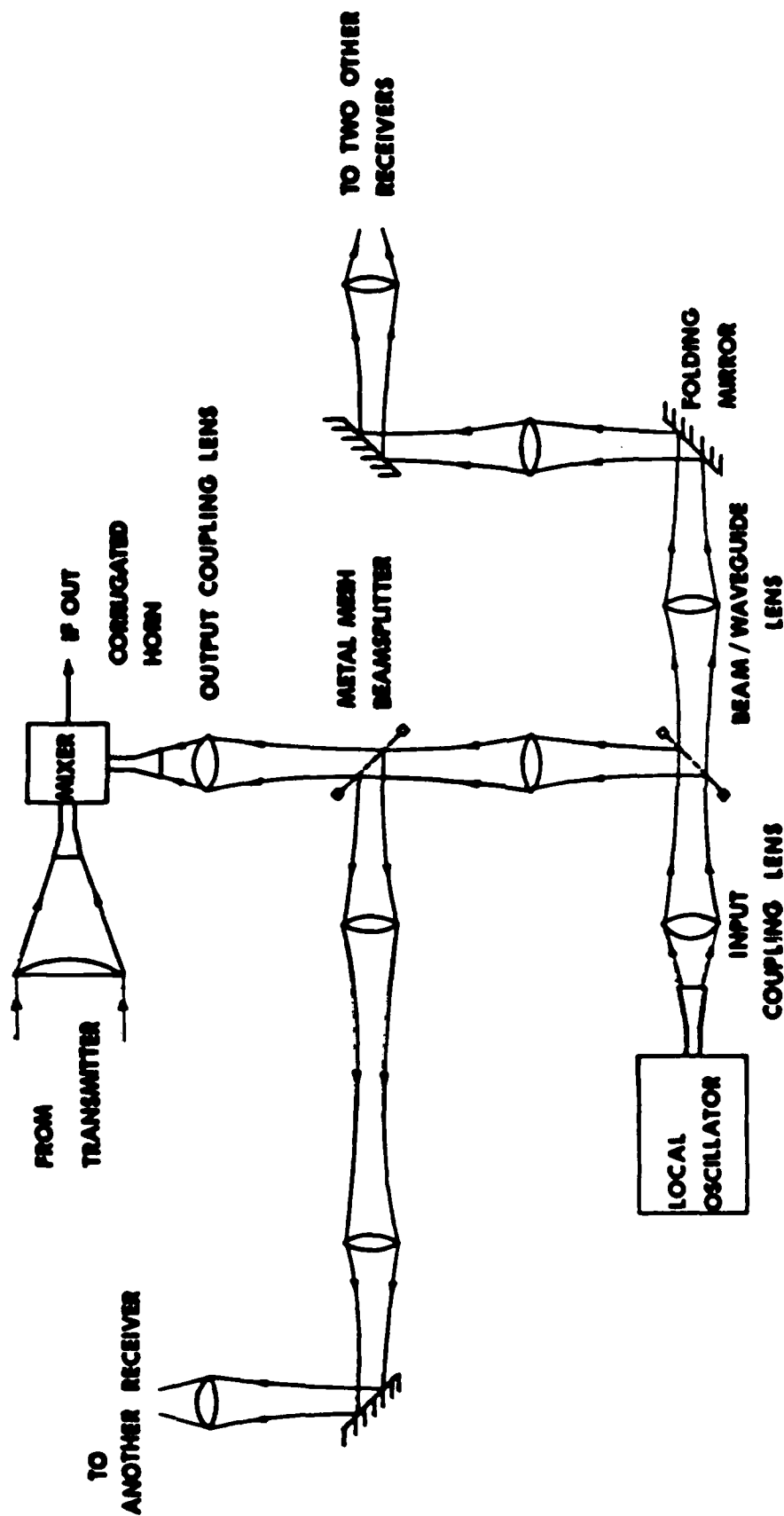


Figure 3-8. Diagram of beam waveguide system used for local oscillator distribution.

3-9 is a photograph of this system. The receivers used double conversion, and RF signal combining and detection were done at the second IF, where signals were combined from the six possible combinations of antennas to give the proper phase relationships for determination of the mutual coherence function. These signals were stored on magnetic tape along with signals from the meteorological instruments by the data acquisition computer.

The receiver mixers were cross-guide X2 harmonic types so that the LO frequency was nominally one-half the signal frequency. The signals were mixed with the second harmonic of the LO to give four 930 MHz first IF signals, which were amplified by low noise amplifiers and transmitted over cable to the signal combiner, where they were further downconverted to the second IF of 30 MHz for signal combining. This frequency was chosen because of the good choice of phase shifters, attenuators, and other devices available in this commonly used band. Figure 3-10 is a block diagram of the receiver subsystem.

The receiver antennas were high-density polyethylene lenses fed by corrugated horns. Steering of the received signals was accomplished by gimbaled mirrors. The receiver windows were also made of high-density polyethylene, and the four windows were protected from the accumulation of rain and snow by canvas and metal awnings. The four receivers and the optical beam waveguide system were mounted to an I-beam, which served as an optical bench. This I-beam was, in turn, fixed to two steel pedestals resting on concrete slabs in the ground. The entire receiver subsystem was housed in a semi-trailer, which was insulated, heated, and air conditioned for all-weather operation. Figure 3-11 is a photograph of the receiver trailer.

A fifth receiver aperture, located below the second aperture from the right as the trailer is viewed from the side on which the apertures are located, was also used for some measurements.

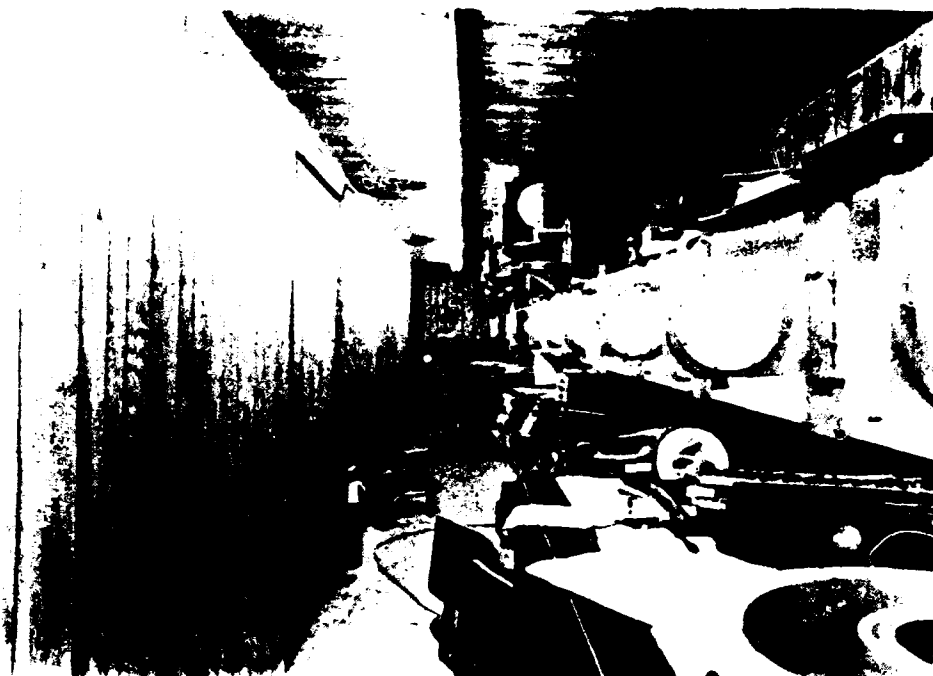


Figure 3-9. Photograph of the interior of the receiver trailer showing beam waveguide lenses. The local oscillator is at the far end of the beam and one of the receiver lenses can be seen near the top of the picture.

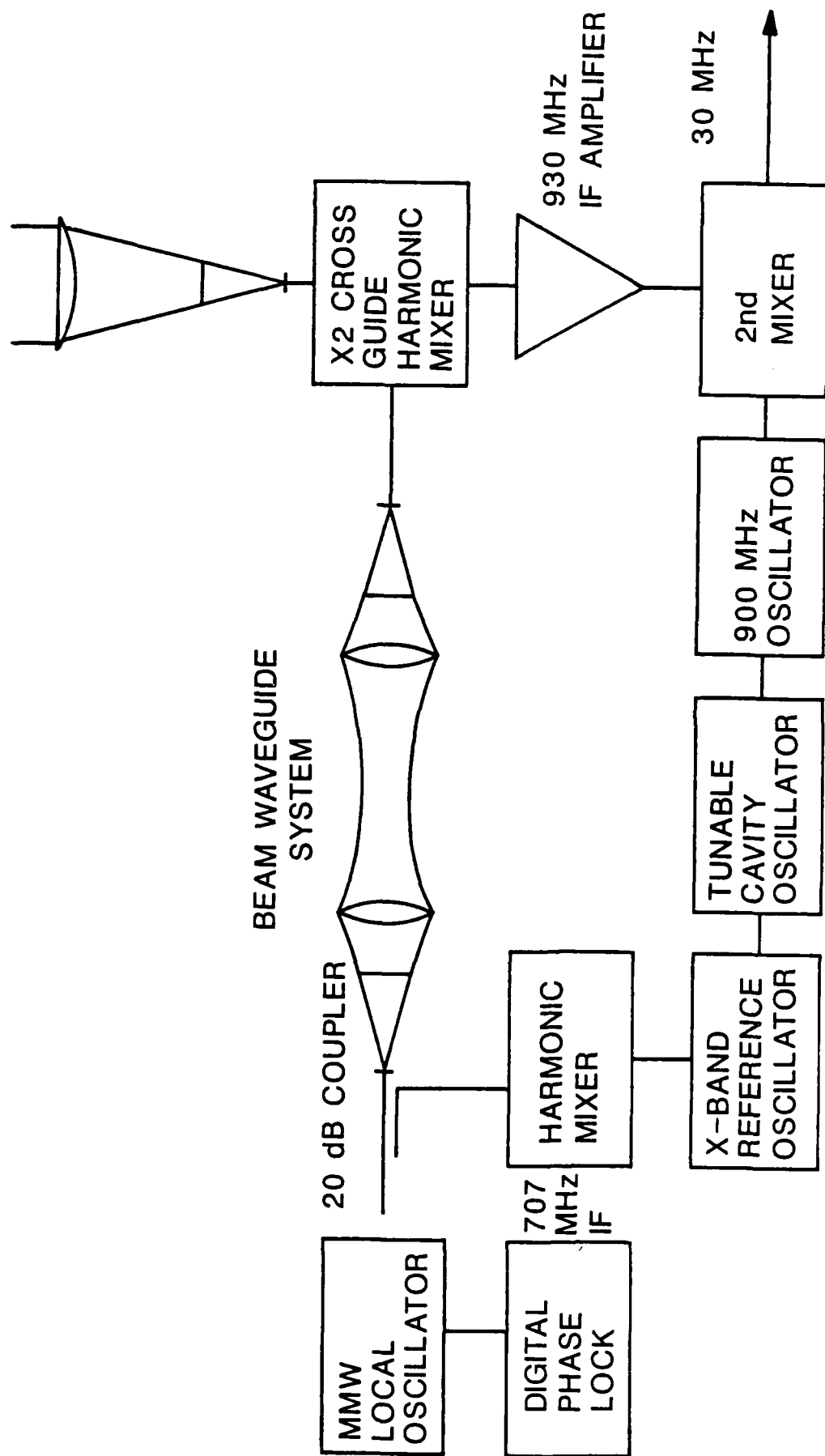


Figure 3-10. Block diagram of the double-conversion receiver showing relationship to beam waveguide.

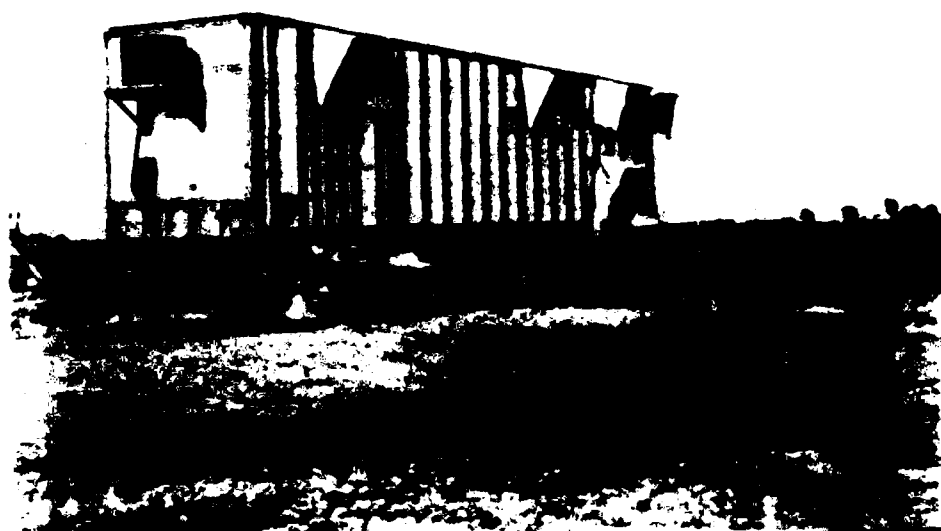


Figure 3-11. Photograph of the receiver trailer showing steel/concrete I-beam supports and aperture awnings.

The vertical spacing of this aperture (number 5) from aperture 2 was chosen to equal the horizontal spacing between apertures 1 and 2. This fifth receiver antenna was rarely used, and almost all of the meaningful measurements obtained at Flatville were made with the horizontal array of four antennas discussed in the paragraph above.

### 3.2.1.3 Signal Combiner

If signals from a pair of antennas are combined vectorially and the resulting power is measured by a receiver, the power measured will be [11]:

$$|V_n|^2 = |V_1|^2 + |V_2|^2 + 2|V_1||V_2|\rho(r)\cos[\alpha_n - \beta(r)] \quad (3-1)$$

where  $V_1$  and  $V_2$  are the individual antenna signals and  $\rho(r)$  and  $\beta(r)$  are the factors of the mutual coherence function, which is a measure of the effects of the atmosphere on propagation of the signal. The term  $\alpha_n$  is a deliberately introduced phase shift which is stepwise variable over the range 0, 90, 180, and 270 degrees. If this phase shift is varied over this range, the four signals  $V_0$ ,  $V_{90}$ ,  $V_{180}$ , and  $V_{270}$  will be generated, and it is possible to solve for  $\beta$  and  $\rho$  in terms of them as follows:

$$\beta(r) = \tan^{-1} \frac{|V_{90}|^2 - |V_{270}|^2}{|V_0|^2 - |V_{180}|^2} ; \quad (3-2)$$

$$[\rho(r)]^2 = \frac{(|V_0|^2 - |V_{180}|^2)^2 + (|V_{90}|^2 - |V_{270}|^2)^2}{16|V_1|^2 |V_2|^2}$$

These combinations of signals are generated from raw data in the signal combiner, which operates at 30 MHz as mentioned above. Figure 3-12 is a block diagram of the signal combining subsystem of the turbulence instrumentation. Only two channels are shown for clarity; the actual system has six such channels, corresponding to the six possible antenna spacings, and the actual combining was done in a slightly different way, although the concept is the same.

#### 3.2.1.4 Meteorological Instrumentation

Although the meteorological instrumentation subsystem was the responsibility of the group from NOAA, it will be briefly described here for completeness. During the times in which millimeter wave data were being acquired, simultaneous measurements of pertinent meteorological parameters were made. These parameters included temperature, humidity, 3-dimensional wind velocity, temperature and humidity structure parameters, optical index of refraction structure parameters, and particle size spectra. These variables were measured at the same height as the MMW propagation path at two different stations placed downwind from the path. These meteorological variables serve to relate the MMW results measured to those obtained from the turbulence theory. Figure 3-3 shows how the stations which collected these met data were situated relative to the propagation path and the prevailing wind, and Figure 3-13 is a photograph of one of these met stations. A total of 39 channels of met data were transmitted over fiber-optic links to the receiver trailer, where they were stored on magnetic tape in time coincidence with the 28 channels of MMW data.

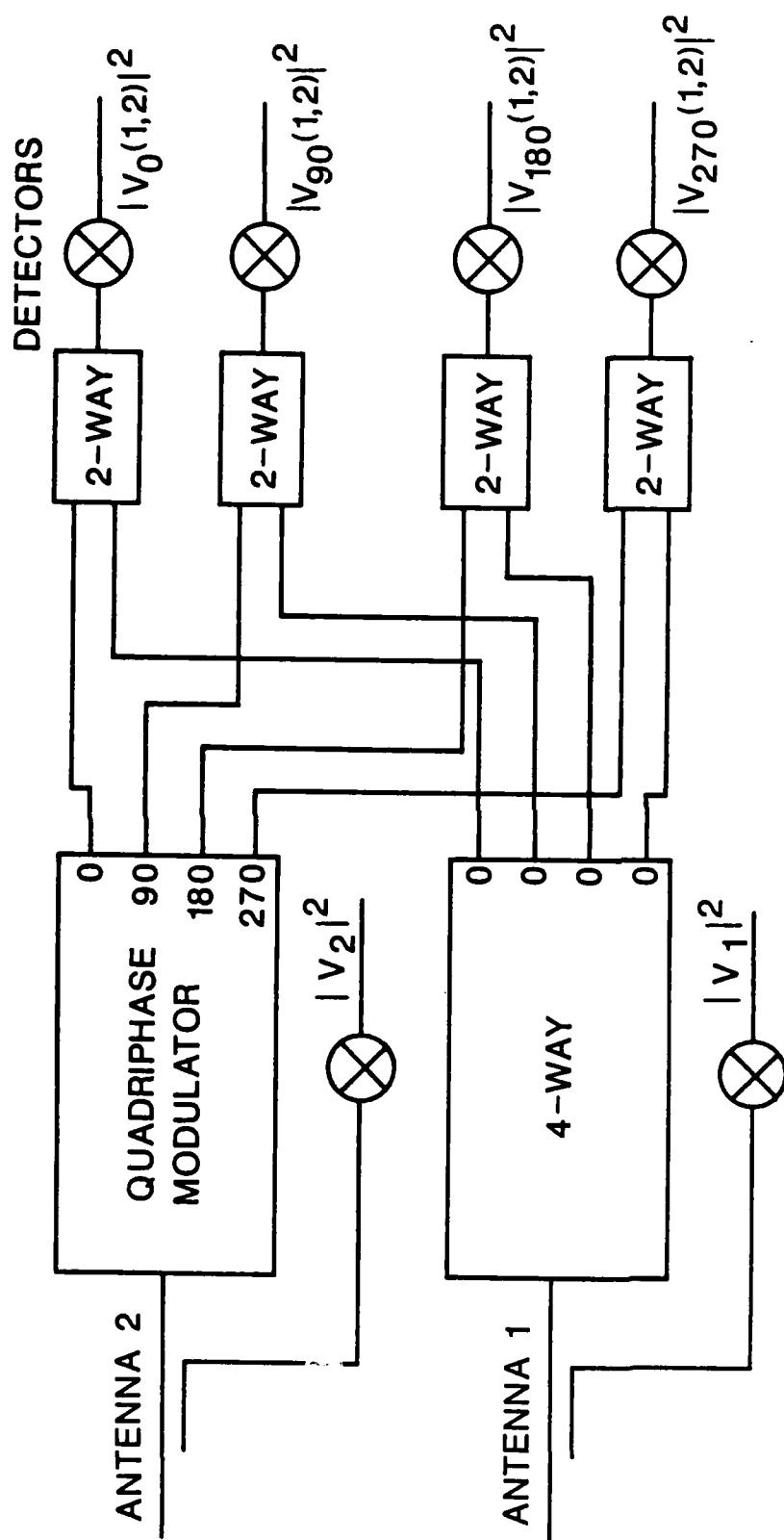


Figure 3-12. Block diagram of one channel of the signal combiner.

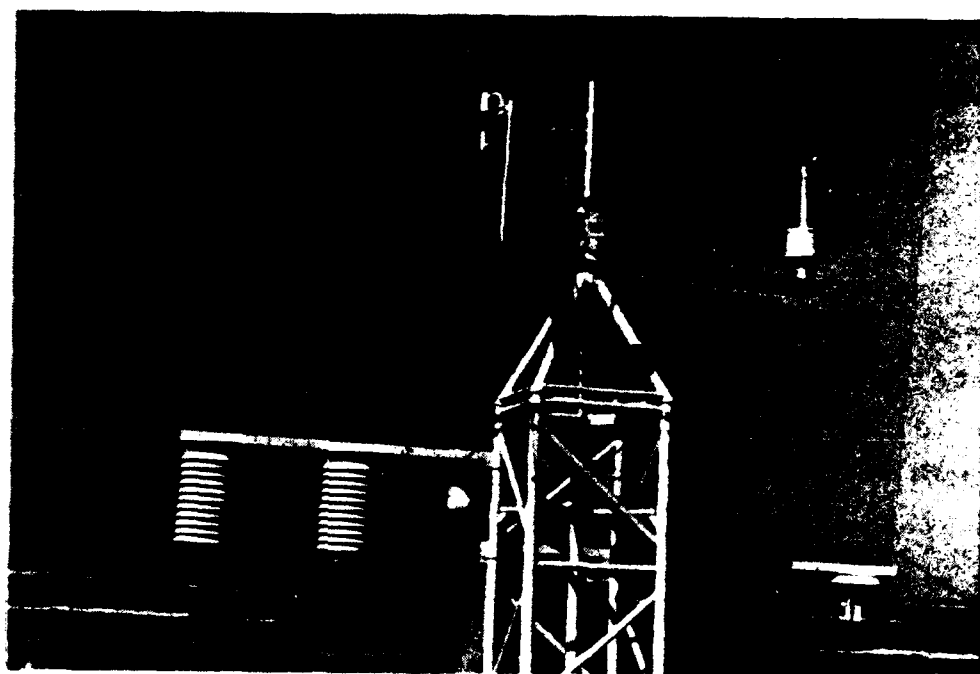


Figure 3-13. Photograph of one of the met stations, showing left to right: a Lyman- hygrometer, a sonic anemometer and a prop-vane anemometer. The Lyman- and sonic anemometer have a fine-wire temperature probe at their centers. On the lower level are two psychrometers and a Vaisala humidiometer.

### 3.2.1.5 Data Collection/Processing Subsystem

The data collection system consisted of three microcomputers operating in parallel, a hard disk, a video monitor, printer, and a magnetic tape system. The 28 MMW signals from the signal combiner discussed above were fed into a bank of signal conditioners, multiplexed to an analog-to-digital (A/D) converter and stored on tape along with the 39 channels of met data. The met data were partially processed and A/D converted by field computers located at the two met stations. The main function of the computer is thus seen to be data accumulation and storage, but it also performed a variety of other functions which monitored the performances of both the MMW and met systems. Among other tasks, the computer performed on-line calculations of  $\rho$  and  $\beta$ , output met data to chart recorders for monitoring, and greatly aided in calibrating the MMW system. Although off-line data processing is normally the province of larger and faster computers, the data collection computer has also performed this function in a limited way, mostly for quick-look calculations on small amounts of data.

### 3.2.2 Results

Although detailed analysis of the MMW turbulence data is still under way, and may continue for some time, some very interesting and useful results are available. Intensity fluctuations range from near zero in a heavy fog to about 50% of the nominal amplitude peak-to-peak on a hot, humid summer day. Fluctuations in rain and snow fall somewhere between these two extremes. Phase fluctuations range out to  $\pm\pi$  on a hot, humid summer day, corresponding to an angle-of-arrival of 200 microradians peak-to-peak. It appears that the log amplitude variance of the amplitude fluctuations increases with frequency as  $\nu^{7/6}$ , as predicted by theory. The distribution of intensity

### 3.2.1.5 Data Collection/Processing Subsystem

The data collection system consisted of three microcomputers operating in parallel, a hard disk, a video monitor, printer, and a magnetic tape system. The 28 MMW signals from the signal combiner discussed above were fed into a bank of signal conditioners, multiplexed to an analog-to-digital (A/D) converter and stored on tape along with the 39 channels of met data. The met data were partially processed and A/D converted by field computers located at the two met stations. The main function of the computer is thus seen to be data accumulation and storage, but it also performed a variety of other functions which monitored the performances of both the MMW and met systems. Among other tasks, the computer performed on-line calculations of  $\rho$  and  $\beta$ , output met data to chart recorders for monitoring, and greatly aided in calibrating the MMW system. Although off-line data processing is normally the province of larger and faster computers, the data collection computer has also performed this function in a limited way, mostly for quick-look calculations on small amounts of data.

### 3.2.2 Results

Although detailed analysis of the MMW turbulence data is still under way, and may continue for some time, some very interesting and useful results are available. Intensity fluctuations range from near zero in a heavy fog to about 50% of the nominal amplitude peak-to-peak on a hot, humid summer day. Fluctuations in rain and snow fall somewhere between these two extremes. Phase fluctuations range out to  $\pm\pi$  on a hot, humid summer day, corresponding to an angle-of-arrival of 200 microradians peak-to-peak. It appears that the log amplitude variance of the amplitude fluctuations increases with frequency as  $\nu^{7/6}$ , as predicted by theory. The distribution of intensity

fluctuations appears to be log normal, and that of phase fluctuations is normal, also predicted by theory. It also has been verified that water vapor in the atmosphere has a strong effect, causing MMW index of refraction structure parameters to be several orders of magnitude larger than those in the visible spectrum. The next few subsections separately present results obtained in clear air, rain, snow, and fog. Some of the figures in these sections are the result of data processing by NOAA, and were furnished by NOAA to Georgia Tech.

#### 3.2.2.1 Clear Air Results

As was mentioned earlier, turbulence fluctuations are larger in clear air than for any other atmospheric condition. It is also true that the theory of turbulence in clear air is much more mature than for other conditions, which is fortunate because the effects of turbulence in turbid weather are more difficult to explain, and if turbid weather effects were dominant, the necessity for explaining them would become more urgent. Figure 3-14 shows intensity fluctuations measured at 142 GHz on a hot, humid summer day, and Figure 3-15 is a copy of a chart recorder trace which shows the corresponding phase fluctuations. Figure 3-16 shows intensity fluctuations measured at 173 GHz under the same types of conditions. These fluctuations are perhaps the largest observed during the Flatville series of measurements. Table 3-I summarizes the atmospheric conditions under which these 173 GHz measurements were made. Figure 3-17 gives the probability distribution of the 173 GHz fluctuations, and shows that the log-normal distribution, predicted by theory, is a better fit to the data than the normal distribution. Figure 3-18 shows the probability distribution of the 173 GHz phase fluctuations, which are normally distributed, in accordance with theory. Figure 3-19 shows measured values of the phase structure

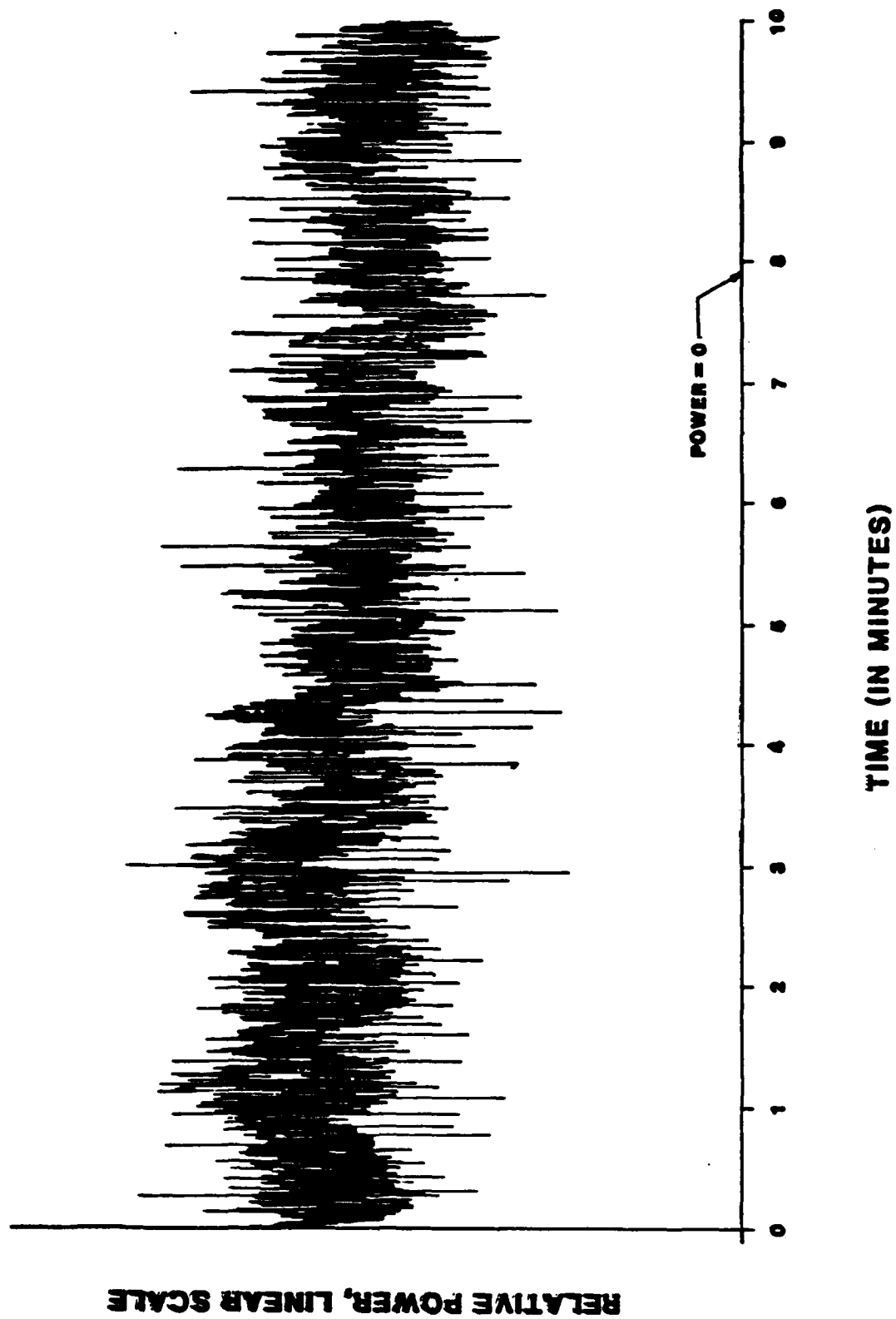


Figure 3-14. Copy of a chart recorder trace showing fluctuations observed at 142 GHz on a hot humid sunny day.

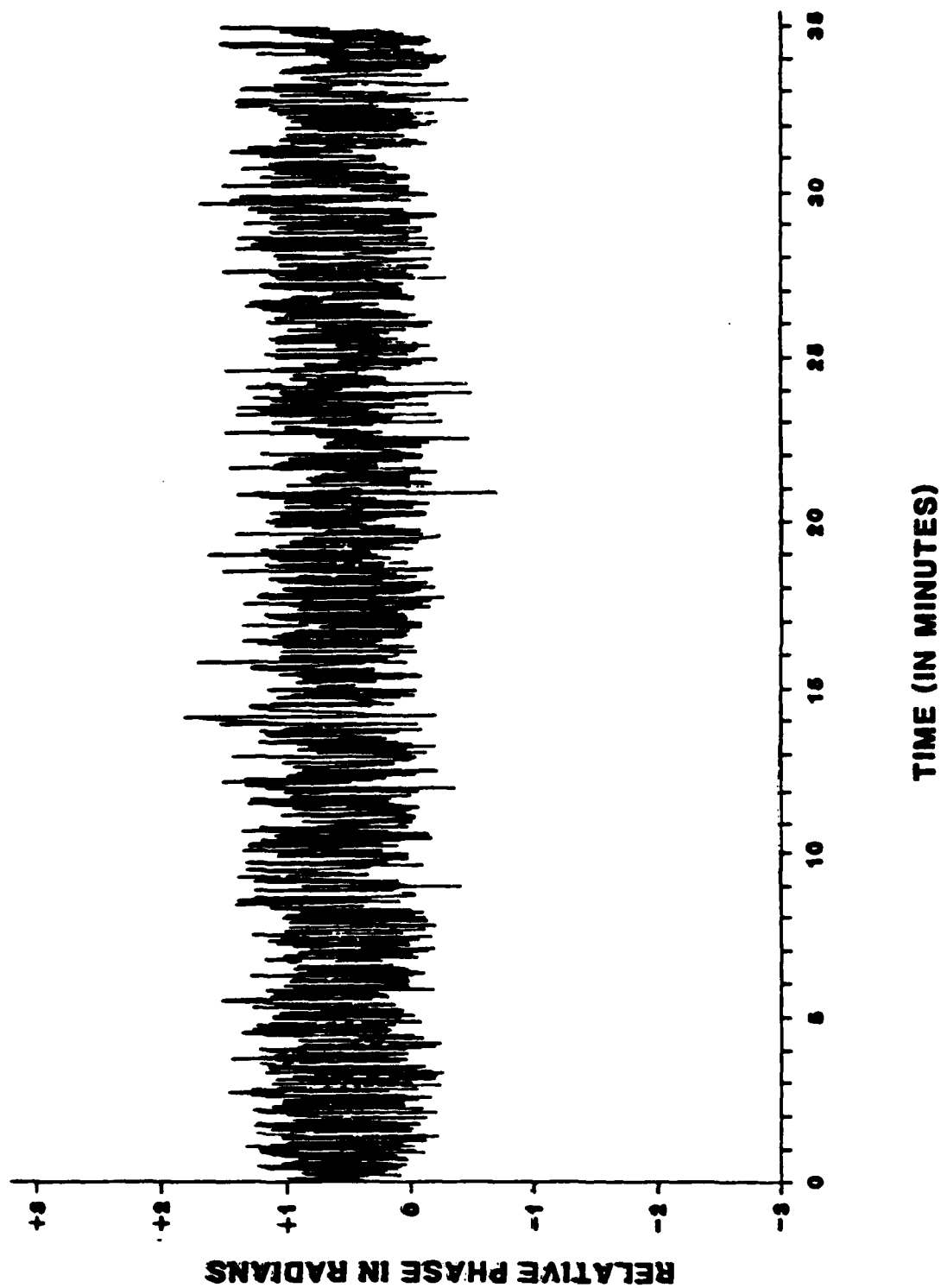


Figure 3-15. Copy of a recorder trace showing phase shift measured between antennas 1 and 4 at 142 GHz. This trace corresponds to the intensity measurement shown in Figure 3-14.

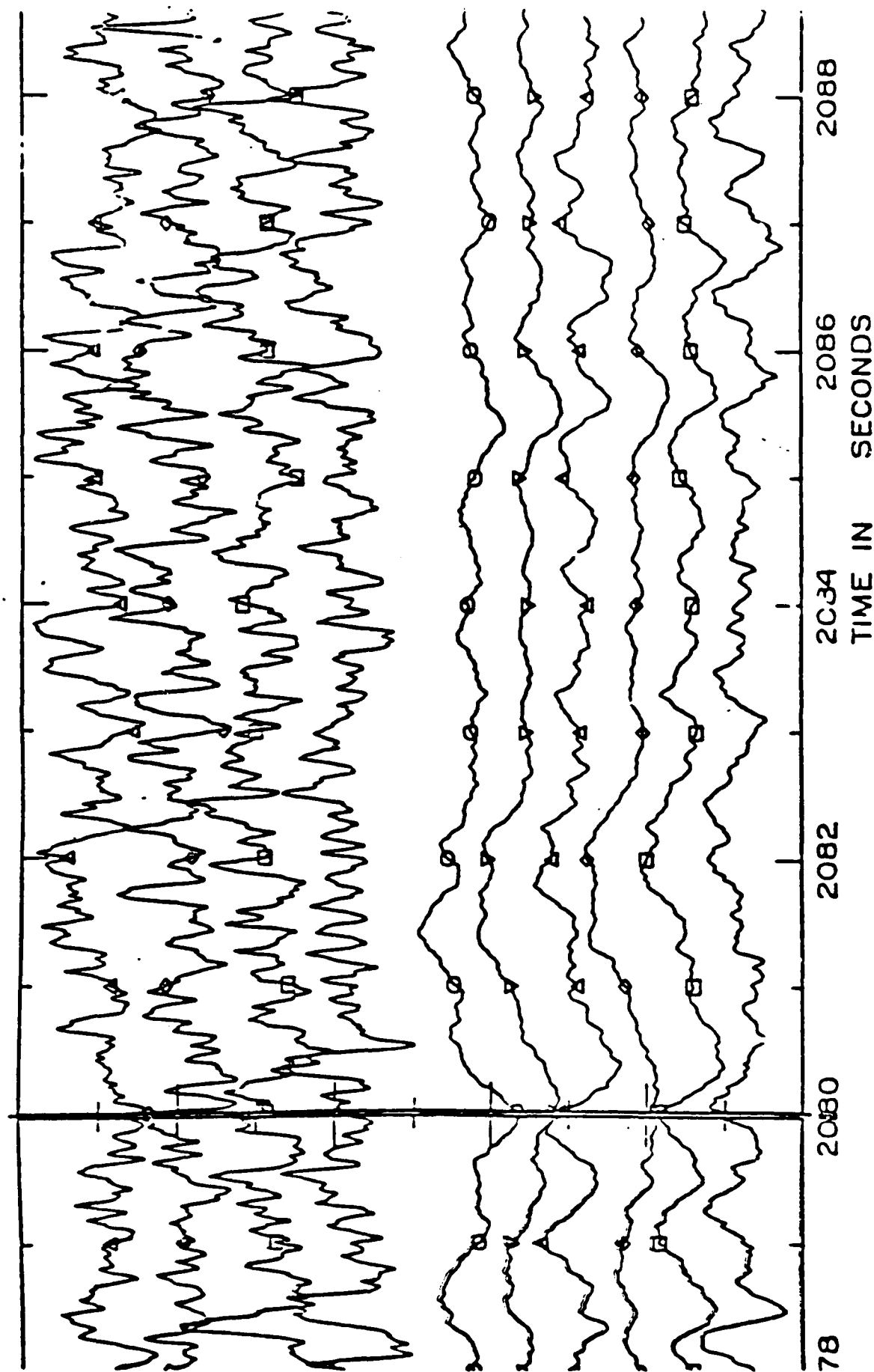


Figure 3-16. Intensity (upper) and phase (lower) fluctuations observed for all four antennas and six antenna pairs at 173 GHz on a hot, humid summer day.

Table 3- I

Summary of Meteorological Parameters  
Corresponding to Figures 3-16 and 3-18.

Average Values	
Humidity	19 g/m <sup>3</sup>
Temperature	32°C
Wind speed	5.3 m/s
Wind angle	10°
Pressure	993 mb
Solar flux	94% of full sun
Wind stress	-0.14 (m/s) <sup>2</sup>
Humidity flux	0.1 (g/m <sup>2</sup> )/s
Temperature flux	0.03°C m/s
Stability	-0.03
Square Roots of Variances	
Humidity	0.72 g/m <sup>3</sup>
Temperature	0.35°C
Wind speed	1.2 m/s
Wind angle	11°
Streamwise wind component	1.1 m/s
Cross-stream wind component	1.0 m/s
Vertical wind component	0.54 m/s
Structure Parameters	
$C_n^2$ from optical scintillometers	$2 \times 10^{-13} \text{ m}^{-2/3}$
$C_T^2$ from optical $C_n^2$	$0.03^\circ\text{C}^2 \text{ m}^{-2/3}$
$C_T^2$ from resistance wires	$0.03^\circ\text{C}^2 \text{ m}^{-2/3}$
$C_q^2$ from Lyman- $\alpha$ hygrometers	$0.2 (\text{g/m}^3)^2 \text{ m}^{-2/3}$
$C_{Tq}$ from resistance wires and Lyman- $\alpha$ hygrometers	$0.075^\circ\text{C} (\text{g/m}^3) \text{ m}^{-2/3}$
$C_n^2$ for radio frequencies	$5.9 \times 10^{-12} \text{ m}^{-2/3}$

## INTENSITY PROBABILITY DISTRIBUTION

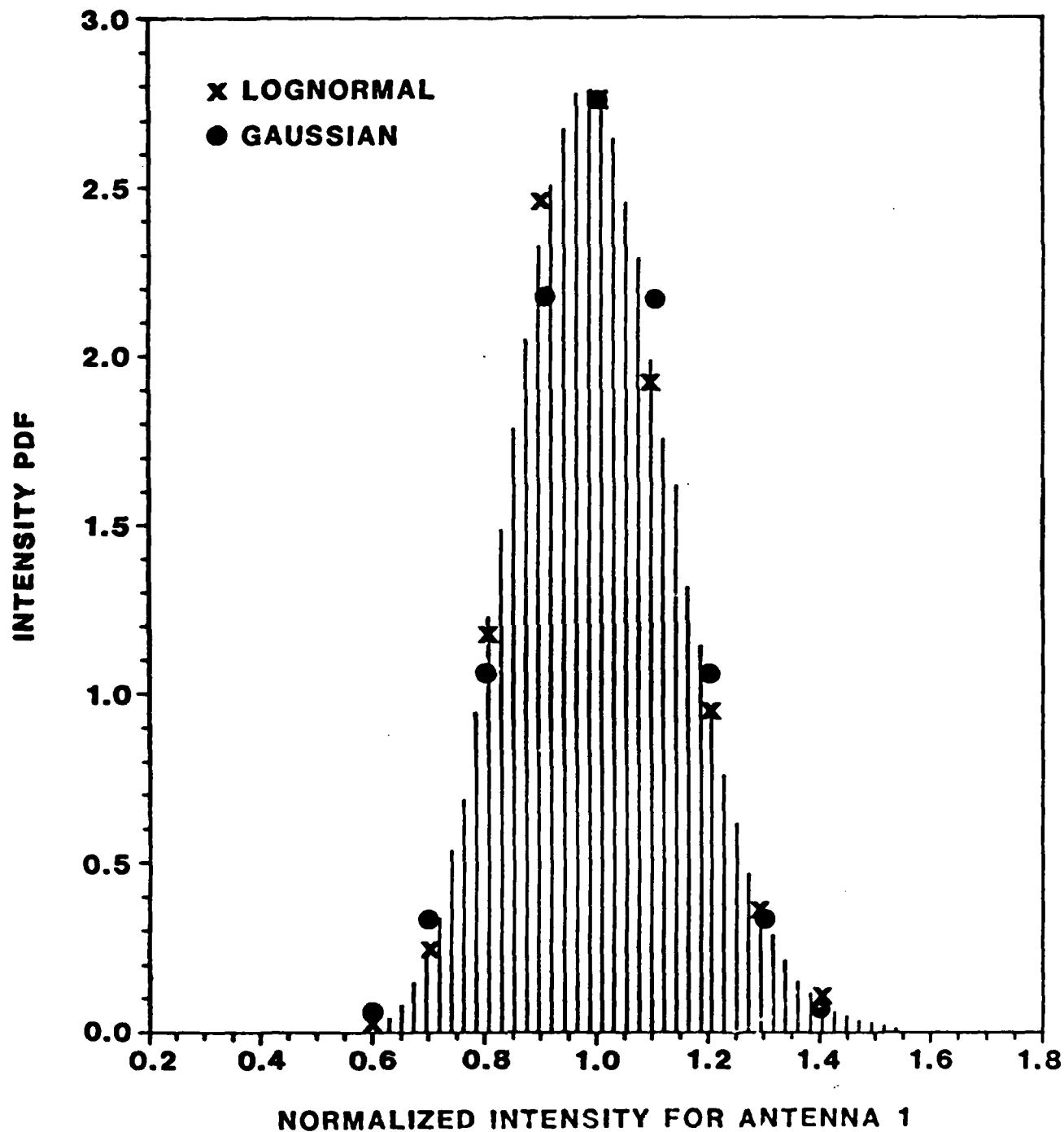


Figure 3-17. Intensity probability distribution function corresponding to Figure 3-16. Note that the log normal distribution is a better fit to the data.

# PHASE PROBABILITY DISTRIBUTION

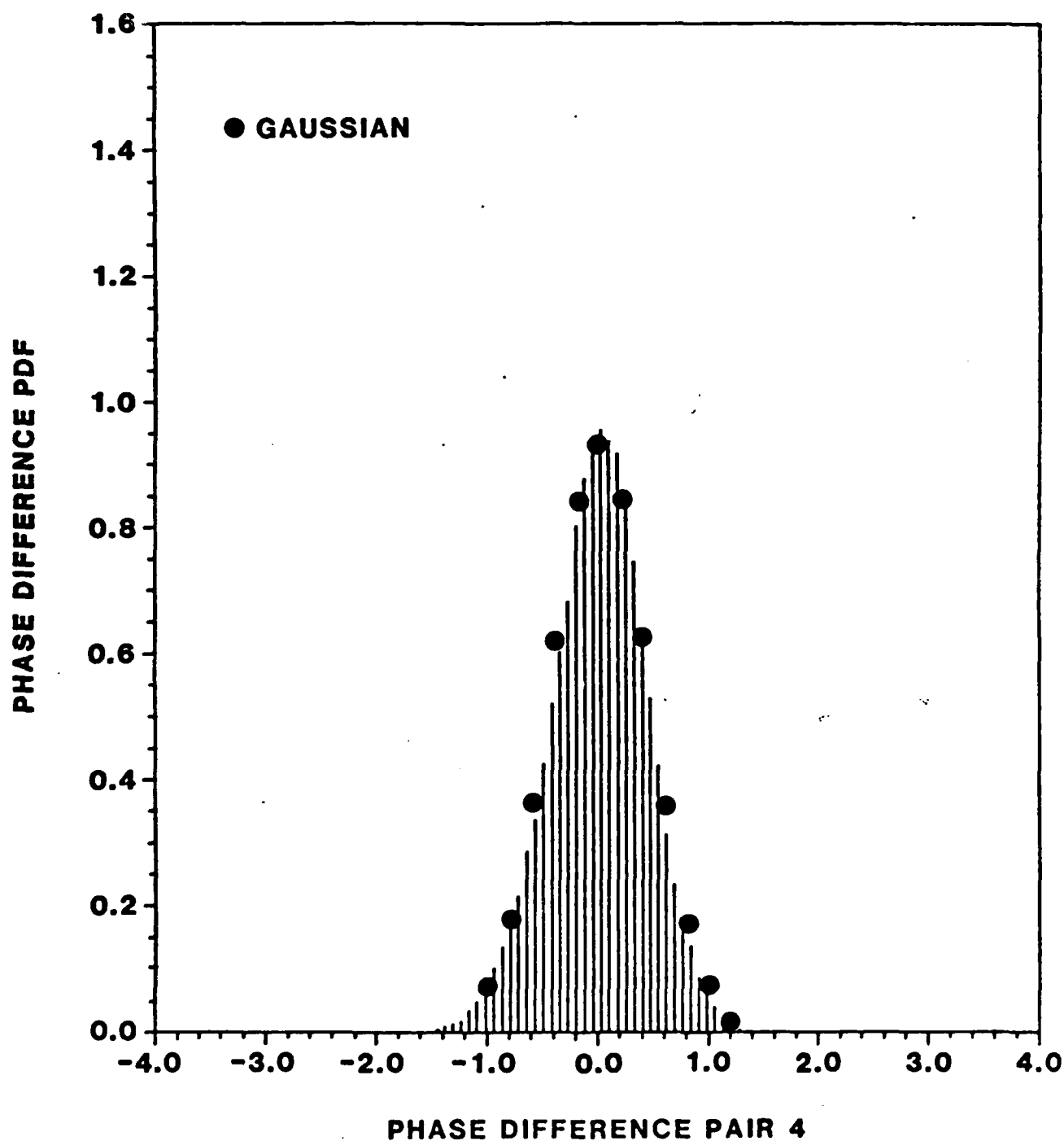


Figure 3-18. Phase probability distribution function for the antenna pair with 10 m spacing, corresponding to Figures 3-16 and 3-17.

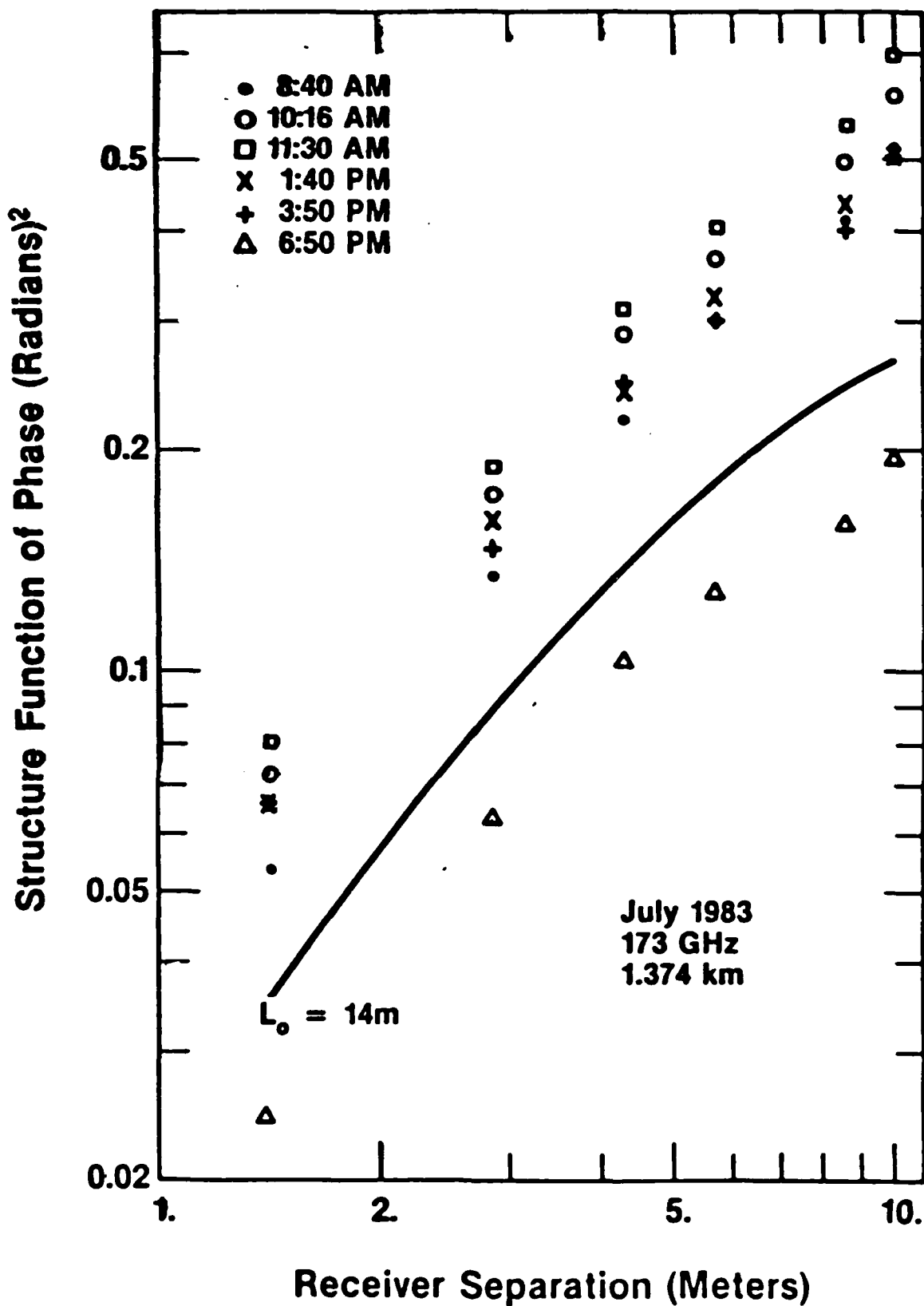


Figure 3-19. Phase structure function for six different runs on the same day. The solid curve is the result of a calculation based on an assumed outer scale dimension of 14 m. 44

function for several different values of  $C_n^2$  at 173 GHz, and Figure 3-20 shows the corresponding values of the mutual coherence function. It is expected that many more results at the other frequencies will become available in the near future as more data tapes are processed and processing algorithms are perfected.

#### 3.2.2.2 Results Obtained in Rain

In the course of the Flatville series of measurements, rain proved to be the only atmospheric effect which caused the propagation link to be essentially totally lost. This result is in accordance with Mie scattering theory, which predicts that attenuation due to rain is essentially constant for a given rain rate for wavelengths ranging from several millimeters to the infrared portion of the spectrum. One of the most interesting results obtained in rain is shown in Figure 3-21, which shows the signal received at 173 GHz as a function of time during a heavy rainstorm. The rain rate during this storm was 60 mm/hr at times, and Figure 3-21 shows that the signals from the transmitter are not detectable at these times. Figure 3-22 is a copy of a chart recorder trace from a weighing bucket rain gauge corresponding to the data of Figure 3-21. For this instrument, the rain rate is proportional to the slope of the trace.

Some rain results were also obtained at 230 GHz. Figure 3-23 shows rain rate as measured by an optical rain gauge, and Figure 3-24 shows the corresponding amplitude probability distribution function. Note that the distribution is much narrower than the corresponding distribution in clear air shown in Figure 3-17. Note also that there are several peaks in the distribution, each apparently corresponding to a time of generally constant rain rate occurring during the data run. The number of peaks in the distribution and the number of regions of

# MUTUAL COHERENCE FUNCTION VARIOUS VALUES OF $C_n^2$ , RANGE-1374 m

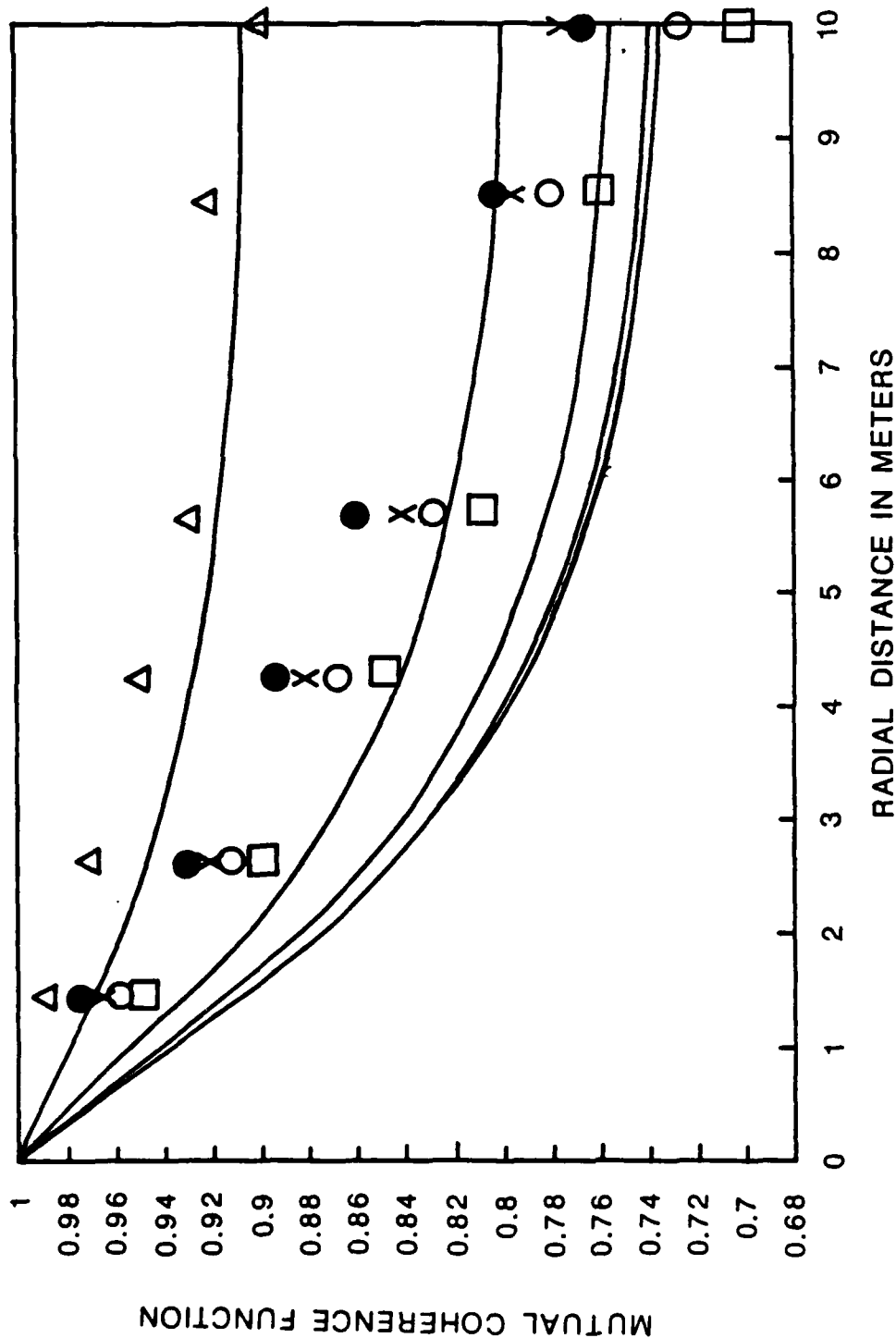
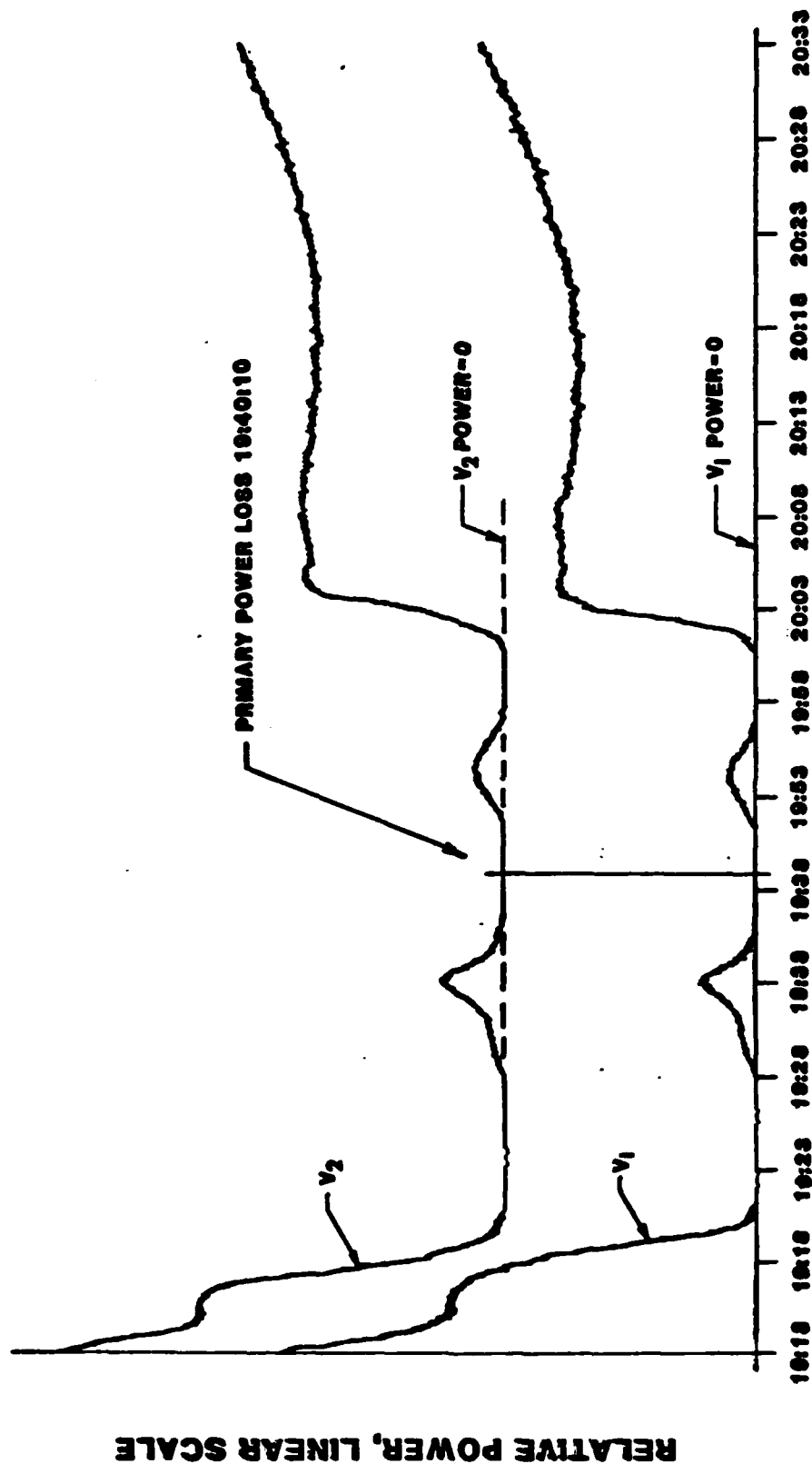


Figure 3-20. Measured and calculated values of the mutual coherence function corresponding to several different runs at 173 GHz. Each curve or series of points corresponds to a different observed value of  $C_n^2$ .

# INTENSITY CHANGES IN RAIN, 173GHZ



TIME

Figure 3-21. Intensity changes observed in rain at 173 GHz for two of the four channels.

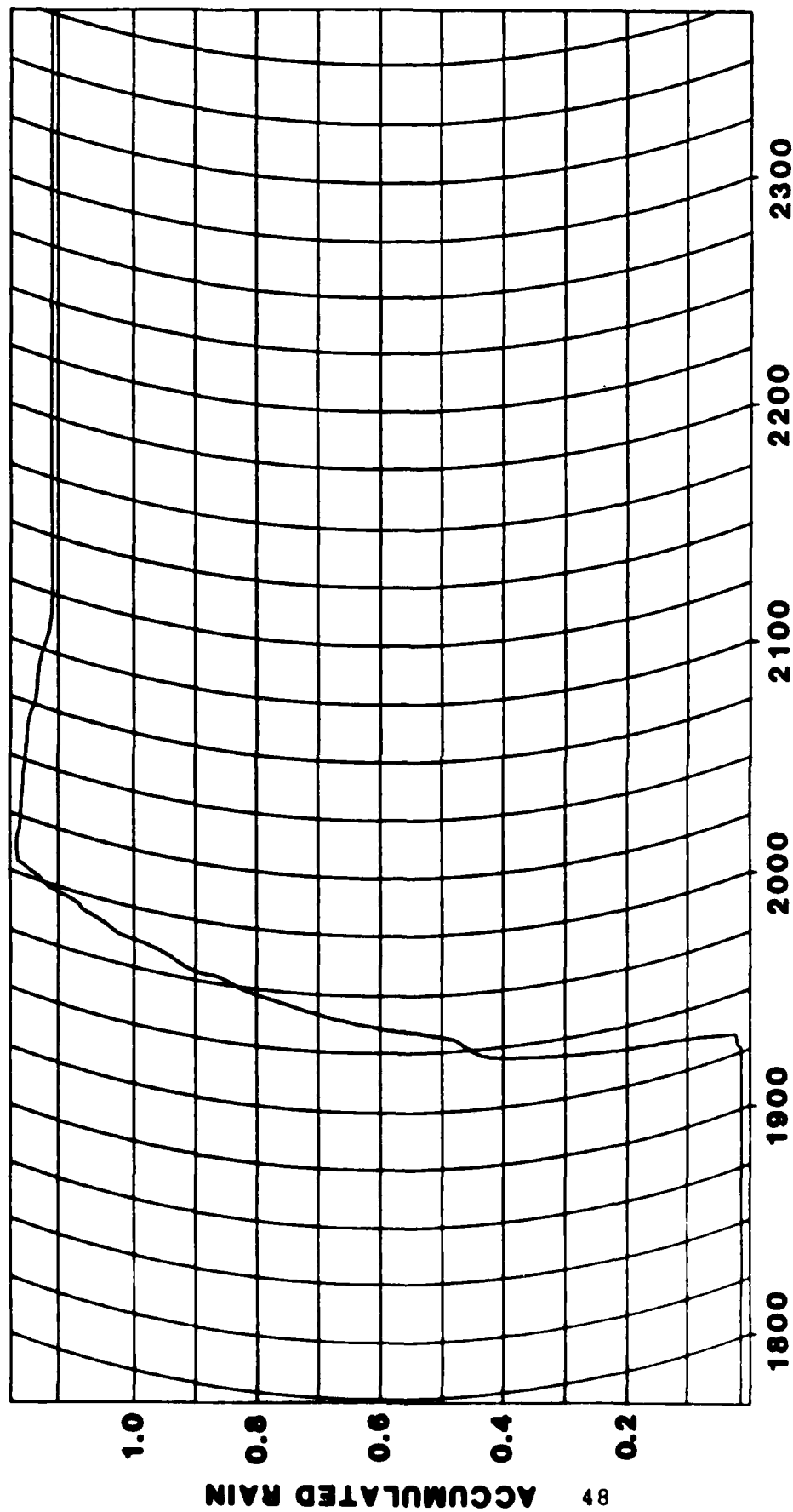


Figure 3-22. Weighing bucket rain gauge chart corresponding to Figure 3-21. The slope of this curve is proportional to rain rate.

# MET STATION 2 OPTICAL RAIN GAUGE

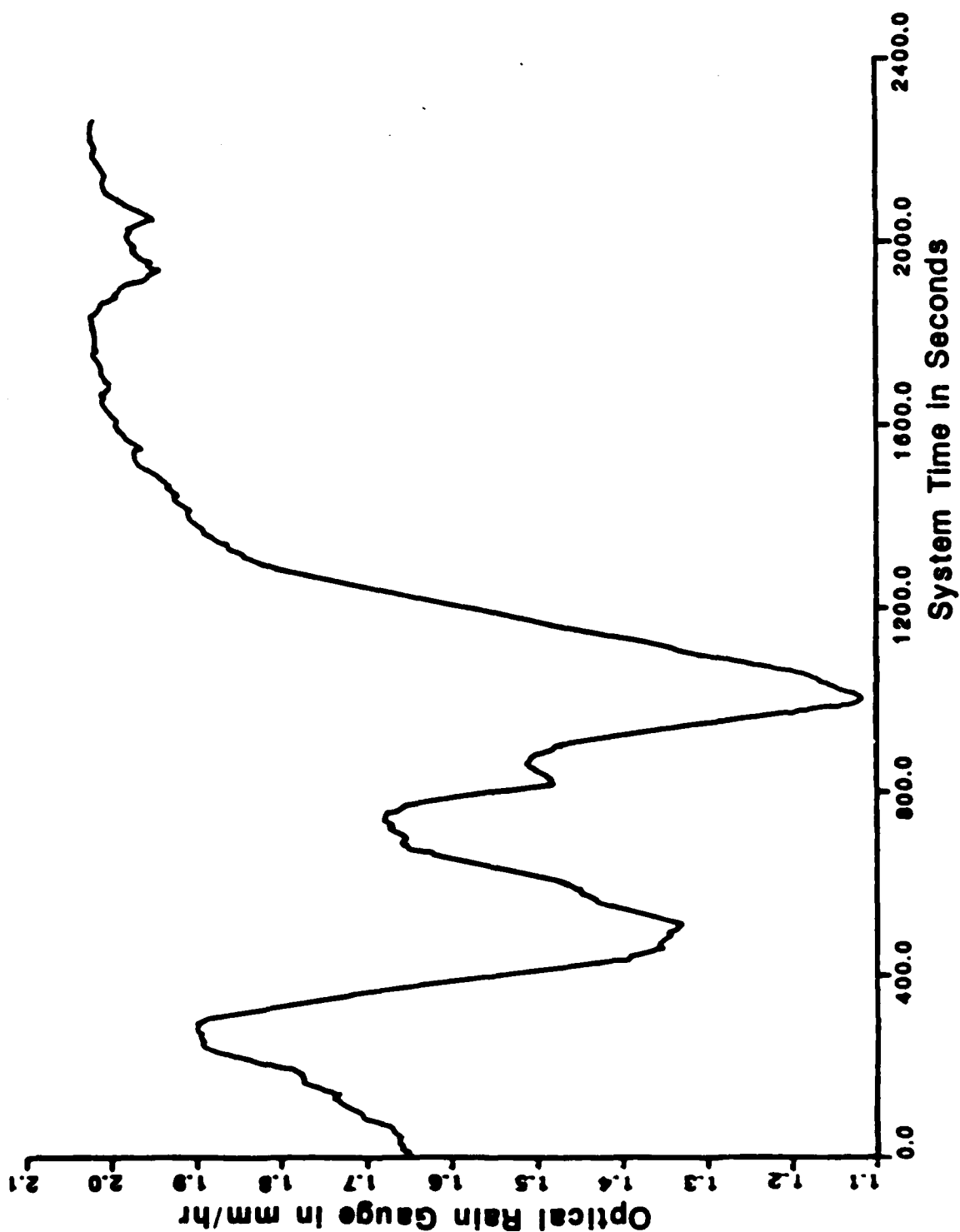


Figure 3-23. Optical rain gauge output for a data run at 230 GHz.

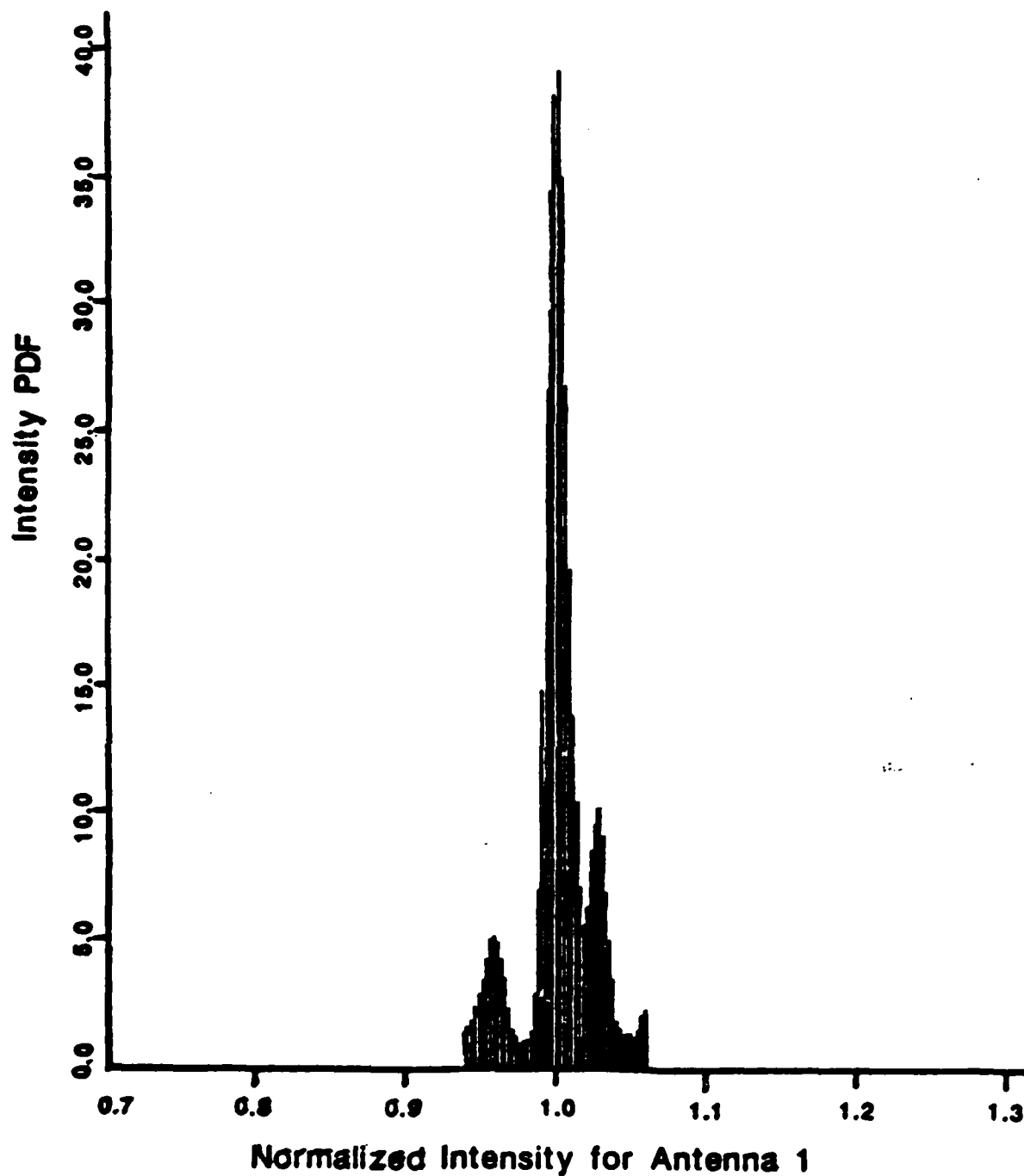


Figure 3-24. Intensity probability distribution function measured at 230 GHz corresponding to the rain gauge trace of Figure 3-23. Note the width of this PDF as compared to Figure 3-17.

constant rain rate may not correlate perfectly because the rain gauge propagation path did not coincide with the MMW path. Note also that the PDF of Figure 3-24 is apparently truncated. Figure 3-25 shows the corresponding phase PDF. This distribution appears to be Gaussian although the rain rate changed significantly during the time that this distribution was measured. Figures 3-26 and 3-27 show the spectra of intensity and phase fluctuations respectively, corresponding to the rain results discussed above. The different spectra shown in each figure correspond to different methods of averaging the results. The solid line spectrum in each case was obtained by dividing the data into up to 20 segments, taking the Fourier transform of each and averaging the results. The dashed line spectrum was obtained by considering the entire data run, or a reasonably stationary part of it, and taking the Fourier transform. As a result of these methods of deriving the spectra, the solid curve may be considered to be more valid for the higher frequencies (2 - 50 Hz), and the dashed curve more valid for the range up to 2 Hz. The large contribution of low frequency phenomena to the spectra results at least partially from instrumental drift, but in several instances, low frequency changes were seen which corresponded to this low-frequency spectral content.

#### 3.2.2.3 Fog Results

The smallest fluctuations in both amplitude and phase measured at Flatville occurred in fog. Apparently the air is very calm and the atmosphere is very stable in terms of changes in temperature and humidity. Figure 3-28 is a copy of a recorder trace of signals received in a heavy fog, showing the extreme quietness of the fluctuations. At the time of these measurements, the visibility was estimated to be about 100 m, but no method of quantitatively determining the visibility was

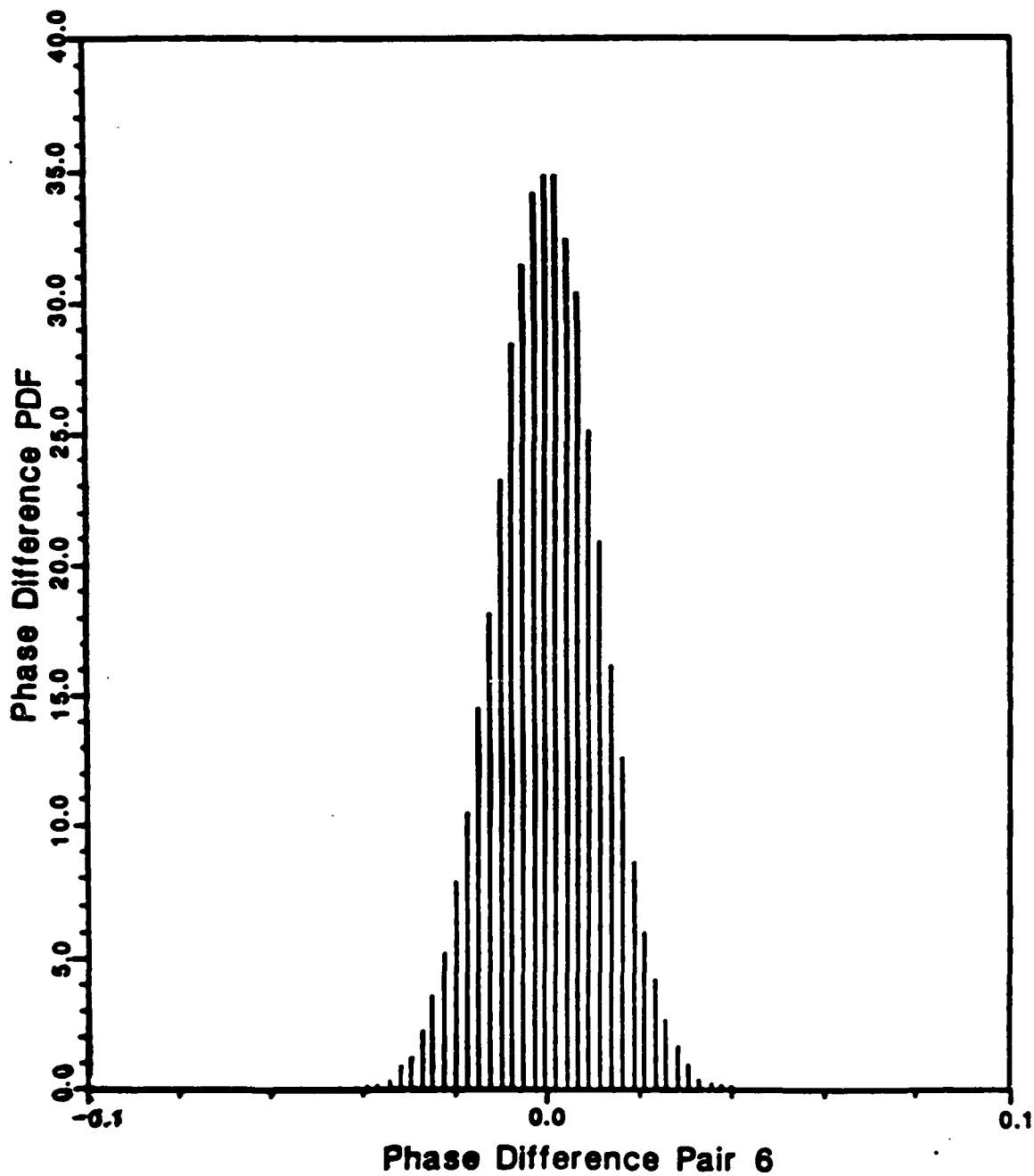


Figure 3-25. Phase probability distribution function corresponding to Figures 3-23 and 3-24. Apparently the gaussian profile is maintained independent of rain rate.

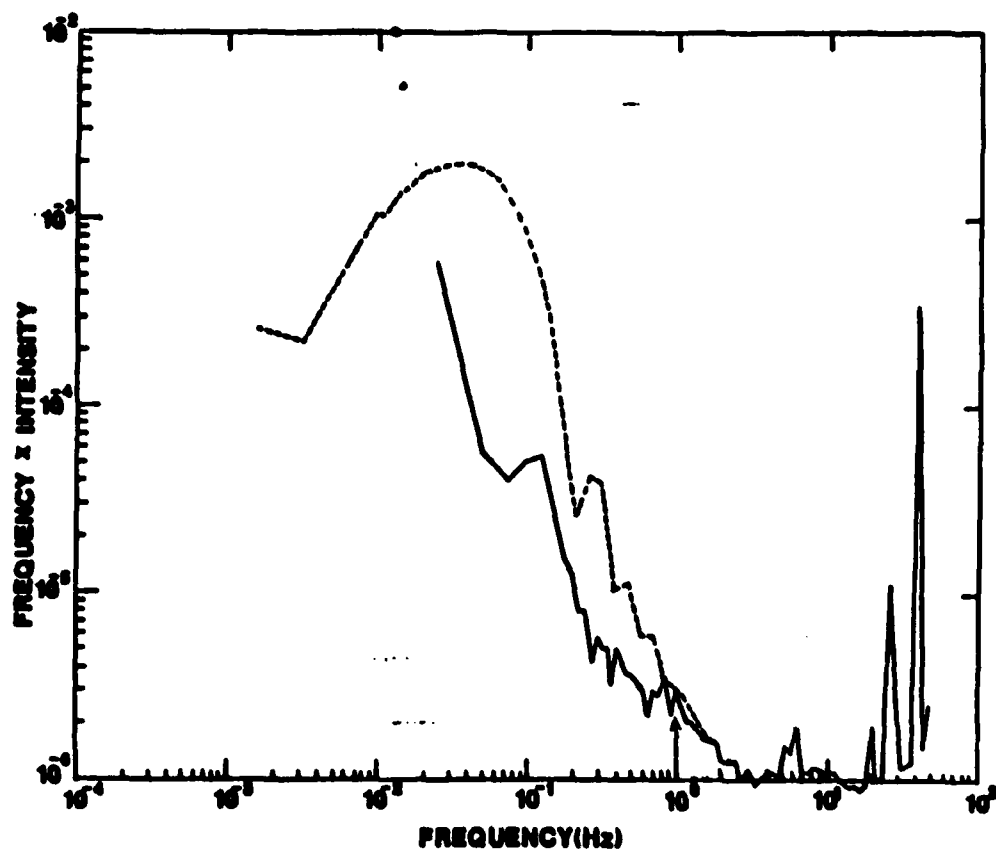


Figure 3-26. Intensity power spectra corresponding to Figures 3-23 through 3-25. The two curves are derived by different averaging methods as described in the text.

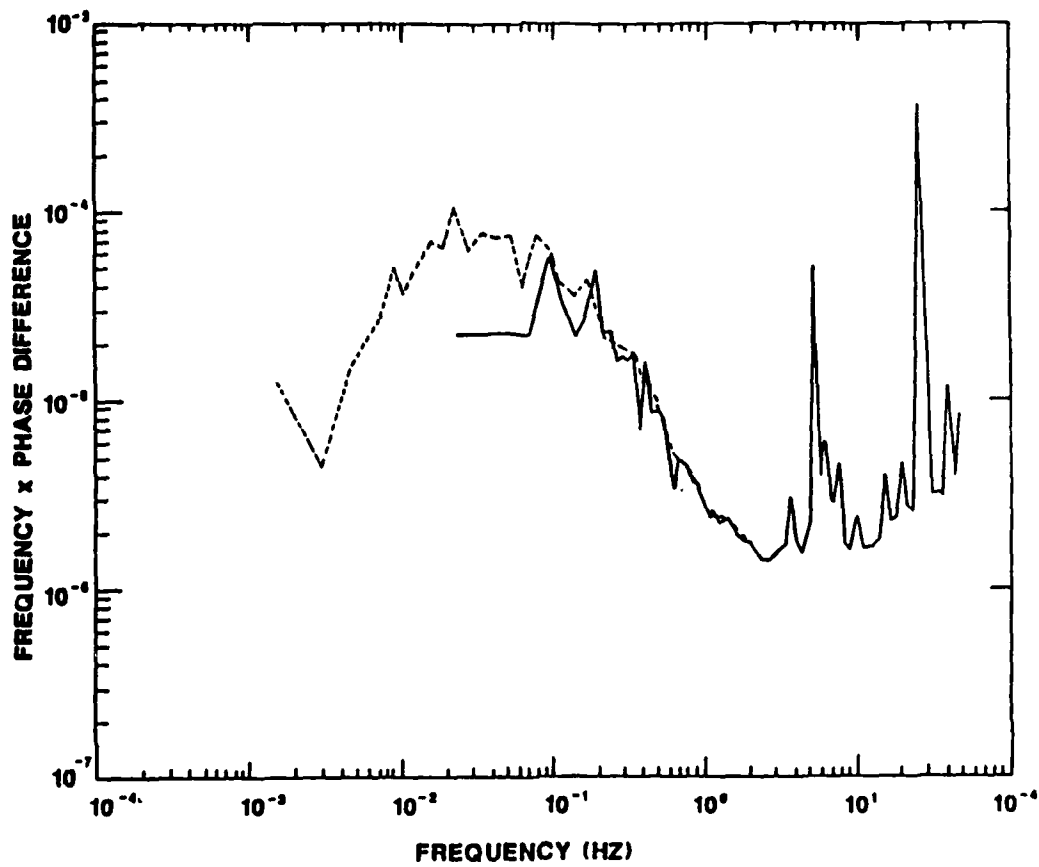


Figure 3-27. Phase difference power spectra corresponding to Figure 3-26.

## INTENSITY CHANGES IN FOG, 142GHz

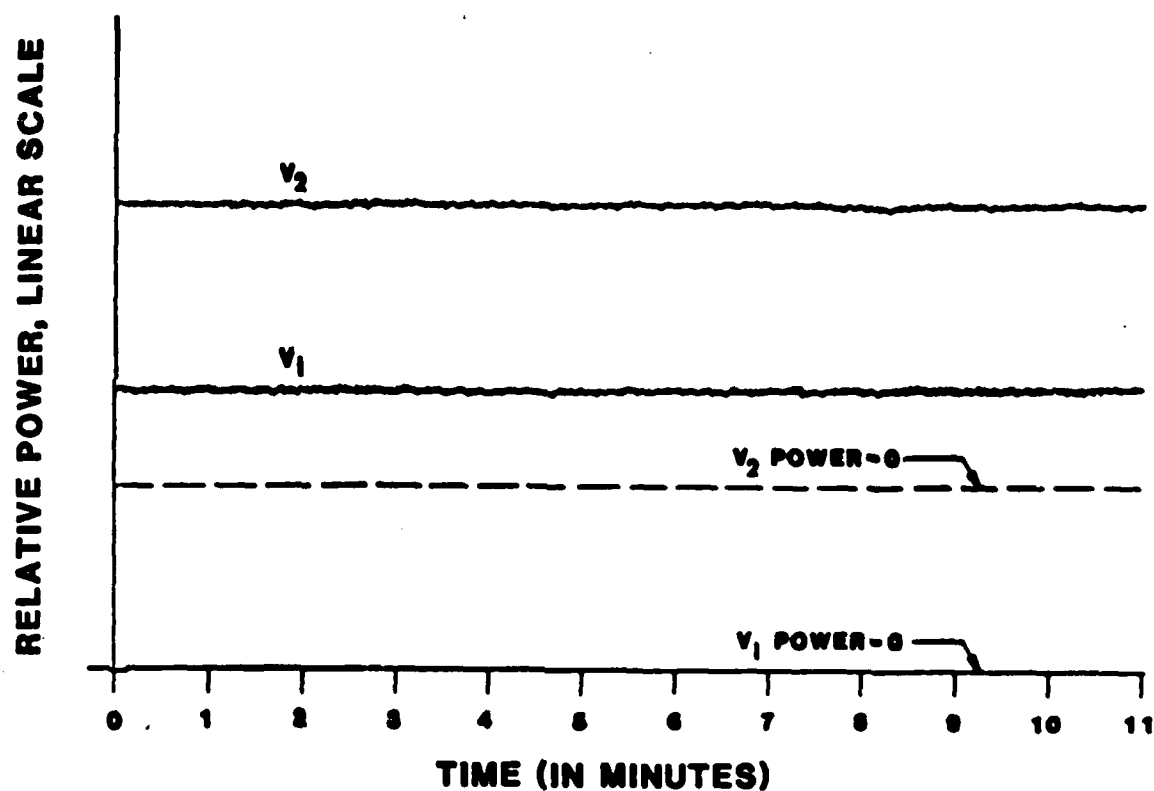


Figure 3-28. Copy of a chart recorder trace of relative power measured in a heavy fog at 142 GHz.

available. Despite this poor visibility, the MMW signals were received with little apparent degradation of signal-to-noise ratio (SNR) compared to the clear-air case.

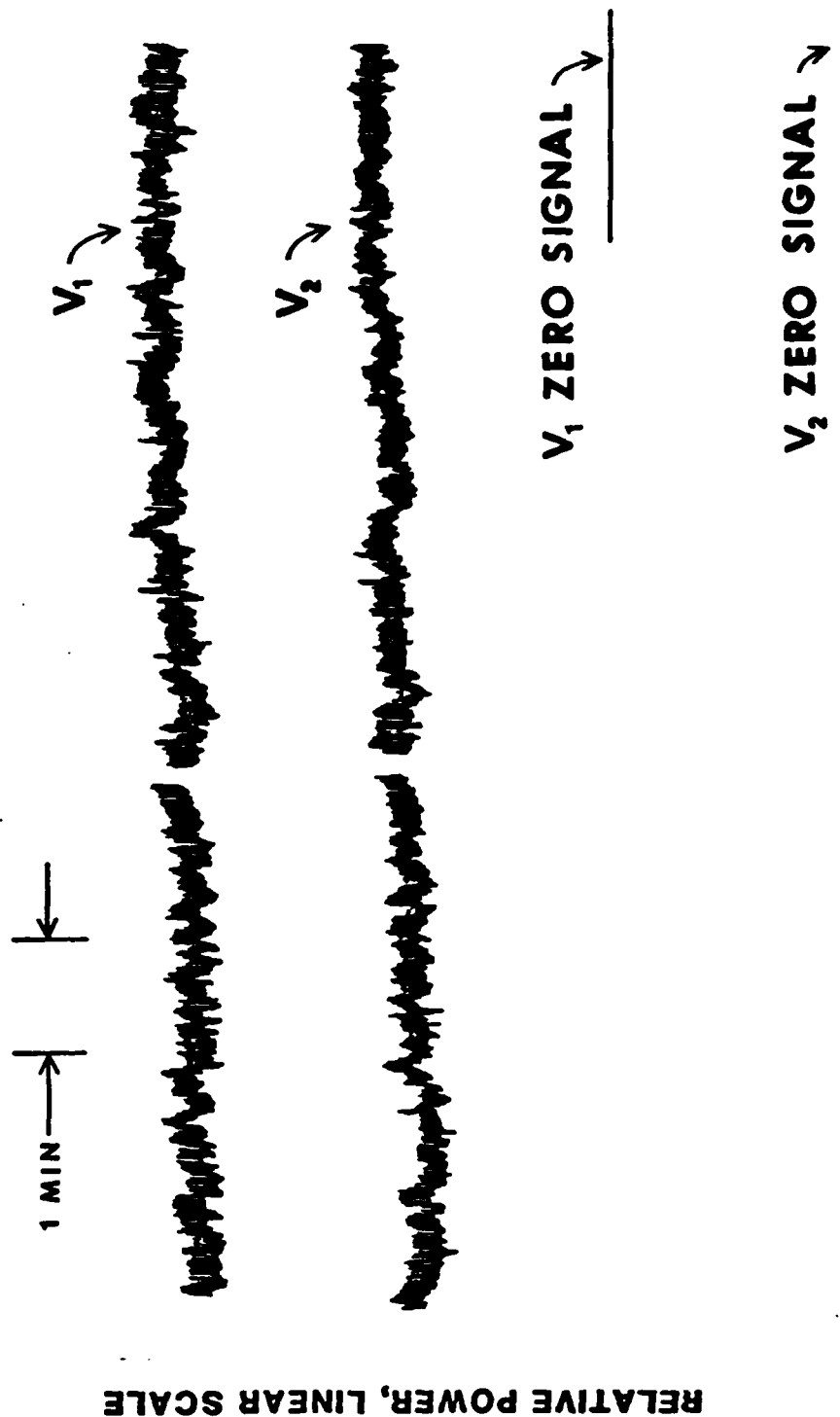
#### 3.2.2.4 Results Obtained in Snow

Several snow events were observed at Flatville, and measurements were obtained at 116, 142 and 230 GHz. A typical snowstorm would deposit perhaps 30 cm of snow in 6-8 hours, and would be accompanied by winds up to 25 m/s. Near the ends of the storms observed at Flatville, it was not possible to differentiate between falling snow and ground blizzards caused by the high winds. Despite these seemingly violent atmospheric conditions, the MMW signals were propagated with little apparent attenuation, since the SNR was always adequate, and the fluctuations in amplitude and phase were much smaller than those observed in clear air. Figure 3-29 is a copy of a recorder trace of signals received at 116 GHz during a heavy snow, and Figures 3-30 and 3-31 show the spectra of power and phase fluctuations, respectively. It is perhaps surprising that during snowstorms, when large particles were in the air and were being violently agitated by high winds, the intensity and phase fluctuation levels would be smaller than those observed during clear-air conditions.

#### 3.2.2.5 Summary of Results Obtained

The largest fluctuations in both intensity and phase occurred in clear air under conditions of high temperature and humidity, and the smallest occurred in fog. Other weather conditions caused effects that were intermediate between these extremes with regard to fluctuations, but rain causes the greatest problems in MMW propagation because of its severe attenuation. Of all atmospheric conditions observed at

# INTENSITY FLUCTUATIONS IN SNOW 116.3 GHz



RELATIVE POWER, LINEAR SCALE

Figure 3-29. Copy of a chart recorder trace of intensity fluctuations measured in snow at 116 GHz.

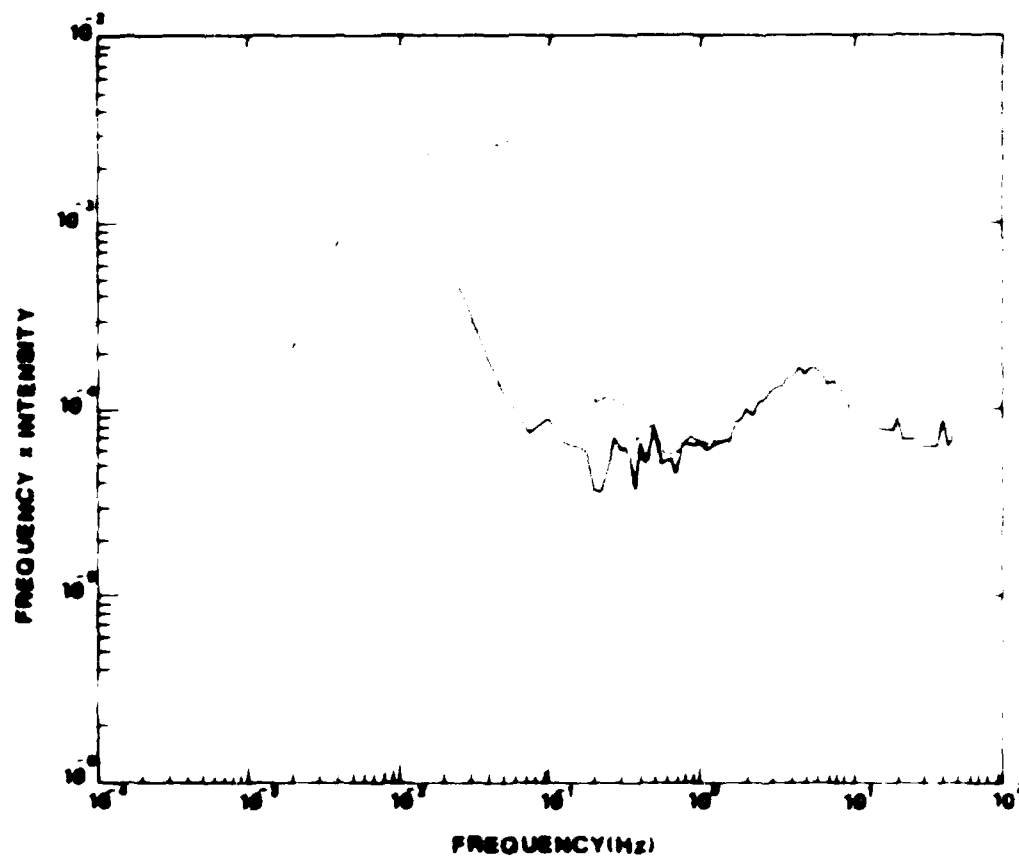


Figure 3-30. Intensity power spectra observed in snow at 230 GHz.

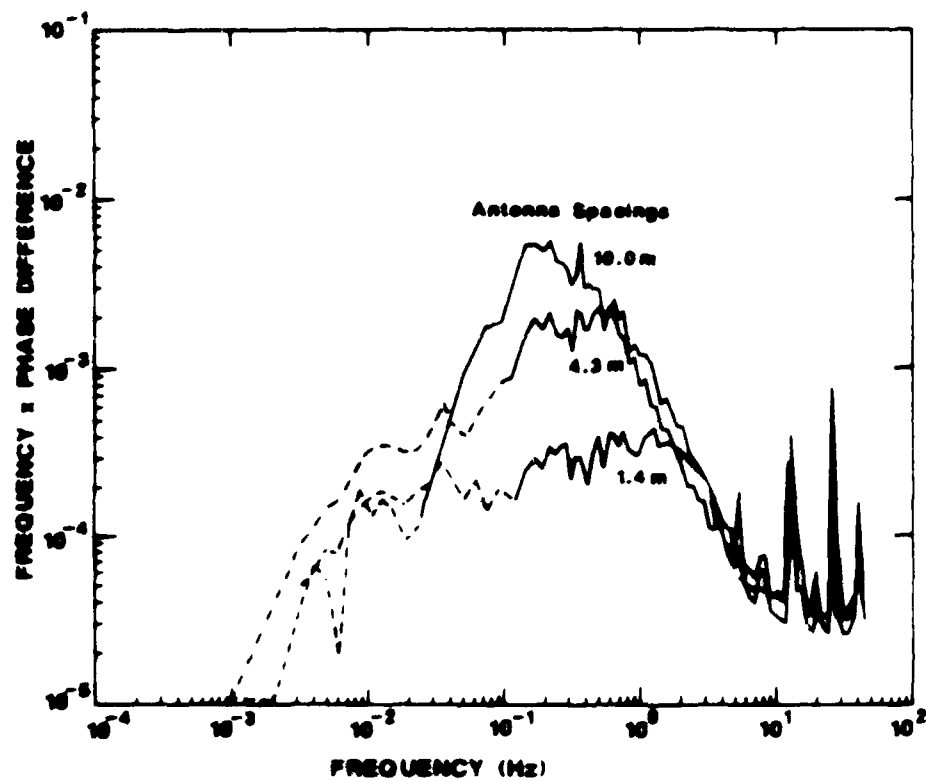


Figure 3-31. Phase difference power spectra observed in snow at 230 GHz for three different antenna spacings.

Flatville, rain was the only one that completely shut down the atmospheric transmission link, and this near total attenuation occurred only once while measurements were being made, as shown in Figure 3-21. At other times during rain events, the signals were observed to fluctuate slowly in correlation with rain rates observed with other instrumentation [17]. Figure 3-32 shows the variance of phase fluctuations measured in clear air and snow at several different frequencies, indicating again that the largest variations occur in clear air. Table 3-II lists typical standard deviations of amplitude and phase fluctuations measured in clear air, rain, snow, and fog. Figure 3-32 and Table 3-II may be considered a summary of the results of the measurements made at Flatville.

In any atmospheric measurement program the bottom line question of whether or not the atmosphere affects system performance must be asked. On the basis of the preliminary results obtained thus far, it must be concluded that the effects are probably not very serious. Intensity fluctuations affect signal detection probability, but only at near maximum ranges where detection may be marginal in any case. Angle-of-arrival fluctuations cause angular errors, but this effect is most severe in clear weather where sighting methods other than MMW could be used. Nevertheless, the results obtained during this series of measurements must be considered by the MMW system designer for each individual system, because degradation of performance caused by turbulence may be considerable in some specific applications.

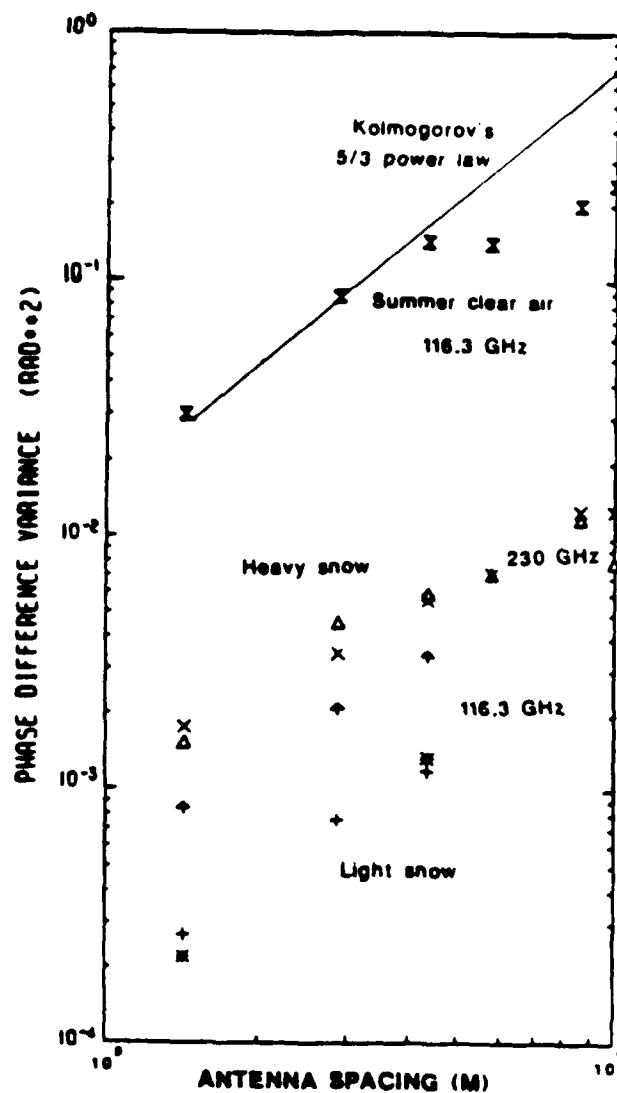


Figure 3-32. Comparison of phase difference variances observed in snow at 116 GHz and 230 GHz to clear-air variances observed at 116 GHz.

Table 3-II

# **TYPICAL FLUCTUATION LEVELS IN MILLIMETER WAVE PROPAGATION**

<b>CONDITION</b>	<b>STANDARD DEVIATIONS</b>	
	<b>INTENSITY (PER CENT)</b>	<b>ANGLE OF ARRIVAL ( <math>\mu</math> rad)</b>
<b>SUMMER DAYTIME CLEAR AIR</b>	<b>7.4</b>	<b>38</b>
<b>SNOW</b>		
<b>-NEAR START</b>	<b>1.9</b>	<b>4.8</b>
<b>-BLIZZARD</b>	<b>2.4</b>	<b>8.4</b>
<b>-GROUND BLIZZARD</b>	<b>1.4</b>	<b>4.4</b>
<b>WINTER RAIN</b>	<b>1.0</b>	<b>3.8</b>
<b>WINTER FOG</b>	<b>0.2</b>	<b>1.1</b>

*Based on 20-second slices of data;  
i.e., 2000 data points.*

#### 4. Conclusions

As mentioned earlier, the agreement between measured and calculated turbulence results seems to be rather good regardless of which theory one uses to describe these phenomena. It has been said that the state of clear-air optical turbulence theory is good enough for all Army applications, and it is suggested here that the same conclusion may be tentatively reached for MMW turbulence theory, with the possible exception of poor-weather turbulence. Optical system performance in poor weather is less of an issue than MMW performance, for obvious reasons, but the theory for optical propagation in poor weather is in need of some attention. The reasons for these gaps in poor-weather theory are obvious; the conditions are highly variable and the calculations are almost intractable. It is of some comfort to realize that the worst conditions of turbulence by far for MMW applications are found in clear weather, so that turbid weather turbulence is not of great concern. The remainder of this section assesses the state of agreement between theory and experiment obtained using the results obtained at Flatville.

The Flatville series of measurements provide essentially all of the basis for the assessment of the state of agreement between theory and experiment available, since this series of measurements was very carefully instrumented. The majority of the Flatville results referred to herein are given in Section 3. To complement these comparisons of theory and experiment, Figure 4-1 [13] shows how the log intensity variance as determined from actual measured data compares to that calculated from  $C_n^2$  determined from the meteorological instrumentation. In determining  $C_n^2$ , the quantity in parentheses in Equation (2-7) is used, with the cross-correlation term given by Equation (2-8). These measurements were made at 173 GHz, and the values of  $C_n^2$  for each of the six data runs made on that particular day in July

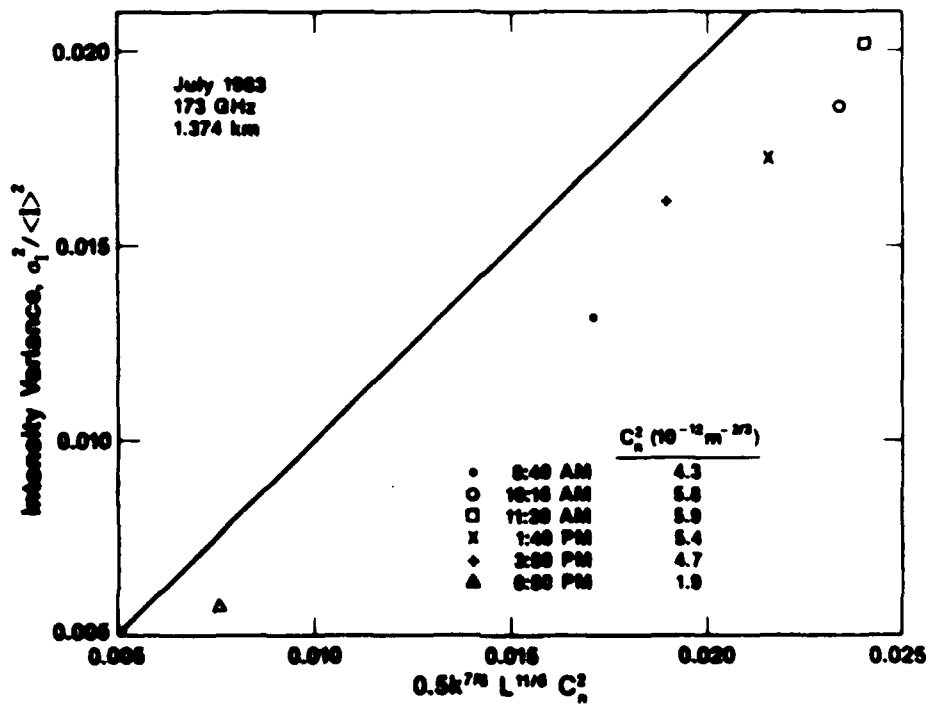


Figure 4-1. Comparison of calculations of  $C_n^2$  using the inertial range formula to measured values.

1983 are given in the table which is part of the figure. This figure shows that the predictions of theory for the log amplitude variance are always slightly higher than the measured values. The conditions shown in this figure represent the worst encountered during the Flatville series of measurements, and the value  $C_n^2 = 5.9 \times 10^{-12} \text{ m}^{-2/3}$  is the largest value of this parameter measured at Flatville, regardless of conditions. This value is considered useful for making calculations of worst-case effects, although larger effects might be observed at other places in the world. It is certainly possible that  $C_n^2$  could be larger under tropical conditions or for an over-water path, but the use of this value gives a good indication of the performance of Army MMW systems under conditions of high atmospheric turbulence. Fluctuations observed at night were generally at least an order of magnitude smaller; evenings were used for calibration of the MMW equipment because the atmosphere was very quiet.

It was indicated above that a possible shortcoming of the results obtained to date on MMW turbulence effects is that they are perhaps limited by the range of climatic conditions observed at Flatville. For example, it was found that the combination of heat and humidity cause the greatest perturbations of MMW signals propagated through the atmosphere. Although very hot and humid during the summer, the conditions at Flatville do not approach those at some locations in the tropics or on paths over water. To assess the effects of turbulence on MMW propagation under these conditions, it has been suggested [18] that a MMW  $C_n^2$  measuring instrument, similar in principle to those developed at NOAA for the measurement of optical  $C_n^2$ , be designed and built. Such a system could be deployed anywhere in the world and would operate unattended, gathering valuable data on the statistical occurrences of extremes of MMW  $C_n^2$ . With two receivers as shown

in Figure 4-2, measurements of relative phase shift and crosswind velocity could also be obtained. After building one such instrument, others could probably be built at fairly low cost, so that a network of such devices would be available for collection of MMW turbulence statistics at several points of interest to the Army throughout the world.

Only minimal comparison of the results of theory and experiment are possible at this time because much of the data analysis is yet to be completed by NOAA. Other examples of plausible agreement obtained during this program or during other studies are the measurements made at Burlington, VT with results shown in Figure 3-2, and those obtained at White Sands Missile Range by workers from Georgia Tech. As far as can be determined, measurements made by Soviet workers also show reasonably good agreement with theory. In summary, it appears that the state of agreement is good, and that further comparisons to be made by NOAA during further study of the Flatville data will further confirm this assessment.

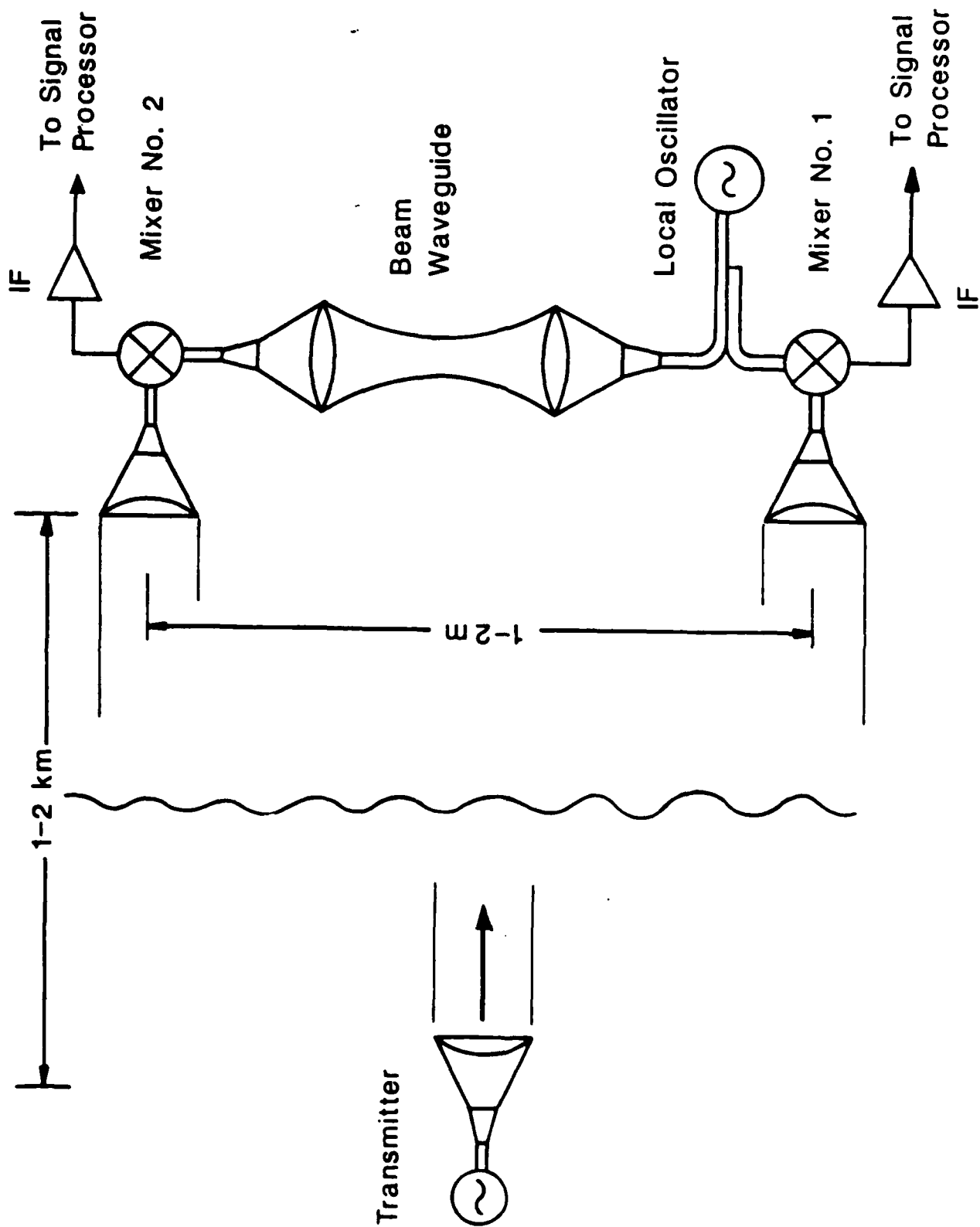


Figure 4-2. Schematic of ground-based MMW system for continuous measurement of  $C_n^2$ , relative phase, and cross wind.

## ACKNOWLEDGEMENTS

It is a pleasure for the authors to acknowledge the contributions of many people who have worked hard to ensure the success of this program. In addition to the authors, GTRI personnel who have contributed to this effort include: M. L. Blyler, V. T. Brady, J. M. Cotton, Jr., R. E. Forsythe, D. O. Gallentine, D. M. Guillory, S. M. Halpern, G. F. Kirkman, J. W. Larsen, R. P. Lilly, R. L. Mandock, A. McSweeney, J. M. Newton, E. M. Patterson, R. H. Platt, G. W. Rosenberg, O. A. Simpson, M. J. Sinclair, and D. J. Swank. Persons contributing from NOAA were: N. L. Abshire, W. Cartwright, S. F. Clifford, R. E. Cupp, T. J. Drey, S. P. Eckes, R. B. Fritz, R. J. Hill, R. J. Lataitis, G. R. Ochs, J. T. Priestley, D. S. Reynolds, J. P. Riley, W. P. Schoenfield, B. Spaur, G. M. Walford, M. Wickers, and J. J. Wilson. From the Atmospheric Sciences Laboratory, contributors include: G. Alvarez, T. Chavez, A. Davis, R. Johnson, R. Okrasinski, R. Olsen, B. E. Rischel, J. Scully, R. Valdez, and K. Walker. D. G. Bauerle of Aberdeen Proving Ground and J. Vogel of the Illinois Water Survey also participated in this effort.

The authors would especially like to acknowledge the help and guidance of W. A. Flood of the Army Research Office and D. E. Snider of the Army Atmospheric Sciences Laboratory.

## REFERENCES

1. J.A. Schiavone, "Prediction of Positive Refractivity Gradients for Line of Sight Microwave Radio Paths", Bell Syst. Tech. J., Vol. 60, No. 6, July-Aug., 1981, pp. 803-822.
2. R.J. Hill, S.F. Clifford, and R.S. Lawrence, "Refractive-Index and Absorption Fluctuations in the Infrared Caused by Temperature, Humidity, and Pressure Fluctuations", J. Opt. Soc. Am., Vol. 70, No. 10, Oct., 1980, pp. 1192-1205.
3. V.I. Tatarski, Wave Propagation in a Turbulent Medium, McGraw-Hill Book Co., New York, 1961, Chapter 7.
4. L.A. Chernov, Wave Propagation in A Random Medium, McGraw-Hill Book Co., New York, 1960, Chapter 5.
5. S. F. Clifford, "Laser Beam Propagation Through Refractive Turbulence," Ninth International Conference on Lasers and Applications, Orlando, FL, Dec. 1986.
6. A.O. Izyumov, "Amplitude and Phase Fluctuations of a Plane Monochromatic Submillimeter Wave in a Near-Ground Layer of Moisture - Containing Turbulent Air", Radio Engineering and Electronic Physics, Vol. 13, No. 7, 1968, pp. 1009-1013.
7. \_\_\_\_\_, "Correlation of Amplitude and Phase Fluctuations of a Plane Monochromatic Wave in Submillimeter Range Propagating in the Surface Layer of a Turbulent Atmosphere. Ibid., Vol. 14, No. 7, 1969, pp. 1133-1135.
8. \_\_\_\_\_, "Frequency Spectrum of Amplitude Fluctuations of a Plane Electromagnetic Wave in Submillimeter Range Propagating in a Surface Layer of Turbulent Atmosphere". Ibid., Vol. 14, No. 10, 1969, pp. 1609-1611.
9. A.S. Gurvich, "Effect of Absorption on the Fluctuation in Signal Level During Atmospheric Propagation," Ibid., Vol. 13, No. 11, 1968, pp. 1687-1694.
10. N.A. Armand, A.O. Izyumov, and A.V. Sokolov, "Fluctuations of Submillimeter Waves in a Turbulent Atmosphere," Ibid., Vol. 10, No. 8, 1971, pp. 1257-1266.
11. R.W. McMillan, R.A. Bohlander, G.R. Ochs, R.J. Hill, and S.F. Clifford, "Millimeter Wave Atmospheric Turbulence Measurements: Preliminary Results and Instrumentation for Future Measurements", Opt. Eng., Vol. 22, No. 1, Jan/Feb. 1983, pp. 32-39.
12. R.A. Bohlander, R.W. McMillan, D.M. Gullory, R.J. Hill, J.T. Priestley, S.F. Clifford, and R. Olsen, "Fluctuations in Millimeter Wave Signals," Tenth Int. Conf. on Infrared and Millimeter Waves, Orlando, FL, Dec. 1986.

13. R.J. Hill, W.P. Schoenfeld, J.P. Riley, J.T. Priestley, S.F. Clifford, S.P. Eckes, R.A. Bohlander, and R.W. McMillan, "Data Analysis of the NOAA-GIT Millimeter-Wave Propagation Experiment Near Flatville, Illinois", NOAA Technical Report ERL 429-WPL 60, Aug., 1985.
14. R.W. McMillan and D.M. Guillory, "Phase and Frequency Control of Millimeter Wave Sources," Proc. SPIE, Vol. 544, Arlington, VA, April 9-10, 1985, pp. 29-32.
15. D.M. Guillory and R.W. McMillan, "Frequency Stabilization of Millimeter Wave Sources," Tenth Int. Conf. on Infrared and Millimeter Waves, Orlando, Florida, Dec. 1985.
16. R.A. Bohlander, V.T. Brady, A. McSweeney, G.F. Kirkman, J.M. Newton, A. Davis, and O.A. Simpson, "A Quasi-Optical Millimeter Wave Transmitter and Receiver Array for Measurements of Angular Scintillation," Eighth International Conference on Infrared and Millimeter Waves, Miami Beach, FL, Dec. 1983.
17. E.M. Patterson, R.A. Bohlander, R.W. McMillan, R.L. Mandock, R.J. Hill, J.T. Priestley, S.F. Clifford, B.E. Rischel, and R. Olsen, "Spectral Density of Intensity and Phase of Millimeter Wave Signals Propagated Through Precipitation," URSI Commission F Open Symposium, University of New Hampshire, Durham, NH, July/August 1986.
18. R.W. McMillan, "Effects of Atmospheric Turbulence on Millimeter Direct Fire Guidance," Final Report on Delivery Order 2070, Battelle Columbus Division, Research Triangle Park, NC, October 1986.

**Bibliography of  
Publications and Presentations on  
Atmospheric Turbulence Effects on  
Millimeter Wave Propagation**

- R. W. McMillan, R. A. Bohlander, G. R. Ochs, R. J. Hill, S. F. Clifford, D. G. Bauerle and J. Nemanich, "Millimeter Wave Atmospheric Turbulence Measurements: Preliminary Results", Proc. SPIE 337: Millimeter Wave Technology, 88 (1982).
- R. W. McMillan, R. A. Bohlander, G. R. Ochs, R. J. Hill and S. F. Clifford, "Millimeter Wave Atmospheric Turbulence Measurements: Preliminary Results and Instrumentation for Future Measurements", Optical Engineering, 22, 32 (1983).
- G. W. Rosenberg, R. W. McMillan and V. T. Brady, "Measurements of Phase Noise Spectra of Selected Millimeter Wave Klystrons", Proc. 8th Intl. Conf. Infrared and Millimeter Waves, M3.4 (1983).
- R. W. McMillan, V. T. Brady, G. W. Rosenberg and G. F. Kirkman, "A Millimeter Wave Radio Frequency System for Atmospheric Turbulence Measurements", Proc. 8th Intl. Conf. Infrared and Millimeter Waves, W6.5, (1983).
- R. A. Bohlander, V. T. Brady, A. McSweeney, G. F. Kirkman, J. M. Newton, A. Davis and O. A. Simpson, "A Quasi-Optical Millimeter Wave Transmitter and Receiver Array for Measurements of Angular Scintillation", Proc. 8th Intl. Conf. Infrared and Millimeter Waves, Th6.4, (1983).
- R. A. Bohlander, R. W. McMillan, V. T. Brady, G. F. Kirkman, M. J. Sinclair, J. W. Larsen, M. L. Blyler, R. P. Lilly, D. O. Gallentine, S. F. Clifford, J. T. Priestley, R. J. Hill, R. E. Cupp, N. L. Abshire, R. B. Fritz, W. Cartwright, G. R. Ochs, R. J. Lataitis, J. J. Wilson and G. M. Walford, "Observations of Amplitude and Angle of Arrival Scintillation in Millimeter Wave Propagation Caused by Turbulence in Clear Air Near the Ground", Proc. 8th Intl. Conf. Infrared and Millimeter Waves, W6.4, (1983).

**Bibliography**  
Continued

- R. W. McMillan, R. A. Bohlander, D. M. Guillory, R. H. Platt, J. M. Cotton, Jr., S. F. Clifford, J. T. Priestley, and R. J. Hill, "Millimeter Wave Atmospheric Turbulence Measurements", presentation at the Annual Review Conference on Atmospheric Transmission Models at the Air Force Geophysics Laboratory, Hanscom AFB, MA, May, 1984.
- R. A. Bohlander, R. W. McMillan, D. M. Guillory, R. H. Platt, S. F. Clifford, J. T. Priestley, R. J. Hill, R. Olsen and B. Rischel, "Millimeter Wave Transmission Fluctuations Due to Snow", Proc. of SNOW Symposium IV, pp. 25-39, Army Cold Regions Research and Engineering Laboratory in Hanover, NH, Aug. 1984.
- R. W. McMillan, R. A. Bohlander, D. M. Guillory, R. H. Platt, J. M. Cotton, Jr., S. F. Clifford, J. T. Priestley, and R. J. Hill, "Millimeter Wave Atmospheric Turbulence Measurements", Proc. 9th Intl. Conf. on Infrared and Millimeter Waves, Osaka, Japan, Oct. 1984.
- R. J. Hill, S. F. Clifford, J. T. Priestley, R. A. Bohlander and R. W. McMillan, "Measurements of Millimeter-Wave Propagation through Atmospheric Surface-Layer Turbulence", Proc. 9th Intl. Conf. on Infrared and Millimeter Waves, Osaka, Japan, Oct. 1984.
- R. W. McMillan, "Near-Millimeter-Wave Sources of Radiation", Proc. IEEE, 73, 86-108 (1985)
- R. A. Bohlander, R. W. McMillan, and J. J. Gallagher, "Atmospheric Effects on Near-Millimeter-Wave Propagation", Proc. IEEE, 73, 49-60 (1985).
- R. J. Hill, W. P. Schoenfeld, J. P. Riley, J. T. Priestley, S. F. Clifford, S. P. Eckes, R. A. Bohlander, and R. W. McMillan, "Data Analysis of the NOAA-GIT Millimeter Wave Propagation Experiment Near Flatville, Illinois", NOAA Technical Report ERL 429-WPL 60, August 1985.

**Bibliography**  
Continued

- R. A. Bohlander, R. W. McMillan, D. M. Guillory, R. J. Hill, J. T. Priestley, S. F. Clifford, and R. Olsen, "Fluctuations in Millimeter Wave Signals," Proc. 10th Intl. Conf. on Infrared and Millimeter Waves, Lake Buena Vista, FL, December, 1985.
- D. M. Guillory and R. W. McMillan, "Frequency Stability of Millimeter Wave Sources", Proc. 10th Intl. Conf. on Infrared and Millimeter Waves, Lake Buena Vista, FL, December, 1985.
- S. F. Clifford, R. J. Hill, J. T. Priestley, R. A. Bohlander and R. W. McMillan, "The Spectra of Amplitude and Phase Difference Fluctuations of Millimeter Waves Propagating in Clear Air", Proc. URSI Symposium, Commission F, Wave Propagation: Remote Sensing and Communications, Univ. of New Hampshire, Durham, NH, July 28-August 1, 1986.
- R. J. Hill, J. T. Priestley, S. F. Clifford, W. P. Schoenfeld, R. W. McMillan, and R. A. Bohlander, "Instrumentation, Data Validation and Analysis, and Results of the NOAA-GIT Millimeter Wave Propagation Experiment", Proc. URSI Symposium, Commission F, Wave Propagation: Remote Sensing and Communications, Univ. of New Hampshire, Durham, NH, July 28-August 1, 1986.
- E. M. Patterson, R. A. Bohlander, R. W. McMillan, R. L. Mandock, R. J. Hill, J. T. Priestley, S. F. Clifford, B. E. Rischel, and R. Olsen, "Spectral Density and Distributions of Intensity and Phase of Millimeter Wave Signals Propagated Through Rain, Fog and Snow", Proc. URSI Symposium, Commission F, Wave Propagation: Remote Sensing and Communications, Univ. of New Hampshire, Durham, NH, July 28-August 1, 1986.
- E. M. Patterson, R. L. Mandock, R. W. McMillan, R. A. Bohlander, R. J. Hill, J. T. Priestley, B. E. Rischel, and R. Olsen, "Correlation of Attenuation of Millimeter Wave Signals with Rain Rate", Proc. URSI Symposium, Commission F, Wave Propagation: Remote Sensing and Communications, Univ. of New Hampshire, Durham, NH, July 28-August 1, 1986.

**APPENDIX A**

**Reprints of Articles Published Under the Contract**

## Millimeter wave atmospheric turbulence measurements: preliminary results

R. W. McMillan, R. A. Bohlander

Georgia Institute of Technology, Engineering Experiment Station, Atlanta, Georgia 30332

G. R. Ochs, R. J. Hill, S. F. Clifford

National Oceanic and Atmospheric Administration, Environmental Research Laboratories

Wave Propagation Laboratory, Boulder, Colorado 80302

D. G. Bauerle

Ballistic Research Laboratory, Aberdeen Proving Ground, Maryland 21005

J. Nemanich

Harry Diamond Laboratories

U.S. Army Electronics Research and Development Command, Adelphi, Maryland 20783

### Abstract

The effects of atmospheric turbulence on millimeter wave propagation are not as well understood as the corresponding effects on optical propagation, generally because of the strong dependence of turbulence effects on the absolute humidity structure parameter  $C_Q^2$  (as opposed to just the temperature structure parameter  $C_T^2$  and the cross-correlation  $C_{TQ}$ ) in this frequency range. Scattered results at 35, 94, 140, and 220 GHz are available, but in almost all cases, available atmospheric data are inadequate, generally because turbulence measurements were obtained incidental to other propagation experiments. This paper attempts to compare available results to theory, and shows that agreement in most cases is plausible. An experiment designed to characterize millimeter wave turbulence at several frequencies of interest, while at the same time determining values of appropriate atmospheric parameters, will be discussed. Included in the planned investigation are measurements of the mutual coherence function showing angle-of-arrival effects and intensity fluctuations.

### Introduction

The recent increase in interest in the use of millimeter waves for both civilian and military applications has caused emphasis to be placed on the study of the effects of the atmosphere on radiation in this frequency range. Attenuation by oxygen and especially water vapor, scattering by aerosols, and perturbations by atmospheric turbulence are among the subjects being studied at several laboratories in this country and throughout the world. One would expect all of these effects to be different for millimeter waves than for either the microwave or the infrared/visible spectrum because of the peculiar problems associated with the propagation of radiation of intermediate wavelengths through the atmosphere.

In considering atmospheric turbulence at millimeter wavelengths, for example, the contribution of the absolute humidity fluctuations, measured by the structure parameter  $C_Q^2$ , must be considered in addition to the fluctuations in temperature, characterized by the structure parameter  $C_T^2$ . Furthermore, the cross-correlation of these quantities,  $C_{TQ}$ , which may be either positive or negative, must also be included in the analysis of millimeter wave turbulence effects. These effects include fluctuations of both intensity and angle-of-arrival, and both of these phenomena will be treated in some detail in this paper.

In the fall of 1978, millimeter wave propagation measurements were made by Georgia Tech at both 94 and 140 GHz at White Sands Missile Range, New Mexico, over a 2 km path<sup>1</sup>. Humidity, temperature, and the visible wavelength index of refraction structure parameter  $C_n^2$  were also measured. Significant intensity fluctuations were observed at both frequencies during these tests. These fluctuations could be explained plausibly by a theory of turbulence effects developed by Armand, et al.<sup>2</sup>, who included the effects of the structure functions of both temperature and humidity in their calculations, although the cross-correlation of these parameters was not adequately treated. A treatment including this cross-correlation has been given by Hill, et al.<sup>3</sup>, whose theory also gives plausible agreement with the White Sands results, as will be shown later. Subsequent measurements were made during winter propagation tests near Burlington, Vermont at frequencies of 35, 95, 140, and 220 GHz<sup>4,5</sup>. Again, little supporting turbulence related meteorological data are available because turbulence results were obtained incidental to the propagation measurements. However, the observed effects of turbulence showed good agreement with the expected theoretical dependence of the log amplitude variance on both frequency and range, as will be discussed later. The results of these measurements, together with a discussion of their comparison to the theory of Hill, et al. is the main thrust of this paper.

Since a complete characterization of the atmosphere was not available because of limitations in instrumentation, it was necessary to make some improvisations in the comparison of theory and experiment. For the White Sands measurements, the log amplitude variance was determined from the chart recorder tracings for both the 94 and 140 GHz propagation links. The values of this parameter were then substituted into the equation for log amplitude variance derived by Hill, et al. to deduce the values of the absolute humidity structure parameter  $C_Q^2$  which according to theory would have caused the millimeter wave effects observed. This parameter (along with  $C_{TQ}$ ) is the only factor in the equation not measured at White Sands. An assumption was made about the relationship between  $C_Q^2$ ,  $C_T^2$ , and  $C_{TQ}$  that provides a value for the cross-correlation as will be explained later. The result of the calculation is that plausible values for  $C_Q^2$  are obtained. For the Burlington measurements, values of the log amplitude variance  $\sigma_\chi^2$  were determined from chart recorder traces for four different frequencies and two different ranges  $L$ . For the longer range,  $\sigma_\chi^2$  follows the theoretical  $L^{11/6}$  variation very well, but the agreement for short path is not as good. The data follow the  $L^{11/6}$  range dependence fairly closely. Both sets of measurements will be discussed in more detail in the following sections.

### Results of Theory

Hill, Clifford, and Lawrence<sup>3</sup> have derived an expression for the log amplitude variance of the fluctuations of electromagnetic radiation propagating through the turbulent atmosphere which holds for microwave through optical frequencies and maintains the dependence on  $C_Q^2$ ,  $C_T^2$ , and  $C_{TQ}$ . This equation comprises separate contributions from the real and imaginary parts and from the cross-correlation of these parts, as follows:

$$\sigma_\chi^2 = \sigma_R^2 + \sigma_I^2 + \sigma_{IR} \quad (1)$$

where R, I, and IR refer to the real, imaginary, and cross-correlation contributions, respectively. The real part of  $\sigma_\chi^2$  is given by

$$\sigma_R^2 = 0.124k^{7/6}L^{11/6} \left[ 1 - 2.73 \left( \frac{L_0}{\sqrt{L/k}} \right)^{-7/3} \right] \cdot \left( A_T^2 \frac{C_T^2}{\langle T \rangle^2} + A_Q^2 \frac{C_Q^2}{\langle Q \rangle^2} + 2 A_Q A_T \frac{C_{TQ}}{\langle T \rangle \langle Q \rangle} \right), \quad (2)$$

where  $k$  is wavenumber,  $\langle T \rangle$  is the mean value of temperature,  $\langle Q \rangle$  is the mean value of absolute humidity, and  $L_0$  is the outer scale dimension. The dimensionless parameters  $A_T$  and  $A_Q$  are given by

$$A_T = \langle T \rangle \frac{\partial N}{\partial T} P, Q \times 10^{-6}, \quad (3)$$

$$A_Q = \langle Q \rangle \frac{\partial N}{\partial Q} P, T \times 10^{-6}, \quad (4)$$

where  $N$  is the refractivity of the atmosphere. A third equation involving  $A_P$  where  $P$  is atmospheric pressure must also be considered but pressure fluctuations are shown in Reference 3 to have a negligible effect on refractive index fluctuations at all frequencies of interest. The refractivity  $N$  is given by:

$$N = (n-1) \times 10^6 = (77.6 \text{ }^\circ\text{K/mb}) \frac{P}{T} + (1.71 \times 10^3 \text{ }^\circ\text{K/g/m}^3) \frac{Q}{T}, \quad (5)$$

where  $P$  is in millibars,  $T$  is in degrees Kelvin, and  $Q$  is in  $\text{g/m}^3$ . This equation neglects terms which represent dispersive contributions to the real part of the refractive index in the neighborhood of millimeter wave absorption lines. References 3 and 6 show plots of the refractivity which support the fact that dispersive contributions are at most a few percent in the frequency regions between lines, and therefore they would not have an important contribution to turbulence phenomena. Combining equations (3), (4), and (5) finally gives for  $A_T$  and  $A_Q$ :

$$A_T = -N \times 10^{-6}, \quad (6)$$

$$A_Q = (1.71 \times 10^3 \text{ }^\circ\text{K/g/m}^3) \frac{Q}{T} \times 10^{-6}. \quad (7)$$

The contributions of the parameters  $\sigma_1^2$  and  $\sigma_{IK}$  to the log amplitude variance are considered negligible because they contain a parameter  $B_Q$  given by:

$$B_Q = \frac{1}{4\pi} \langle Q \rangle \left( \frac{\partial B}{\partial Q} \right)_{T,P} \quad (1)$$

where  $B$  is the atmospheric absorption coefficient. In the low-frequency window regions, this parameter is considered negligible, as is borne out by calculations displayed graphically in References 3 and 4.

Finally, it is necessary to devise some sort of value for the cross-correlation term in Equation (2). Hill, et al.<sup>3</sup> suggest that an order-of-magnitude estimate for  $C_{TQ}$  is

$$\frac{C_{TQ}}{\langle T \rangle \langle Q \rangle} = \pm \left( \frac{C_Q^2}{\langle Q \rangle^2} \frac{C_T^2}{\langle T \rangle^2} \right)^{1/2} \quad (2)$$

assuming a correlation coefficient of  $\pm 1$ . For calculations in this paper, the positive sign was chosen because data were taken on sunny days when the surface was a source of both humidity and heat - implying that humidity and temperature fluctuations would have a strong positive correlation.

Using the above results, it is possible to substitute into Equation (2) and calculate values of  $C_Q^2$  based on substituting values of  $\sigma_X^2$  obtained from chart recorder tracings of field measurements. A later section treats the comparison of values of  $C_Q^2$  determined in this way at 94 and 140 GHz, and also compares the frequency and range dependences of field measurements to those given by Equation (2).

#### Description of Experiments

Two sets of measurements are used for comparison with theory in this paper, namely the propagation tests mentioned earlier that were conducted at White Sands Missile Range, NM, and those conducted at Burlington, VT. For both sets of tests, meteorological data including temperature, humidity, wind speed and direction, and optical  $C_n^2$  were generally available; but unfortunately many of the sensors for the Burlington measurements were damaged in a storm the night before the measurements were made. Measurements of  $C_Q^2$  and  $C_{TQ}$  were not available for either case, which emphasizes a serious need for making dedicated measurements of millimeter wave turbulence effects. Both sets of turbulence data were obtained incidental to other propagation tests. A system designed for making such dedicated measurements is described in Reference 7.

Figure 1 is a sketch of the experimental arrangement used for the White Sands tests, which were conducted at 94 and 140 GHz over a 2 km path in the desert. The transmitters used for both frequencies were free-running klystron oscillators with about 50 mW power output. A precision rotary vane attenuator was used to calibrate several levels of attenuation for the 94 GHz system, but it was necessary to calibrate the 140 GHz attenuation by simply blocking or unblocking the transmitter. The transmitters were 100% modulated with a 1 kHz square wave to facilitate the use of phase sensitive detection. Both transmitter and receiver antennas were horn-lens combinations with beamwidths of 2 degrees for each frequency, and measurements were made simultaneously.

Superheterodyne receivers were used for both frequencies. The 94 GHz receiver used a fundamental mixer with a local oscillator near 94 GHz, while the 140 GHz receiver used a harmonic mixer pumped by a 70 GHz klystron. Phase sensitive detection with lock-in amplifiers was used for both channels, with the 1 kHz reference from the transmitter modulator transmitted over twisted-pair line to the receiver. Under these conditions, it was necessary to reduce transmitted power to avoid saturating the receiver. Receiver outputs were recorded on a dual channel chart recorder.

Two different systems were used to make the Burlington measurements. The first system used transmitter and receiver vans separated by about 600 m, and operated at frequencies of 94, 140, and 220 GHz. The transmitters were based on the pulsed extended interaction oscillator tube built by Varian Canada, and the receivers were simple video detectors. Cassegrain antennas with 60 cm diameters were used for both transmitters and receivers. Unfortunately, the data obtained with this system did not have sufficient gain to permit accurate determinations of the values of  $\sigma_X^2$  from the recorder tracings. Data from the second system were therefore used for the comparison to be discussed in the next section.

The second system included pulsed radars at 35, 95, 140, and 217 GHz which used INPATT transmitters and local oscillators. This system used corner cube reflectors at ranges of 152 and 610 m to generate returns and was originally designed to measure absolute atmospheric attenuation at these frequencies. Figure 2 is a schematic diagram of the second system.

### Comparison of Theory and Experiment

The measurements made at White Sands Missile Range were divided into a number of separate "events" in which an explosive charge was detonated in the propagation path and the subsequent deterioration of millimeter wave signals was observed at the receiver. Measurements of turbulence effects were necessarily confined to times slightly before and after these events, because the primary purpose of the experiments was to observe propagation through dust. Unfortunately, there were only five events in which both the 94 and 140 GHz systems operated simultaneously well enough to meaningfully compare turbulence effects.

In comparing theory and experiments, measured values of  $\sigma_X^2$ ,  $P$ ,  $T$ , and  $Q$  were substituted into Equations (2), (3), (4), and (5) to determine values of  $C_Q^2$  for both 94 and 140 GHz. Table I gives values of parameters used to make these calculations.  $C_T^2$  was determined from measurements of optical scintillation by using the relation

$$C_T^2 = \left( \frac{C_n T^2}{79P} \times 10^6 \right)^2, \quad (10)$$

where  $C_n^2$  is the visible wavelength index of refraction structure parameter, and  $P$  is measured in millibars. Table II gives values of  $\sigma_X^2$  obtained from chart recorder tracings and values of  $C_T^2$  determined using Equation (10), for each event. Simultaneous data at the two frequencies were not obtained for Events A-1 and S-1, as indicated in the Table. Figure 3 compares  $C_Q^2$  determined in this way from 94 and 140 GHz measurements for each of the five events for which simultaneous data were obtained. The solid curve has unity slope, and all of the points should, of course, lie on this straight line for ideal agreement with theory.

It is also possible to compare measurements of the frequency dependence of the log amplitude variance to theory. The log amplitude variances calculated at the two frequencies are related by

$$\sigma_X^2(140) = \left( \frac{140}{94} \right)^{7/6} \sigma_X^2(94), \quad (11)$$

according to Equation (2). Figure 4 shows the comparison between values of this parameter measured at the two frequencies for the five events. Again, the points should lie on the straight line given by Equation (11).

The variance of angle-of-arrival fluctuations for a spherical wave is given by<sup>8</sup>

$$\sigma_A^2 = 0.54 LC_n^2 r^{-1/3} \quad (12)$$

where  $r$  is antenna spacing and  $\sigma_A$  is measured in radians. Although angle-of-arrival fluctuations were not measured at White Sands, it is of interest to determine their magnitude using values of  $C_n^2$  calculated from Equation (2). In making this determination, note that the factor in parentheses in this equation involving  $C_T^2$ ,  $C_Q^2$ , and  $C_TQ$  is just the millimeter wave  $C^2$ . Figure 5 is a plot of peak-to-peak ( $6\sigma_A$ ) angle of arrival fluctuations versus  $C_n^2$  using values of this parameter derived at 94 GHz. Since  $\sigma_A^2$  in millimeter wave atmospheric windows is approximately independent of frequency, by Equation (12) neglecting dispersion, the results in Figure 5 may be taken as a representative prediction for millimeter wave windows. Values of  $C_n^2$  are noted on the curve, although this curve is not intended to compare theory and experiment. It is simply intended to show expected values of angle-of-arrival for the observed range of  $C_n^2$ . An antenna spacing of 0.1 m was used for these calculations.

That the values obtained for  $C_Q^2$  are reasonable can be seen from the following plausibility arguments. If water vapor were thoroughly mixed so that its density fluctuations were driven solely by temperature fluctuations, the following relation would hold

$$\frac{\langle (\delta Q)^2 \rangle^{1/2}}{\langle Q \rangle} = \frac{\langle (\delta T)^2 \rangle^{1/2}}{\langle T \rangle}, \quad (13)$$

and

$$\frac{C_Q^2}{\langle Q \rangle^2} = \frac{C_T^2}{\langle T \rangle^2}$$

or

$$\frac{C_Q^2}{C_T^2} = \frac{\langle Q \rangle^2}{\langle T \rangle^2}$$

However, in the case of very strong humidity fluctuations<sup>3</sup>,

$$\frac{\langle (\delta Q)^2 \rangle^{1/2}}{\langle Q \rangle} = \frac{100 \langle (\delta T)^2 \rangle^{1/2}}{\langle T \rangle}$$

or

$$\frac{C_Q^2}{C_T^2} = \frac{10^4 \langle Q \rangle^2}{\langle T \rangle^2} \quad (11)$$

Table II gives calculated values of  $C_Q^2/C_T^2$  for each of the events treated. In comparing the average value of this ratio, which is  $0.55 \text{ g}^2/\text{m}^3\text{-}^\circ\text{K}^2$ , to the average value of  $\langle Q \rangle^2/\langle T \rangle^2 = 8.65 \times 10^{-6} \text{ g}^2/\text{m}^3\text{-}^\circ\text{K}^2$  in Table I, one obtains

$$\frac{C_Q^2}{C_T^2} \approx 640 \frac{\langle Q \rangle^2}{\langle T \rangle^2}, \quad (12)$$

which is a reasonable result, indicating that the values of  $C_Q^2$  obtained in this way are plausible.

Finally, the frequency and range dependences of  $\sigma_\chi^2$  measured at Burlington were compared to experiment at 35, 95, 140, and 217 GHz. Values of  $\sigma_\chi^2$  obtained from the chart recorder tracings are plotted as a function of frequency for the 610 m path in Figure 6. The best-fit curve having a  $\nu^{1/6}$  dependence was drawn through these points (virtually a straight line). A change in  $\sigma_\chi^2$  corresponding to  $(L_2/L_1)^{11/6}$  was then scaled downward on the graph, and a second straight line was drawn parallel to the first. Values of  $\sigma_\chi^2$  for a range of 152 m were plotted on this graph. As seen in the figure, the agreement with the  $\nu^{1/6}$  dependence is very good for the longer path, but not as good for the shorter. It is possible that near-field effects contributed to errors in the latter data. Also, these data were unaccountably noisier than the long path data. However, Figure 6 shows that the agreement between theory and experiment for the frequency and range dependencies of  $\sigma_\chi^2$  is generally good.

#### Future Measurements

A dedicated millimeter wave turbulence measuring facility with several appropriate meteorological sensors is being assembled by Georgia Tech and NOAA with support from the U.S. Army Research Office. This system will consist of bistatic transmitter and receiver systems housed in trucks and will probe all of the atmospheric windows and absorption lines in the range 118 GHz to 340 GHz.

The transmitter will be a phase-locked klystron oscillator with an offset paraboloid antenna mounted in a step-van. Four receivers with separations varying from 1.4 to 10 m and pumped by a single local oscillator will be used to measure turbulence induced phase and amplitude fluctuations, from which the atmospheric mutual coherence function can be derived. These results will also give the log amplitude variance and the magnitudes of phase fluctuations from which the angle-of-arrival of the transmitted wavefront can be determined. The receivers will be mounted in a semi-trailer van and will use horn-lens antennas. Power from the single phase-locked klystron local oscillator will be distributed to the four receiver mixers by a system of optical beam splitters and beam waveguides. The propagation path is expected to be about 2 km in length.

A complete set of meteorological instrumentation will provide atmospheric data coincident with the measured phase and amplitude fluctuations. Measurements of  $C_T^2$ ,  $C_Q^2$ ,  $C_{TQ}$ , temperature, humidity, wind speed and direction, and aerosol parameters will be made. Data acquisition and some limited preprocessing will be accomplished by a microprocessor-based computer system, which will simultaneously store atmospheric parameters and turbulence data on tape. Provision is also being made to record measured results on chart recorders and CRT terminals to continuously monitor the data acquisition process.

This facility is expected to be operational in the fall of 1982 with frequency coverage from 118-174 GHz, with the other frequencies being added later. Reference 7 gives a detailed description of this measurement system.

#### Conclusions

This paper compares theory to experiment based on two sets of millimeter wave propagation measurements obtained with limited meteorological data. Agreement in all cases is generally good, but it is again emphasized that dedicated millimeter wave turbulence measurements must be made before realistic conclusions can be drawn. At the present time, only scattered data are available. The millimeter wave turbulence measuring facility discussed briefly in the preceding section is designed to meet the need for more detailed, dedicated measurements.

Due to the nature of the measurements discussed in this paper, some care should be taken in relating them to actual situations or in using them to design millimeter wave systems. Although the agreements achieved have been generally good, they may be fortuitous. It does appear, however, that the magnitudes of the effects are great enough so that turbulence should be considered in the design of millimeter wave systems.

#### Acknowledgements

This work was supported by the U.S. Army Research Office under Contract DAAG29-81-K-0173. The authors gratefully acknowledge the help of R. J. Wellman of the U.S. Army Harry Diamond Laboratories for his help in obtaining propagation data. The continuing support and interest of D. E. Snider of the U.S. Army Atmospheric Sciences Laboratory is also gratefully acknowledged.

#### References

1. R. W. McMillan, J. C. Wiltse, D. E. Snider, "Atmospheric Turbulence Effects on Millimeter Wave Propagation," IEEE EASCON Conference Record, Arlington, VA., October 1979.
2. N. A. Armand, A. O. Izyumov, and A. V. Sokolov, "Fluctuations of Submillimeter Waves in a Turbulent Atmosphere", Radio Engineering and Electronic Physics, Vol. No. 8, 1971, pp. 1257-1266.
3. R. J. Hill, S. F. Clifford, and R. S. Lawrence, "Refractive-Index and Absorption Fluctuations in the Infrared Caused by Temperature, Humidity, and Pressure Fluctuations", J. Opt. Soc. Am., Vol. 70, No. 10, Oct. 1980, pp. 1192-1205.
4. H. B. Wallace, "Millimeter-Wave Propagation Measurements at the Ballistic Research Laboratory", Proceedings of the SPIE Conference on Atmospheric Effects on Electro-Optical, Infrared, and Millimeter Wave Systems Performance, August 27-28, 1981, San Diego, CA.
5. J. Nemerich, R. J. Wellman, D. Rocha, and G. B. Wetzel, "Characteristics of Near-Millimeter Wave Propagation in Snow", Ibid.
6. R. J. Hill and S. F. Clifford, "Contribution of Water Vapor Monomer Resonances to Fluctuations of Refraction and Absorption for Submillimeter through Centimeter Wavelengths", Radio Science, 16, pp. 77-82, 1981.
7. R. W. McMillan, R. A. Bohlander, and G. R. Ochs, "Instrumentation for Millimeter Wave Turbulence Measurements", Proceedings of the SPIE Conference, op. cit.
8. R. L. Fante, "Electromagnetic Beam Propagation in Turbulent Media", Proc. IEEE, 63, pp. 1669-1692, 1978.

Table I

Parameters Used in Calculations  
Based on White Sands Data

Frequencies	94 and 140 GHz
Path Length L	2 km
Outer Scale Dimension $L_0$	2.5 m
$A_T$	$-3.22 \times 10^{-4}$
$A_Q$	$5.03 \times 10^{-5}$
$\langle T \rangle$	289°K
$\langle Q \rangle$	$8.5 \text{ g/m}^3$
$C_T^2$	Calculated from Optical $C_n^2$
$C_Q^2$	Calculated
$\gamma_x^2$	Determined from Recorder Tracings

Table II

Values of  $C_T^2$ ,  $\sigma_x^2$ , and  $C_Q^2/C_T^2$

Events	$C_T^2 (\text{m}^2 \text{K}^{-2/3})$	$\sigma_x^2$		$C_Q^2/C_T^2 (\text{g}^2/\text{m}^6 \text{K}^{-2})$
		94 GHz	140 GHz	
A-1	0.109	$1.19 \times 10^{-3}$		0.77
B-1	0.545		$1.20 \times 10^{-4}$	0.066
B-3	0.163	$9.32 \times 10^{-4}$	$1.14 \times 10^{-3}$	0.41
B-4	0.0436	$2.12 \times 10^{-4}$	$3.76 \times 10^{-4}$	0.41
B-6	0.0218	$1.86 \times 10^{-4}$	$4.96 \times 10^{-4}$	0.72
D-1	0.0654	$2.66 \times 10^{-4}$	$3.12 \times 10^{-4}$	0.32
D-2	0.00654	$1.46 \times 10^{-4}$	$2.12 \times 10^{-4}$	1.20

Note: Values of  $C_Q^2/C_T^2$  were calculated by dividing  $C_Q^2$ , determined by averaging 94 and 140 GHz results, by  $C_T^2$ .

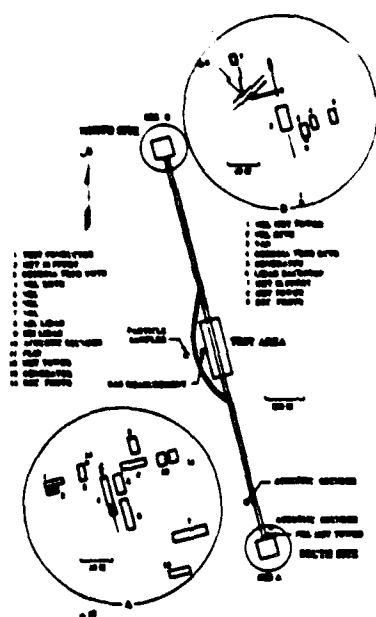


Figure 1. Plan View of Experimental Arrangement Used for White Sands Tests.

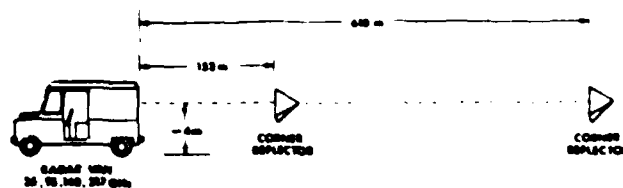


Figure 2. Schematic of Burlington Tests.

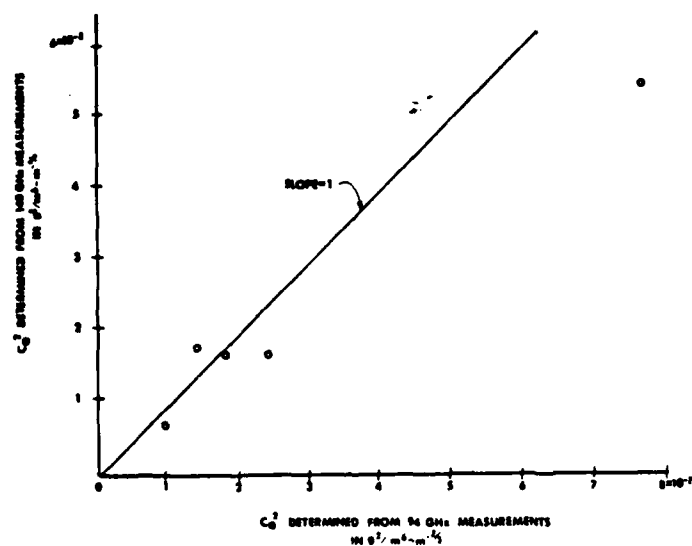


Figure 3. Comparison of  $C_G^2$  Determined from 94 and 140 GHz Measurements.

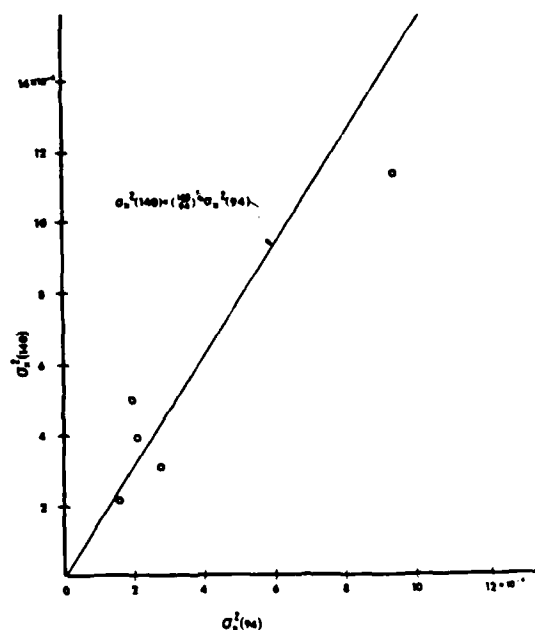


Figure 4. Comparison of  $\sigma_X^2$  Determined from 94 and 140 GHz Measurements.

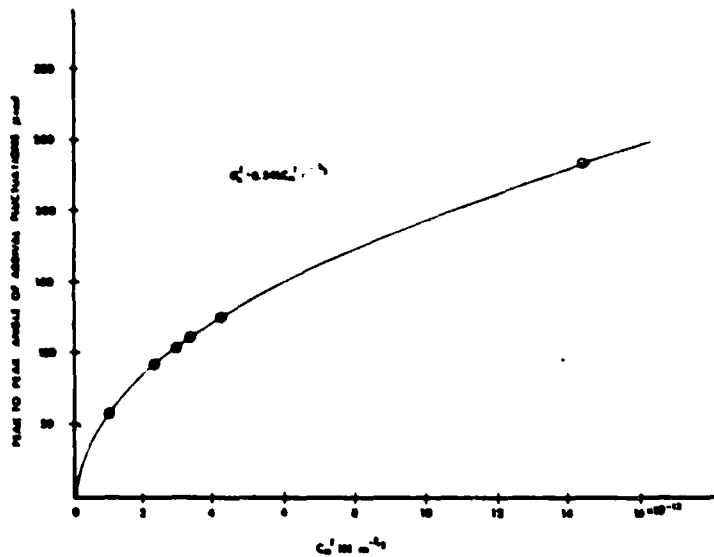


Figure 5. Calculated Peak-to-Peak Angle-of-Arrival Fluctuations.

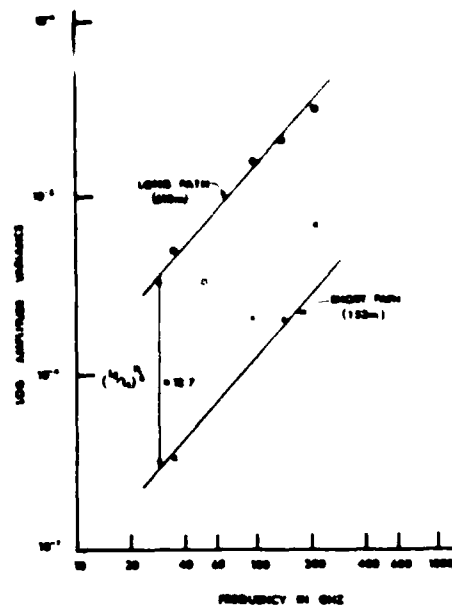


Figure 6. Comparison of the Frequency and Range Dependence of Turbulence Measurements to Theory.

# Millimeter wave atmospheric turbulence measurements: preliminary results and instrumentation for future measurements

R. W. McMillan  
R. A. Bohlander

Georgia Institute of Technology  
Engineering Experiment Station  
Atlanta, Georgia 30332

G. R. Ochs  
R. J. Hill  
S. F. Clifford

National Oceanic and  
Atmospheric Administration  
Environmental Research Laboratories  
Wave Propagation Laboratory  
Boulder, Colorado 80302

**Abstract.** Increasing emphasis is being placed on the study of the effects of atmospheric turbulence on the propagation of millimeter and submillimeter waves because of the potential usefulness of these frequency bands in both military and civilian applications. The characterization of millimeter wave turbulence effects is more complicated than that of the optical propagation case because of a strong dependence on the humidity structure parameter  $C_Q^2$ , as well as on the temperature structure parameter  $C_T^2$ . In addition, there is a dependence on the cross-correlation of these two parameters, denoted by  $C_{TQ}$ . Measured results on the effects of atmospheric turbulence on millimeter wave propagation, which include both amplitude and phase fluctuations, are very limited and have generally been obtained incidental to other propagation measurements. However, comparison of these limited experimental results with theory has shown good agreement. This paper compares scattered results measured at 35, 94, 140, and 220 GHz to theory, and shows that agreement in most cases is plausible. A future experiment specifically designed to characterize millimeter wave turbulence, with special emphasis on measurement of the pertinent atmospheric parameters, is also described.

**Keywords:** obscuration effects on electro-optic, infrared, and millimeter wave systems performance; millimeter wave propagation; millimeter wave instrumentation; millimeter wave turbulence measurements; atmospheric measurements; angle-of-arrival fluctuations.

*Optical Engineering* 22(1), 032-039 (January/February 1983).

## CONTENTS

1. Introduction
2. Results of theory
3. Description of experiments
4. Comparison of theory and experiment
5. Future millimeter wave measurements
6. Atmospheric measurements
7. Conclusions
8. Acknowledgments
9. References

## 1. INTRODUCTION

The recent increase in interest in the use of millimeter waves for both civilian and military applications has caused some emphasis to be placed on the study of the effects of the atmosphere on radiation in this frequency range. Attenuation by oxygen and especially water vapor, scattering by aerosols, and perturbations by atmospheric turbulence are among the subjects being studied at several laboratories. One would expect all of these effects to be different for millimeter waves than for either the microwave or the infrared-visible spectrum because of the peculiar problems associated with the propagation of radiation of intermediate wavelengths through the atmosphere.

In considering the effects of atmospheric turbulence at millimeter wavelengths, for example, the contribution of the absolute humidity fluctuations, measured by the structure parameter  $C_Q^2$ , must be considered in addition to the fluctuations in temperature, characterized by the structure parameter  $C_T^2$ . Furthermore, the cross-correlation of these quantities,  $C_{TQ}$ , which may be either positive or negative, must also be included in the analysis of millimeter wave turbulence effects. These effects include fluctuations of both intensity and angle-of-arrival, and both of these phenomena will be treated in some detail in this paper.

In the fall of 1978, millimeter wave propagation measurements were made by Georgia Tech at both 94 and 140 GHz at White Sands Missile Range, New Mexico, over a 2 km path.<sup>1</sup> Humidity, temperature, and the visible wavelength index of refraction structure parameter  $C_n^2$  were also measured. Significant intensity fluctuations were observed at both frequencies during these tests. These fluctuations could be explained plausibly by a theory of turbulence effects developed by Armand et al.,<sup>2</sup> who included the effects of the structure functions of both temperature and humidity in their calculations, although the cross-correlation of these parameters was not adequately treated. A treatment including this cross-correlation has been given by Hill et al.,<sup>3</sup> whose theory also gives plausible agreement with the White Sands results, as will be shown later. Subsequent measurements were made during winter propagation tests near Burlington, Vermont, at frequencies of 35, 95, 140, and 220 GHz.<sup>4,5</sup> However, little supporting turbulence related meteorological data are available because turbulence results were obtained incidental to the propagation measurements. The observed effects of turbulence showed good agreement with the expected theoretical dependence of

Invited Paper SP-104 received Aug. 11, 1982; revised manuscript received Sep. 20, 1982; accepted for publication Sep. 20, 1982; received by Managing Editor Oct. 26, 1982. This paper is a revision of Paper 305-12 which was presented at the SPIE seminar on Atmospheric Effects on Electro-Optic, Infrared, and Millimeter Wave Systems Performance, Aug. 27-28, 1981, San Diego, CA. The paper presented there appears (unrevised) in SPIE Proceedings Vol. 305.

© 1983 Society of Photo-Optical Instrumentation Engineers

the log amplitude variance on both frequency and range, as will be discussed later. The results of these Burlington and White Sands measurements, together with a discussion of their comparison to the theory of Hill et al., are treated in this paper.

Since a complete characterization of the atmosphere was not available because of limitations in instrumentation, it was necessary to make some improvisations in the comparison of theory and experiment. For the White Sands measurements, the log amplitude variance was determined from the chart recorder tracings for both the 94 and 140 GHz propagation links. The values of this parameter were then substituted into the equation for log amplitude variance derived by Hill et al. to deduce the values of the absolute humidity structure parameter  $C_Q^2$  which according to theory would have caused the millimeter wave effects observed. This parameter (along with  $C_{TQ}$ ) is the only factor in the equation not measured at White Sands. An assumption was made about the relationship between  $C_Q^2$ ,  $C_T^2$ , and  $C_{TQ}$  that provides a value for the cross-correlation, as will be explained later. The result of the calculation is that plausible values for  $C_Q^2$  are obtained. For the Burlington measurements, values of the log amplitude variance  $\sigma_x^2$  were determined from chart recorder traces for four different frequencies  $\nu$  and two different ranges  $L$ . For the longer range, the dependence of  $\sigma_x^2$  follows the theoretical  $\nu^{7/6}$  variation very well, but the agreement for the short path and the  $L^{11.6}$  range dependence is not as good. Both sets of measurements will be discussed in more detail in the following sections.

## 2. RESULTS OF THEORY

Hill, Clifford, and Lawrence<sup>3</sup> have derived an expression for the log amplitude variance of the fluctuations of electromagnetic radiation propagating through the turbulent atmosphere which holds for microwave through optical frequencies and maintains the dependence on  $C_T^2$ ,  $C_Q^2$ , and  $C_{TQ}$ . This equation comprises separate contributions from the real and imaginary parts and from the cross-correlation of these parts, as follows:

$$\sigma_x^2 = \sigma_R^2 + \sigma_I^2 + \sigma_{IR} \quad (1)$$

where R, I, and IR refer to the real, imaginary, and cross-correlation contributions, respectively. For spherical wave propagation, the real part of  $\sigma_x^2$  is given by

$$\sigma_R^2 = 0.124 k^{7/6} L^{11.6} \left[ 1 - 2.73 \left( \frac{L_0}{L, k} \right)^{-7/3} \right] \cdot \left( A_T^2 \frac{C_T^2}{\langle T \rangle^2} + A_Q^2 \frac{C_Q^2}{\langle Q \rangle^2} + 2 A_Q A_T \frac{C_{TQ}}{\langle T \rangle \langle Q \rangle} \right) \quad (2)$$

where  $k$  is the wave number  $2\pi/\lambda$ ,  $\langle T \rangle$  is the mean value of temperature,  $\langle Q \rangle$  is the mean value of absolute humidity, and  $L_0$  is the outer scale dimension. The dimensionless parameters  $A_T$  and  $A_Q$  are given by

$$A_T = \langle T \rangle \left( \frac{\partial N}{\partial T} \right)_{T, P} \times 10^{-6}$$

$$A_Q = \langle Q \rangle \left( \frac{\partial N}{\partial Q} \right)_{T, P} \times 10^{-6}$$

where  $N$  is the refractive index of the atmosphere,  $P$  is the atmospheric pressure, and  $T$  is the atmospheric temperature. The refractive index is a function of pressure, temperature, and absolute humidity, but pressure fluctuations are considered negligible in this context. The refractive index  $N$  is given by

$$N = (n - 1) \times 10^6 = (77.6^\circ \text{K} \cdot \text{mb}) \frac{P}{T} + (1.71 \times 10^3^\circ \text{K} \cdot \text{g} / \text{m}^3) \frac{Q}{T} \quad (3)$$

where  $P$  is in millibars,  $T$  is in degrees Kelvin, and  $Q$  is in  $\text{g} / \text{m}^3$ . This equation neglects terms which represent dispersive contributions to the real part of the refractive index in the neighborhood of millimeter wave absorption lines. References 3 and 6 show plots of the refractivity which support the fact that these terms contribute at most a few percent in the frequency regions between lines, and therefore they would not have an important contribution to turbulence phenomena. Combining Eqs. (3), (4), and (5) finally gives, for  $A_T$  and  $A_Q$ ,

$$A_T = -N \times 10^{-6}$$

$$A_Q = \left( 1.71 \times 10^3^\circ \text{K} / \text{g} / \text{m}^3 \right) \frac{Q}{T} \times 10^{-6}$$

The contributions of the parameters  $\sigma_I^2$  and  $\sigma_{IR}$  to the log amplitude variance are also considered negligible because they contain parameter  $B_Q$  given by

$$B_Q = \frac{1}{4\pi\nu} \langle Q \rangle \left( \frac{\partial B}{\partial Q} \right)_{T, P}$$

where  $B$  is the atmospheric absorption coefficient. In the millimeter wave frequency window regions, this parameter is considered negligible because borne out by calculations displayed graphically in Reference 3.

Finally, it is necessary to devise some sort of value for the cross-correlation term in Eq. (2). Hill et al. suggest that a reasonable magnitude estimate for  $C_{TQ}$  is

$$\frac{C_{TQ}}{\langle T \rangle \langle Q \rangle} = \pm \left( \frac{C_Q^2}{\langle Q \rangle^2} - \frac{C_T^2}{\langle T \rangle^2} \right)$$

assuming a correlation coefficient of  $\pm 1$ . In this paper, the positive sign was chosen because on 14 days when the surface was a source of moisture, implying that humidity and temperature had a strong positive correlation.

Using the above results, it is possible to calculate values of  $\sigma_x^2$  based on values of  $C_T^2$  from chart recorder tracings. This paper treats the comparison of the 94 and 140 GHz measurements and the dependence of log amplitude variance on range.

## 3. DESCRIPTION OF EXPERIMENT

Two sets of measurements were made. The first set was made at White Sands, New Mexico, and the second set was made at Burlington, North Carolina. The White Sands measurements were made during the summer of 1967, and the Burlington measurements were made during the summer of 1968. The measurements were made using a millimeter wave radiometer which was described in detail in Reference 1. The radiometer was used to measure the log amplitude variance of the fluctuations of electromagnetic radiation propagating through the turbulent atmosphere. The measurements were made at two different frequencies, 94 GHz and 140 GHz, and at two different ranges, 100 m and 200 m. The results of the measurements are presented in the following sections.

NO-A184 837

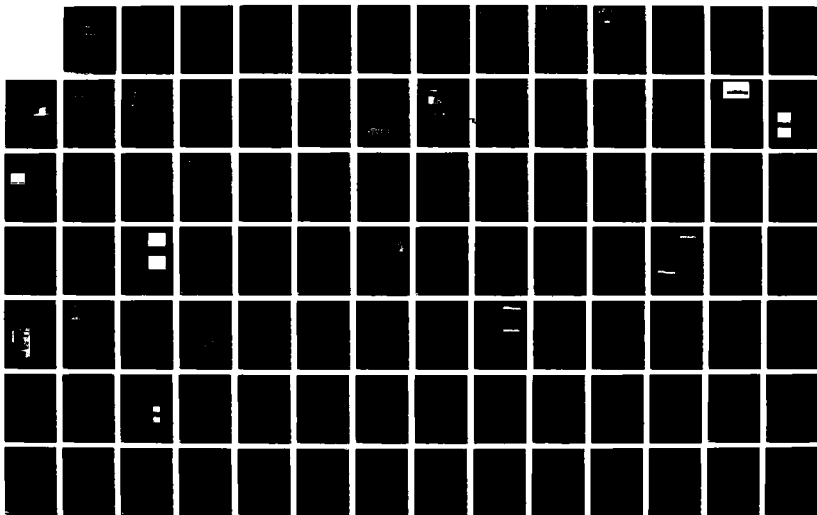
AN INVESTIGATION OF MILLIMETER WAVE PROPAGATION IN THE  
ATMOSPHERE: MEASUR. (U) GEORGIA TECH RESEARCH INST  
ATLANTA R W MCHILLAN ET AL. 17 JUN 87 ARO-18457.12-05  
DAGG29-81-K-0173

2/3

UNCLASSIFIED

F/G 20/14

NL





MICROCOPY RESOLUTION TEST CHART  
NATIONAL BUREAU OF STANDARDS-1963-A

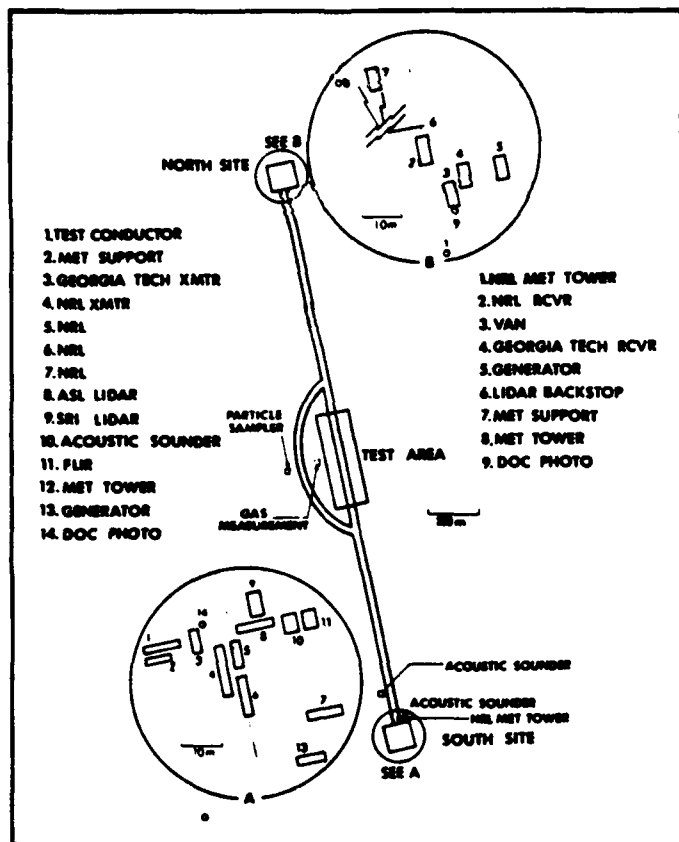


Fig. 1. Plan view of White Sands test range.

output. A precision rotary vane attenuator was used to calibrate several levels of attenuation for the 94 GHz system, but it was necessary to calibrate the 140 GHz attenuation by simply blocking or unblocking the transmitter. The transmitters were 100% modulated with a 1 kHz square wave to facilitate the use of phase sensitive detection. Both transmitter and receiver antennas were horn-lens combinations with beamwidths of 2 degrees for each frequency, and measurements at the two frequencies were made simultaneously.

Superheterodyne receivers were used for both frequencies. The 94 GHz receiver used a fundamental mixer with a local oscillator near 94 GHz, while the 140 GHz receiver used a harmonic mixer pumped by a 70 GHz klystron. Phase sensitive detection with lock-in amplifiers was used for both channels, with the 1 kHz reference from the transmitter modulator transmitted over twisted-pair line to the receiver. Under these conditions, it was necessary to reduce transmitted power to avoid saturating the receiver. Receiver outputs were recorded on a dual channel chart recorder.

Two different systems were used to make the Burlington measurements. The first system used transmitter and receiver vans separated by about 600 m and operated at frequencies of 94, 140, and 220 GHz. The transmitters were based on the pulsed extended interaction oscillator tube built by Varian Canada, and the receivers were simple video detectors. Cassegrain antennas with 60 cm diameters were used for both transmitters and receivers. Unfortunately, the data obtained with this system did not have sufficient gain to permit accurate determinations of the values of  $\sigma_x^2$  from the recorder tracings. Data from the second system were therefore used for the comparisons to be discussed in the next section.

The second system included pulsed radars at 35, 95, 140, and 217 GHz which used IMPATT transmitters and local oscillators. This system employed corner cube reflectors at ranges of 152 and 610 m to generate returns and was originally designed to measure absolute atmospheric attenuation at these frequencies. Figure 2 is a schematic diagram of the second system.

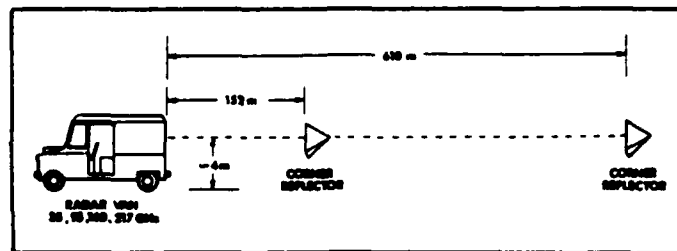


Fig. 2. Diagram of system used for Burlington tests.

#### 4. COMPARISON OF THEORY AND EXPERIMENT

The measurements made at White Sands Missile Range were divided into a number of separate "events" in which an explosive charge was detonated in the propagation path and the subsequent deterioration of millimeter wave signals was observed at the receiver. Measurements of turbulence effects were necessarily confined to times slightly before and after these events because the primary purpose of the experiments was to observe propagation through dust. Unfortunately, there were only five events in which both the 94 and 140 GHz systems operated simultaneously well enough to meaningfully compare turbulence effects.

In comparing theory and experiments, measured values of  $\sigma_x^2$ ,  $P$ ,  $T$ , and  $Q$  were substituted into Eqs. (2), (3), (4), and (5) to determine values of  $C_T^2$  for both 94 and 140 GHz. Table I gives values of parameters used to make these calculations.  $C_T^2$  was determined from measurements of optical scintillation by using the relation

$$C_T^2 = C_n^2 \left( \frac{T^2}{79P} \times 10^6 \right)^2 \quad (10)$$

where  $C_n^2$  is the visible wavelength index of refraction structure parameter, and  $P$  is measured in millibars. Table II gives values of  $\sigma_x^2$  obtained from chart recorder tracings and values of  $C_T^2$  determined using Eq. (10) for each event. Simultaneous data at the two frequencies were not obtained for Events A-1 and B-1, as indicated in the table. Figure 3 compares  $C_Q^2$  determined in this way from 94 and 140 GHz measurements for each of the five events for which simultaneous data were obtained. The solid curve has unity slope, and all of the points should, of course, lie on this straight line for ideal agreement with theory.

It is also possible to compare measurements of the frequency dependence of the log amplitude variance to theory. The log amplitude variances calculated at the two frequencies are related by

$$\sigma_x^2(140) = \left( \frac{140}{94} \right)^{7.6} \sigma_x^2(94) \quad (11)$$

according to Eq. (2). Figure 4 shows the comparison between values

TABLE I. Parameters Used in Calculations Based on White Sands Data

Frequencies	94 and 140 GHz
Path length $L$	2 km
Outer scale dimension $L_0$	2.5 m
$A_T$	$-3.22 \times 10^{-4}$
$A_Q$	$5.03 \times 10^{-5}$
$\langle T \rangle$	289 K
$\langle Q \rangle$	8.5 g/m <sup>3</sup>
$C_T^2$	Calculated from optical $C_n^2$
$C_Q^2$	Calculated
$\sigma_x^2$	Determined from recorder tracings

TABLE II. Values of  $C_T^2$ ,  $\sigma_A^2$ , and  $C_Q^2/C_T^2$ 

Event	$C_T^2 (^\circ K^2 m^{-2/3})$	$\sigma_A^2$		$C_Q^2/C_T^2 (g^2/m^5 \text{ } ^\circ K^2)$
		94 GHz	140 GHz	
A-1	0.109	$1.19 \times 10^{-3}$		0.77
B-1	0.545		$1.20 \times 10^{-4}$	0.066
B-3	0.163	$9.32 \times 10^{-4}$	$1.14 \times 10^{-3}$	0.41
B-4	0.0436	$2.12 \times 10^{-4}$	$3.76 \times 10^{-4}$	0.41
B-6	0.0218	$1.86 \times 10^{-4}$	$4.96 \times 10^{-4}$	0.72
D-1	0.0654	$2.66 \times 10^{-4}$	$3.12 \times 10^{-4}$	0.32
D-2	0.00654	$1.46 \times 10^{-4}$	$2.12 \times 10^{-4}$	1.20

\*Note: Values of  $C_Q^2/C_T^2$  were calculated by dividing  $C_Q^2$ , determined by averaging 94 and 140 GHz results, by  $C_T^2$ .

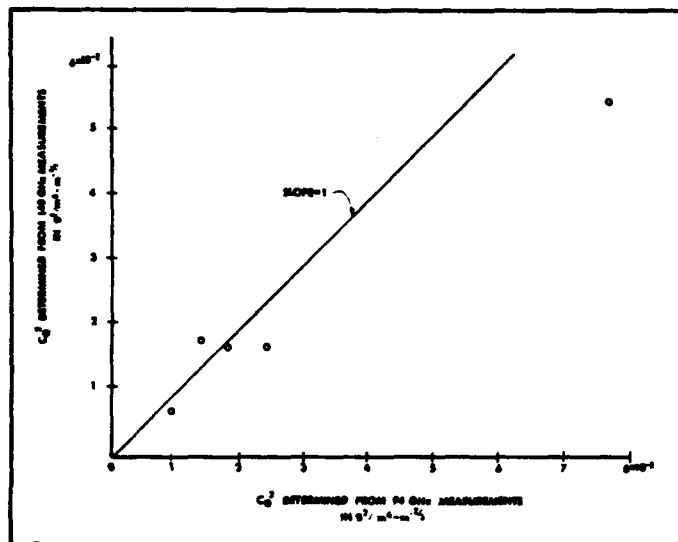


Fig. 3. Comparison of  $C_Q^2$  determined from 94 and 140 GHz measurements.

of this parameter measured at the two frequencies for the five events. Again, the points should lie on the straight line given by Eq. (11), and do fall fairly close to it. This is consistent with the findings of Cole et al.,<sup>8</sup> who looked at the frequency dependence of  $\sigma_A^2$  between 35 and 110 GHz.

The variance of angle-of-arrival fluctuations for a spherical wave is given approximately by<sup>9</sup>

$$\sigma_A^2 = 0.54 LC_n^2 r^{-1/3} \quad (12)$$

where  $\sigma_A$  is measured in radians, and where  $r$  may be interpreted as the spacing of the small antennas or the width of a large antenna. Although angle-of-arrival fluctuations were not measured at White Sands, it is of interest to determine their magnitude using values of the millimeter wave  $C_n^2$  calculated from Eq. (2). In making this determination, note that the factor in parentheses in this equation involving  $C_T^2$ ,  $C_Q^2$ , and  $C_{TQ}$  is just the millimeter wave  $C_n^2$ . Figure 5 is a plot of peak-to-peak ( $6\sigma_A$ ) angle-of-arrival fluctuations versus  $C_n^2$  using values of this parameter derived at 94 GHz. Since  $\sigma_A^2$  in millimeter wave atmospheric windows is approximately independent of frequency, by Eq. (12) neglecting dispersion, the results in Fig. 5 may be taken as a representative prediction for millimeter wave windows. Values of  $C_n^2$  are noted on the curve, although this curve is not intended to compare theory and experiment. It is simply intended to show expected values of angle-of-arrival for the observed range of  $C_n^2$ . An antenna spacing of  $r = 1$  m was used for these calculations.

That the values obtained for  $C_Q^2$  are reasonable can be seen from the following plausibility arguments. If water vapor were thoroughly

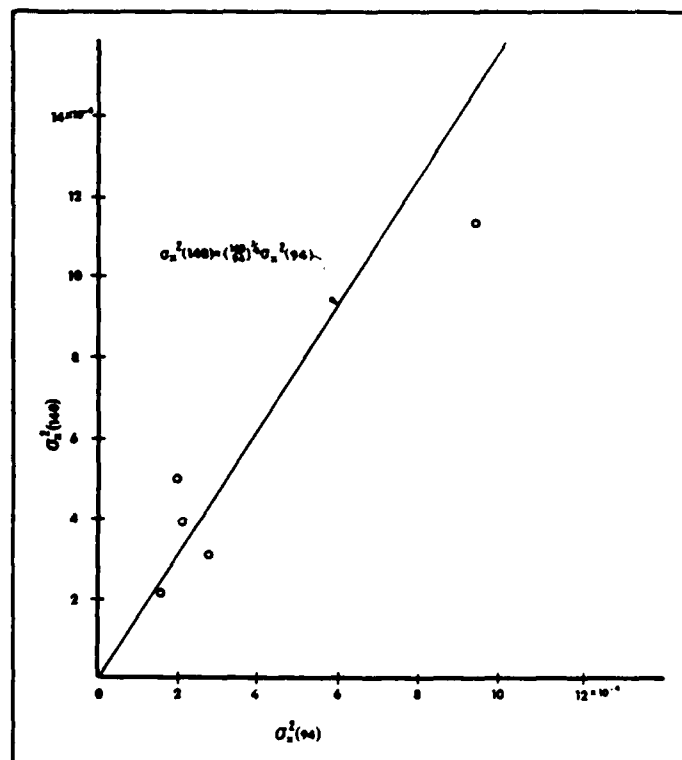


Fig. 4. Comparison of  $\sigma_A^2$  determined from 94 and 140 GHz measurements.

mixed so that its density fluctuations were driven solely by temperature fluctuations, the following relation would hold:

$$\frac{\langle (\delta Q)^2 \rangle^{1/2}}{\langle Q \rangle} = \frac{\langle (\delta T)^2 \rangle^{1/2}}{\langle T \rangle} \quad (13)$$

and

$$\frac{C_Q^2}{\langle Q \rangle^2} = \frac{C_T^2}{\langle T \rangle^2} \quad (14)$$

or

$$\frac{C_Q^2}{C_T^2} = \frac{\langle Q \rangle^2}{\langle T \rangle^2} \quad (15)$$

However, in the case of very strong humidity fluctuations,<sup>1</sup>

$$\frac{\langle (\delta Q)^2 \rangle^{1/2}}{\langle Q \rangle} \approx \frac{100 \langle (\delta T)^2 \rangle^{1/2}}{\langle T \rangle} \quad (16)$$

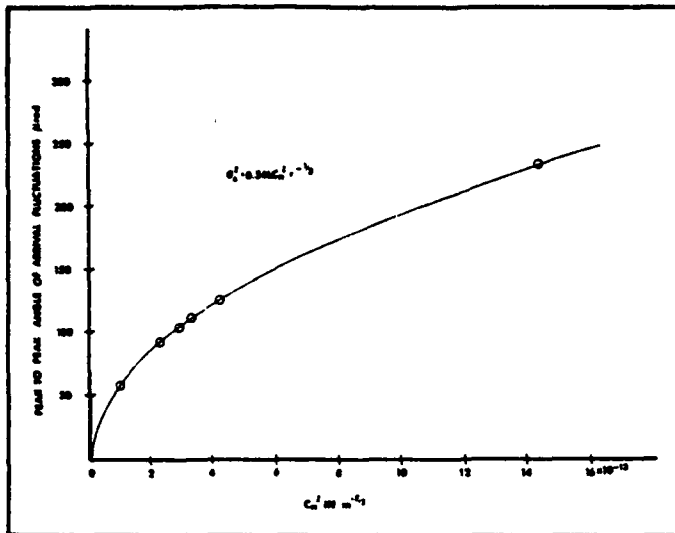


Fig. 5. Calculated peak-to-peak angle-of-arrival fluctuations.

or

$$\frac{C_Q^2}{C_T^2} \approx \frac{10^4 \langle Q \rangle^2}{\langle T \rangle^2} \quad (17)$$

Table II gives calculated values of  $C_Q^2/C_T^2$  for each of the events treated. In comparing the average value of this ratio, which is  $0.55 \text{ g}^2/\text{m}^6 \cdot \text{K}^2$ , to the average value of  $\langle Q \rangle^2/\langle T \rangle^2 = 8.65 \times 10^{-4} \text{ g}^2/\text{m}^6 \cdot \text{K}^2$  in Table I, one obtains

$$\frac{C_Q^2}{C_T^2} \approx 640 \frac{\langle Q \rangle^2}{\langle T \rangle^2} \quad (18)$$

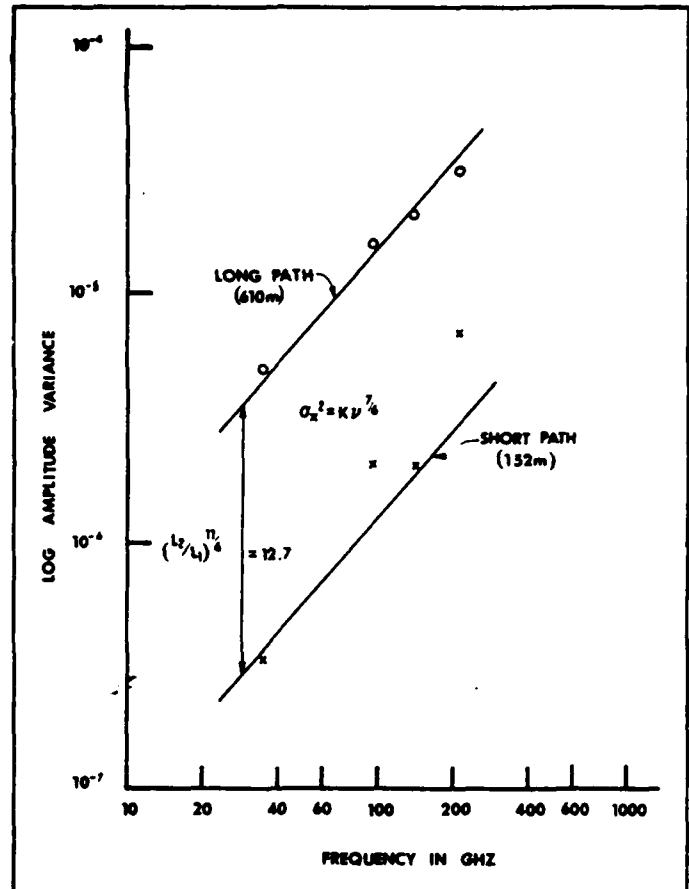
which is a reasonable result, indicating that the values of  $C_Q^2$  obtained in this way are plausible.

Finally, the frequency and range dependences of  $\sigma_x^2$  measured at Burlington were compared to experiment at 35, 94, 140, and 217 GHz. Values of  $\sigma_x^2$  obtained from the chart recorder tracings are plotted as a function of frequency for the 610 m path in Fig. 6. The best-fit curve having a  $\nu^{7/6}$  dependence was drawn through these points (virtually a straight line). A change in  $\sigma_x^2$  corresponding to  $(L_2/L_1)^{11/6}$  was then scaled downward on the graph, and a second straight line was drawn parallel to the first. Values of  $\sigma_x^2$  for a range of 152 m were plotted on this graph. As seen in the figure, the agreement with the  $\nu^{7/6}$  dependence is very good for the longer path, but not as good for the shorter. It is possible that near-field effects contributed to errors in the latter data. Also, these data were unaccountably noisier than the long path data. However, Fig. 6 shows that the agreement between theory and experiment for the frequency and range dependences of  $\sigma_x^2$  is generally good.

## 5. FUTURE MILLIMETER WAVE MEASUREMENTS

Since there is a lack of properly instrumented experimental results on millimeter wave turbulence and some indication that turbulence may significantly affect the performance of millimeter wave systems, Georgia Tech is undertaking a three-year program, with support from the U.S. Army Research Office, to make dedicated measurements of these effects using apparatus specifically designed for this purpose. This apparatus will measure the most general characteristic of electromagnetic propagation, namely, the mutual coherence function, and the remainder of this paper is a detailed discussion of the methods to be used for these measurements. In addition, thorough meteorological characterization will be done, as will also be described.

To obtain a nearly complete description of the effects of turbulence


 Fig. 6. Comparison of the frequency and range dependence of  $\sigma_x^2$  to theory.

on millimeter wave propagation, it is desired to measure the function

$$\begin{aligned} F(\vec{r}, t) &= V_1(\vec{r}_1, t) V_2^*(\vec{r}_1 + \vec{r}, t) \\ &= \rho(\vec{r}, \vec{r}_1, t) e^{i\beta(\vec{r}, \vec{r}_1, t)} \end{aligned} \quad (19)$$

where  $V_1$  and  $V_2$  are the complex signal amplitudes from two antennas,  $t$  is time,  $\beta$  is relative phase, and  $\vec{r}$  is the spatial separation between the two antennas. The vector  $\vec{r}_1$  locates the centroid of the receiver antenna array in space. Note that the time average of Eq. (19) is the mutual coherence function<sup>10</sup> if the ergodic hypothesis, which states that a time average may replace an ensemble average, is used. Furthermore, it is assumed that the field is statistically homogeneous and isotropic in the measurement plane so that  $F(\vec{r}, t) = F(r, t)$  depends only on the antenna spacing at a given time. This hypothesis and this assumption are supported by results obtained in optical turbulence measurements. In the determination of  $F(r, t)$  the measurement time is longer than many periods of the propagating frequency, but is short compared to the period of the highest frequency fluctuations.

Actually, the assumption of statistical homogeneity is not really correct for the entire vertical plane containing the measurement apparatus because the atmosphere naturally changes with height above ground. Moreover, angle-of-arrival effects may differ for antennas separated by a vertical space as compared with the same separation in a horizontal direction. Provision is made in the proposed experiment to sense this effect, as described later in this paper.

The apparatus of Fig. 7 may be used to measure  $F(r, t)$  for a given value of  $r$ . Note that the power measured by the receiver will be<sup>10</sup>

$$|V_n|^2 = |V_1|^2 + |V_2|^2 + 2|V_1||V_2|\rho(r)\cos[\alpha_n - \beta(r)] \quad (20)$$

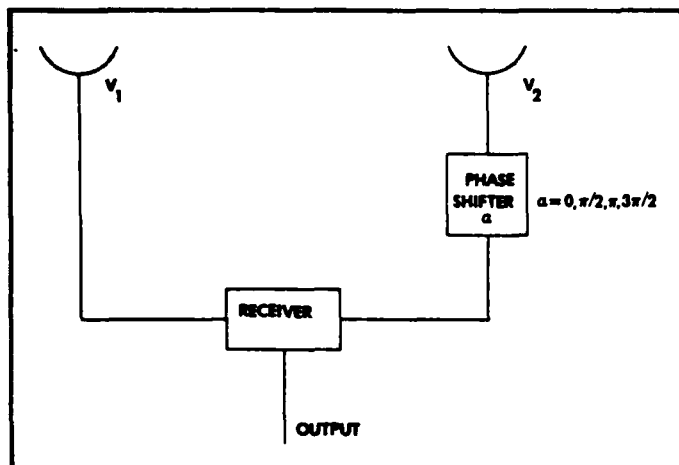


Fig. 7. Schematic diagram of apparatus which may be used to measure  $F(r, t)$ .

where the time dependence is implicit. The parameter  $\alpha_n$  is a stepwise variable phase shift that is varied to provide a means of measuring  $\beta$  and  $\rho$ , and  $V_n$  is the signal corresponding to  $\alpha_n$ . The time dependence is retained in Eq. (20) because the circuitry is capable of making measurements in a time short compared to the period of the highest frequency atmospheric fluctuations. By varying  $\alpha_n$  in steps through the range  $0, \pi/2, \pi$ , and  $3\pi/2$ , a set of four equations is obtained which may be solved for  $\rho$  and  $\beta$  to give

$$\beta(r) = \tan^{-1} \frac{|V_{90}|^2 - |V_{270}|^2}{|V_0|^2 - |V_{180}|^2}; \quad (21)$$

$$[\rho(r)]^2 = \frac{(|V_0|^2 - |V_{180}|^2)^2 + (|V_{90}|^2 - |V_{270}|^2)^2}{16|V_1|^2 |V_2|^2}. \quad (22)$$

The quantities  $|V_0|^2 \dots |V_{270}|^2$  are measured by varying  $\alpha$  as noted, and the quantities  $|V_1|^2$  and  $|V_2|^2$  are measured by sequentially blocking the two channels and making individual measurements. Note that all of these measurements must be made in a time short compared to the period of the highest frequency of atmospheric fluctuations, but these timing requirements are well within the capability of available coaxial switches, phase shifters, and a microprocessor used for making the calculations indicated above. The advantage of this technique is that the receiver acts simply as an rf voltmeter, and the phase dependent parameters are ratios of real measured quantities.

The above apparatus may also be used to measure the intensity and angle-of-arrival fluctuations. The intensity is simply either  $|V_1|^2$  or  $|V_2|^2$ , which are both needed for determination of  $\rho(r)$ . To determine angle-of-arrival, note that the quantity  $\beta(r)$  is the instantaneous phase between the antennas. Assuming that the angle subtended by the antennas is small, it is possible to show<sup>11</sup> that the angle-of-arrival  $\theta$  is related to the phase difference between antennas by the relation

$$\beta = kr\theta. \quad (23)$$

The apparatus discussed above then measures intensity and angle-of-arrival fluctuations in addition to  $F(r, t)$  and mutual coherence function (MCF).

In deriving Eqs. (21) and (22) from (20), four different discrete phase shifts are assumed. Note that it would be possible to calculate  $\rho(r)$  and  $\beta(r)$  by using only two phase shifts, namely,  $0^\circ$  and  $90^\circ$ , but values derived in this way are strongly dependent on the measured intensities  $|V_1|^2$  and  $|V_2|^2$  indicating that the two receivers should be carefully balanced to give accurate results. The four-phase shift

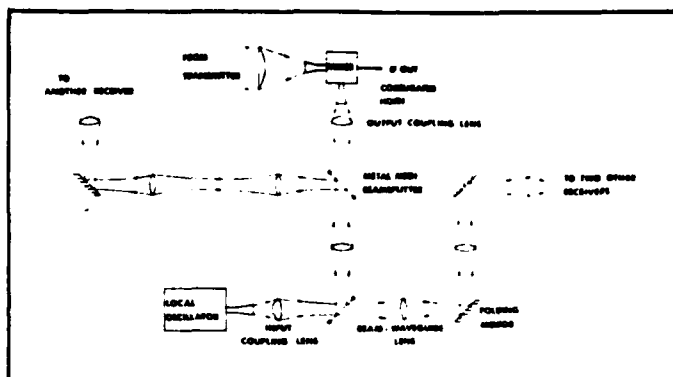


Fig. 8. Diagram of beam waveguide system to be used for local oscillator distribution. The reflectivity and transmissivity of the wire mesh beam splitters will be varied to apportion the power almost equally to the four mixers.

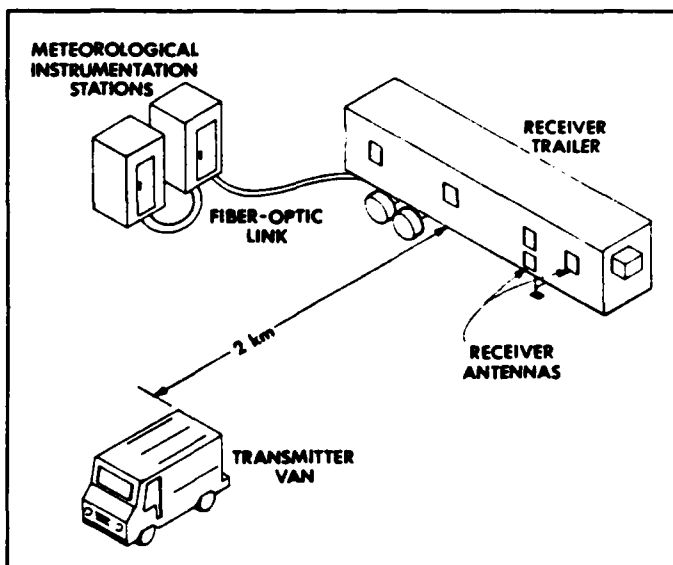


Fig. 9. Schematic diagram of the four antenna turbulence measurement system being fabricated at Georgia Tech.

approach eliminates much of this dependence and thus makes receiver calibration easier.

A fairly serious shortcoming of a two-antenna system is that it gives  $F(r, t)$ , intensity, and angle fluctuations for only one spacing, but measurements at several different spacings are required to determine how these parameters vary with  $r$ . For complete characterization of  $F(r, t)$  it is necessary to use a multiple antenna system with many different spacings. In particular, a four-antenna system with six possible spacings will be used, with the maximum spacing being about 10 meters. Since a common local oscillator (L.O) must be used for all four receivers, it will be necessary to use an optical beam waveguide<sup>12</sup> for transmission of the low power L.O over these distances. Figure 8 is a diagram of such a beam waveguide, which is expected to have a loss of about 4 dB over the longest path between antennas.<sup>13</sup>

The four receiver antennas will be mounted on an I beam which is in turn mounted in a semitrailer truck and will therefore sense phase variations in the horizontal plane. A fifth antenna will be mounted orthogonal to the other four and will have limited ability to sense vertical plane variations with only one possible spacing. Figure 9 is a schematic of the measurement system, showing the transmitter van, the receiver trailer, and the meteorological measurement stations.

Measurements will be made at selected frequencies in the 110 to 170 and the 220 to 340 GHz bands. This combined coverage includes

the oxygen absorption at 118 GHz, the transmission windows at 140, 220, and 340 GHz, and the water vapor absorption at 325 GHz. Measurements made near the peaks of absorption lines may show damping of fluctuations. This was shown earlier in measurements by Izyumov<sup>14</sup> and preliminary consideration has been given to theories which may explain it.<sup>1</sup> Further measurements will provide an additional perspective for improvements of the theory.

The receiver will use subharmonically pumped balanced mixers, in which the LO frequency is an integral submultiple of the signal frequency. In this way, the local oscillator klystron tubes will need only to cover the range 55 to 85 GHz to provide coverage of the 110 to 170 and the 220 to 340 GHz bands.

The transmitter will use klystrons operating in the range 110 to 170 GHz for the low band and will double these sources for the high band. To provide for narrow receiver bandwidths which contribute to good noise figures, both transmitter and receiver klystrons will be phase-locked, and the receivers will employ double conversion with a narrow band filter in the second intermediate frequency band. Table III gives expected ranges under various conditions for each of the frequencies to be used.

The phase shifting implied in Fig. 7 will be done at the intermediate frequency, and the phase shift switching will be microprocessor controlled, as will all data gathering, preliminary processing, and storage. Both millimeter wave and atmospheric data will be stored simultaneously on the same tape.

## 6. ATMOSPHERIC MEASUREMENTS

To make meaningful measurements of the results of turbulence on millimeter wave propagation, it is absolutely essential that the pertinent atmospheric parameters be carefully measured. The turbulence related parameters  $C_T^2$ ,  $C_Q^2$ , and  $C_{TQ}$ , which combine to give the millimeter wave refractive index structure parameter  $C_n^2$ , are especially important and are also difficult to measure. Other parameters of a more conventional nature that must be measured are wind speed and direction, temperature, and dew point. If measurements are made in turbid weather, characterization of particle sizes and densities is important.

The temperature structure parameter is measured in a fairly standard way by using two fine wire probes, separated by a distance of a few centimeters. These wires each carry a small current, and their resistances are strongly dependent on temperature, so that they can be calibrated as very sensitive temperature probes. For small temperature changes, the differential current through the probes is proportional to the differential temperature between them. In this way, the temperature structure parameter is

$$C_T^2 = \left( \frac{\Delta T}{r^{1/3}} \right)^2 \quad (24)$$

The apparatus may be calibrated by individually comparing the two probes to a thermometer of known accuracy.

The humidity structure parameter is more difficult to measure than the temperature parameter. The best approach appears to be the Lyman- $\alpha$  hygrometer described by Buck,<sup>15</sup> which makes use of the strong ultraviolet absorption of the hydrogen Lyman- $\alpha$  spectral line by water vapor at a wavelength of 121.6 nm. The Lyman- $\alpha$  hygrometer consists of a hydrogen lamp source and a nitric oxide ion chamber detector, separated by a distance of 0.3 to 5 cm. The detector drives an electrometer, whose output in turn feeds a logarithmic amplifier. The humidity structure parameter  $C_Q^2$  is measured by using two such hygrometer sensors separated by a distance of a few centimeters, and is given by

$$C_Q^2 = \left( \frac{\Delta Q}{r^{1/3}} \right)^2 \quad (25)$$

To determine  $C_{TQ}$  it is necessary that the  $C_T^2$  and  $C_Q^2$  sensors sample the same volume of space as nearly as possible, so the sensors

TABLE III. Maximum Ranges for 20 dB Signal-to-Noise Ratio

Frequency (GHz)	Transmitter power output (mW)	Range (km)		
		Clear	Rain	Fog
118	100	19.8	7.9	9.2
140	100	25.8	8.1	9.5
170	100	9.8	5.0	4.3
230	5	12.2	4.9	4.2
280	5	5.6	4.3	3.1
333	5	3.4	1.7	1.5
340	5	5.2	2.0	1.8

must be placed on the same mount. The parameter  $C_{TQ}$  is the cross-correlation of  $C_T$  and  $C_Q$  and is given by

$$C_{TQ} = \frac{\langle [T(r) - T(0)] [Q(r) - Q(0)] \rangle}{r^{2/3}} \quad (26)$$

where  $r$  is the separation between sensors, and the brackets denote a time average. Note that  $C_{TQ}$  can be negative, whereas  $C_T^2$  and  $C_Q^2$  are positive definite. This is a further indication of the importance of considering this cross-correlation in determining the effects of turbulence on millimeter wave propagation.

As a check on the performance of the  $C_T^2$  and  $C_Q^2$  sensors, the optical refractive index structure parameter  $C_n^2$  will also be measured. This measurement will be made using an optical scintillometer developed by Wang et al.<sup>16</sup> This device actually determines  $C_n^2$  by measuring the variance of the log-amplitude of a propagated optical beam and makes provision for rendering the effects of saturation of scintillation negligible.

The remainder of the atmospheric parameters are measured by generally accepted techniques using standard instruments. The outputs of all of these sensors will be recorded simultaneously with the millimeter wave data to avoid errors in data coincidence. Depending on the flatness of the measurement site and the proximity of trees and buildings, it will be necessary to duplicate the  $C_T^2$  and  $C_Q^2$  measuring apparatus several times over the path. For nearly homogeneous propagation paths, only one or two sets of instruments may be required.

## 7. CONCLUSIONS

This paper compares theory to experiment based on two sets of millimeter wave propagation measurements obtained with limited meteorological data. Agreement in all cases is generally good, but it is again emphasized that dedicated millimeter wave turbulence measurements must be made before stringent conclusions can be drawn. At the present time, only scattered data are available. Due to the nature of the measurements discussed in this paper, some care should be taken in relating them to actual situations or in using them to design millimeter wave systems. Although the agreements achieved have been generally good, they may be fortuitous. It does appear, however, that the magnitudes of the effects are great enough so that turbulence should be considered in the design of millimeter wave systems.

This paper also describes a planned experiment that is capable of measuring intensity and angle-of-arrival fluctuations, as well as the mutual coherence function, for millimeter wave propagation up to a frequency of 340 GHz. The experiment will make use of a series of klystron oscillators in such a way that the number of these expensive sources is minimized. The MCF can be measured for antenna spacings up to 10 m by using a beam waveguide for distributing the local oscillator power to the individual receivers. A total of four receivers is planned, giving six possible antenna spacings for determination of the MCF.

Measurement of the turbulence related atmospheric parameters  $C_T^2$ ,  $C_Q^2$ , and  $C_{TQ}$  will also be made, as well as the optical  $C_n^2$ . Other atmospheric parameters to be measured include wind speed and

direction, temperature, humidity, and dew point. For measurements in rain and fog, particle size distributions as well as rain rate will be measured. All of these atmospheric data will be stored on magnetic tape, simultaneously with the millimeter wave data, to avoid errors in data coincidence. The experiment will be microprocessor controlled as far as possible. All of the phase switching functions, preliminary calculations, and data measurement will be handled by the processor.

Preliminary calculations show that angle-of-arrival fluctuations may be of more significance than intensity fluctuations because the fade margin of most systems is likely to be adequate for the latter effects. Based on calculations in this paper, angle-of-arrival peak-to-peak deviations are expected to be in the range 50 to 250 microradians.

## 8. ACKNOWLEDGMENTS

This work was supported by the U.S. Army Research Office under Contracts DAAG29-81-K-0173 and DAAG29-77-C-0026. The authors gratefully acknowledge the help of J. Nemanich and R. J. Wellman of the U.S. Army Harry Diamond Laboratories and D. G. Bauerle of the Ballistic Research Laboratory for help in obtaining propagation data. The continuing support and interest of D. E. Snider of the U.S. Army Atmospheric Sciences Laboratory and W. A. Flood of the U.S. Army Research Office is also gratefully acknowledged.

## 9. REFERENCES

1. R. W. McMillan, J. C. Wiltse, and D. E. Snider, IEEE EASCON Conference Record, Arlington, VA (Oct. 1979).
2. N. A. Armand, A. O. Izumov, and A. V. Sokolov, Radio Eng. Electron. Phys. 1(8), 1257(1971).
3. R. J. Hill, S. F. Clifford, and R. S. Lawrence, J. Opt. Soc. Am. 70(10), 1192(1980).
4. H. B. Wallace, Proc. SPIE 305, 224(1981).
5. J. Nemanich R. J. Wellman, D. Rocha, and G. B. Wetzel, Proc. SPIE 305, 261(1981).
6. R. J. Hill and S. F. Clifford, Radio Sci. 16, 77(1981).
7. R. W. McMillan, R. A. Bohlander, and G. R. Ochs, Proc. SPIE 305, 253(1981).
8. R. S. Cole, K. L. Ho, and N. D. Mavroukoulakis, IEEE Trans. Antennas Propag. AP-26 (5), 712(1978).
9. V. I. Tatarski, *Wave Propagation in a Turbulent Atmosphere*, Nauka, Moscow (1967) (in Russian).
10. M. Born and E. Wolf, *Principles of Optics*, 3rd Ed., Chap. 10, Pergamon Press, New York (1965).
11. M. Born and E. Wolf, *Principles of Optics*, Chap. 7.
12. G. Goubau and F. Schwering, IRE Trans. Antennas Propag. AP-9, 248(1961).
13. J. R. Christian and G. Goubau, IRE Trans. Antennas Propag. AP-9, 256(1961).
14. A. O. Izumov, Radio Eng. Electron. Phys. 13(7), 1009(1968).
15. A. Buck, "Notes on the Fabrication of a Fixed-path Lyman-Alpha Hygrometer," RSF #040-032-004, National Center for Atmospheric Research, Boulder, CO (Dec. 1979).
16. Ting-i Wang, G. R. Ochs, and S. F. Clifford, J. Opt. Soc. Am. 68(3), 334(1978).

# Near-Millimeter-Wave Sources of Radiation

ROBERT W. MCMILLAN, SENIOR MEMBER, IEEE

*Invited Paper*

*This paper describes coherent sources of radiation useful in the near-millimeter-wavelength spectrum, generally taken to span the range of about 80 to 1000 GHz; however, both optically pumped and discharge pumped lasers are excluded from this treatment, since these devices are adequately covered elsewhere. Included in this discussion are solid-state sources such as IMPATTs and Gunn devices; tube sources such as klystrons, magnetrons, and backward-wave oscillators; and newer sources including TUNNETTs, gyrotrons, and relativistic electron-beam devices. Because of the large amount of material to be covered, the treatment is limited to a brief description of each device and an enumeration of its capabilities; no attempt is made to give a detailed discussion of device physics, as references are available for this purpose. Phase and frequency control of near-millimeter-wave sources is becoming increasingly important because of applications of this spectrum to Doppler radar, communication, and measurement systems. The paper concludes with a presentation of phase and frequency control results for both tube and solid-state sources.*

## I. INTRODUCTION

There are three basic types of near-millimeter-wave (NMMW) sources: 1) solid-state sources such as Gunn and IMPATT diodes, 2) vacuum-tube sources including klystrons, magnetrons, and gyrotrons, and 3) laser sources including both discharge and optically pumped devices. Technology in all three source areas has been advancing rapidly for the past ten years, with tubes such as the extended interaction oscillator (EIO), the backward-wave oscillator (BWO) or carcinotron, and the gyrotron being rapidly improved. These devices are capable of usable power outputs into the hundreds of gigahertz, and the capabilities of the gyrotron and related devices as high-power, high-frequency oscillators are just beginning to be realized. Solid-state sources such as the Gunn oscillator and the IMPATT (Impact Ioniza-

tion Avalanche Transit Time) diode continue to advance rapidly and are being complemented by newer sources such as the TUNNETT (Tunneling Transit Time) and MITATT (Mixed Tunneling and Avalanche Transit Time) oscillators. At one time, solid-state sources were exclusively relegated to perform as local oscillators, but recent advances in IMPATT technology have led to coherent radar transmitters that perform well in the 90-GHz range, and it appears that a 140-GHz transmitter capable of useful power output could be built with existing technology. NMMW lasers are also becoming increasingly useful, and these devices are discussed in a separate paper in this issue by Tobin [1].

The usefulness of both tube and solid-state sources has been greatly enhanced by improved methods of phase and frequency control. Both injection and phase-locking techniques are used to generate the high coherent power outputs required for Doppler radar systems. Solid-state- and tube-type amplifiers in the near-millimeter wave spectrum are used to generate coherent outputs by excitation with lower power phase-locked sources.

Power combining of solid-state sources is used to generate useful transmitter power in the NMMW spectral range. This approach provides compact and reliable transmitters operating from low voltages, and allows for the fabrication of all solid-state systems at near-millimeter wavelengths. Circuit-level power combining is used exclusively at the frequencies of interest, but chip-level combining may be feasible for future sources. Power combining is discussed briefly in Section II.

Sections II and III of this paper treat solid-state and tube devices, respectively. Section IV discusses phase and frequency control of near-millimeter-wave sources, and Section V gives some conclusions reached during this study. No attempt is made to provide a treatment of NMMW device physics, as such a treatment is beyond the scope of this paper. Rather this paper attempts to give the reader an understanding of device capabilities through a discussion of power, frequency, bandwidth, and other characteristics

Manuscript received August 18, 1983; revised September 14, 1984. Support for the measurements reported on in this paper was provided as part of an atmospheric research program funded by the U.S. Army Research Office under Contract DAAG29-81-K-0173.

The author is with Georgia Tech Research Institute, Georgia Institute of Technology, Atlanta, GA 30332, USA.

0018-9219/85/0100-0086\$01.00 ©1985 IEEE

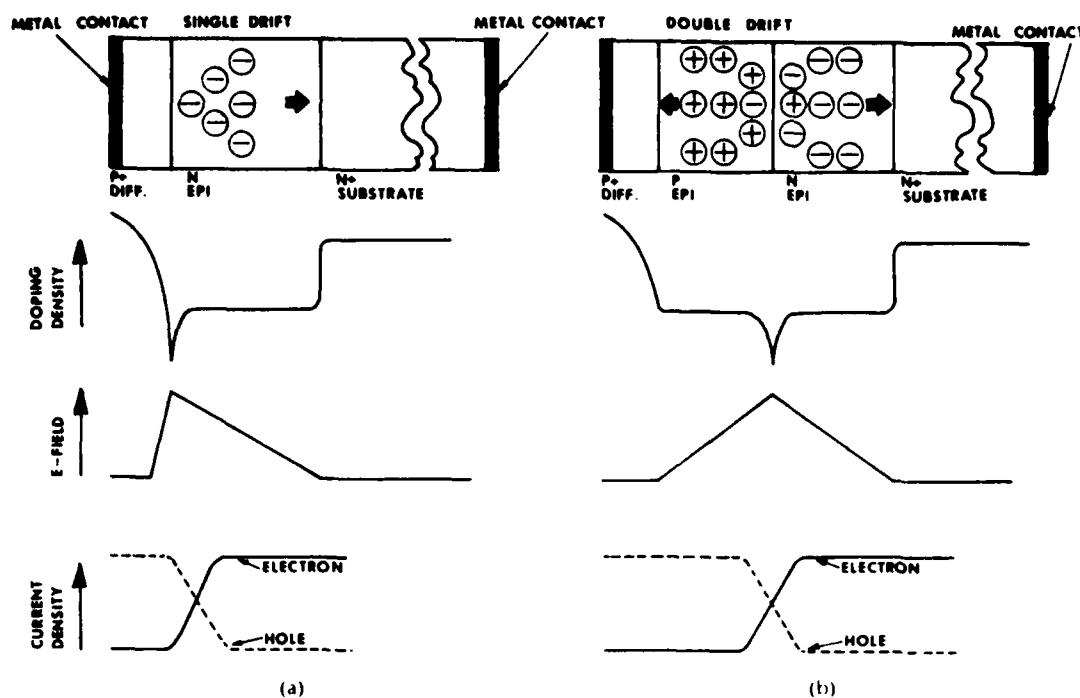


Fig. 1. Schematic diagram of two manifestations of IMPATT device fabrication [4], single-drift (a) and double-drift (b) structures, respectively.

which would aid him or her in making the best choice for a given source application. References are provided for those who wish to study these sources further.

## II. SOLID-STATE SOURCES

Solid-state near-millimeter-wave sources include IMPATTs, Gunn-effect oscillators, TUNNETTs, MITATTs, and harmonic generators. Gunn devices are also called transferred-electron oscillators (TEOs) because of the way in which negative resistance is generated in these sources by transfer of carriers from a high-mobility energy band to one of lower mobility, as will be discussed shortly. A brief description of the operation of each of these solid-state sources will be given, followed by a discussion of device capabilities. The field-effect transistor (FET) is not discussed because its highest frequency of operation to date is about 70 GHz; however, these devices may be capable of operating at frequencies greater than 90 GHz in the near future.

### IMPATT Oscillators

As the name implies, IMPATT oscillators employ impact-ionization and transit-time properties of semiconductor structures to give negative resistance at microwave frequencies. Typically, a  $p^+-n-n^+$  device structure is biased slightly into avalanche breakdown by an external voltage [2], [3]. Avalanche electrons, generated by impact ionization near the  $p^+$  region, drift across the  $n$  region with a transit time determined by the device parameters. This transit time causes the current to lag the voltage, and oscillation is possible if this delay exceeds one-quarter cycle. It is assumed that the high-frequency components of the thermal-noise voltage start these oscillations, which are

then sustained by the negative resistance behavior of the device. An excellent discussion of IMPATT theory has been given by Kuno [4], [5] and by Kramer [6] who also gives an extensive list of references to this subject.

Fig. 1 [4] is a schematic diagram of two manifestations of IMPATT device fabrication. Fig. 1(a) shows the single-drift structure discussed above, and Fig. 1(b) shows the so-called double-drift structure. In the single-drift device, which is characterized by a  $p^+-n$  junction, only the  $n$  region contributes to IMPATT operation, but in the double-drift structure, which has a  $p$ - $n$  junction, both  $p$  and  $n$  regions contribute to operation. As might be expected, the single-drift device is better for higher frequencies since the mobility of electrons, which are the primary current carriers in the drift region, is greater than that of holes.

IMPATTs are packaged as shown in Fig. 2 [4], with the indicated structure being sealed for devices used up to 110 GHz and open for reduced parasitics [5] for higher frequencies. Fig. 3 [4], [5] shows how the device of Fig. 2 is typically mounted in its waveguide circuit.

The state of the art in IMPATT power output capability as of October 1982 is shown in Figs. 4 and 5 [7], [8] for pulsed and CW devices, respectively. These figures are a compilation of published data from Hughes, Plessey, and Raytheon. The regions of  $f^{-1}$  and  $f^{-2}$  slope are caused by thermal and circuit limitations, respectively [4].

Efficiencies of IMPATT devices approaching 8 percent at 140 GHz have been reported. Fig. 6 shows the efficiencies of both double- and single-drift IMPATTs at frequencies up to 140 GHz, as measured by Gokgor *et al.* [9]. This figure shows the roll-off in double-drift efficiency caused by hole mobility limitations at about 100 GHz, an effect that does not occur for single-drift devices until frequencies have

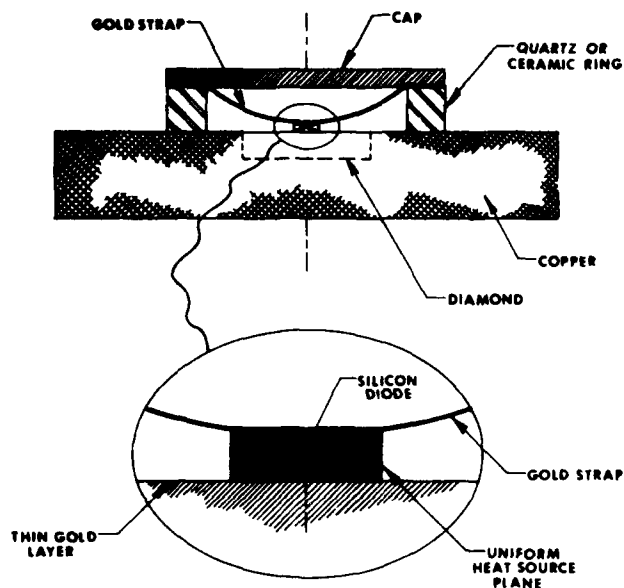


Fig. 2. IMPATT diode packaging techniques [4].

exceeded approximately 140 GHz. The upper frequency limit of these devices is about 300 GHz, and operation at frequencies up to 255 GHz has been demonstrated. Limitations of IMPATTs are based on the ability of the semiconductor to dissipate heat from the small volumes required

for high-frequency operation. An efficiency of 0.5 percent at 230 GHz has been achieved for IMPATT oscillators [6].

Since IMPATTs depend for their operation on avalanche breakdown in a semiconductor junction, they are inherently broad-band, noisy devices. For many applications, such as receiver local oscillators, this noise output is prohibitive, but it is possible to phase lock these diodes so that they are useful in many applications. Methods of phase locking IMPATTs will be discussed in Section IV.

Single-port CW IMPATT amplifiers capable of power outputs equal to that of equivalent oscillators have also been devised [6]. An IMPATT device is configured as an amplifier by using a three-port circulator as an input device as shown in Fig. 7. Pulsed amplifiers are more difficult to stabilize, and injection-locked oscillators generally replace amplifiers for pulsed applications.

### Gunn Oscillators

The Gunn oscillator is a solid-state device which depends on the bulk properties of the semiconductor for its operation, unlike the IMPATT which is a junction device [2], [3]. Its operation is based on electric-field-induced differential negative resistance, caused by a transfer of conduction band electrons from a low-energy, high-mobility energy valley to a higher energy low-mobility valley. A bulk semiconductor exhibiting differential negative resistance is inherently unstable, since a random fluctuation of carrier density within the semiconductor causes a momentary space

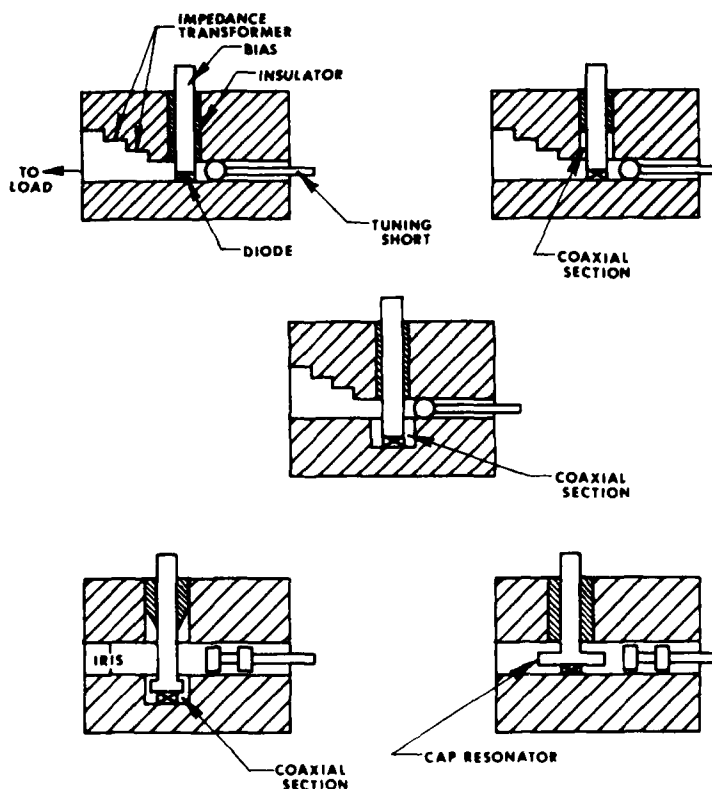


Fig. 3. Five methods of mounting IMPATT devices in waveguide circuits showing methods of matching to the higher waveguide impedance [4], [5]. Similar mounting methods are used for Gunn oscillators.

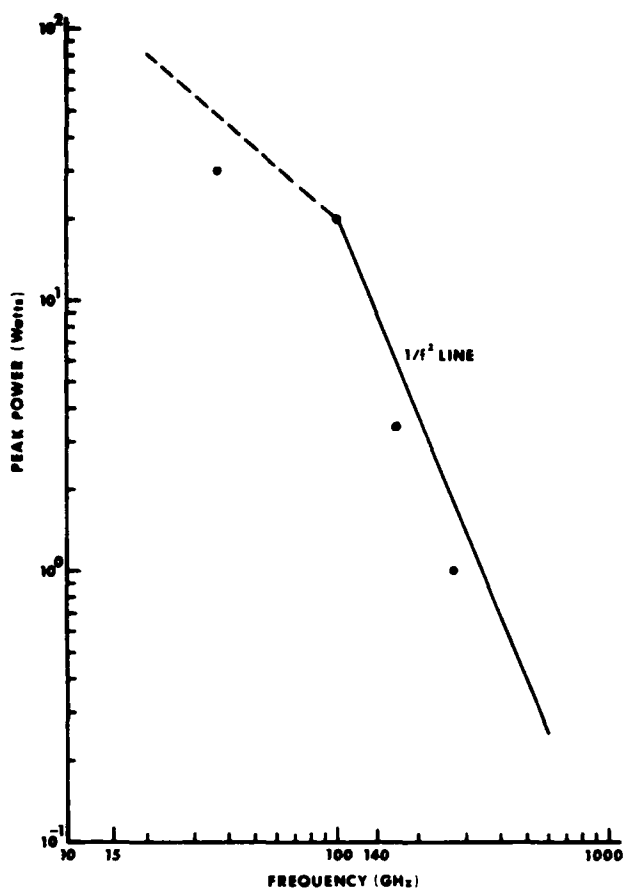


Fig. 4. State of the art in pulsed IMPATT power capability based on data from Hughes, Plessey, and Raytheon [7], [8].

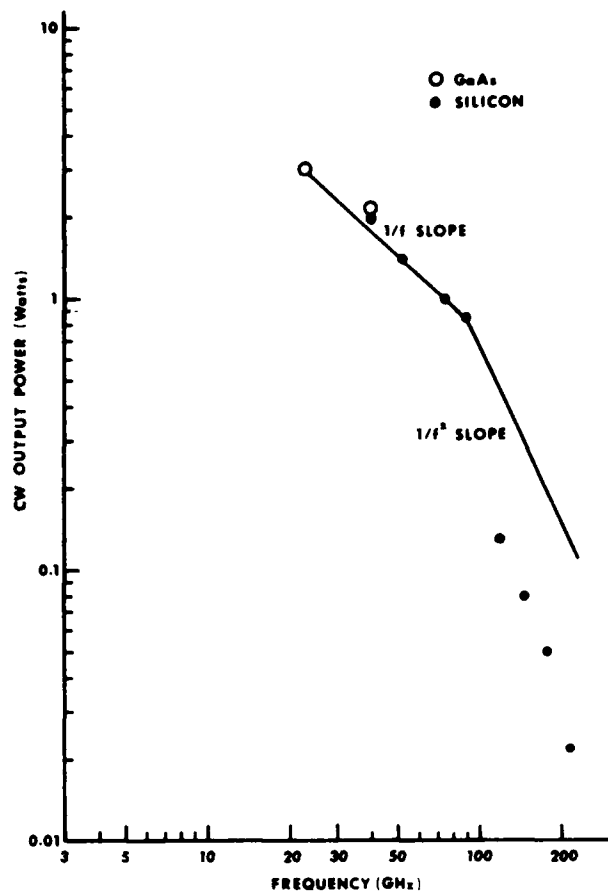


Fig. 5. CW IMPATT power capability based on data from Hughes, Plessey and Raytheon [7], [8].

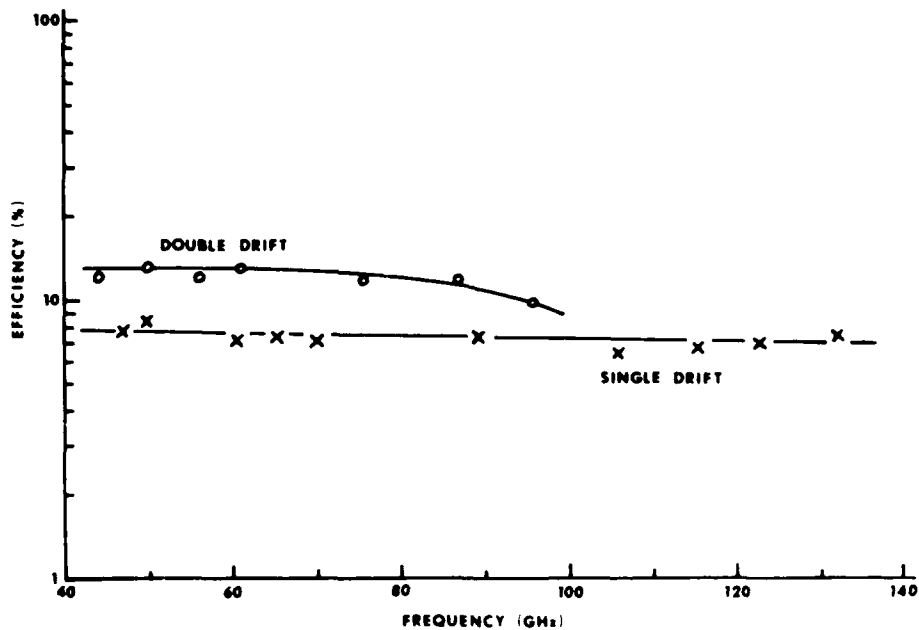


Fig. 6. Efficiencies of single- and double-drift IMPATTs at frequencies up to 140 GHz [9]

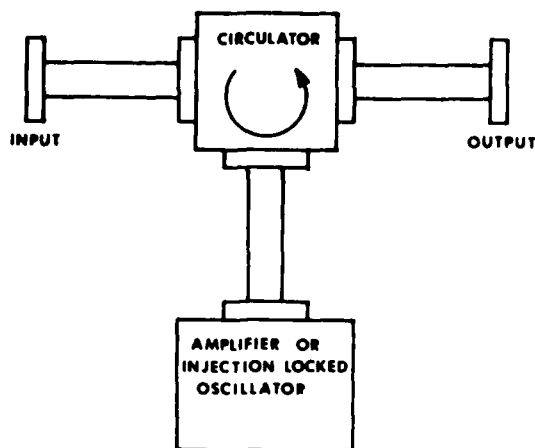


Fig. 7. An IMPATT configured as an amplifier or injection-locked oscillator [8]. A similar configuration is used for Gunn amplifiers.

charge which grows exponentially in space and time. These negative-resistance-induced space-charge fluctuations move through the bulk device, giving rise to microwave oscillations. Fig. 8 is a simplified schematic diagram of the energy levels in a GaAs Gunn oscillator.

The upper frequency limit of GaAs Gunn oscillators is about 110 GHz, a limitation imposed by carrier mobility. However, Gunns made from InP have exhibited power outputs approaching 100 mW CW and 250 mW pulsed at 100 GHz, and appear to have an upper frequency limit of about 200 GHz [10]–[14].

Since Gunn sources depend for operation on bulk rather than junction semiconductor effects, and do not operate in the avalanche mode, they are much quieter than IMPATT devices. For this reason, they are generally useful as receiver local oscillators. It is also possible to phase lock these devices in the same way as IMPATTs are phase locked, as will be discussed in Section IV.

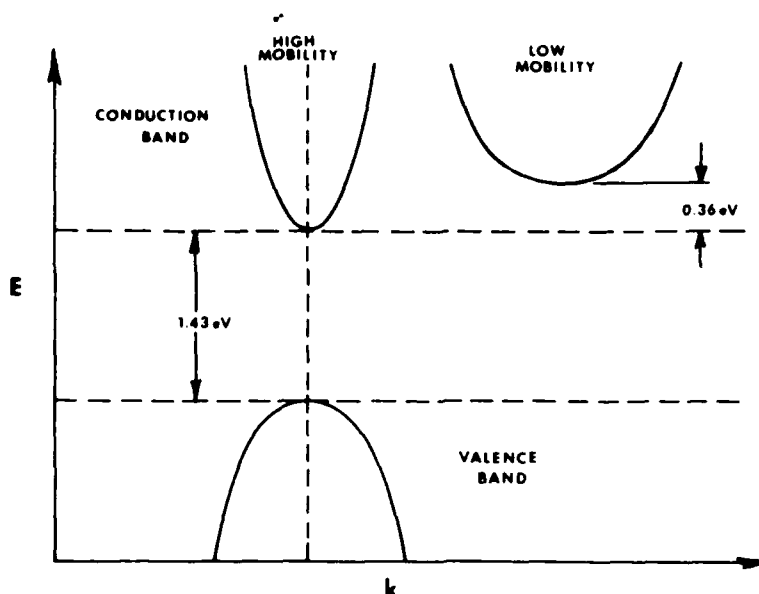


Fig. 8. Simplified schematic diagram of the energy levels in a Gunn oscillator. Negative resistance results when carriers are excited into the higher energy low-mobility level.

Fig. 9 [6] shows the CW power output and efficiency achieved as a function of frequency for GaAs Gunn oscillators. These devices are not generally operated in pulsed mode because the pulsed power output is not much greater than that of the CW mode. Fig. 10 shows the power output achieved as a function of frequency for CW InP Gunn devices. Table 1 [14] shows the CW performance of several InP Gunn oscillators in the 89–100 GHz range, and Table 2 [14] shows InP pulsed performance in the range 89–94 GHz.

Indium phosphide Gunn devices have shown great promise as amplifiers, and have exhibited full waveguide band performance at the lower millimeter-wave frequencies, although 90-GHz amplifiers have not yet been built. The

Table 1 Performance of CW InP Gunn Oscillators [11]

Frequency (GHz)	Power Output (mW)	Efficiency %
85.5	125	3.3
89.6	107	3.5
90.1	100	2.8
93.1	91	3.0
93.2	79	2.8
94.5	71	2.5
94.8	68	2.5
94.9	63	2.4
100.5	44	1.5
87.7	35	4.7

Table 2 Performance of Pulsed InP Gunn Oscillators [11]

Frequency (GHz)	Power Output (mW)	Efficiency (%)
89.8	240	2.7
92.0	215	2.7
90.0	248	2.7
89.8	255	1.4
90.3	236	4.3
89.8	195	3.6
93.7	155	3.3

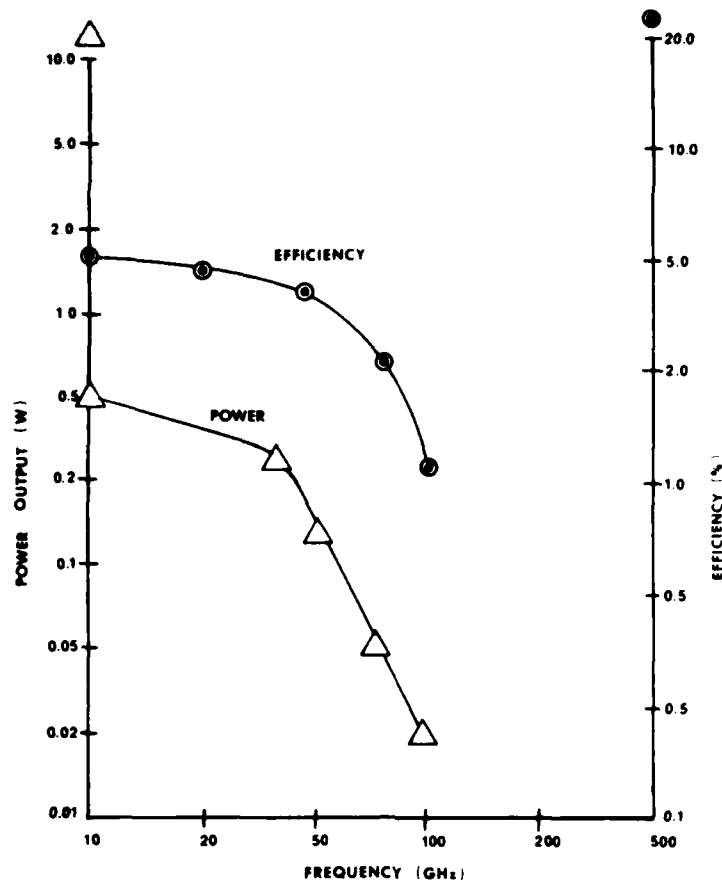


Fig. 9. Power output and efficiency of GaAs Gunn oscillators [6]

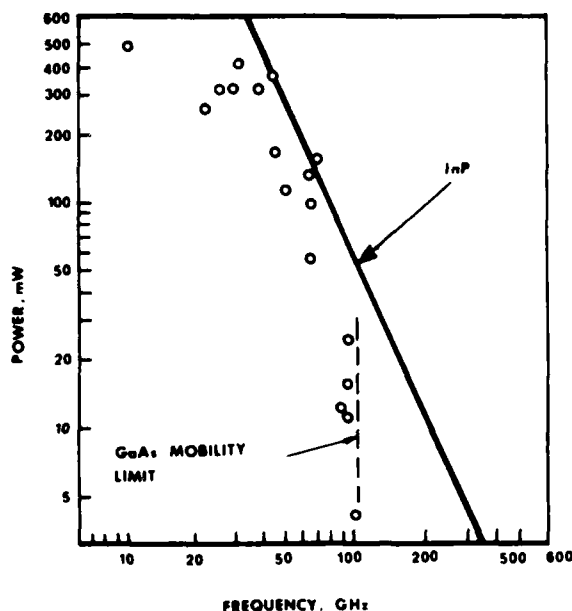


Fig. 10. Predicted power output as a function of frequency for CW InP Gunn devices (solid line). The circles indicate performance achieved by CW GaAs Gunn oscillators for comparison.

amplifier configuration is single-port, as shown in Fig. 7 for IMPATT amplifiers. One limitation on broad-band amplifier performance is that imposed by the circulator, because these devices are not available in broad-band low-loss versions which match amplifier performance.

#### TUNNETT and MITATT Oscillators

The TUNNETT [15] is a potentially useful solid-state millimeter-wave source which uses quantum-mechanical tunneling to generate carriers which in turn generate millimeter waves through negative-resistance transit-time effects. These devices are still in the experimental stage, but show promise of combining the capability of the IMPATT oscillator with the quiet operation of the Gunn devices. The MITATT oscillator uses a mixture of tunneling and impact ionization effects to generate carriers.

TUNNETTs have been fabricated by Nishizawa *et al.* [16] which operate at 338 GHz with an efficiency of 0.12 percent. Elta *et al.* [17] have reported the fabrication of a MITATT which had a CW output power of 3 mW at 150 GHz. Pan and Lee [15] emphasize that TUNNETTs and MITATTs should operate most efficiently in the range 100 to 800 GHz, and their calculations predict an efficiency of 5 percent at 500 GHz. TUNNETTs are difficult to fabricate because of the required abrupt junction doping profile [18], but these devices have the potential for good efficiency at submillimeter wavelengths [19].

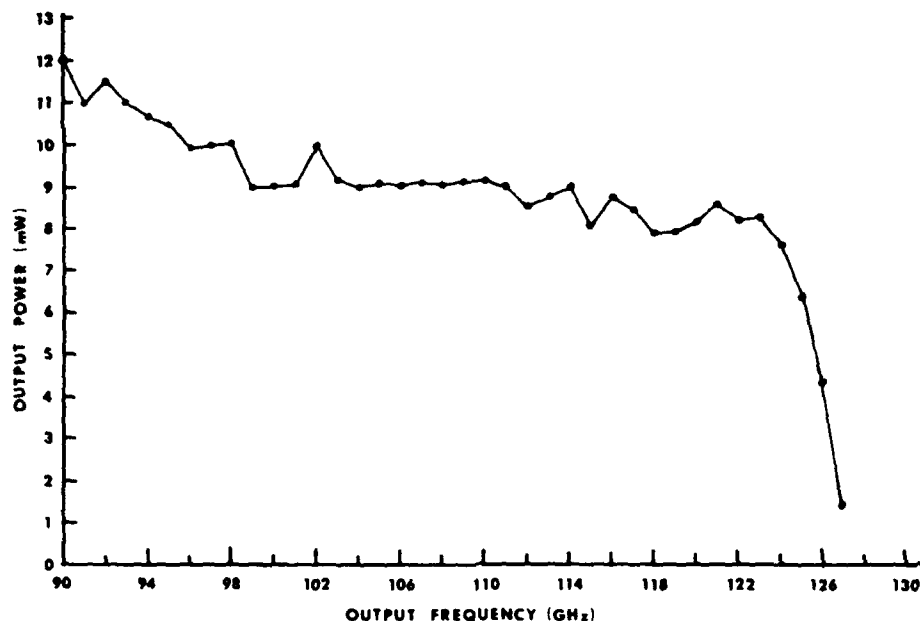


Fig. 11. Power output of a cross-guide multiplier over the range 90–124 GHz [21]. This curve represents an efficiency of 20 percent over this range.

### Harmonic Generators

Solid-state diode multipliers are also useful millimeter-wave sources, whether driven by solid-state or tube-type oscillators. Multipliers in a crossed-waveguide configuration have long been used for spectroscopic applications, where power requirements may be only on the order of a few microwatts. This arrangement is inherently broad-band, and may typically cover the entire bands of the waveguides used in the device. Useful power outputs at frequencies greater than 600 GHz have been obtained using this approach.

The basic cross-guide multiplier has been greatly improved by Archer *et al.* [20], [21], who used a suspended substrate quartz stripline filter to couple the fundamental power to a Schottky-barrier varactor diode situated in the output waveguide. By optimizing tuning and bias for each operating frequency, they were able to achieve a conversion loss of about 20 percent over the output range 90–124 GHz as shown in Fig. 11. If the tuning and bias are held fixed, a minimum conversion loss of 10 percent is achieved over the output range 80–120 GHz. Fix-tuned varactor multipliers have recently been used with good results. These multipliers are two-port devices in which fundamental power enters one port and multiplied power exits from the other port. They are carefully tuned to suppress higher harmonics and are therefore very efficient, but are also not tunable over a range greater than a few tenths of one percent. Efficiencies of 35 and 15 percent, respectively, have been obtained in doubling from 70–140 GHz and from 90–180 GHz for input powers of 43 and 100 mW. The 70–140 GHz result was obtained using a solid-state oscillator. Fig. 12 is a photograph of the 90–180 GHz device.

### Power Combining Methods for NMMW Solid-State Sources

In the frequency range up to 140 GHz (90–140 GHz for the purpose of this discussion) much of the power output



Fig. 12. Photograph of fix-tuned narrow-band doubler capable of 15-percent efficiency in doubling from 91.5 to 183 GHz with 100-mW input.

deficiency of solid-state sources relative to tube-type sources has been overcome by the use of power combining. When considered on the bases of reliability and circuit simplicity, a power-combined solid-state source might be a better choice for an NMMW systems application than a tube-type source. This section briefly discusses the methods of power combining which have proven useful in NMMW applications; namely, resonant cavity, hybrid, spatial, and resonant cap devices.

Resonant-cavity combiners are based on a design by Kurokawa and Magalhaes [22] originally used for X-band IMPATT oscillators. In this device, the individual oscillators are placed in an oversized rectangular waveguide a distance of  $\lambda_g/2$  apart, with the end devices placed  $\lambda_g/4$  from the end wall or from an iris, as shown in Fig. 13. This combiner has high efficiency ( $\sim 90$  percent), is amenable to use at frequencies up to 300 GHz, and has built-in isolation between diodes [23]. However, bandwidth is limited to a few percent because of the diode spacing requirement, and the number of diodes that can be used at the higher frequen-

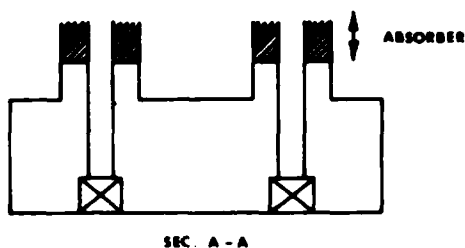
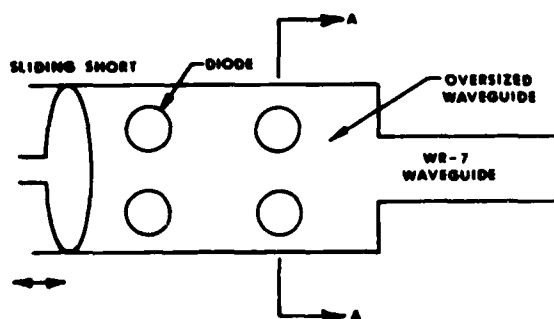


Fig. 13. Resonant cavity power combiner used for solid-state oscillators [23]

ries is limited because the number of cavity modes increases with waveguide dimensions. Variations of the Kurokawa combiner have been used with IMPATTs to generate 20.5 W pulsed from two diodes at 92.4 GHz with 82-percent combining efficiency, 40 W from four diodes at 80-percent efficiency at the same frequency, and 9.2 W pulsed from four diodes at 140 GHz with 80-percent efficiency [23]. This design has also been scaled up to 217 GHz to give 1.05 W from two diodes with a combining efficiency of 87 percent [24]. A modified Kurokawa combiner has been used by Thoren and Virostkos [25] to generate 1.3-W peak over a 10-percent mechanical tuning range at W-band (75–110 GHz).

Hybrid-coupled combiners are generally used as amplifiers or injection-locked oscillators, and these circuits offer 5-percent bandwidth and inherent isolation between sources. Fig. 14 is a schematic diagram of this type power combiner. Power injected at port 1 is split between ports 2 and 3 where it is amplified. The amplified power combines

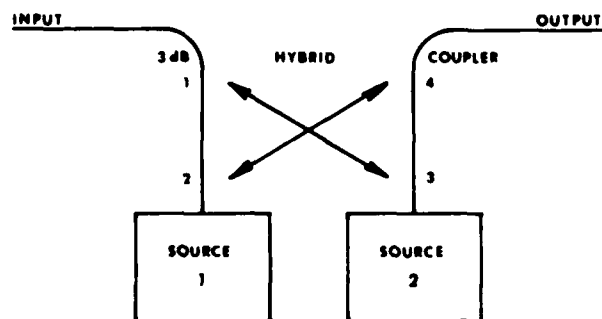


Fig. 14. Schematic diagram of a hybrid coupled power combiner configured as an amplifier [23]. If port 1 is terminated, this circuit may be used to combine oscillators.

in-phase at port 4 and out-of-phase at port 1 if the sources are properly matched. If port 1 is terminated, it is possible to combine oscillators using this technique. It is also possible to use sources combined by another method, such as the resonant cavity method, as the sources on ports 2 and 3 of the hybrid. At W-band, a hybrid combining scheme was used to combine four two-diode combiners to give 63-W peak [26].

The combining efficiency  $\eta$  for a two-source hybrid circuit configured as an amplifier is given by [27]

$$\eta = \frac{1 + 10^{(D/10)} + (2 \cos \theta) 10^{(D/20)}}{2[1 + 10^{(D/10)}]}$$

where  $D$  is the power difference between sources in decibels and  $\theta$  is the phase angle deviation from the proper phase relationship required for optimum combining. The phase error is more critical than the power difference in attaining good efficiency, since greater than 50-percent combining efficiency can be achieved for a wide range of power differences if the phase deviation is kept below 30° [23].

Spatial combiners use radiating elements having the proper phase relationship to combine power from many such elements in space. This approach was first demonstrated at UHF frequencies, but has not been extensively used at NMMW frequencies except recently by Wandinger and Nalbandian, [28], who combined the output of two Gunn oscillators in a Fabry-Perot resonator at 60 GHz to achieve 54-percent combining efficiency. This work is mentioned because of the possible application of this technique to higher frequency sources. Such quasi-optical techniques have proven useful for solving NMMW circuit problems on many occasions.

Cap resonators sometimes used for mounting Gunn oscillators may be used to combine these devices. Such a combiner is shown in Fig. 15, in which two resonant cap structures are mounted in a common waveguide with a common moveable short. It is also possible to place both oscillators under the same cap. This technique has been used to combine four 90-GHz InP Gunn oscillators to give 260-mW power output and 93-percent combining efficiency. Table 3 [14] shows results obtained at 90 GHz for two- and four-diode resonant cap combiners in several different cases.

There are several other combining techniques that are not presently used in the NMMW spectrum, but which should be useful in these bands after further development. In particular, chip level combining [29], [30], which has been successfully used up to 70 GHz, shows some promise if the thermal and parasitic problems can be solved. Reference [23] is a useful synopsis of both microwave and NMMW power combining techniques.

Table 3 Performance of CW 2- and 4-Device Combining Circuits Using InP Gunn Oscillators [14]

Number of Devices	Frequency (GHz)	Power Output (mW)	Efficiency (%)	Combining Eff (%)
2	85.6	170	2.9	93
2	90.3	150	2.7	82
2	91.8	97	1.6	106
4	90.6	260	1.6	94
4	90.8	230	1.4	107

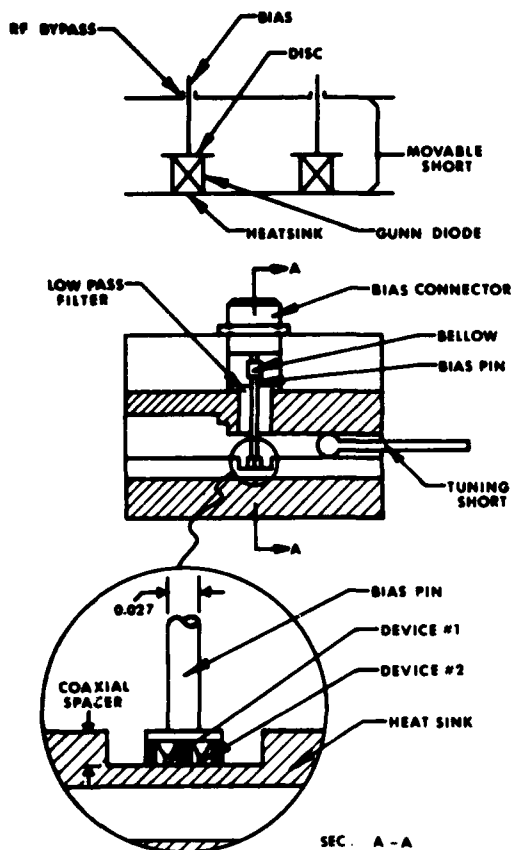


Fig. 15. A cap resonator arrangement used to combine solid-state oscillators [23].

### III. VACUUM-TUBE SOURCES

To complement and extend the capabilities of the early tube sources such as the klystron and magnetron, several very interesting and useful vacuum-tube sources for the near-millimeter-wavelength range have become available fairly recently. These sources include the extended interaction oscillator (EIO) and its amplifier version (EIA), the backward-wave oscillator (BWO) or carcinotron, the gyrotron; and such fairly exotic sources as the ledatron, the peniotron, and relativistic electron-beam devices. Each of these sources will be discussed in this section, with emphasis on those generally available for systems applications.

Most NMMW tubes suffer from limitations similar to those imposed on solid-state sources; namely, the frequency-determining elements become small with increasing frequency so that fabrication is difficult and heat dissipation problems are severe. This problem is also manifested in the design of electron guns for NMMW tubes. The ratio of cathode area to electron-beam size should be kept below about 120 for reliable tube design [31], yet higher frequency linear beam tubes generally require smaller electron beams of higher density for useful power output. Furthermore, currently used tungsten-matrix cathodes should be operated with a loading of less than about 3 A/cm<sup>2</sup> for long tube life. Fortunately, new cathode materials, such as the tungsten-iridium matrix have become available during the last few years, so that emission loadings of up to 10 A/cm<sup>2</sup> for long time periods may be used in the future.

As cathodes become smaller, gridded electron guns be-

come more difficult to build. An example of this problem occurred in the early EIOs, which were cathode-pulsed devices. The electron optics problem is made more severe by the defocusing effect of the control grid. Grid designs in which the grid is mounted on the surface of the cathode, actually embedded in the cathode surface, or bonded to the cathode, offer good promise for solving many of the electron gun problems associated with NMMW tubes.

#### The Magnetron

Magnetron oscillators have been widely used in radar transmitters, usually at frequencies lower than the near-millimeter-wavelength region. In recent years, magnetrons have been developed which are capable of power outputs of 3 kW at frequencies as high as 95 GHz [32], and these devices have been used in systems operating in this frequency range. The frequency/power capabilities of the magnetron were actually extended upward to 115 GHz and 3.3 kW by the Columbia University Radiation Laboratory as early as 1954.

The multiple cavity magnetron traveling-wave oscillator operates on the principle that electrons, spiraling into the anode of the tube, contribute energy to an electromagnetic wave which travels around the anode containing the cavities. Power is extracted from this traveling wave in one of these cavities. Magnetrons are not widely used as millimeter-wave sources above about 70 GHz because they suffer from the basic limitation of having the frequency-determining elements, which are the cavities, integral with the anode. At the higher millimeter frequencies this anode cavity structure becomes very small, resulting in greater difficulty in cooling the tube, and erosion of the cavities giving reduced output. At very high frequencies, the delicate anode structure will not withstand the anode currents required to give useful, reliable output. The 95-GHz source mentioned above has an expected life of 750 h, and probably represents the useful upper frequency limit of current magnetron technology.

#### The Reflex Klystron

The reflex klystron has historically been a very useful millimeter-wave source, and remains the source of choice for many millimeter applications. Klystrons are available which are capable of 100 mW at 140 GHz, and a few have been constructed which give a few milliwatts of power at frequencies as high as 220 GHz [33]. These tubes are especially useful as local oscillators because they are inherently quiet and are not difficult to phase lock. These features also make klystrons useful as laboratory spectroscopic sources for millimeter applications.

Klystrons are velocity-modulated tubes in that a negatively charged reflector causes electrons to periodically "bunch up," giving rise to a moving periodic charge variation and therefore electromagnetic radiation. As with the magnetron, the klystron suffers from the limitations of having a very small delicate cavity at the shorter wavelengths, which also must collect the electron-beam current. This limitation results in very high frequency klystrons being short lived, expensive, and sometimes noisy, but it appears that they will continue to be used mainly for the applications named above, although Gunns and IMPATTs are replacing them in many areas. Fig. 16 shows the output power capability of these tubes as a function of frequency [33].

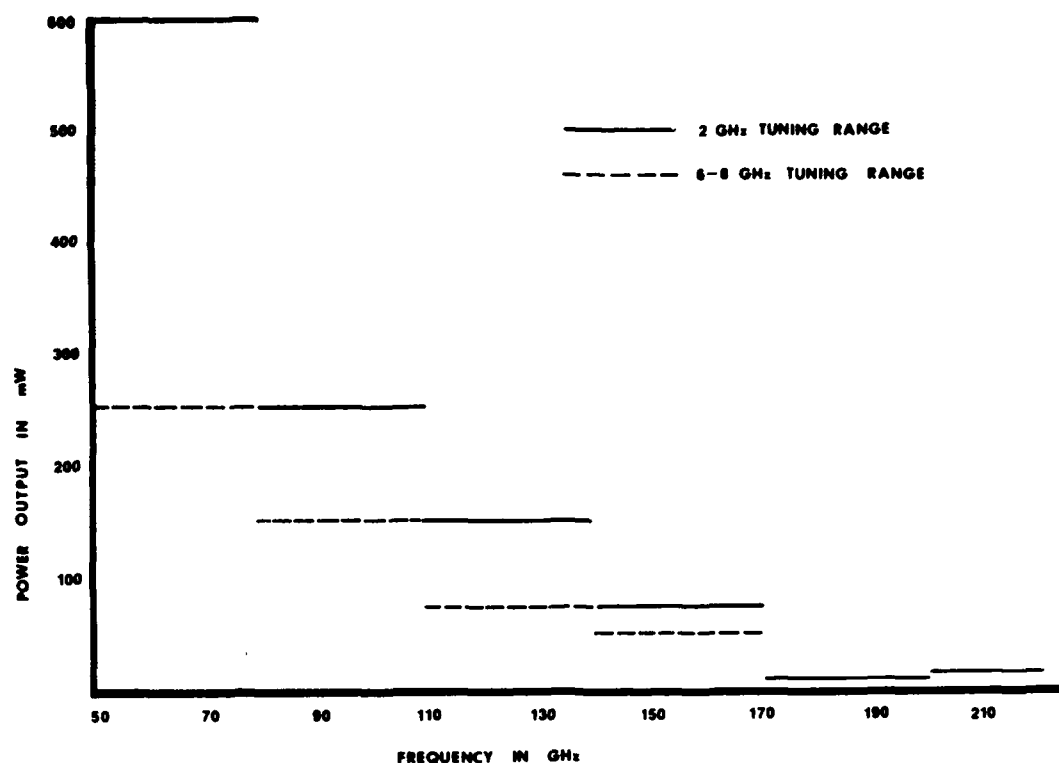


Fig. 16. Power output capability of reflex klystrons as a function of frequency [33]. The higher output indicated for the 210-GHz tube relative to the 190-GHz device is a result of few device samples in these regions.

#### The Extended Interaction Oscillator (EIO)

The EIO is a comparative newcomer to the family of millimeter-wave sources. A similar device was sold by Oki of Japan in the early 1960s, but during recent years, Varian of Canada has been building millimeter-wave EIOs at frequencies up to 260 GHz [34]. Both pulsed and CW versions of this tube are available. Pulsed EIOs can currently be purchased which have power outputs of several kilowatts at 40 GHz varying down to 100 W at 220 GHz. EIOs designed for CW outputs of 50 W at 100 GHz are also available. Fig. 17 shows the achieved power outputs as a function of frequency for pulsed and CW EIOs [35]. Other typical ranges are: pulse duty factors up to 0.01, pulse lengths between 2 ns and 25  $\mu$ s, and repetition rates limited by the capability of the modulator. The EIO can be mechanically or electronically tuned in frequency over ranges of 2 GHz for mechanical tuning and 200 MHz for electronic tuning at a center frequency of 95 GHz.

EIOs overcome the limitation of klystrons and magnetrons, caused by delicate frequency-determining structures having to collect beam current, by allowing the electron beam to pass through the structure, be modulated by it, and collected on the other side. The frequency-determining element in this case is a periodic or slow-wave structure, generally machined from copper with a small hole for electron passage. Since only stray electrons are collected by this element, the tube can operate at high beam currents despite the fact that the structure is very delicate. Millimeter-wave power is generated by the modulation of the electron beam as it passes through the periodic structure. Fig. 18 is a schematic diagram of an EIO. Limitations on this type of tube are imposed by the small size of the frequency-determining elements, and by the electron-optics

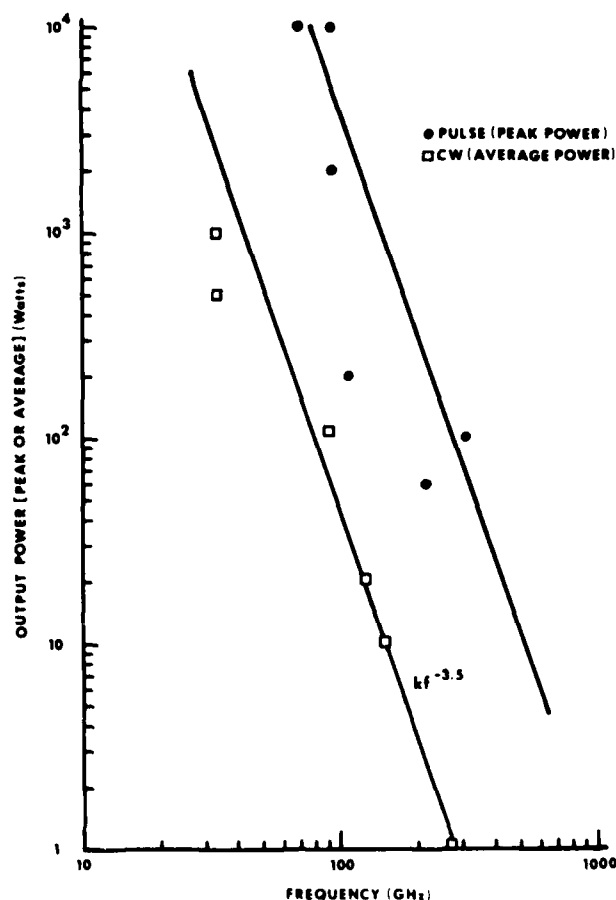


Fig. 17. Achieved power outputs for CW and pulsed extended interaction oscillators [34].

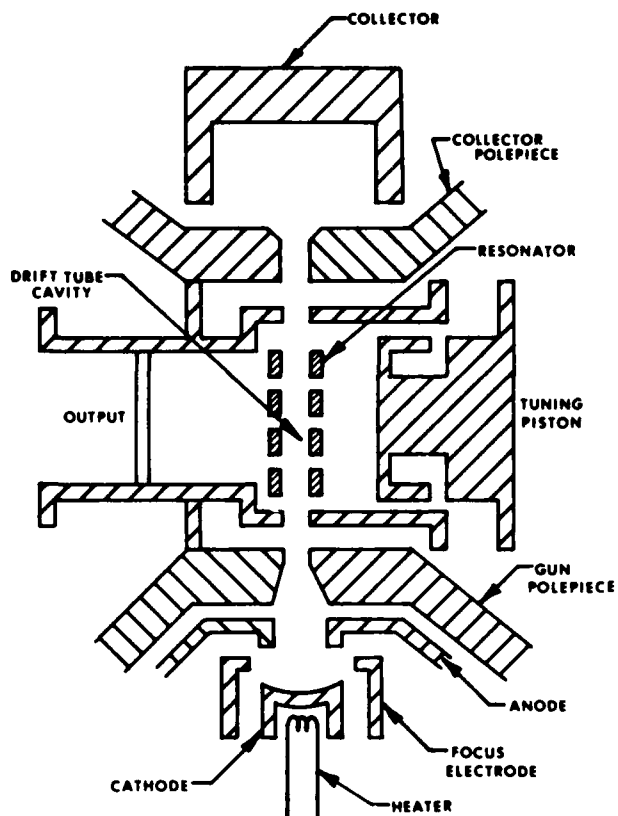


Fig. 18. Schematic diagram of an extended interaction oscillator. In higher frequency tubes, the drift tube cavity is small and difficult to fabricate.

problem of focusing a high-current electron beam through a small hole. A significant advantage of these tubes is their very long lifetimes. The 95-GHz version is guaranteed for 1000 h with an expected lifetime of greater than 5000 h.

### The Extended Interaction Amplifier (EIA)

The EIA is the amplifier version of the EIO, although it is more mechanically complex due to the need for three frequency-determining structures instead of the one used by the EIO. These ladder networks are used on the input, output, and in the interaction region in between. EIAs are not currently available at frequencies greater than 95 GHz or in CW versions, although some work has been done on a pulsed 220-GHz tube of this type [36]. Currently available 95-GHz EIAs have a small-signal gain of 40 dB and a saturated gain of 30 dB. Fig. 19 shows the gain, power output, and bandwidth achieved for a particular 95-GHz EIA. Both EIOs and EIAs have recently been improved by the addition of a control grid which allows for pulsed operation with a 1–2-kV modulator pulse instead of the 15-kV cathode pulse required for earlier versions [37]. This improvement greatly simplifies modulator design for these sources and results in improved frequency stability in the case of the pulsed EIO because the tube frequency is strongly dependent on cathode voltage variations, which are difficult to control during a 15-kV pulse that may be only several tens of nanoseconds long.

The EIA is an RF amplifier, rather than a resonant-cavity oscillator, and thus can amplify low-level signals with complex waveforms such as frequency chirp, FM/CW, frequency agile, or phase coded. Good radar MTI performance should be possible. Solid-state transmitters can provide these complex waveforms at least up to 100 GHz, but the advantage of an EIA transmitter would be that the output power would be as much as two orders of magnitude higher. EIAs have mechanical and electronic tuning bandwidths similar to those attained by EIOs.

### The Backward-Wave Oscillator (BWO)

The BWO or carcinotron is a very versatile near-millimeter-wave source because of its capabilities in the areas of

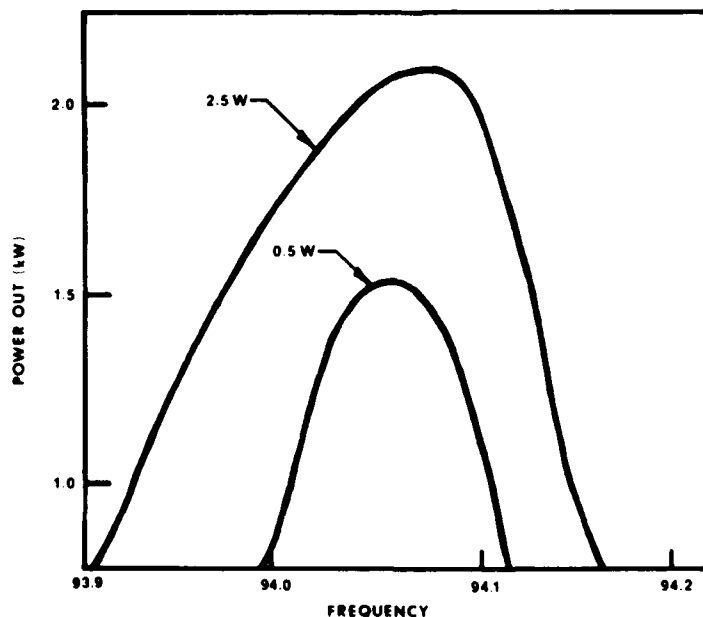


Fig. 19. Power output of a pulsed extended interaction amplifier near 94 GHz [36]. The two curves are for 0.5- and 2.5-W inputs and represent small-signal and saturated gains, respectively.

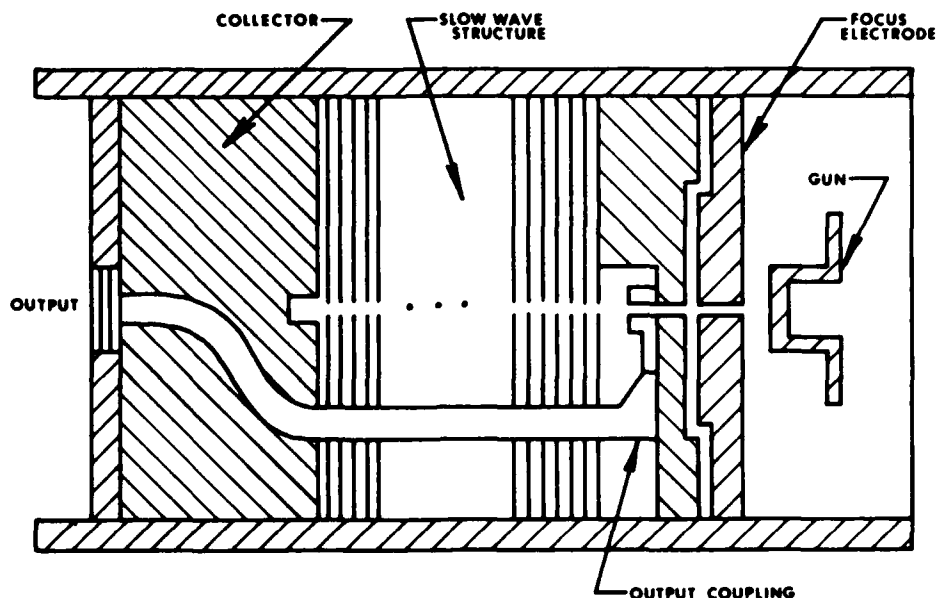


Fig. 20. Schematic diagram of a typical backward-wave oscillator. This drawing does not show the external magnet which focuses the electron beam through the slow-wave structure.

broad bandwidth and high power [38]. Tubes of this type have been fabricated which are capable of covering an entire waveguide band with useful power output at frequencies up to 170 GHz [39]. Alternatively, power outputs of up to 1 W are available in 10-percent bandwidths at 300 GHz [40], and Soviet workers have reported useful operation of BWOs at frequencies up to 1200 GHz [41]. BWOs with full-waveguide band capability may be incorporated into broad-band sweepers and frequency synthesizers [42]. A disadvantage of these tubes is that they require a multiple-output, well-regulated high-voltage power supply for successful operation.

Like the EIO, the BWO uses a periodic or slow-wave structure as the frequency-determining element. Fig. 20 is a schematic diagram of a typical BWO. In the backward-wave oscillator, the signal builds up from the collector, where it encounters the electron beam density-modulated by the earlier signal and the periodic structure. There is therefore feedback via the bunched electrons of the density-modulated beam, and the resulting electromagnetic wave propagates in a direction opposite to that of the beam. The value of the beam current then determines the degree of feedback. When a certain value is exceeded, the feedback energy is so high that the tube oscillates. In this way the signal is amplified until it reaches the output which is situated near the input to the slow-wave structure. Limitations on the BWO are again imposed by the small size and delicate nature of the periodic structure, and by the associated electron-optics problem.

#### The Traveling-Wave Tube (TWT)

The TWT and its amplifier version the TWTA, are linear-beam tubes that are roughly similar in operation to the EIO and the BWO in that they use periodic or slow-wave structures to determine the frequency. At frequencies up to 50 GHz, this structure takes the form of a helix, and such tubes have average power outputs of several hundred watts

and bandwidths of about 10 GHz [6], [43]. At near-millimeter-wave frequencies, however, machined structures similar to those used with EIOs and BWOs are used, and bandwidths are limited to about 1–2 percent [44], although power outputs of 100 W CW or average have been achieved at 95 GHz. Availability of NMMW TWTs is currently limited to this frequency, although Kramer [6] has published a set of curves shown in Fig. 21 which show achieved and predicted performance up to 100 GHz. Kramer also gives an excellent synopsis of TWT theory of operation. Problems with high-frequency operation of TWTs are again caused by fabrication of the very small periodic structures and by removal of heat from them.

#### The Gyrotron

The gyrotron is a high-power millimeter-wave vacuum-tube oscillator that uses stimulated cyclotron emission of electromagnetic waves by electrons [45], [46]. This tube is an axially symmetric device having a large cathode, an open cavity, and an axial magnetic field. Electrons are emitted from the cathode with a component of velocity perpendicular to the magnetic field so that they are caused to spiral as they are accelerated through the magnetic field to a collector. This spiraling occurs at the cyclotron frequency of the electrons, and it is this frequency that is radiated by the tube. Harmonics of this frequency may also be radiated. The coupling between the electron beam and the millimeter-wave radiation allows the beam and microwave circuit dimensions to be large compared to a wavelength, so that the power density and related circuit dimension problems encountered in almost all other NMMW tubes are avoided [47]. As a result, gyrotrons are capable of very high output powers and efficiencies. However, the large circuit dimensions generally contribute higher order output modes which may not be compatible with conventional millimeter-wave techniques. Workers in the Soviet Union have obtained 22 kW CW at 2 mm, 210 kW pulsed at 2.4 mm, and 1.2 kW CW

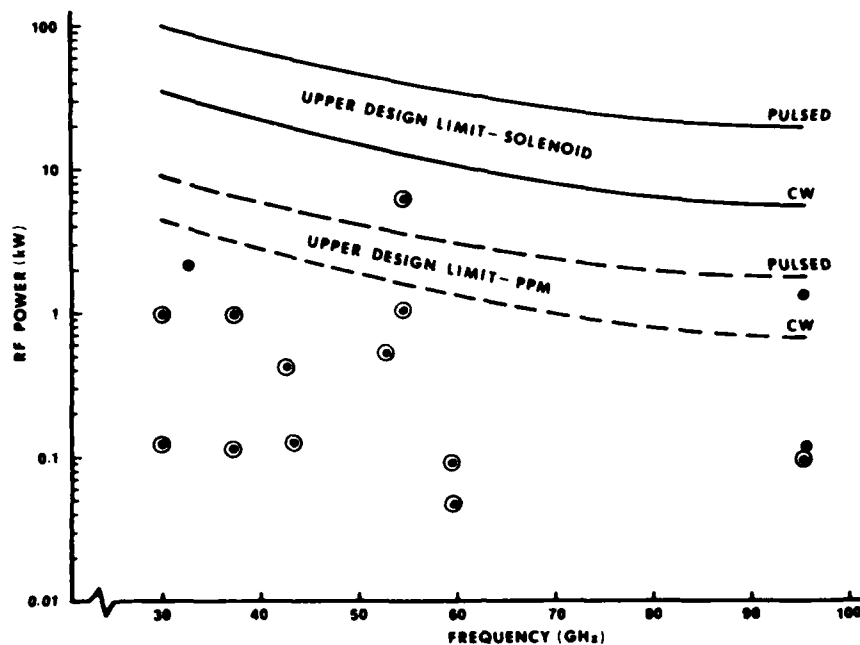


Fig. 21. Demonstrated and projected TWT output power for pulsed (solid circles) and CW (concentric circles) devices [6]. Projections are shown for solenoid and periodic permanent magnet (PPM) focused tubes.

at 0.9 mm, with efficiencies as high as 30 percent [31], [43]. In the US, workers at Varian have achieved 205 kW CW at 5 mm.

Fig. 22 [48] is a schematic diagram of a gyrotron oscillator showing the cathode, anodes, cavity, collector, and output window. Fig. 23 is a detail drawing of the cathode region showing the spiral electron trajectories which result from the electrons being emitted nearly perpendicular to the axial magnetic field direction. Since the output frequency  $\omega$

is related to the magnetic field  $B$  by

$$\omega = \frac{eB}{m}$$

where  $e/m$  is the ratio of electronic charge to effective electron mass, NMMW frequencies are seen to require very high magnetic fields, necessitating the use of superconducting magnets for frequencies greater than about 60 GHz [47].

Amplifier variants of the gyrotron, called the gyroklystron

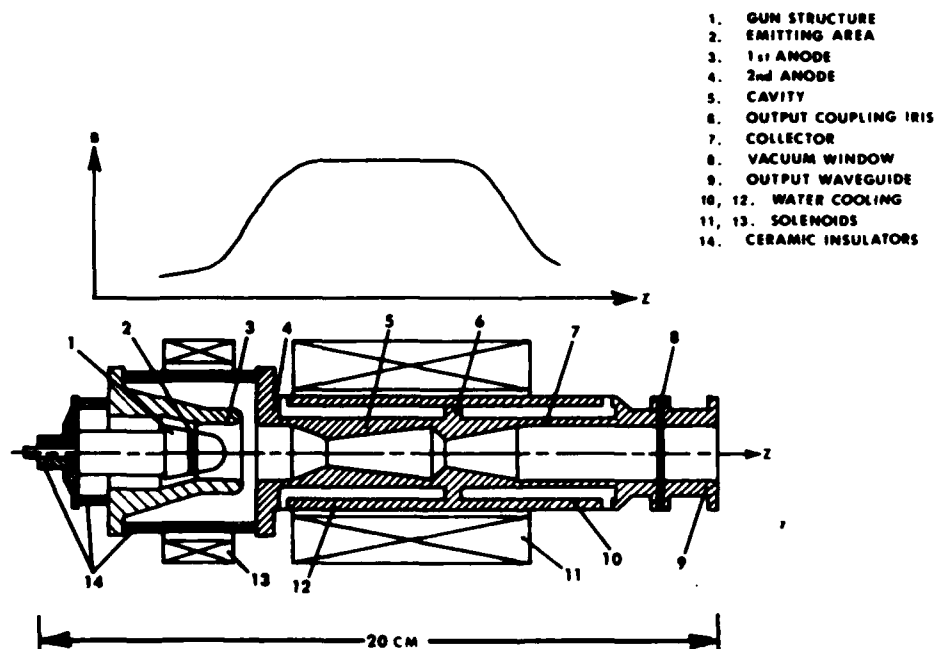


Fig. 22. Schematic diagram of a gyrotron oscillator [47]. Also shown is the magnetic field variation over the length of the tube.

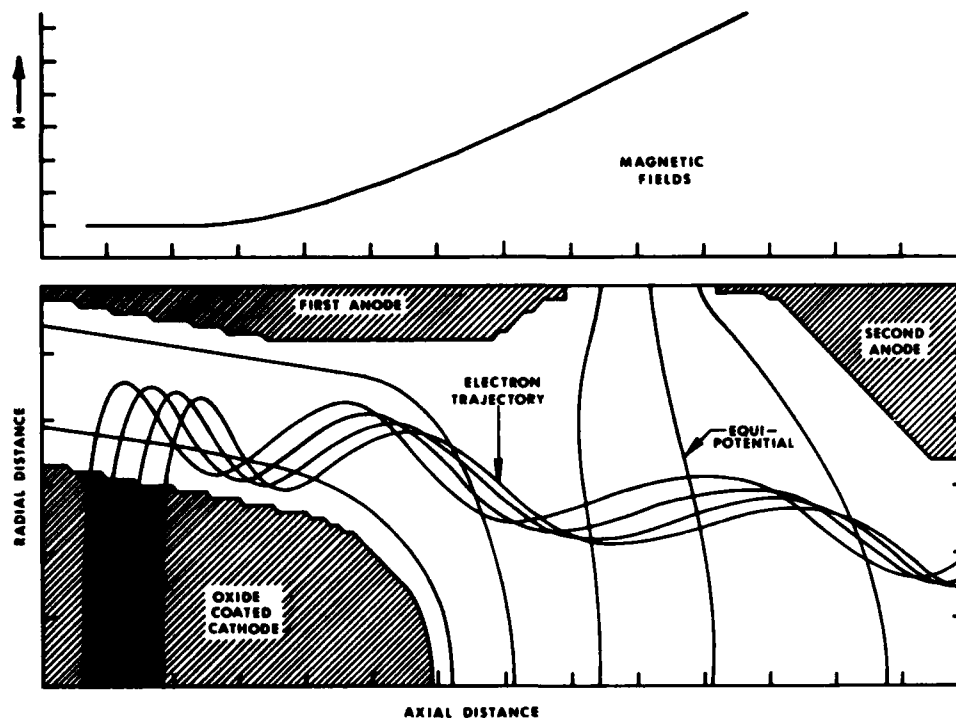


Fig. 23. Detail of the cathode area of a gyrotron showing electron trajectories, equipotential lines, and the magnetic field near the cathode [47].

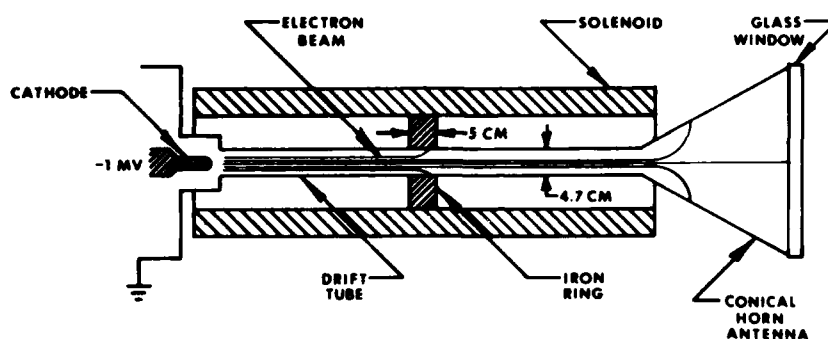


Fig. 24. Schematic of a relativistic electron-beam device [50]

and the gyro-TWT, are under development in this country [47] and have been successfully operated at the higher microwave frequencies. It is likely that further development in this area will lead eventually to useful NMMW devices.

#### Relativistic Electron-Beam (REB) Devices

Relativistic electron-beam (REB) devices have been emphasized by workers in this country, mainly at the Naval Research Laboratory [49]–[51]. Probably the most successful device of this type operates on the principle of scattering of a low-frequency high-power electromagnetic wave by a relativistic electron beam. High-power millimeter-wave radiation is thought to be generated by a Doppler shift which occurs when the low-frequency radiation is scattered by the relativistic beam. Another type of REB uses an undulator arrangement to perturb the passage of the high-energy electron beam, thus causing acceleration and subse-

quent emission of electromagnetic radiation. Fig. 24 [50] shows a REB device of this type which uses an iron ring as the undulator.

Because of the high currents and necessarily high accelerating voltages, REB devices are limited to pulsed operation. Peak output powers of up to 1 MW have been obtained. In addition to being limited to pulsed operation, REBs require high currents and high acceleration voltages, which make them very large and therefore useful only in the laboratory. Many workers in this field, however, feel that REB devices can be scaled to tractable sizes by careful design.

#### The Ledatron

Another type of vacuum tube which avoids the decreasing size and increasing power density problems inherent in the periodic structures of BWOs, EIOs, and TWTs is the

ledatron [52]. This device uses a Fabry-Perot interferometer as the resonant element and takes advantage of the fact that these resonators are several orders larger than a wavelength and are therefore much easier to fabricate. Two different modes of interaction between the electron beam and the resonator are used in the ledatron. In the Fabry-Perot mode, the beam interacts directly with the standing-wave pattern in the resonator, but in the surface-wave mode, the interaction is between the beam and a backward wave contained in the surface wave guided by the diffraction grating, which forms one element of the Fabry-Perot resonator.

Although the maximum predicted frequency of the ledatron is 3 THz, experimental models have been constructed which operate at 60–80 GHz with 100 mW of output power. It is expected that the ledatron will eventually find its place as a submillimeter-wave oscillator with power output up to 1 W and a tuning range of 30 percent.

The orotron is a variant of the ledatron which operates in the Fabry-Perot mode. Manifestations of this tube which have been built by Harry Diamond Laboratories [53], [54] in this country use a curved output coupling mirror so that a semi-confocal interferometer is formed. Fig. 25 is a schematic diagram of this device.

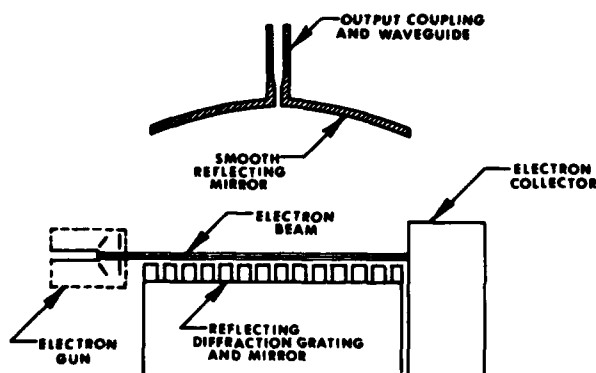


Fig. 25. Schematic diagram of an orotron oscillator [54].

#### Other Tube-Type NMMW Sources

The peniotron is a variant of the gyrotron in that a cylindrical electron beam with a large initial transverse velocity component executes cyclotron motion in a longitudinal magnetic field [32]. In the peniotron, however, the interaction region is a longitudinal double-ridged waveguide, and the angular frequency is twice the fundamental gyrotron frequency. The theoretical conversion efficiency for transverse beam energy is nearly 100 percent, and a 94-GHz 1-kW amplifier is under development.

The ubitron is a relativistic electron-beam device which uses a spatially periodic magnetic field to produce a spatially undulating electron beam which interacts with the RF field in a circular waveguide [32], [41]. As with other REB devices, the ubitron has good potential at NMMW frequencies, but initial work has been carried out at 54 GHz, where 150 kW with 5-percent efficiency have been obtained.

The orbitron [32], [55] is a very simple MMW oscillator

that consists only of an aluminum cylinder (a beer can was used for the prototype) with an axial wire situated in a partial vacuum, as shown in Fig. 26. A positive pulse applied to the wire ionizes the low-pressure air, producing electrons attracted to the central wire. Electrons with a transverse velocity component will then orbit the wire, with attraction opposed by centrifugal force. Pulses of MMW power up to 54 GHz have been produced by this device, and other configurations are under investigation. The orbitron offers the great advantage of electrostatic confinement, with no external magnetic field required.

#### IV. PHASE AND FREQUENCY CONTROL OF NMMW SOURCES

Increasing use of millimeter-wave frequency bands for communications, radar, and measurement functions has created the need for more sophisticated and higher frequency methods of precisely controlling the frequency and phase of sources of radiation in these bands. The availability of higher frequency sources and more sensitive receivers has pushed functional millimeter-wave technology to the limit of usefulness as determined by the atmospheric transmission bands, and phase-locking techniques have been used in laboratory experiments to lock lasers at frequencies as high as 28 THz [56], resulting in determinations of the speed of light to nine significant figures and providing methods of precisely determining the values of other fundamental physical constants. It is probably safe to say that no other physical quantity has been measured with the precision with which frequency has been measured using phase-locking techniques. The reason for this precision of course is that a fairly ordinary crystal oscillator, which may have a long-term stability on the order of one part in  $10^6$ , can serve as a reference for phase locking a millimeter-wave source, whose frequency is then known to the same accuracy. This accuracy can be greatly improved upon by using, for example, a commercially available rubidium frequency standard with an accuracy of one part in  $10^{11}$ . Coherent radar systems have for years relied on phase or injection-locked transmitters as well as phase-locked receiver local oscillators to give the level of frequency control required for determination of target velocities by the Doppler effect. Furthermore, the very sophisticated methods of data processing resulting in target detection in the presence of clutter rely heavily on precise methods of frequency and phase control of transmitter and local oscillator.

Several methods of frequency and phase control are used for NMMW sources. The frequency discriminator may be used to control frequency to approximately a few parts in  $10^6$ . The phase lock will control frequency to the accuracy of the phase-lock reference, which may be as good as one part in  $10^{11}$ , as mentioned earlier, and will also control the relative phase of the source and reference to an accuracy of a few degrees, after a suitable warm-up period. The most powerful phase-locking techniques combine the wide capture range of the discriminator with the precise phase control of the phase lock to result in a frequency control system that has excellent frequency stability and better immunity to perturbations which cause loss of phase lock. Injection locking of solid-state sources is also a useful technique, and this approach is usually used in conjunction

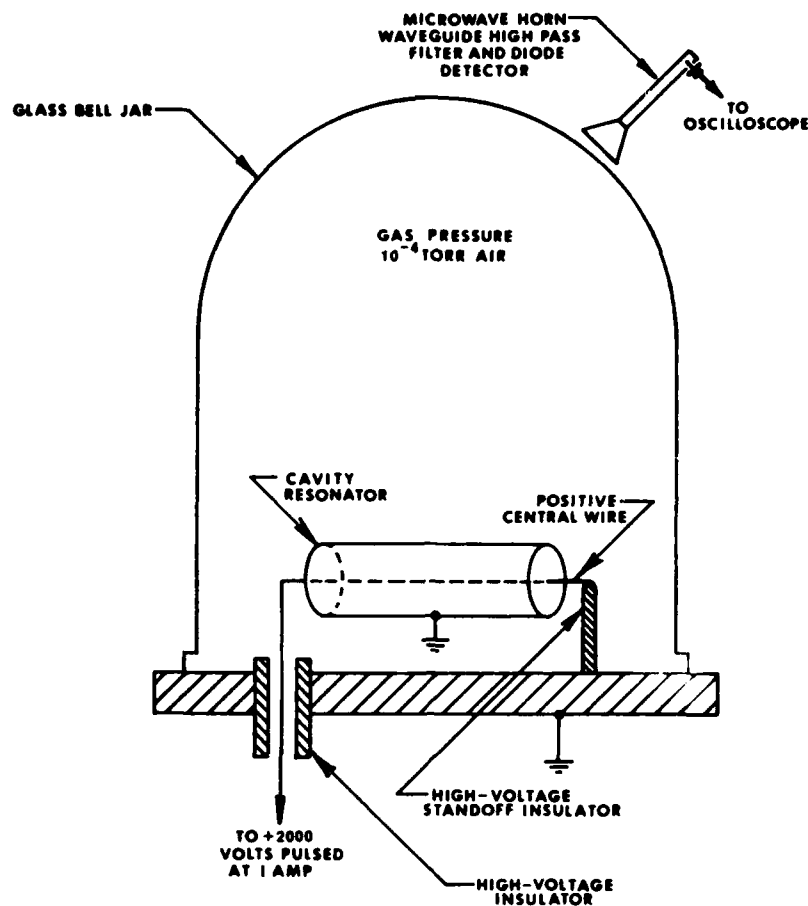


Fig. 26. A drawing of the orbitron, a millimeter-wave oscillator which needs no external magnetic field [55].

with phase or frequency locking. Each of these methods of phase and frequency control will be discussed in the following paragraphs.

#### Phase and Frequency Control Fundamentals

A block diagram of a basic phase-locking system is shown in Fig. 27 [57], [58]. The output of the voltage-controlled oscillator (VCO) mixes with that of the reference oscillator in a phase detector mixer to generate a phase error signal, which is in turn fed back through the loop filter to control the phase of the VCO. The VCO is a phase integrator and its transfer function is  $K_0/s$  where  $K_0$  is the VCO constant

in rad/sec · V and  $s$  is the Laplace transform differentiation operator.  $K_d$  is the phase detector constant in V/rad and  $F(s)$  is the (generally active) loop filter transfer function, chosen to give the best combination of phase-lock-loop frequency stability and phase noise performance.

Frequency control of a VCO is effected by a discriminator, which is a device that has an output voltage proportional to the difference between the VCO frequency and some reference frequency. Since discriminator error voltage is proportional to frequency and not phase, frequency-control loops are not as "tight" as phase-control loops, and the frequency errors are therefore greater.

It was mentioned that the combination of a frequency-

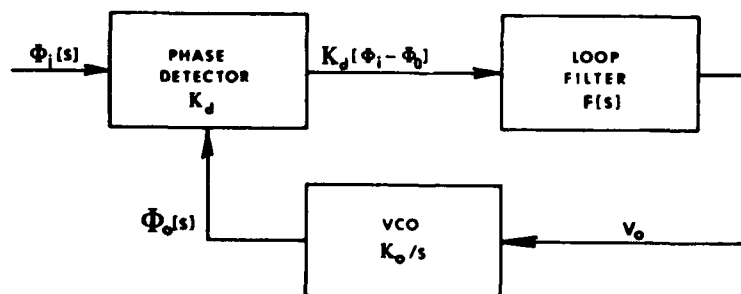


Fig. 27. Block diagram of a basic phase-locked voltage-controlled oscillator.

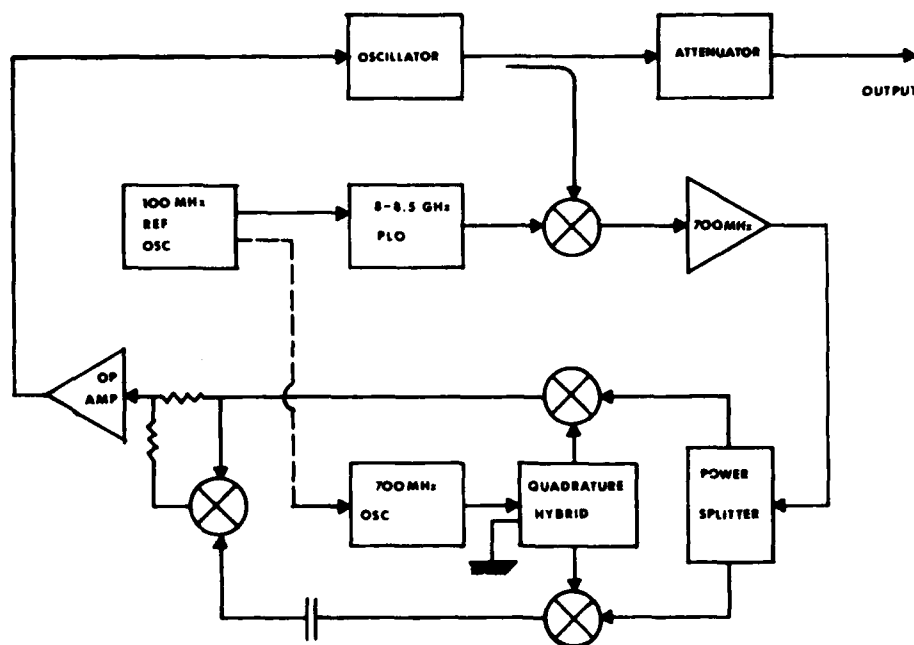


Fig. 28. Block diagram of the Henry [59] phase and frequency control circuit. The devices represented by crossed circles are mixers.

and a phase-control loop provides a very powerful phase-locking method. Such a circuit has been devised by Henry [59], who designed his circuit to lock klystrons used for radio-astronomical applications, although the same techniques apply to millimeter-wave sources in general. Pickett [60] has modified Henry's circuit to operate with a digital phase-frequency detector. Fig. 28 is a block diagram of the Henry phase lock showing the phase- and frequency-control loops. Assuming that the source is not locked, it will generally be oscillating at a frequency such that the difference between the IF and the reference oscillator is outside the capture range of the phase-lock loop. In this case, the discriminator captures the tube and pulls it within range of the phase lock, where the discriminator is disabled. In this way the phase- and frequency-control loops do not interfere with each other but act in a complementary way to combine the wide capture range of the discriminator with the precise frequency and phase control of the phase-lock loop.

Another approach to extending the capture range of the phase-lock loop involves activating a sweep-search mode if the source loses lock. Since most phase-lock loops have much narrower capture range than sources have electronic tuning range, a source will likely remain unlocked if it is unlocked because of a perturbation or upon initially applying power. If this occurs, the sweep-search mode is initiated to sweep the source through the proper frequency repetitively until lock is regained. The sweep is usually a 1-Hz ramp that is applied to the frequency control input of the source when diagnostic circuitry senses that lock is broken. Fig. 29 is a block diagram of a circuit used extensively to lock solid-state oscillators [61], which incorporates a sweep-search mode for wide frequency capture range. The sweep-search circuitry is incorporated in the loop electronics and driver block.

Injection locking is a method of phase control in which

power from the reference oscillator is injected directly into the output of the oscillator to be controlled by means of a circulator [62]. It is generally used for pulsed sources, because the methods of phase control discussed earlier are more easily used for CW sources. The rationale for injection locking is that radiation from all oscillators builds up initially from broad-band noise in the device. The injected signal provides a coherent basis for this buildup, causing the source to oscillate in phase with this reference signal. The reference signal is a phase-locked oscillator generally controlled by the methods described earlier.

The frequency of a phase-locked source is characterized by both short- and long-term stability. Long-term stability is almost totally determined by the quality of the reference source, and is usually specified as parts per million of frequency deviation per unit time. Times for this specification are usually long—1 h, or one day are common specification times. Short-term stability is determined by the quality of the reference source, the inherent FM noise of the phase-locked source, and the response of the phase-lock loop. Short-term stability is usually characterized as phase noise, which is a measure of the FM noise in a given bandwidth at a given frequency displacement from the carrier. It is normally measured in decibels below the carrier peak, and for convenience, the specified measurement bandwidth is sometimes chosen to be 1 Hz.

Another property of phase-locked sources is that such a source can never have a better phase-noise spectrum than its reference oscillator; in particular, it is not difficult to show [57] that the phase noise of the NMMW source can never be better than  $20 \log N$  plus the phase noise of the reference, where  $N$  is the frequency multiplication ratio. Fig. 30 shows the relationships between reference phase noise and NMMW source phase noise. At frequencies at which the phase-lock loop has control, the  $20 \log N$  relationship is maintained, as shown. When the loop begins to

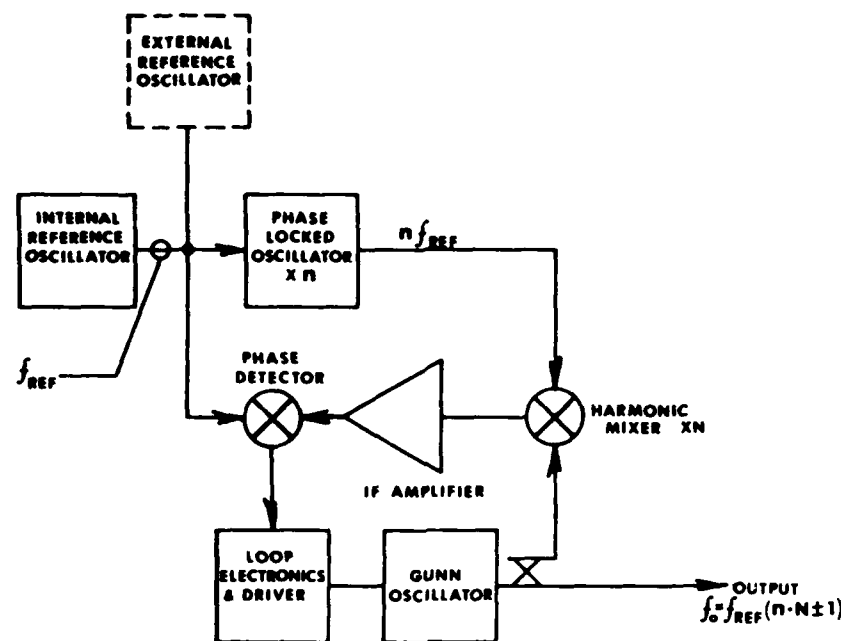


Fig. 29. Schematic diagram of a circuit used extensively to lock solid-state oscillators [62].

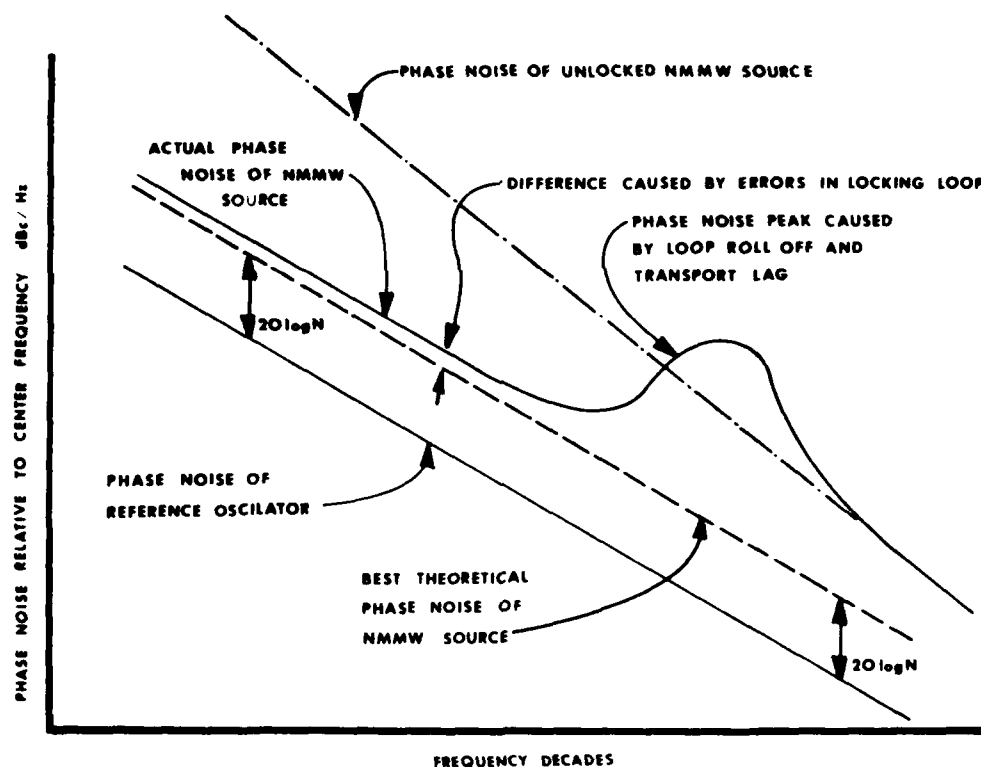


Fig. 30. Relationships between phase noise outputs of reference oscillator and NMMW source.

lose control, the phase margin of the loop decreases because of phase shift in the loop filter and transport lag, and the phase noise of the locked NMMW source may actually be worse than that of the unlocked source, as shown in the figure. However, it is possible to minimize the phase noise peak by careful design. When the loop totally loses control,

the phase noise reverts to that of the unlocked source, again shown in the figure.

#### Phase-Locking Results

Fig. 31 shows the spectrum of a phase-locked Gunn oscillator, locked using the circuit of Fig. 29. The corre-

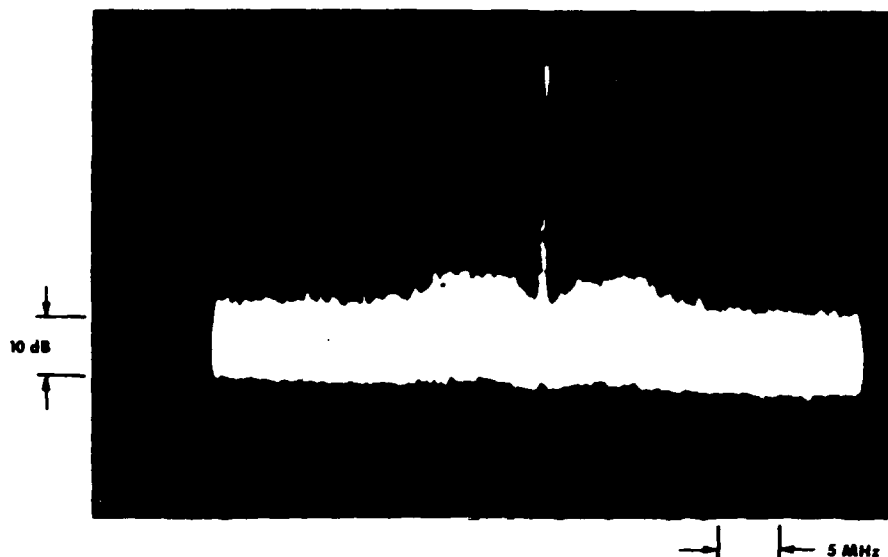


Fig. 31. Spectrum of phase-locked 94-GHz Gunn oscillator. Scales for 5 MHz (horizontal) and 10 dB (vertical) are indicated on the figure.

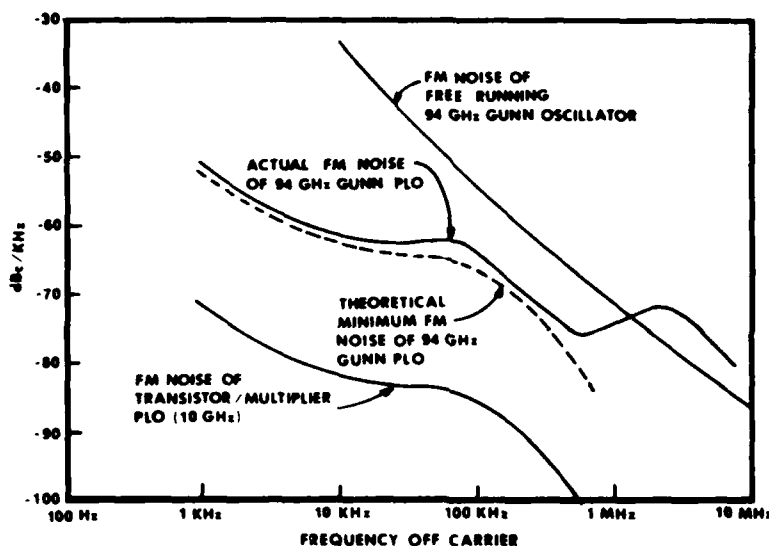


Fig. 32. Measured phase noise of 94-GHz Gunn oscillator showing relationships between the reference source, the phase-locked oscillator, and the free-running oscillator [62].

sponding phase noise spectrum of this source is shown in Fig. 32, which also clearly shows the relationships discussed in the last section. It has also been possible to lock an IMPATT oscillator at 116 GHz using this circuit [63]. The phase noise of a reflex klystron oscillator at 116 GHz is shown in Fig. 33 [64] and photographs of the spectrum of this source are given in Figs. 34 and 35, which show near-carrier and broad-band results, respectively.

By using the phase-locking techniques discussed above, it has been possible to build broad-band sophisticated IMPATT-based frequency synthesizers at frequencies up to *W*-band (70–110 GHz) [65], [66]. A full waveguide band synthesizer based on the BWO has also been built for *U*-band (40–60 GHz) [42], with indications that the same techniques could be used up to *D*-band (110–170 GHz). Fig. 36 is a block diagram of such a synthesizer. The desired frequency is entered into the microcomputer, which sets the frequency of the reference synthesizer to the proper

value and also generates a coarse frequency control voltage for the source through the D/A converter. This latter voltage pulls the source frequency within range of the phase-lock loop which captures it and locks it to the desired frequency. In the *U*-band synthesizer mentioned above, a discriminator was used to augment the capture range of the phase-lock loop. Also, the IMPATT-based synthesizer uses bias tuning of the source, whereas the BWO synthesizer applies the coarse frequency control voltage to a different tube electrode than the phase control voltage.

Injection-locked IMPATT oscillators have been used in an all solid-state pulsed coherent *W*-band radar [67]. Fig. 37 is a block diagram of the transmitter output stages which have a peak output of greater than 10 W, and Fig. 38 shows the spectrum of this transmitter. Note that this spectrum departs little from the theoretically ideal  $\text{sinc}^2 x/x^2$  for a rectangular pulse.

Injection priming of EIO tubes has also been used to

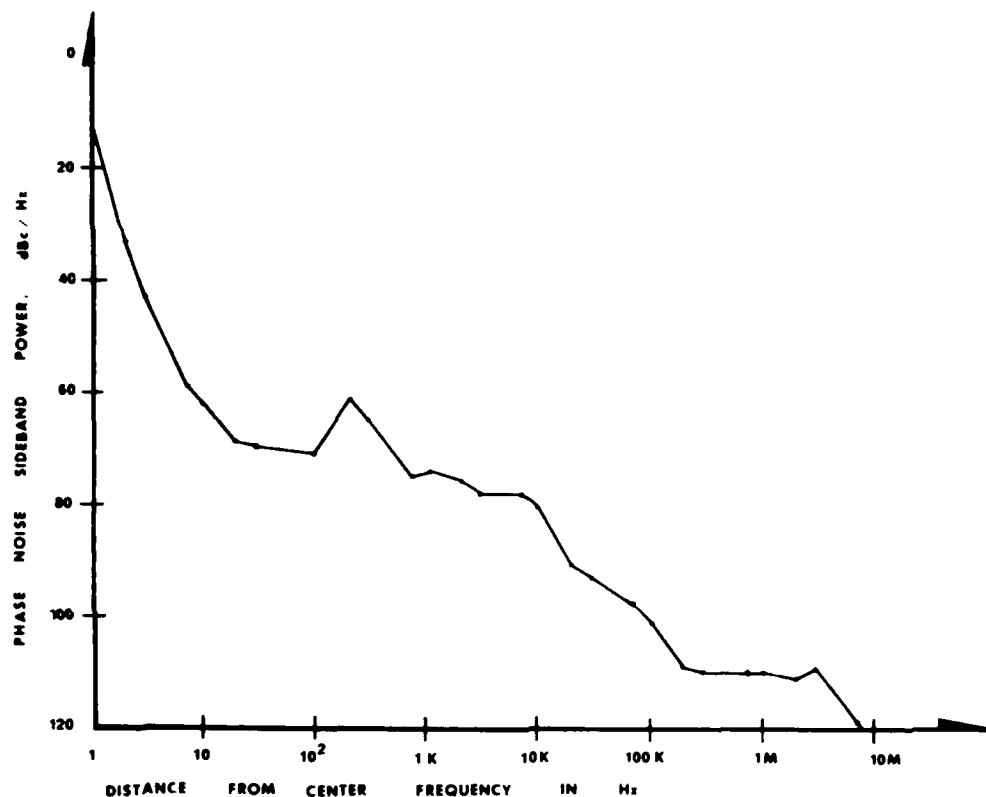


Fig. 33. Measured phase noise of klystron oscillator at 116 GHz [65]. Spurious responses at 60 and 120 GHz due to the power line are not shown and are 20 dB above the indicated result.

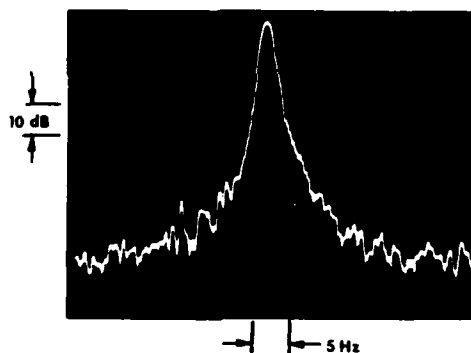


Fig. 34. Near-carrier spectrum of klystron oscillating at 116 GHz [65]. Horizontal (5-Hz) and vertical (10-dB) scales are shown. Similar results were obtained at 140 and 173 GHz.

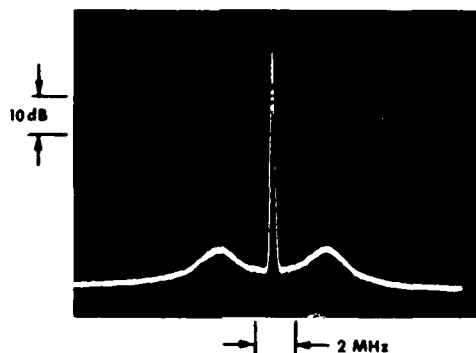


Fig. 35. Broad-band spectrum of klystron oscillating at 116 GHz [65]. Horizontal (2-MHz) and vertical (10-dB) scales are shown. Similar results were obtained at 140 and 173 GHz.

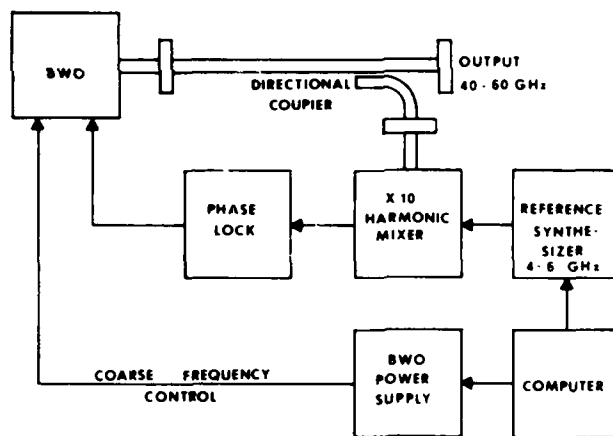


Fig. 36. Schematic diagram of BWO-based full-waveguide-band 40-60-GHz frequency synthesizer [42].

improve the spectrum of this source [68], [69]. The term "priming" instead of locking is used because generally not enough power is available for true injection locking of this device. Besides improving the spectrum, injection priming has been shown to effectively eliminate start-up jitter in the EIO, allowing output pulsewidths as short as 2 ns.

## V. CONCLUSIONS

It is safe to say that solid-state and tube-type NMMW sources have advanced in power and frequency coverage to the point of being useful in all of the atmospheric windows in which realistic systems can be built (up to about 340

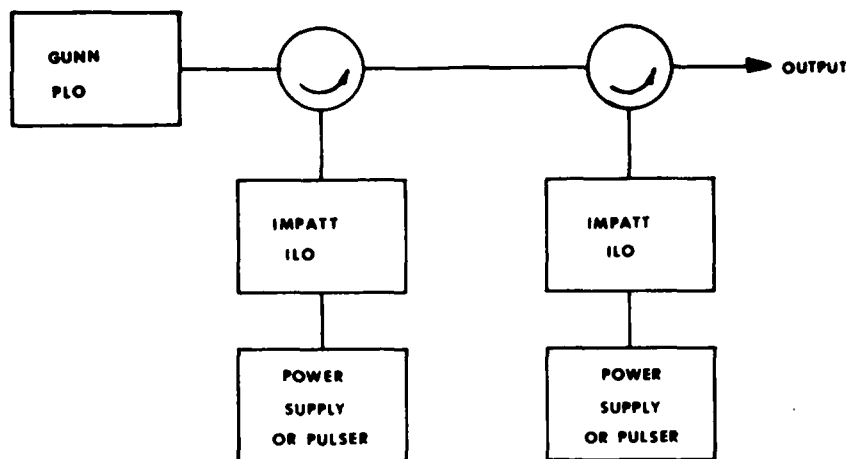


Fig. 37. Block diagram of a pulsed 94-GHz 10-W injection-locked solid-state transmitter [68].

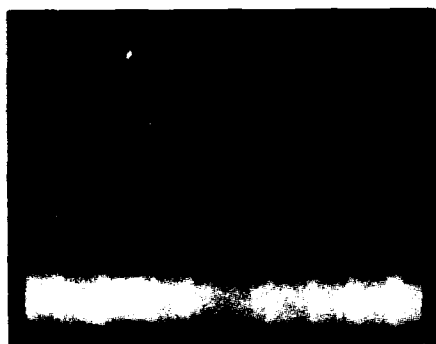


Fig. 38. Spectrum of pulsed 94-GHz 10-W injection-locked solid-state transmitter [68]. This photograph was made with a pulsewidth of 60 ns and a PRF of 100 kHz. The spectrum analyzer was set for 300-kHz bandwidth, 20-MHz/div horizontal scale, and 10-dB/div vertical scale.

GHz). If NMMW lasers are considered, this limit of system usefulness has been exceeded; however, lasers may still be used in many laboratory applications not affected by the atmosphere. Advances in solid-state sources have brought reliability, simplicity, and long life to systems that were previously very complicated or nearly impossible to build using tubes. On the other hand, the power and frequency capabilities of tube-type sources, based on fairly recent advances, have been improved to the extent that there are still many functions which only tubes can perform. However, it should be noted that more bandwidth capability is needed for both solid-state and tube-type NMMW sources.

Frequency and phase control of NMMW sources has kept pace with other advancements in these devices. Improved harmonic mixers and better methods of phase locking have contributed greatly to this advance. It is a fact that higher frequency sources generally have broader noise bandwidths, necessitating continuing improvements in phase-locking techniques to provide coherent NMMW sources. Phase locking provides the basis for the most accurate measurements of physical quantities ever made.

Existing NMMW sources will continue to improve, and new approaches in both source and source-utilization tech-

nology will continue to be found. As these advances are made, the ideal simple, reliable, broad-band, high-power NMMW source will be more closely approached.

#### ACKNOWLEDGMENT

Contributions to the phase-noise measurements presented in Section IV were made by G. W. Rosenberg of the Norwegian Defense Research Establishment, Kjeller, Norway, while a visiting scientist at Georgia Tech, and by V. T. Brady, now with Motorola GEC, Scottsdale, AZ.

#### REFERENCES

- [1] M. S. Tobin, "A review of optically pumped NMMW lasers," this issue, pp. 61-85.
- [2] R. J. Chaffin, *Microwave Semiconductor Devices: Fundamentals and Radiation Effects*. New York: Wiley-Interscience, 1973, chs. 8, 9.
- [3] S. M. Sze, *Physics of Semiconductor Devices*. New York: Wiley-Interscience, 1969, chs. 4, 5.
- [4] H. J. Kuno, "IMPATT devices for generation of millimeter waves," in *Infrared and Millimeter Waves*, Vol. 1, K. J. Button, Ed. New York: Academic Press, 1979, ch. 2.
- [5] H. J. Kuno, "Solid state millimeter-wave power sources and combiners," *Microwave J.*, vol. 24, pp. 21-34, June 1981.
- [6] N. B. Kramer, "Sources of millimeter-wave radiation: Traveling-wave tube and solid-state sources," in *Infrared and Millimeter Waves*, Vol. 4, K. J. Button and J. C. Wiltse, Eds. New York: Academic Press, 1981, ch. 4.
- [7] R. S. Ying, "Millimeter-wave solid state transmitter sources," in *Proc. Military Microwaves '82 Conf.* (London, England, Oct. 1982), pp. 468-471.
- [8] R. Ying, "Recent advances in millimeter-wave solid-state transmitters," *Microwave J.*, vol. 26, p. 69, June 1983.
- [9] H. S. Gokgor, I. Davies, H. M. Howard, and D. M. Brookbanks, "High-efficiency millimetre-wave silicon IMPATT oscillators," *Electron. Lett.*, vol. 17, pp. 744-745, Oct. 1, 1981.
- [10] J. J. Gallagher, "InP: A promising material for EHF semiconductors," *Microwaves*, vol. 21, pp. 77-84, Feb. 1982.
- [11] F. B. Fank and J. D. Crowley, "Gunn effect devices move up in frequency and become more versatile," *Microwave J.*, vol. 25, pp. 143-147, Sept. 1982.
- [12] J. D. Crowley, J. J. Sowers, B. A. Janis, and F. B. Fank, "High efficiency 90 GHz InP Gunn oscillators," *Electron. Lett.*, vol. 16, pp. 705-706, 1980.
- [13] I. G. Eddison, I. Davies, and D. M. Brookbanks, "Indium

- phosphide proves itself for millimeter applications." *Micro-wave Syst. News*, vol. 12, pp. 91-96, Feb. 1982.
- [14] F. B. Fank, "InP emerges as near-ideal material for prototype millimeter-wave devices," *Microwave Syst. News*, vol. 12, pp. 59-72, Feb. 1982.
  - [15] D. S. Pan and N. Lee, "GaAs abrupt junction MITATT and TUNNETT," presented at the 6th Int. Conf. on Infrared and Millimeter Waves, Miami Beach, FL, Dec. 7-12, 1981, paper M-5-3.
  - [16] J. Nishizawa, K. Motoya, and Y. Okuno, "Submillimeter wave oscillation from GaAs TUNNETT diode," presented at the 9th European Microwave Conf., Brighton, England, Sept. 17-20, 1979.
  - [17] M. E. Elta, H. R. Fetterman, W. V. Macropoulos, and J. J. Lambert, "150 GHz GaAs MITATT source," *IEEE Electron Device Lett.*, vol. EDL-1, pp. 115-116, June 1980.
  - [18] D. S. Pan and N. Lee, "Investigation of narrow band-gap semiconductors for TUNNETTs," presented at the 6th Int. Conf. on Infrared and Millimeter Waves, Miami Beach, FL, Dec. 7-12, 1981, paper M-5-8.
  - [19] M. E. Elta and G. I. Haddad, "High-frequency limitations of IMPATT, MITATT, and TUNNETT mode devices," *IEEE Trans. Microwave Theory Tech.*, vol. MTT-27, pp. 442-449, May 1979.
  - [20] J. W. Archer, B. B. Cregger, R. J. Matlack, and J. D. Oliver, "Harmonic generators have high efficiency," *Microwaves*, vol. 21, pp. 84-88, Mar. 1982.
  - [21] J. W. Archer, "A high performance frequency doubler for 80-120 GHz," *IEEE Trans. Microwave Theory Tech.*, vol. MTT-30, pp. 824-825, May 1982.
  - [22] K. Kurokawa and F. M. Magalhaes, "An X-band 10-Watt multiple-IMPATT oscillator," *Proc. IEEE*, vol. 59, pp. 102-103, Jan. 1971.
  - [23] K. Chang and S. Sun, "Millimeter-wave power combining techniques," *IEEE Trans. Microwave Theory Tech.*, vol. MTT-31, pp. 91-107, Feb. 1983.
  - [24] K. Chang, W. F. Thrower, and G. M. Hayashibara, "Millimeter-wave silicon IMPATT sources and combiners for the 110-260 GHz range," *IEEE Trans. Microwave Theory Tech.*, vol. MTT-29, pp. 1278-1284, Dec. 1981.
  - [25] G. R. Thoren and M. J. Virostko, "A high-power W-band (90-99 GHz) solid-state transmitter for high duty cycles and wide bandwidth," *IEEE Trans. Microwave Theory Tech.*, vol. MTT-31, pp. 183-188, Feb. 1983.
  - [26] H. C. Yen and K. Chang, "A 63 W W-band injection-locked pulsed solid-state transmitter," *IEEE Trans. Microwave Theory Tech.*, vol. MTT-29, pp. 1292-1297, Dec. 1981.
  - [27] J. R. Nevarex and G. J. Herokowitz, "Output power and loss analysis of 2" injection-locked oscillators combined through and ideal and symmetric hybrid combiner," *IEEE Trans. Microwave Theory Tech.*, vol. MTT-17, pp. 2-10, Jan. 1969.
  - [28] L. Wandinger and V. Nalbandian, "Millimeter-wave power combiner using quasi-optical techniques," *IEEE Trans. Microwave Theory Tech.*, vol. MTT-31, pp. 189-193, Feb. 1983.
  - [29] C. T. Rucker, J. W. Amoss, and G. N. Hill, "Chip level IMPATT combining at 40 GHz," in 1981 *IEEE MTT S Int. Microwave Symp. Dig.*, pp. 347-348, June 1981.
  - [30] H. Suzuki, O. Kurita, M. Ito, T. Makimura, and M. Ohmori, "Power considerations on IMPATT diode arrays with incomplete thermal isolation," *IEEE Trans. Microwave Theory Tech.*, vol. MTT-28, pp. 632-638, June 1980.
  - [31] A. E. Acker, "Interest in MM waves spurs tube growth," *Microwaves*, vol. 21, pp. 55-74, July 1982.
  - [32] A. J. Grant, "A review of millimetre wave devices," Royal Signals and Radar Establishment, Memo. 3572, June 1981. (Notes from an invited talk given at the Conference on Millimetre and Far-Infrared Spectroscopy organized by the British Radio Frequency Spectroscopy Group at St. Andrews University, Apr. 1981.)
  - [33] "Millimeter reflex klystrons," Varian of Canada Data Sheet 2561-65M 12/70, Varian Canada, 45 River Drive, Georgetown, Ont.
  - [34] "Extended interaction oscillators selection guide," Varian of Canada Data Sheet, Varian Canada, 45 River Drive, Georgetown, Ont.
  - [35] "Introduction to millimeter extended interaction klystrons," Varian Canada, Georgetown, Ont. 1982.
  - [36] M. Evans, Varian Canada, private communication, 1982.
  - [37] N. C. Currie, D. S. Ladd, and J. C. Butterworth, "EIA technology comes of age," *Military Electron./Countermeas.*, vol. 7, pp. 34-42, May 1981.
  - [38] G. Kantorowicz and P. Palluel, "Backward wave oscillators," in *Infrared and Millimeter Waves*, Vol. 1, K. J. Button, Ed. New York: Academic Press, 1979, ch. 4.
  - [39] "Siemens traveling wave tube data book 1977-78," Siemens AG, Munich, Germany.
  - [40] "Millimeter wave and submillimeter wave C-type backward wave oscillators," Thomson-CSF Publ. NTH 1348, Thomson-CSF, Boulogne-Billancourt, France, Nov. 1978.
  - [41] J. M. Baird, "Survey of fast wave tube developments," in *IEEE IEDM Tech. Dig.*, pp. 156-161, 1979.
  - [42] R. W. McMillan, M. G. Ellis, J. Seals, E. C. Burdette, V. T. Brady, M. L. Studwell, and S. M. Sharpe, "A millimeter wave frequency synthesizer covering the 40-60 GHz waveguide band," to be published.
  - [43] P. R. Kerrigan, "RF sources for millimeter wave systems," presented at IEEE Southcon 81, Atlanta, GA, Jan. 1981.
  - [44] "Hughes TWT and TWTA 1980 selection guide," Hughes Aircraft Co., Torrance, CA, 1980.
  - [45] V. A. Flayagin, A. V. Gaponov, M. I. Petelin, and V. K. Yulpatov, "The gyrotron," *IEEE Trans. Microwave Theory Tech.*, vol. MTT-25, pp. 514-521, June 1977.
  - [46] J. L. Hirshfield, "Gyrotrons," in *Infrared and Millimeter Waves*, Vol. 1, K. J. Button, Ed. New York: Academic Press, 1979, ch. 1.
  - [47] "Introduction to gyrotrons," Varian Publ. 430P, Varian Electron Device Group, Palo Alto, CA.
  - [48] P. R. Kerrigan, Varian Associates, private communication, 1982.
  - [49] P. Sprangle, R. A. Smith, and V. L. Granatstein, "Free electron lasers and stimulated scattering from relativistic electron beams," in *Infrared and Millimeter Waves*, Vol. 1, K. J. Button, Ed. New York: Academic Press, 1979, ch. 7.
  - [50] V. L. Granatstein, M. Herndon, R. K. Parker, and S. P. Schlesinger, "Strong submillimeter radiation from intense relativistic electron beams," *IEEE Trans. Microwave Theory Tech.*, vol. MTT-22, pp. 1000-1005, Dec. 1974.
  - [51] V. L. Granatstein and P. Sprangle, "Mechanisms for coherent scattering of electromagnetic waves from relativistic electron beams," *IEEE Trans. Microwave Theory Tech.*, vol. MTT-25, pp. 545-550, June 1977.
  - [52] K. Mizuno and S. Ono, "The lsdatron," in *Infrared and Millimeter Waves*, Vol. 1, K. J. Button, Ed. New York: Academic Press, 1979, ch. 7.
  - [53] D. E. Wortman and R. P. Leavitt, "Research study on near millimeter wave orotrons," Harry Diamond Laboratories Rep. HDL-SR-80-4, Adelphi, MD, July 1980.
  - [54] D. E. Wortman, R. P. Leavitt, and H. Droppa, "The orotron emerges as a millimeter wave source," *Microwaves*, vol. 21, pp. 126-128, May 1982.
  - [55] E. Alexeff and E. Dyer, "Millimeter wave emission from a maser by use of plasma produced electrons orbiting a positively charged wire," *Phys. Rev. Lett.*, vol. 4, pp. 399-401, Aug. 4, 1960.
  - [56] K. M. Evenson, C. W. Day, E. S. Weiss, and F. L. Miller, "Extension of absolute frequency measurements to the low He-Ne laser at 99.144 GHz (1.34  $\mu$ m)," *Appl. Phys. Lett.*, vol. 19, pp. 33-35, Feb. 1972.
  - [57] S. E. Weitenkamp and K. F. Wong, "Transportation of a phase-locked loop," Tech. Notes, The Aerospace Johnson Co., Palo Alto, CA, 1978.
  - [58] E. M. Gaudner, *Phase-Lock Techniques*, 2nd ed., New York: Wiley, 1979.
  - [59] P. S. Henry, "Frequency agile millimeter wave phase-locked system," *Rev. Sci. Instrum.*, vol. 4, pp. 100-101, Sept. 1973.
  - [60] H. M. Pickett, "Locking millimeter wave on a frequency stabilized phase frequency detector," *Rev. Sci. Instrum.*, vol. 4, pp. 100-101, June 1973.
  - [61] M. Crandall and E. E. Bernice, "Oscillator lock-in circuit at W-band," *Microwave Syst. News*, vol. 1, pp. 10-11, Dec. 1981.
  - [62] "Solid state millimeter wave products," Data Book, Hughes Aircraft Company, Torrance, CA, 1982.

- [63] R. G. Strauch, W. T. Smith, and V. E. Derr, "Injection locking of a laddertron at 35 kMc," *IEEE Trans. Microwave Theory Tech.*, vol. MTT-13, pp. 473-474, 1965.
- [64] J. M. Cadwallader, M. M. Morishita, and H. C. Bell, "217 GHz phase-locked IMPATT oscillator," *Microwave J.*, pp. 106-109, Aug. 1982.
- [65] G. W. Rosenberg, R. W. McMillan, and V. T. Brady, "Measurements of phase noise spectra of selected millimeter wave klystrons," presented at the 8th Int. Conf. on Infrared and Millimeter Waves, Miami Beach, FL, Dec. 1983, paper M3.4.
- [66] M. P. Fortunato and K. Y. Ishikawa, "A broadband solid state millimeter-wave synthesizer," in *IEEE MTT-S Int. Microwave Symp. Dig.* (Dallas, TX, June 1982), pp. 494-496.
- [67] ———, "MM-wave synthesizer has 8-15 GHz bandwidth," *Microwaves*, vol. 21, pp. 119-124, May 1982.
- [68] M. D. Simonutti, D. L. English, and F. J. Bernues, "Performance of 94 GHz coherent pulsed IMPATT transmitters," in *1980 IEEE MTT-S Int. Microwave Symp. Dig.*, (Washington, DC, May 1980), pp. 75-77.
- [69] R. W. McMillan, R. G. Shackelford, and J. J. Gallagher, "Millimeter wave beam rider and radar systems," in *Proc. SPIE Tech. Symp.* 259, (Huntsville, AL, Sept. 1980), pp. 166-171.
- [70] D. S. Ladd, "Nanosecond behavior of extended interaction oscillators," in *Proc. 9th DARPA Millimeter Wave Conf.* (Huntsville, AL, Oct. 20-22, 1981), pp. 377-384 (unclassified paper).

# Atmospheric Effects on Near-Millimeter-Wave Propagation

RONALD A. BOHLANDER, ROBERT W. MCMILLAN, SENIOR MEMBER, IEEE, AND JAMES J. GALLAGHER, FELLOW, IEEE

*Invited Paper*

*Utilization of the near-millimeter-wave band is limited by atmospheric effects on propagation. Although this paper is restricted to clear-air effects, it is pointed out that these phenomena, which are molecular in origin, are also present to a significant degree in adverse weather. The paper surveys theoretical and observational knowledge concerning absorption, emission, refraction, and turbulence effects in clear air and in the spectral range 90 to 1000 GHz. Modeling practices are also reviewed.*

## I. INTRODUCTION

The effects of the atmosphere have been paradoxically both a hindrance and a boon to the development of near-millimeter-wave technology. For many years, this spectral range was handicapped, not only by formidable development problems, but also by concerns about atmospheric attenuation which is significantly higher than at longer wavelengths. A resurgence of interest in near-millimeter waves came about in response to problems at shorter wavelengths. Infrared systems, while able to operate in both day and night, are frequently unable to perform through clouds, fog, or smoke. Near-millimeter waves are able to penetrate these obscurants with reasonable compromises in range and angular resolution. Activity in near-millimeter-wave propagation research has increased in recent years in response to needs for better definitions of the limitations. In addition, it is recognized that certain processes in molecular physics or atmospheric optics can be studied with special advantage in this part of the electromagnetic spectrum.

A number of commendable reviews have appeared (e.g., [1]–[7]) which examine in some detail the available literature. The present review will not attempt to repeat their critical efforts but rather provide a relatively terse account summarizing what is known and what are the frontier issues. The review will cover effects of importance in the frequency range 90 to 1000 GHz and will be divided in two parts to be published separately. In this first part, the effects

of molecular absorption, emission, and refraction and those due to turbulence will be covered. These are normally thought of as clear-air phenomena, but they are also an important component of adverse weather effects, which will be reviewed in a later paper.

## II. MOLECULAR ABSORPTION

### A. Theory

The major molecular absorbers in the near-millimeter wavelength region are  $H_2O$  and  $O_2$ . A few minor constituents can be seen weakly, such as  $O_3$ , and have been the subject both of ground-based and high-altitude investigations (e.g., [8], [9]). However, these have a negligible impact on utilizations of the band for communications, radar, and the like. Molecular absorption at these frequencies occurs principally through the excitation of rotational transitions, and its strength is usually determined by the size of the molecule's electric dipole moment. Molecular oxygen is the weaker of the two principal absorbers because it is a homonuclear diatomic with no electric dipole moment. It is able to make relatively weak transitions since it exists in a triplet-sigma ground state with two uncoupled (electron) spins, which give the molecule a magnetic moment. Absorption due to oxygen shows up clearly not from its intrinsic strength but from the large concentration of  $O_2$  in the atmosphere. The water molecule on the other hand has a strong electric dipole, and in spite of the light atoms in the molecule, the spacing of the absorption resonances is relatively close due to the molecule's bent shape and the consequent asymmetry of its rotational inertia. Absorption resonances of both oxygen and water molecules are shown in the calculated spectrum in Fig. 1. The level of absorption between these resonances has a considerable contribution from the wings of strong resonances of water at higher frequencies.

An important tool in modeling atmospheric absorption is the compilation of atmospheric absorption resonance parameters which is maintained by the Air Force Geophysics Laboratory [10]; parallel efforts should also be recog-

Manuscript received September 10, 1984; revised September 13, 1984. The on-going investigation by the authors in the areas reviewed in this paper is supported by the U.S. Army Research Office under Contracts DAAG-29-80-K-005 and DAAG-29-81-K-0173.

The authors are with Georgia Tech Research Institute, Georgia Institute of Technology, Atlanta, GA 30332, USA.

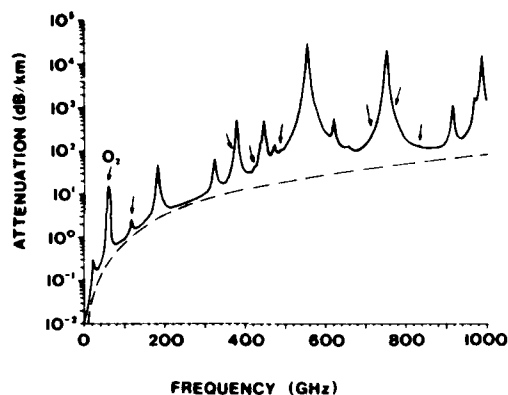


Fig. 1. Atmospheric absorption coefficient for a horizontal path near sea level calculated with the model in [37]. Solid line is the total predicted for absorption by water and oxygen molecules in the atmosphere. The positions of oxygen lines are indicated with arrows. The dashed line shows the continuum component of the model calculated with (2). Conditions assumed:  $T = 288$  K, dry air pressure  $P_d = 101.3$  kPa (1013 mbar), partial pressure of water vapor  $e = 1.7$  kPa (17 mbar, i.e., saturated). After [37].

nized [11], [12]. A word about nomenclature is appropriate here. The term resonance, to denote regions of peak molecular absorption, is physically more satisfying; however, the convention in spectroscopy is to call these peaks "lines," and this paper will comply to avoid confusion with the literature. The AFGL tables comprise extensive lists of line positions, intensities, widths, and energy levels from which the absorption coefficient at a given frequency  $\nu$  may be calculated according to

$$\alpha(\nu) = q \sum_{ij} S_{ij} f(\nu, \nu_{ij}, \gamma_{ij}) \quad (1)$$

where  $\nu_{ij}$  is the line position,  $S_{ij}$  is the intensity,  $f(\nu, \nu_{ij}, \gamma_{ij})$  is a function which describes the shape of the lines,  $\gamma_{ij}$  is the linewidth, and  $q$  is the concentration of the absorber. As shown, a simple summation is made over all lines in a band, since line-coupling effects may be neglected for atmospheric molecules in the near-millimeter spectrum [13]. Allowance is made for the temperature dependence of the line intensities with the help of tabulated energy levels, and for the temperature dependence of linewidths, with the help of detailed calculations for at least two temperatures [14], [15]. Since the width of lines in the troposphere arises from collisional broadening, this parameter depends on the barometric pressure and the partial pressure of the absorbing gas [14], [15]. As a result, in the gaps between lines, absorption by water vapor has two terms, one that increases linearly with water molecule concentration (line broadening by air), and one that increases quadratically with water molecule concentration (self-broadening). The accuracy of tabulated data on line parameters is reviewed in [10] and is generally adequate for modeling. Widths are difficult to measure, but by far the most uncertain item in any model is the shape of the lines a few linewidths away from line center, particularly when an entirely theoretical description is used.

Interest in the physics of line shape has been spurred in the near-millimeter spectrum since much of this region's utility lies in the intervals of frequency between lines, and there significant limitations are imposed by molecular absorption, even more so than in those regions commonly

used in the infrared. For many years, collisional line shape formulas have been used which were derived [16]–[18] with a simplification known as the "impact approximation" in which it is assumed that collisions occur in infinitesimal intervals of time. This can give a fairly accurate picture of the line shape within intervals of frequency equal to a few times the linewidth since this regime corresponds to time intervals of the order of the time between collisions, or longer. (One can think of collisional line broadening as a kind of modulation process.) The details of the events within collisions begin to have an effect on the line shape as the frequency difference from a given line center approaches the reciprocal of the collision durations. Recent work has made progress in methods to include the finite duration of collisions in the theory [19], [20], and some general constraints on the shape of lines far from line center have been clarified. For frequencies distant from a given line by more than the reciprocal of typical collision durations, some type of exponential decrease is required in the line shape formula [21]. This represents less absorption in the far wings of lines than has been heretofore predicted by impact approximation formulas and is understandable as a smoothing of the modulation process. However, the inclusion of a mean collision duration is not the last hurdle to the development of an adequate theory, as may be seen from an appreciation of the physics of the collision process as well as from comparisons of observation with prediction.

The problem faced in understanding atmospheric spectra is that the water molecule, the prime absorber, undergoes molecular interactions complicated by relatively strong attractive forces which are to some degree not spherically symmetric due to the shape of the molecule. Attractive interactions are believed to be responsible for the observation of increased absorption between lines when temperature decreases. There has been a controversy about whether this absorption signals the formation of dimers or should be understood as monomer line wings sensitive to the attractive part of the potential energy of interaction. For simpler molecules (which have spherically symmetric shapes), absorption caused by unbound, metastable, and bound pairs can be predicted in the correct proportions at a given temperature [22], [23]. In general when the temperature is low by comparison with the binding energy of molecular pairs, dimers are numerous and play an important role in the absorption of such simple molecules. Although this condition is met for pairs of water molecules (the heat of formation is believed to be at least as large as 0.12 eV as compared with  $k_B T = 0.025$  eV [24]), the theory of the relative importance of different kinds of pair interactions has not been extended as yet to asymmetric molecules.

Microwave transitions of water dimers have been observed in molecular beams [25] and are consistent with the lowest energy structure calculated from molecular orbital theory (e.g., [26]). However, molecular beams provide what is an essentially very cold molecular environment, and an analysis of observed room-temperature laboratory spectra shows no band structures simply related to the known low-temperature form of the dimer [24]. If dimers do contribute a significant part of the absorption at room temperature, it would appear that they must exist in many structures different from the lowest energy form. While theory does not yet predict how the spectrum of the dimer evolves with increasing temperature, one would expect considerable changes since current calculations [26] indicate that the nonspherical part of the potential energy function,

which defines the particular configuration of lowest energy, is relatively weak.

In the complementary arena of line broadening theory, some progress is being made toward the inclusion of more aspects of the intermolecular potential energy, but a complete inclusion of what is known [26] will be a formidable undertaking. Thus a satisfactory, completely theoretical description of water vapor absorption is not presently available, and current models of atmospheric transmission are empirical.

### B. Observations

There are several fairly recent reviews of data on the transmission of clear air or of atmospheric constituents measured in the laboratory [2], [6], [24], [27]. Such data are not easily obtained as may be elaborated briefly by the following generalizations concerning the various methods used.

1) Spectra can be obtained with Fourier spectroscopy, but available black-body, wide-band sources are weak, and require liquid-helium-cooled detectors and relatively long integration times for satisfactory results. Spectroscopy performed instead with multiple or tunable narrow-band sources sometimes requires tedious tuning operations, but generally offers greater accuracy at a given frequency.

2) Laboratory studies have the advantage of better control of the subject constituents, their pressures and temperatures, but the disadvantage of limited path lengths relative to the kilometer size links important in applications of the band. These frontiers have been pushed back through extreme care in fabrication of open-resonator cells [28] and through the development of large, untuned resonator cells [29].

3) In direct atmospheric research there is relatively greater difficulty in specifying the atmospheric conditions and, of course, a lack of control of these conditions, but in several on-going researches, a greater effort on characterization is being made. There are also difficulties in obtaining an absolute scale of transmission or absorption, since the atmosphere cannot be "pumped out" in order to obtain signals from the same experimental apparatus with no atmospheric absorption and thereby to make allowance for instrumental losses and losses due to beam divergence. Narrow-band measurements have something of an advantage in that the beam divergence in the far field can be calculated and experiments involving multiple paths can be analyzed in such a way that instrumental losses are eliminated [30]. Those who employ Fourier spectroscopy, and many who use narrow-band sources, must settle for relative transmission measurements from which the change of attenuation for a given change in humidity or temperature can be obtained. When the database is large enough, extrapolation to zero water vapor is possible [31], and an absolute scale for the important water vapor component can be established.

4) Slant-path radiometry has also been used to measure emission and absorption, but the difficulty of knowing the atmospheric constituent concentrations and temperatures over the path complicates the interpretation of the results.

Despite the diversity of methods, a consensus is forming on data of sufficient quality and consistency [2], [6], [24], [27] that an adequate basis exists to construct empirical models useful over a fair range of clear air conditions in the atmosphere. The spectrum in Fig. 1 illustrates such a calculation

### C. Anomalous Attenuation and Recent Work

Several significant researches have been reported since the reviews mentioned above which have been motivated by another controversy involving claims for the existence of anomalous attenuation ascribed to complexes of water of various sizes [32]–[34]. The conditions under which this is said to be observable are ones of high humidity with clear air or fog present, and ones of low temperatures in which relatively weakly bound complexes might plausibly be favored. Consequently, such conditions have been given more attention in recent work. Examples of anomalous absorption indications are given by a narrow-band laboratory study in a special untuned cavity at frequencies of 115–126 and 213 GHz [29], [35] and a Fourier spectroscopic investigation of atmospheric transmission in the range 150–870 GHz [36]. Both showed increases in specific attenuation with decreasing temperature (below 290 K) which were much larger than expected both by comparison with previously observed temperature dependences in higher temperature ranges and by consideration of the temperature dependences likely to be associated with energy levels in the water molecule and expected intermolecular interaction energies. Moreover, the absolute attenuations derived from these experiments were considerable in engineering terms; namely, in the range 5–20 dB/km at various frequencies between about 210 and 300 GHz, values which if correct would have a noticeable impact on applications of near-millimeter waves. A number of results have appeared since which do not show these effects and raise doubts concerning their validity.

A careful laboratory study has recently appeared of attenuation at 138 GHz [28]. An open resonator was used in which care was taken to avoid adsorbed layers of water on the reflecting surfaces which might add spurious attenuation. Results were obtained for temperatures of 282 and 300 K and for various mixtures of nitrogen and water vapor. This has been used to determine empirical corrections to model spectra (see below) which have been used to make comparisons with other data. No support for low-temperature or high-humidity anomalies was found and agreement with data in previously mentioned reviews [2], [6], [24], [27] is good. Reasonable agreement has also been found [37] with new results at 110 GHz [38], [39] in which techniques were used that were closely similar to those [29], [35] which previously showed anomalous attenuation, although an alternate analysis [39] still finds an anomalous low-temperature effect at several frequencies between 29.9 and 110 GHz, its contribution to total absorption is not large.

New Soviet studies have recently been described [40], [41] of measured attenuation in the frequency range 180–420 GHz over a 1.5-km-long atmospheric path. The zero of the attenuation scale was found by extrapolation from relative measurements at various humidities, a method that was mentioned earlier. Excellent signal-to-noise ratios were obtained, and no indication of anomalous temperature dependences or unexpected spectral features were found in the temperature range 263 to 282 K. Previous work by these investigators [42] is consistent with an absence of such effects, and recent Soviet laboratory results also support these conclusions [41].

Although proponents of the existence of anomalous absorption caution that their observations may apply to occasional nonequilibrium events [32], the tide appears to be running toward a belief that such conditions are either

quite rare or nonexistent. Nevertheless, recent activity spurred  $\gamma$  this controversy has fostered significant improvements in millimeter-wave propagation models [28], [37], and further benefits can be anticipated.

#### D. Empirical Models of Clear-Air Transmission

There have been major efforts to develop computer models of near-millimeter-wave propagation at several national laboratories, the U.S. Air Force Geophysics Laboratory [43], [44]; e.g., the U.S. Army Atmospheric Sciences Laboratory [45], and the National Telecommunications and Information Administration [28], [37], [46]–[48]. All have been extended to include effects of adverse weather, which will be considered in a later paper.

In the interest of computing speed, the general practice in these models is to compute the summation in (1) only for lines near the region of interest and to add to this a term that slowly increases with frequency. This represents all the contributions due to the wings of lines at other frequencies and due to other possible absorption mechanisms in water vapor which have been mentioned. It has been customary in this field to refer to this term as "continuum absorption" although this is not entirely consistent with previous usage in spectroscopy. Its magnitude has been determined by fitting to observations and thus compensates for the limitations which exist in current theory. In early empirical modeling efforts [49], data for limited conditions of barometric pressure, absolute humidity, and temperature were utilized in the fit, and thus there was inadequate underpinning to the assumptions made concerning the dependence of the magnitude of this term on those variables. In particular, inadequate attention was paid to the effect of self-broadening on the humidity dependence and to the steepness of the temperature dependence in the gaps between lines. A recent formulation of the continuum term  $\alpha_c$  [28], [37] given by

$$\alpha_c = (0.397eP_dT^{-0.5} + 4605e^{10}T^{-3.5})\nu^2 \quad (2)$$

is much improved in this regard and is illustrated in Fig. 1 by the dashed curve. Here, the water vapor partial pressure  $e$  is in kPa (= 10 mbar), the dry air pressure  $P_d$  is in kPa, frequency  $\nu$  is in GHz, and the continuum absorption coefficient  $\alpha_c$  is in dB/km. In another approach, a continuum has been derived from the wings of an empirically modified line shape that has been successfully fitted to data in parts of the millimeter- and near-millimeter-wave regions as well as to the infrared, with only four fitting parameters being necessary [43].

Comparisons between formulations of  $\alpha_c$ , such as in [28], are difficult to make and assess since the lines included in the line-by-line part of a given model and the line shape formula used are seldom the same from one model to the next. These choices can have a dramatic effect not only on the magnitude of the complementary continuum term, but also, for example, on its apparent frequency dependence. Some workers show a continuum with a simple frequency dependence like that in (2) and others a continuum with two or more inflection points [2], [24], [27], [43]. The apparent temperature dependence of the continuum is similarly affected by the lines selected for explicit inclusion in a model calculation and may vary with frequency [24]. In the use of continuum formulas it is crucial to remember that this so-called continuum is not yet a separable physical

phenomenon but rather an artifice which is added in to simplify calculations and improve agreement with observations. Unnecessary discrepancies with observations can result when parts of a model are obtained from different sources and happen to be incompatible. There is a considerable need for future standardization of practice to avoid this source of confusion. Further work is underway on comparisons of the effectiveness of competing current models as regards agreement with observations. In the course of the present review, it was noted that the recent Soviet results [40], [41] mentioned above differ from predictions based on the model in [28], [37] by plus and minus 1–7 dB/km, depending on the frequency or conditions studied (see Note Added in Proof on p. 58).

Besides the advantages of computational speed from restricting the number of lines that are calculated explicitly, improvements have also been made in the speed with which regions near line centers can be calculated [43]. This has facilitated modeling of vertical or slant paths in which many layers are included in the calculation, some of which are at low pressures and consequently have very narrow lines. Fig. 2 is an example of such a calculation for a

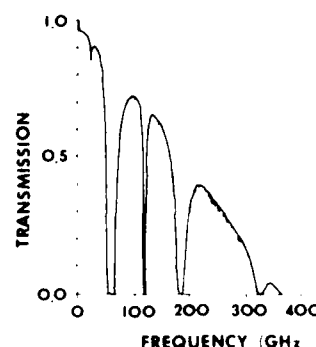


Fig. 2. Transmission of a vertical path through the U.S. Standard Atmosphere calculated with the AFGL FASCODE model [43]. The small line absorption lines, especially noticeable between 200 and 300 GHz, are due to minor atmospheric constituents, such as ozone. After [43].

standard atmosphere, from which it may be seen that only in the gaps between lines below 360 GHz are there channels with zenith attenuations which are less than 25 dB for one-way zenith transmission.

### III. EMISSION AND REFRACTION

Emission and refraction by the atmosphere need be treated only briefly since predictions of these phenomena can be derived in large measure from a knowledge of the absorption spectrum, provided that there is an adequate characterization of the meteorology of a situation. Emission is related to absorption by Kirchhoff's law [50] and refraction by the Kramers-Kronig relationship [51].

#### A. Emission

In the near millimeter and in the microwave regions thermal energy emitted is proportional to the temperature of the emitting substance in accordance with the Rayleigh-Jeans approximation. As a result, emission in these regions is frequently expressed as a brightness temperature  $T_b$  or "antenna temperature" related to the power

$P$  received from the atmosphere by a radiometer at frequency  $\nu$  by [51]

$$P(\nu) = k_B T_B(\nu) \nu^2 d\nu A \Omega / c^2 \quad (3)$$

where  $d\nu$  is the receiver bandwidth and  $A$  and  $\Omega$  are the effective receiver areas and beam solid angles, respectively. If the atmosphere could be represented by one homogeneous slab of air,  $T_B$  would be given by

$$T_B = T_a(1 - t) + T_c(\nu)t \quad (4)$$

where  $t$  is the transmission through the slab,  $T_a$  is the air temperature, and the last term is due to the cosmic background and is small.

In (4) it is assumed that the atmosphere is in thermodynamic equilibrium, and thus its thermal emissivity, by Kirchhoff's law, is equal to its fractional absorption  $(1 - t)$ . Gradients with height of both temperature and molecular concentration are modeled by approximating the integral relationship

$$T_B(\nu) = \int_0^\infty T_a(z) K(\nu, z) dz + T_c(\nu)t \quad (5)$$

by a summation over thin spherical shells in the atmosphere which are taken to have uniform conditions. Here  $K(\nu, z)$  is a weighting function which determines the contribution of the air temperature at altitude  $z$  to the sky brightness temperature and is given by

$$K(\nu, z) = \frac{d}{dz} t(0, z) \quad (6)$$

where

$$t(0, z) = 10^{-0.1 \int_0^z \alpha(z') dz'} \quad (7)$$

if  $\alpha$  is expressed in dB/km.

When one wishes to determine the transmission of the atmosphere over vertical or slant paths, one can in principle point a radiometer at a source of radiation outside the atmosphere, such as the sun, and correct the received signal for what is known of the source radiance and the antenna coupling efficiency (both functions of frequency). In practice, these corrections are difficult and some simplifications may be realized if, instead, emission from the atmosphere is measured and the corresponding transmission is inferred [52]. If the distribution of atmospheric temperature with height is known, from radiosonde observations for example, measured spectra of  $T_B$  can be inverted through (5)–(7) to find the transmission of the path. If the water vapor distribution is also known or can be estimated, a mean radiating temperature can be assigned by a Curtis–Godson-type approximation [50], [53]. Then (4) can be used to obtain a simple approximate inversion to transmission. An example of data inverted by this means [52] is shown in Fig. 3 and compared with a calculation based on a recent empirical model [43].

This and other recent comparisons [37], [54], [55] between models and slant-path observations have shown reasonable agreement. The significance of these comparisons is tempered, however, by the scant amount of data available concerning the humidity and temperature profiles over the paths studied. Some workers have attempted to derive continuum expressions for use in empirical models on the basis of slant-path emission observations [52]. Although these do not greatly differ in predicted absorption from the

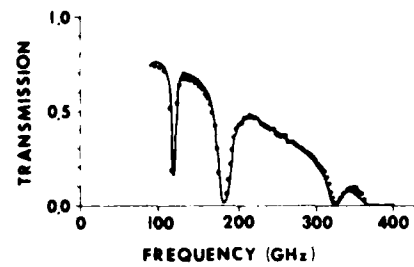


Fig. 3. Slant-path transmission inferred from emission measurements [52] (dots) and compared with a model calculation of transmission [43]. Slant secant = 1.09, integrated water vapor column density, derived from radiosonde data = 9.1 mm precipitable. After [43].

models referenced in the previous section, they should probably be given less weight of confidence than models based on laboratory or horizontal-path measurements where the atmospheric conditions can be better specified.

There is interest, of course, in levels of atmospheric emission for their own sake as they impact astronomical observations [52], [54], [55], communications [6], [56], and radiometric surveillance.

### B. Refraction

In the near-millimeter-wave range, atmospheric refractivity can be described as a sum of a constant term  $N_0$ , derived from a sum of contributions by lines at all frequencies, and a dispersion term  $N_d$ , due to the water and oxygen lines in the region

$$N = N_0 + N_d \quad (8)$$

(Note: refractivity is equal to the refractive index minus one and is usually expressed in parts per million of unity, ppm, equivalent to the term  $N$ -units which is frequently seen.) In common with the radio-frequency and microwave regions of the spectrum, the nondispersive term used in near-millimeter-wave models [57]

$$N = K_1(P_a/T)Z_a^{-1} + K_2(e/T)Z_w^{-1} + K_3(e/T^2)Z_w^{-1} \quad (9)$$

depends strongly on the amount of water vapor present in the atmosphere (expressed here as the partial pressure  $e$ ). This differs from the case in the visible or near-infrared parts of the spectrum, where the nondispersive refractivity depends almost entirely on barometric pressure (equal to  $e$  plus the partial pressure of dry air  $P_a$ ) and temperature  $T$ . Equation (9) is not an exact theoretical form but, with  $K_1 = 7.760$  K/kPa,  $K_2 = 7.15$  K/kPa, and  $K_3 = 3.750 \times 10^4$  K<sup>2</sup>/kPa, one which fits [57], [58] observations well. The factors  $Z_a$  and  $Z_w$  are nearly equal to unity [58], [59] and correct for the nonideal gas relation between density and pressure. It is interesting that a small but statistically significant discrepancy has been found [57] between the above values of  $K_2$  and  $K_3$  and those which best fit theoretical refractivity calculated from tables of line parameters. It has been suggested [57] that this indicates either an error in values of the strength of certain key lines in the water vapor pure rotation band or an effect of association by water molecules.

The dispersive term is calculated [37], [46], [47], [60], [61] as a summation over lines, similar to (1), but with a line shape derived from  $\mathcal{L}$  by application of the Kramers–Kronig relation. A typical value of  $N_0$  is 350 ppm, and by compari-

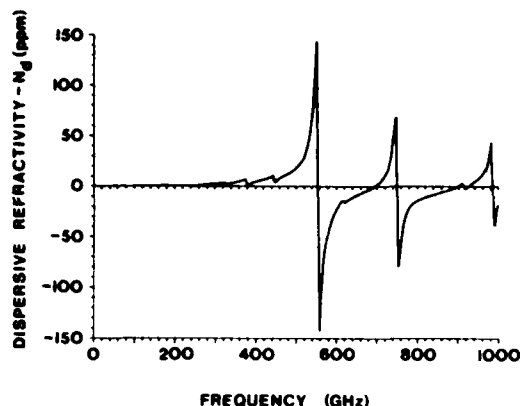


Fig. 4. The dispersive part of the atmosphere's refractivity calculated with the same model and conditions as in Fig. 1. For these conditions the total refractivity at 0 Hz is 350 ppm.

son, the dispersive term illustrated in Fig. 4 is important only in the vicinity of the strong lines, such as those at 557, 752, and 988 GHz. Observations of dispersion in the near-millimeter range are thus far available only at low resolution from dispersive Fourier transform spectroscopy [62], but no significant discrepancies with models have been identified.

The practical effects of clear-air refractivity are to produce phenomena which may be grouped into ones resulting from large-scale structures in the atmosphere, such as diurnal and weather changes, overall temperature and water vapor gradients or inversions, tidal effects, and the like, and those involving small-scale structures such as those produced by turbulence. The former will produce varying propagation delays, beam bending, beam ducting, multipath interference, etc. Except in the immediate vicinity of strong water vapor lines, as mentioned above, these effects should be closely similar to those found in the microwave region, since the refractivities in the two regions are very nearly equal and the sizes of the atmospheric structures are large compared with the wavelength in both cases. One distinction may, however, be found for multipath-type effects near the ground where reflected signals off the ground may contribute to a propagated wave. In this case, the ground effects will differ at near-millimeter-wave frequencies from those at lower frequencies due to significantly different scattering properties. Little experimental attention has thus far been given to these large-scale phenomena in near-millimeter-wave propagation. Studies are being made of the effects of small-scale phenomena, however, as described in the following sections.

#### IV. TURBULENCE

When the wind carries inhomogeneities in the atmosphere through a propagation path, fluctuations in several properties of the propagation result. In clear air, turbulence is the cause of inhomogeneities in both the refractive index and the absorption coefficient of the air. The refractive variations explain the familiar visible phenomena of star twinkling and the shimmering of distant images on a horizon on a hot day. Many aspects of the effects at visible and near-infrared wavelengths have been explored, after seminal theoretical work by Rytov [63], Chernov [64], and Tatarski [65], and detailed reviews are available [5], [66], [67].

Significant work has also been done in the microwave region (e.g., [68]), but millimeter-wave or near-millimeter-wave studies have only recently been given prominent attention. The possible propagation effects which may be catalogued are fluctuations in received intensity, angle of arrival, propagation delay, frequency, and polarization, of which the first three may be expected to be significant at near-millimeter wavelengths. In image formation, the phenomena can be manifested as scintillation, image dancing, and image blooming, of which the first two are important at such wavelengths.

As pointed out in [3], turbulence effects have sometimes been discounted for near-millimeter waves, since scattering by turbulent eddies is a diffractive effect, which naturally is stronger at shorter wavelengths. This is demonstrated by the following expression for the expected log-intensity variance of a received signal [60]:

$$\sigma_{\ln I}^2 = 0.4\% k^{7/6} L^{11/6} \left[ 1 - 2.73 \left( \frac{L_0}{\sqrt{L/k}} \right)^{-7/3} \right] C_n^2(10)$$

in which  $k$  is the wavenumber  $2\pi/\lambda$ ,  $L$  is the propagation path length,  $L_0$  is the size of the largest turbulence eddies, and  $C_n^2$  is the refractive index structure parameter, a measure of the spatial variance of refractive index. The reason that turbulence effects cannot be neglected in the near-millimeter-wave picture is the significant contribution by water vapor to the refractive index that distinguishes this regime from shorter wavelength regions, as mentioned earlier, and the fact that water vapor inhomogeneities in the atmosphere can be large. Fluctuating signal strength is not the only propagation issue of interest. Since at these wavelengths, high-precision tracking and adequate image formation systems may be constructed with antennas of moderate size, it is particularly of interest to know whether fluctuations in angle of arrival may show up as significant [69].

The near-millimeter-wavelength regime is of considerable interest for a number of other reasons. Some controversy has arisen over the interpretation of observations near the center of water vapor lines of moderate strength where the refractive index must be treated as complex, as will be discussed further in later sections. Such frequencies are of practical interest as possible choices for controlled-range communication links. Another distinction from shorter wavelengths is that near-millimeter wavelengths are no longer much smaller than turbulent eddies, but rather are comparable with the smallest ones. This so-called inner scale of turbulence  $\ell_0$  is of the order of a few millimeters. On the other hand, it is possible to construct antennas or antenna arrays which are as large as the largest eddies, or the outer scale of turbulence  $L_0$ , which ranges from a meter to a few meters in size for propagation near the ground, and possible to have propagation ranges for which the Fresnel zone of size  $\sqrt{\lambda L}$  is also comparable with  $L_0$ . This has given investigators an opportunity for interesting tests and extensions of theoretical models.

#### A. Theory

If one may assume that turbulent eddies are distributed in the neighborhood of a propagation path in a homogeneous and isotropic fashion, the Kolmogorov model [66] of the eddy spectrum says that the refractive index spatial

variance is proportional to the two-thirds power of the separation of two measurement points  $\Delta r$  when  $\Delta r$  is between  $\ell_0$  and  $L_0$ ; i.e.,

$$\langle \Delta n^2 \rangle = C_n^2 \Delta r^{2/3}. \quad (11)$$

The brackets denote ensemble averages which can usually be replaced by time averages (according to an ergodic hypothesis). The constant of proportionality  $C_n^2$ , which also appeared in (10), is the key refractive index structure parameter relating the turbulence structure to the resulting optical effects. In general, the index of refraction must be considered to be complex, and strictly, terms should be added to (10) for the contributions of the variance of the real and imaginary parts and for the covariance of these components. The terms involving the imaginary part are due to spatial variations in absorption, and it has been estimated that, except in special circumstances, the contribution of absorption to fluctuations will be difficult to observe in the near-millimeter-wavelength range [60], [61]. The discussion will return later to this topic, but for the time being can be simplified by ignoring the terms involving the imaginary part of the refractive index.

Since both air density and water vapor concentration affect the refractive index, the structure parameter  $C_n^2$  can be expressed in terms of analogous structure parameters for temperature, humidity, and barometric pressure. Pressure variations can generally be neglected [60], and  $C_n^2$  is given by

$$C_n^2 = A_T^2 \frac{C_T^2}{\langle T \rangle^2} + A_Q^2 \frac{C_Q^2}{\langle Q \rangle^2} + 2A_TA_Q \frac{C_{TQ}}{\langle T \rangle \langle Q \rangle} \quad (12)$$

where the  $A$  coefficients have been calculated from the refractive index spectrum [60], [61] and  $Q$  denotes water vapor concentration. Frequently, the earth's surface evaporates or transpires a considerable amount of water vapor. In these instances, the humidity fluctuations in the boundary layer are considerably larger in relative terms than the temperature fluctuations [60], [70], say

$$\frac{C_Q^2}{\langle Q \rangle^2} \approx 10^4 \frac{C_T^2}{\langle T \rangle^2}$$

and humidity variance dominates the refractive index structure. This can result in values of the near-millimeter wave  $C_n^2$ , which are larger by an order of magnitude or more than ones in the infrared, which are mainly sensitive to temperature structure.

That this is not always the case may be seen from the following considerations. The last term in (12) is proportional to the covariance of temperature and humidity,  $C_{TQ} = \langle \Delta T \Delta Q \rangle / \Delta r^{1/3}$ , which can generally be approximated for the boundary layer by [60]

$$\frac{C_{TQ}}{\langle T \rangle \langle Q \rangle} \approx \pm \left[ \frac{C_Q^2}{\langle Q \rangle^2} \frac{C_T^2}{\langle T \rangle^2} \right]^{1/2} \quad (13)$$

The positive sign is usually found during the day and the negative sign during the night, due to a change in the direction of the temperature gradient near the ground. Since  $A_T$  is negative (i.e., refractive index decreases with increasing temperature), the last term in (12) acts to reduce the near-millimeter-wave refractive index structure. Under some dry conditions, it can substantially cancel the contribution of the other two terms [71] and result in a situation

for which the value of  $C_n^2$  is smaller in the near-millimeter region than in the near infrared.

A formulation was given earlier in (10) for the expected level of intensity fluctuations that applies [60] when 1) the wavefronts are spherical, 2) the transmitting and receiving antennas are small relative to a Fresnel zone  $\sqrt{\lambda L}$ , and in turn, 3) the Fresnel zone is small compared with the outer scale  $L_0$ . The corresponding expression for angle of arrival variance is [64]

$$\sigma_A^2 = 0.54 L C_n^2 \rho^{-1/3} \quad (14)$$

where  $\rho$  may be interpreted as the spacing of small antennas (or the width of a large antenna) used in measuring the angle. Since with two or more antennas in an array, one actually measures the phase difference variance, known as the phase structure function  $D_\phi$ , an alternate description is

$$D_\phi = \langle \Delta \phi^2 \rangle = 1.09 k^2 L C_n^2 \rho^{5/3} \quad (15)$$

where, in both (14) and (15), the dependence on  $\rho$  holds when  $\sqrt{\lambda L} < \rho < L_0$  [72]. At larger antenna spacings, one can sense the outer scale by a drop-off in the slope of  $D_\phi$  with  $\rho$ . A transverse coherence length  $\rho_0$  is sometimes used which is the value of  $\rho$  for which  $D_\phi = 2 \text{ rad}^2$ . Since in the near-millimeter-wave range antennas are usually smaller than or comparable with  $\rho_0$ , the main source of image degradation expected from turbulence is from image dancing rather than image blooming.

In early derivations of expressions such as (10), (14), and (15), it was assumed that scattering by eddies was weak (i.e., that scattering angles were small) and to reinforce this assumption, it was additionally assumed that  $\lambda^3 L \ll \ell_0^4$ , or more simply, that  $\lambda \ll \ell_0$ . Whereas these inequalities are readily satisfied at visual wavelengths, they are not so in the near-millimeter range, where  $\lambda \sim \ell_0$ . It is reasonable to ask whether small eddies are able to sustain significant resonant scattering in this regime, similar to that familiar in Mie scattering from rain drops. However, recent work [73]–[75] has shown that the formulas derived under the assumption of weak scattering are still a good approximation when  $\lambda > \ell_0$  provided that  $\lambda < \rho_0$  or  $L_0$ .

An important dimension underlying the phenomena discussed thus far is the spatial spectrum of turbulent eddies and the resulting time spectra of modulations in propagation. Between the inner and outer scales of turbulence, the Kolmogorov model gives [67]

$$\Phi_n(\kappa) = 0.033 C_n^2 \kappa^{-11/3} \quad (16)$$

for the spectrum of refractive index as a function of spatial wavenumber  $\kappa$ . For smaller scales (larger wavenumbers than  $2\pi/\ell_0$ ), refractive index variations are small and a Gaussian tail can be added to (16) [65], [67]; for larger scales (smaller wavenumbers than  $2\pi/L_0$ ), turbulent phenomena merge with the large-scale variations in the atmosphere that were enumerated in Section III-B and are ill-defined in form. In general, the variations in refractive index continue to increase in size as the wavenumber decreases below  $\kappa = 2\pi/L_0$  but with some decrease in slope until some considerably smaller wavenumber is reached.

When a transverse wind carries the turbulence structure through a propagation path, the spatial spectrum helps to determine the resulting modulation spectrum for propagating electromagnetic waves. An approximation that is frequently invoked is that turbulent eddies are "frozen in",

i.e., last for times which are long by comparison with the time taken to cross the path. Not all eddies are equally effective in creating modulation, and so fluctuation spectra measured in a propagation experiment do not closely parallel (16). For instance, eddies approximately equal in size to the Fresnel zone are particularly effective in producing intensity fluctuations, and the resulting spectrum of such fluctuations does not fall off rapidly with increasing frequency  $f$  until  $f > f_0 = v(2\pi\lambda L)^{-1/2}$  [76], as illustrated in Fig. 5(a), where  $v$  is the cross wind speed. For fluctuations in the phase difference between two receivers separated by  $\rho$ , eddies of a scale similar to  $\rho$  are particularly effective, and the fluctuation spectrum has the form illustrated in Fig. 5(b). In contrast, the total phase in a link fluctuates slowly with a spectrum dominated by the largest scales in turbulence and by the other large-scale phenomena which have been mentioned. For this reason, it is not meaningful to give an expression analogous to (15) for the overall phase

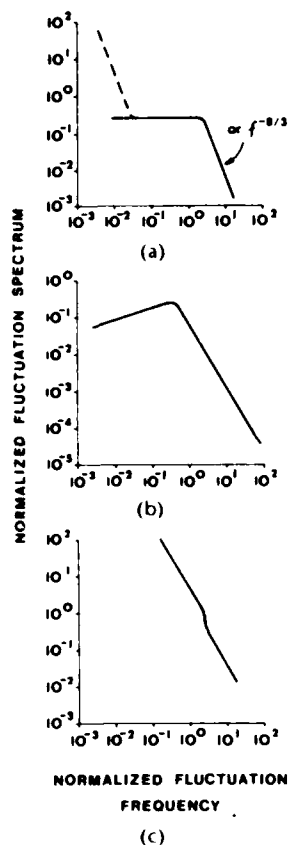


Fig. 5. Theoretical form of fluctuation spectra for the propagation of spherical electromagnetic waves [76]. (a) Log-intensity spectral density normalized by multiplying by the factor  $f_0/\sigma_{int}^2$ . Frequency scale normalized by dividing the fluctuation frequency  $f$  by  $f_0 = v(2\pi\lambda L)^{-1/2}$  where  $v$  = cross wind speed. The dashed line shows expected low-frequency behavior when absorption adds significant fluctuations. The exact frequency where it joins the solid line will depend on relative importance of absorption and refraction [81]. (b) Phase difference spectral density normalized by dividing by the phase structure function  $D_\phi$ . Frequency scale normalized by dividing the fluctuation frequency  $f$  by  $v/\rho$ , where  $\rho$  is the spacing of the points with different phase. (c) Total phase fluctuation spectral density normalized by multiplying by the factor  $4f/\sigma_{int}^2$ . The fluctuation frequency scale is normalized as in (a).

variance [67]. In summary, for Fresnel zones which are typically one to a few meters in size and for receiver antennas or arrays of the order of one to a few meters in size, the important fluctuation frequencies are expected to be in the low part of the audio spectrum in clear air turbulence.

## B. Observations

The preponderance of experimental efforts have thus far been directed at intensity fluctuation effects as these require less apparatus. The frequency dependence [70], [77] and path length dependence [70] in (10) have been verified by simultaneous observations at multiple frequencies in ranges covering 36 to 230 GHz and over paths of different lengths. Expected changes when the outer scale  $L_o$  happens to become smaller than a Fresnel zone have also been observed [77]. Less attention heretofore has been given to verification of the refractive index factor in (10) due to the requirement for a considerable investment in micrometeorological instrumentation to enable predictions of  $C_n^2$  to be made. This need was perceived in recent years [69] and several significant efforts are now underway. A comparison of observed microwave values of  $C_n^2$  with ones calculated from measured values of  $C_O^2$ ,  $C_T^2$ , and  $C_{TQ}$  has shown reasonable agreement [71]. Observations have recently been obtained for near-millimeter-wave intensity fluctuations (in the range 116 to 173 GHz) as well as for detailed micrometeorological parameters [70], [78], and a direct test of (10) will thus be possible.

Observations of the spectrum of intensity scintillation have also netted interesting results. The general form of Fig. 5(a) has been confirmed [79], including the expected falloff with fluctuation frequency to the  $-8/3$  power at high frequencies [76]. Studies in the neighborhood [80], [81] of the oxygen absorption band near 55 GHz, somewhat below the near-millimeter range, have demonstrated that inhomogeneities in absorption in the atmosphere produce an expected increase [81]–[83] in fluctuations at low fluctuation frequencies, above those due only to the real part of the refractive index, as sketched by the dashed line in Fig. 5(a). One would expect similar effects to be observed near significant water vapor absorption lines in the near-millimeter-wave region.

Observations have been reported, however, of effects which have the opposite sense; namely, striking decreases (by a factor of five) in the relative intensity fluctuation levels in the center of a moderately strong water vapor line near 325 GHz [84], [85], as compared with nearby regions between lines. Attempts at theoretical treatments [85], [86], have taken account of the fact that propagation paths have to be much shorter in such instances due to the high level of absorption (30 dB or more) and thus refractive scattering can become relatively more important than diffractive scattering. Although it has been shown that in particular circumstances, a decrease in fluctuations can occur, present theories predict much smaller decreases than those observed [85], [86]. A small departure has also been reported [87] from the usually expected log-normal distribution of intensity for a region of high absorption in the millimeter-wave spectrum. There is an opportunity here for further work to consolidate the picture of phenomena that accompany high absorption, which are of more than academic

interest due to potential applications in the communications field, for example. In further investigations, it would be advisable to eliminate some of the existing uncertainty through observations supported by detailed micrometeorology of the temperature and humidity structure.

Relatively little attention has been given until recently to the important topic of angle of arrival or phase difference fluctuations. Apart from measurements conducted at microwave frequencies [68], there were some observations near 150 GHz based on the use of a receiver which switches between two apertures, which showed angle of arrival fluctuations with a standard deviation of about  $100 \mu\text{rad}$  [88]. The present authors, with collaborators from the National Oceanic and Atmospheric Administration and the U. S. Army Atmospheric Sciences Laboratory, have been engaged in a new study in the frequency range 116 to 173 GHz that covers both intensity and angle of arrival effects [78]. It is being conducted over extremely flat and uniform ground cover to eliminate as many complications as possible to the turbulent structure. Simultaneous measurements of the micrometeorological parameters that characterize humidity and temperature structure are being made along with observations of standard meteorological parameters. Near- and mid-infrared scintillations are also recorded. Measurements have been conducted in a wide range of weather conditions throughout one year, but are at the time of writing in only a very preliminary state of reduction. The angle of arrival measurements are derived from a 10-m-wide by 1.5-m-high interferometric receiver array, and an example of results typical of summer daytime conditions dominated by humidity fluctuations is given in Fig. 6 as a function of horizontal receiver spacing. The Kolmogorov 5/3 power law (15) is shown for comparison, and one can

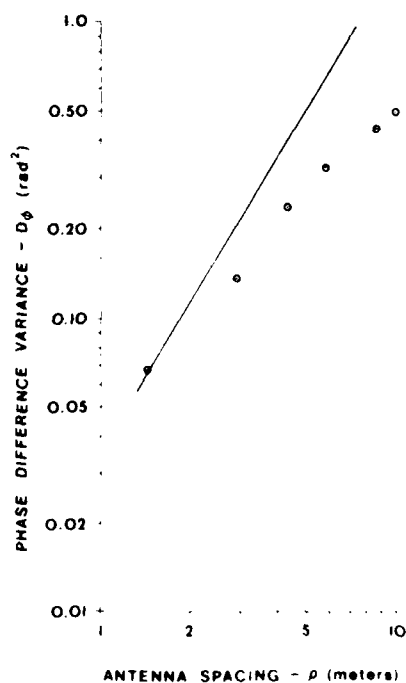


Fig. 6. Observed phase structure function (dots) at 173.95 GHz for clear air, with the sun shining near midday in the summer [78]. The straight line shows the Kolmogorov 5/3 power law for comparison. The departure at the larger values of antenna separation is due to a similarity between the size of these separations and the outer scale of turbulence.

see clearly the expected departure at larger spacings due to the effects of the finite size of the outer scale of turbulence [72].

In the longer term, such studies will be useful in affording the opportunity for detailed comparisons with theory, but for the present they have also provided useful orientations concerning the qualitative importance of various types of weather in producing degradation in propagation due to turbulence (or turbidity from suspended or falling hydrometeors). Summertime conditions when transpiration or evaporation of humidity are strong have provided the largest fluctuations yet seen. Over a path of about 1.4 km, intensity fluctuations up to 40 percent peak-to-peak and angle of arrival fluctuations of a few hundred microradians have been observed. At the other end of the spectrum have been fog conditions in stationary air, for which fluctuation levels have been about thirty times lower [78]. Generally, precipitation events have provided intermediate levels of fluctuations. This may at first seem surprising since during a rain storm, for example, there is plenty of available humidity and, in addition, fluctuations from scattering by rain. Offsetting those influences which increase the effect of turbulence, is a typical decrease due to cloud cover and the removal of strong heating at the ground. Even so, of the factors which increase the fluctuations during a storm, preliminary indications appear to rank the humidity effects as being the most important [78], pretty much in line with expectation [89]. This stresses the importance of the study of turbulence not only in clear air but also as it is superimposed on adverse weather.

The discussion of turbulence effects in this review has been confined essentially to horizontal paths fairly near the ground where the atmospheric conditions can be reasonably uniform and readily characterized by *in situ* measurements. Little attention has been given to turbulence effects on near-millimeter-wave propagation over slant paths. One might argue that slant-path effects will be smaller in most regards due to shorter interactions with the layers nearest the ground where the refractive index structure constant is expected to be highest. The foregoing discussion has also been restricted to spherical wavefronts as these are often encountered in practice. However, models for plane-wave and beam-wave cases also are available (e.g., [67], [76], [90]).

## V. CONCLUDING REMARKS

An understanding of the effects of the clear atmosphere on near-millimeter-wave propagation is fundamental to a wider understanding of effects in all types of weather. A few of the salient needs for further work, which were discussed in the preceding sections, will be outlined here.

1) Present models of nonresonant absorption by water vapor, the so-called continuum between the lines, are empirical. A breakthrough to an *a priori* description of the role of the molecular attractive forces of water in collision broadening of absorption lines and in dimer formation would be of major consequence. It would provide a better understanding of hydrogen bonding for a key molecule as well as better predictions of atmospheric absorption as a function of temperature.

2) Even within empirical approaches to predictions of atmospheric absorption there is room for improvement. Much needless confusion arises by a lack of standardization

over the definition of what nearby lines to include in explicit line-by-line calculations. There is little on which to base a choice, but the procedure used by the investigators at the U.S. Air Force Geophysic Laboratory [43] has the advantage that it is useable over a wide spectral range. An effort to bring about standardization and a consolidation of present observations and predictions into a format where more thorough comparisons can be drawn would be welcomed.

3) The discrepancy between theory and the observed temperature dependence of the radio-frequency refractivity is tantalizing [57]. The phenomenology of large-scale refractive effects at near-millimeter wavelengths, such as beam bending and multipath propagation, have so far been given little attention.

4) Greater prominence is now being given to studies of turbulence effects. Several interesting confirmations of theory have been completed and many more comparisons are in the offing. One puzzle which has appeared is the report of a strong diminution of intensity fluctuations near the center of a line at 325 GHz (e.g., [85]).

Important effects in adverse weather will be covered in a future publication.

#### Note Added in Proof

The author recently received a preprint of an article by H. J. Liebe in which revisions of the model in [28], [37] are presented. The improvements are based on revised line data and a more refined analysis of data obtained in his laboratory. They appear to bring the model into substantially better agreement with the Soviet data [40], [41].

#### ACKNOWLEDGMENT

The authors would like to acknowledge helpful discussions with S. F. Clifford, R. J. Hill, H. J. Liebe, and J. T. Priestley.

#### REFERENCES

- [1] J. W. Waters, "Absorption and emission by atmospheric gases," in *Methods of Experimental Physics*, vol. 12B, M. L. Meeks, Ed., New York: Academic Press, 1976, ch. 23.
- [2] D. E. Burch and D. A. Gryvnak, "Continuum absorption by H<sub>2</sub>O Vapor in the infrared and millimeter regions," in *Atmospheric Water Vapor*, A. Deepak, T. D. Wilkerson, and L. H. Ruhnke, Eds., New York: Academic Press, 1980, pp. 47-76.
- [3] S. M. Kulpa and E. A. Brown, "Near-millimeter wave technology base study, vol. 1. Propagation and target/background characteristics," U.S. Army Harry Diamond Laboratory Rep. HDL-SR-79-8, chs. 1, 2, Nov. 1979.
- [4] T. Oguchi, "Electromagnetic wave propagation and scattering in rain and other hydrometeors," *Proc. IEEE*, vol. 71, pp. 1029-1078, Sept. 1983.
- [5] R. L. Fante, "Electromagnetic beam propagation in turbulent media: an update," *Proc. IEEE*, vol. 68, pp. 1424-1443, Nov. 1980.
- [6] R. K. Crane, "Fundamental limitations caused by RF propagation," *Proc. IEEE*, vol. 69, pp. 196-209, Feb. 1981.
- [7] R. J. Emery and A. M. Zavod, "Atmospheric propagation in the frequency range 100-1000 GHz," *Radio Electron. Eng.*, vol. 49, pp. 370-380, July/Aug. 1979.
- [8] J. E. Harnes, "Infrared and submillimeter spectroscopy of the atmosphere," in *Infrared and Millimeter Waves*, vol. 6, K. I. Bultou, Ed., New York: Academic Press, 1982, ch. 1.
- [9] K. F. Kunzi and E. R. Carlson, "Atmospheric CO volume mixing ratio profiles determined from ground-based measurements of the J = 1 - 0 and J = 2 - 1 emission lines," *J. Geophys. Res.*, vol. 87, no. C9, pp. 7235-7241, Aug. 20, 1982.
- [10] L. S. Rothman, R. R. Gamache, A. Barbe, A. Goldman, J. R. Gillis, L. R. Brown, R. A. Toth, J.-M. Flaud, and C. Camy-Peyret, "AFGL atmospheric absorption line parameters compilation 1982 edition," *Appl. Opt.*, vol. 22, pp. 2247-2256, Aug. 1, 1983.
- [11] J.-M. Flaud, C. Camy-Peyret, and R. A. Toth, *Selected Constants, Water Vapour Line Parameters from Microwave to Medium Infrared*, Oxford, England: Pergamon, 1981.
- [12] J. K. Messer, F. C. De Lucia, and P. Helminger, "The pure rotational spectrum of water vapor—A millimeter, submillimeter, and far infrared analysis," *Int. J. Infrared Millimeter Waves*, vol. 4, pp. 505-539, 1983.
- [13] K. S. Lam, "Application of pressure broadening theory to the calculation of atmospheric oxygen and water vapor microwave absorption," *J. Quant. Spectrosc. Radiat. Transfer*, vol. 17, pp. 351-383, 1977.
- [14] W. S. Benedict and L. D. Kaplan, "Calculation of line widths in H<sub>2</sub>O-N<sub>2</sub> collisions," *J. Chem. Phys.*, vol. 30, pp. 388-399, 1959.
- [15] ———, "Calculation of line widths in H<sub>2</sub>O-H<sub>2</sub>O and H<sub>2</sub>O-O<sub>2</sub> collisions," *J. Quant. Spectrosc. Radiat. Transfer*, vol. 4, pp. 453-469, 1964.
- [16] J. H. Van Vleck and V. F. Weisskopf, "On the shape of collision-broadened lines," *Rev. Mod. Phys.*, vol. 17, pp. 227-236, Apr.-July, 1945.
- [17] E. P. Gross, "Shape of collision-broadened spectral lines," *Phys. Rev.*, vol. 97, pp. 395-403, 1955.
- [18] D. L. Huber and J. H. Van Vleck, "The role of Boltzmann factors in line shape," *Rev. Mod. Phys.*, vol. 38, pp. 187-204, 1966.
- [19] S. A. Clough, F. X. Kneizys, R. Davies, R. Gamache, and R. Tipping, "Theoretical line shape for H<sub>2</sub>O vapor: Application to the continuum," in *Atmospheric Water Vapor*, A. Deepak, T. D. Wilkerson, and L. H. Ruhnke, Eds., New York: Academic Press, 1980, pp. 25-46.
- [20] G. Birnbaum, "The shape of collision broadened lines from resonance to the far wings," *J. Quant. Spectrosc. Radiat. Transfer*, vol. 21, pp. 597-607, 1979.
- [21] R. W. Davies, R. H. Tipping, and S. A. Clough, "Dipole autocorrelation function for molecular pressure broadening: A quantum theory which satisfies the fluctuation-dissipation theorem," *Phys. Rev. A*, vol. 26, pp. 3378-3394, 1982.
- [22] D. E. Stogryn and J. O. Hirschfelder, "Contribution of bound, metastable, and free molecules to the second virial coefficient and some properties of double molecules," *J. Chem. Phys.*, vol. 31, pp. 1531-1545, 1959; Errata: vol. 33, pp. 942-943, 1960.
- [23] A. T. Prengel and W. S. Cornall, "Raman scattering from colliding molecules and Van der Waals dimers in gaseous methane," *Phys. Rev. A*, vol. 13, pp. 253-262, Jan. 1976.
- [24] R. A. Bohlander, R. J. Emery, D. T. Hlewellyn-Jones, G. G. Gimmetstad, H. A. Gebbie, O. A. Simpson, J. J. Gallagher, and S. Perkowitz, "Excess absorption by water vapor and comparison with theoretical dimer absorption," in *Atmospheric Water Vapor*, A. Deepak, T. D. Wilkerson, and L. H. Ruhnke, Eds., New York: Academic Press, 1980, pp. 241-254.
- [25] T. R. Dyke, K. M. Mack, and J. S. Muentert, "The structure of water dimer from molecular beam electric resonance spectroscopy," *J. Chem. Phys.*, vol. 86, pp. 498-510, Jan. 15, 1977.
- [26] E. Clementi and P. Habitz, "A new two body water-water potential," *J. Phys. Chem.*, vol. 87, pp. 2815-2820, 1983.
- [27] D. E. Burch, "Continuum absorption by atmospheric H<sub>2</sub>O," *Proc. SPIE (Atmospheric Transmission)*, vol. 277, pp. 39-49, 1981.
- [28] H. J. Liebe, "The atmospheric water vapor continuum below 300 GHz," *Int. J. Infrared Millimeter Waves*, vol. 7, pp. 207-227, 1984.
- [29] D. T. Hlewellyn-Jones, "Laboratory measurements of absorption by water vapour in the frequency range 100 to 1000 GHz," in *Atmospheric Water Vapor*, A. Deepak, T. D. Wilkerson, and L. H. Ruhnke, Eds., New York: Academic Press, 1980, pp. 255-264.
- [30] A. B. Crawford and D. C. Hogg, "Measurement of atmospheric attenuation at millimeter wavelengths," *Bell Syst. Tech. J.*, vol. 35, pp. 907-916, July 1956.

- [31] Yu. A. Dryagin, A. G. Kislyakov, L. M. Kukin, A. I. Naumov, and L. I. Fedoseev, "Measurement of the atmospheric absorption in the range 1.36–3.0 mm," *Izv. VUZ. Radiofizika*, vol. 9, no. 6, pp. 1078–1084, 1966.
- [32] H. A. Gebbie, "Observations of anomalous absorption in the atmosphere," in *Atmospheric Water Vapor*, A. Deepak, T. D. Wilkerson, and L. H. Ruhnke, Eds. New York: Academic Press, 1980, pp. 133–141.
- [33] ———, "Resonant absorption by water polymers in the atmosphere," *Nature*, vol. 296, pp. 422–424, Apr. 1, 1982.
- [34] H. R. Carlon and C. S. Harden, "Mass spectroscopy of ion-induced water clusters. An explanation of the infrared continuum absorption," *Appl. Opt.*, vol. 19, pp. 1776–1786, June 1, 1980.
- [35] D. T. Llewellyn-Jones, R. J. Knight, and H. A. Gebbie, "Absorption by water vapour at 7.1 cm<sup>-1</sup> and its temperature dependence," *Nature*, vol. 274, pp. 876–878, Aug. 31, 1978.
- [36] G. G. Gimmetstad and H. A. Gebbie, "Measurements of near-millimeter wave atmospheric attenuation in the temperature range 259K to 282K," *Int. J. Infrared Millimeter Waves*, vol. 3, pp. 77–82, Jan. 1982.
- [37] H. J. Liebe, "An atmospheric millimeter wave propagation model," NTIA Rep. 83-137, Dec. 1983.
- [38] D. T. Llewellyn-Jones and R. J. Knight, "Molecular absorption by atmospheric gases in the 100–1000 GHz region," in IEE Conf. Publ. No. 195, ICAP 81, pp. 81–83, 1981.
- [39] ———, "Measurements of water vapour absorption in the RAL untuned cavity," Rutherford Appleton Laboratory Rep. RL-82-051, July 1982.
- [40] L. I. Fedoseev and L. M. Koukin, "Comparison of the results of summer and winter measurements of atmospheric water vapor absorption of wavelengths 1.15 to 1.55 mm," *Int. J. Infrared Millimeter Wave*, vol. 5, pp. 953–963, July 1984.
- [41] N. I. Furashov, V. Yu. Katkov and V. Ya. Ryadov, "On the anomalies in submillimeter absorption spectrum of atmospheric water vapor," *Int. J. Infrared Millimeter Waves*, vol. 5, pp. 971–984, July 1984.
- [42] L. M. Koukin, Yu. N. Nodrin, V. Ya. Ryadov, L. I. Fedoseev, and N. I. Furashov, "Determination of the contribution of water vapor monomers and dimers to atmospheric absorption from measurement data in the 1.15 to 1.55 mm band," *Radio Eng. Electron. Physics*, vol. 20, no. 10, pp. 7–13, Oct. 1975.
- [43] S. A. Clough, F. X. Kneizys, L. S. Rothman, and W. O. Gallery, "Atmospheric spectral transmittance and radiance FAS-CODIB," *Proc. SPIE (Atmospheric Transmission)*, vol. 277, pp. 152–166, 1981.
- [44] V. J. Falcone, Jr. and L. W. Abreu, "Millimeter wave propagation modeling," *Proc. SPIE (Millimeter Optics)*, vol. 259, pp. 58–66, 1980.
- [45] L. D. Duncan and R. C. Shirkey, "EOSAEL 82: library of battlefield obscuration models," *Opt. Eng.*, vol. 22, pp. 20–23, Jan./Feb. 1983.
- [46] H. J. Liebe and G. G. Gimmetstad, "Calculation of clear air EHF refractivity," *Radio Sci.*, vol. 13, pp. 245–251, Mar./Apr. 1978.
- [47] H. J. Liebe, "Modeling attenuation and phase of radio waves in air at frequencies below 1000 GHz," *Radio Sci.*, vol. 16, pp. 1183–1199, Nov./Dec. 1981.
- [48] ———, "Atmospheric EHF window transparencies near 35, 90, 140, and 220 GHz," *IEEE Trans. Antennas Propagat.*, vol. AP-31, pp. 127–135, Jan. 1, 1983.
- [49] K. C. Allen and H. J. Liebe, "Tropospheric absorption and dispersion of millimeter waves," *IEEE Trans. Antennas Propagat.*, vol. AP-31, pp. 221–223, Jan. 1, 1983, Errata: *IEEE Trans. Antennas Propagat.*, vol. AP-31, p. 1004, Nov. 1983.
- [50] N. E. Gaut and E. C. Reitenstein, III, "Interaction model of microwave energy and atmospheric variables," Environmental Research and Technology, Inc., Tech. Rep. 13, Feb. 17, 1971.
- [51] J. T. Houghton and S. D. Smith, *Infrared Physics*. Oxford, England: Clarendon, 1966.
- [52] J. D. Kraus, *Radio Astronomy*. New York: McGraw-Hill, 1966, p. 98.
- [53] D. P. Rice and P. A. R. Ade, "Absolute measurements of the atmospheric transparency at short millimetre wavelengths," *Infrared Phys.*, vol. 19, pp. 575–584, 1979.
- [54] W. A. Traub and M. T. Sher, "Theoretical atmospheric transmission in the mid- and far-infrared at four altitudes," *Appl. Opt.*, vol. 15, pp. 364–377, Feb. 1976.
- [55] C. C. Zammit and P. A. R. Ade, "Zenith atmospheric attenuation measurements at millimetre and sub-millimetre wavelengths," *Nature*, vol. 293, pp. 550–552, Oct. 5, 1981.
- [56] C. C. Zammit, R. E. Hills, and R. W. Barker, "Atmospheric emission and attenuation in the range 100 to 600 GHz measured from a mountain site," *Int. J. Infrared Millimeter Waves*, vol. 3, pp. 189–203, 1982.
- [57] E. K. Smith, "Centimeter and millimeter wave attenuation and brightness temperature due to atmospheric oxygen and water vapor," *Radio Sci.*, vol. 17, pp. 1435–1464, Nov./Dec. 1982.
- [58] R. J. Hill, R. S. Lawrence, and J. T. Priestley, "Theoretical and computational aspects of the radio refractive index of water vapor," *Radio Sci.*, vol. 17, pp. 1251–1257, Sept./Oct. 1982.
- [59] G. D. Thayer, "An improved equation for the radio refractive index of air," *Radio Sci.*, vol. 9, pp. 803–807, Oct. 1974.
- [60] J. S. Owens, "Optical refractive index of air: Dependence on pressure, temperature, and composition," *Appl. Opt.*, vol. 6, pp. 51–58, 1967.
- [61] R. J. Hill, S. F. Clifford, and R. S. Lawrence, "Refractive-index and absorption fluctuations in the infrared caused by temperature, humidity, and pressure fluctuations," *J. Opt. Soc. Amer.*, vol. 70, pp. 1192–1205, 1980.
- [62] R. J. Hill and S. F. Clifford, "Contribution of water vapor monomer resonances to fluctuations of refraction and absorption for submillimeter through centimeter wavelengths," *Radio Sci.*, vol. 16, pp. 77–82, Jan./Feb. 1981.
- [63] A. J. Kemp, J. R. Birch, and M. N. Afsar, "The refractive index of water vapour: a comparison of measurement and theory," *Infrared Phys.*, vol. 18, pp. 827–833, 1978.
- [64] S. M. Rytov, *Introduction to Statistical Radiophysics*. Moscow, USSR: Nauka, 1966.
- [65] L. Chernov, *Wave Propagation in a Random Medium*. New York: Dover, 1967.
- [66] V. I. Tatarski, *Wave Propagation in a Turbulent Medium*. New York: McGraw-Hill, 1961.
- [67] R. L. Fante, "Electromagnetic beam propagation in turbulent media," *Proc. IEEE*, vol. 63, pp. 1669–1692, Dec. 1975.
- [68] R. S. Lawrence and J. W. Strohbehn, "A survey of clear-air propagation effects relevant to optical communications," *Proc. IEEE*, vol. 58, pp. 1523–1545, Oct. 1970.
- [69] H. B. Janes, M. C. Thompson, Jr., and D. Smith, "Tropospheric Noise in Microwave Range-Difference Measurements," *IEEE Trans. Antennas Propagat.*, vol. AP-21, pp. 256–260, Mar. 1973.
- [70] M. C. Thompson, Jr., L. E. Wood, H. B. Janes, and D. Smith, "Phase and Amplitude Scintillations in the 10–40 GHz band," *IEEE Trans. Antennas Propagat.*, vol. AP-23, pp. 792–797, Nov. 1975.
- [71] W. A. Flood, "Overview of near-millimeter wave propagation," *Proc. SPIE (Millimeter Optics)*, vol. 259, pp. 52–57, 1980.
- [72] R. W. McMillan, R. A. Bohlander, G. R. Ochs, R. J. Hill, and S. F. Clifford, "Millimeter wave atmospheric turbulence measurements: preliminary results and instrumentation for future measurements," *Opt. Eng.*, vol. 22, pp. 32–39, Jan./Feb. 1983.
- [73] J. T. Priestley and R. J. Hill, "Measuring high frequency humidity, temperature, and radio refractive index in the surface layer: Simultaneous observations with Lyman-alpha and near infrared hygrometers, a refractometer, and fine-wire thermometers," accepted for publication in *J. Atm. Ocean Technol.*, 1985.
- [74] S. F. Clifford, G. M. B. Bourcius, G. R. Ochs, and M. A. Ackley, "Phase variations in atmospheric optical propagation," *J. Opt. Soc. Amer.*, vol. 61, pp. 1279–1284, 1971.
- [75] S. F. Clifford and J. W. Strohbehn, "The theory of microwave line-of-sight propagation through a turbulent atmosphere," *IEEE Trans. Antennas Propagat.*, vol. AP-18, pp. 264–274, Mar. 1970.
- [76] S. F. Clifford and R. J. Tatatis, "Mutual coherence function for line-of-sight microwave propagation through atmospheric turbulence," *Radio Sci.*, accepted for publication, Jan. or Feb. 1985.
- [77] R. W. Lee and J. C. Harp, "Weak scattering in random media with applications to remote probing," *Proc. IEEE*, vol. 57, pp. 375–406, Apr. 1969.
- [78] S. F. Clifford, "Temporal-frequency spectra for a spherical wave propagating through atmospheric turbulence," *J. Opt. Soc. Amer.*, vol. 61, pp. 1285–1292, Oct. 1971.
- [79] R. S. Cole, K. L. Ho and M. D. Makrokooulakis, "The effect

- of the outer scale of turbulence and wavelength on scintillation fading at millimeter wavelengths," *IEEE Trans. Antennas Propagat.*, vol. AP-26, pp. 712-715, Sept. 1978.
- [78] R. A. Bohlander, R. W. McMillan, D. M. Guillery, R. H. Platt, R. J. Hill, S. F. Clifford, J. T. Priestley, R. E. Cupp, R. Olsen, B. E. Rishel, and R. Okrasinski, "Millimeter wave transmission fluctuations due to snow," to be published in *Proc. Snow Symp. IV*, U.S. Army Cold Regions Research and Engineering Laboratory, Hanover, NH, Aug. 1984.
  - [79] N. D. Mavroukoulakis, K. L. Ho, and R. S. Cole, "Temporal spectra of atmospheric amplitude scintillations at 110 GHz and 36 GHz," *IEEE Trans. Antennas Propagat.*, vol. AP-26, pp. 875-877, 1978.
  - [80] F. C. Medeiros Filho, D. A. R. Jayasuriya, and R. S. Cole, "Spectral density of amplitude scintillations on a 55 GHz line of sight link," *Electron. Lett.*, vol. 17, pp. 25-26, Jan. 8, 1981.
  - [81] F. C. Medeiros Filho, D. A. R. Jayasuriya, R. S. Cole, and C. G. Helms, "Spectral density of millimeter wave amplitude scintillations in an absorption region," *IEEE Trans. Antennas Propagat.*, vol. AP-31, pp. 672-676, July 1983.
  - [82] R. T. Ott and M. C. Thompson, Jr., "Atmospheric amplitude spectra in an absorption region," *IEEE Trans. Antennas Propagat.*, vol. AP-26, pp. 329-332, 1978.
  - [83] A. S. Gurvich, "Effect of absorption on the fluctuation in signal level during atmospheric propagation," *Radio Eng. Electron. Phys.*, vol. 13, no. 11, pp. 1687-1694, 1968.
  - [84] A. O. Izyumov, "Amplitude and phase fluctuations of a plane monochromatic submillimeter wave in a near-ground layer of moisture-containing turbulent air," *Radio Eng. Electron. Phys.*, vol. 13, no. 7, pp. 1009-1013, 1968.
  - [85] N. A. Armand, A. O. Izyumov, and A. V. Sokolov, "Fluctuations of submillimeter waves in a turbulent atmosphere," *Radio Eng. Electron. Phys.*, vol. 16, no. 10, pp. 1259-1266, 1971.
  - [86] M. B. Kanevskii, "The problem of the influence of absorption on amplitude fluctuations of submillimeter radio waves in the atmosphere," *Izv. VUZ. Radiofizika*, vol. 15, no. 12, pp. 1486-1487, 1972.
  - [87] F. C. Medeiros Filho, D. A. R. Jayasuriya, and R. S. Cole, "Probability distribution of amplitude scintillations on a line-of-sight link at 36 and 55 GHz," *Electron. Lett.*, vol. 17, pp. 393-394, June 11, 1981.
  - [88] G. A. Andreyev, V. A. Golunov, A. T. Ismailov, A. A. Parshikov, B. A. Rozanov, and A. A. Tanyigin, "Intensity and angle of arrival fluctuations of millimetric radiowaves in turbulent atmosphere," in *Proc. Anglo-Soviet Seminar on Atmospheric Propagation at Millimetre and Submillimetre Wavelengths* (Institute of Radioengineering and Electronics, Moscow, USSR, Nov. 28-Dec. 3, 1977).
  - [89] H. T. Yura, K. G. Barthel, and W. Buchtemann, "Rainfall-induced optical phase fluctuations in the atmosphere," *J. Opt. Soc. Amer.*, vol. 73, pp. 1574-1580, Nov. 1983.
  - [90] R. M. Manning, F. L. Merat, and P. C. Claspy, "Theoretical investigations of millimeter wave propagation through a clear atmosphere," *Proc. SPIE (Millimeter Wave Technology)*, vol. 337, pp. 67-80, 1982.

# MEASUREMENTS OF PHASE NOISE SPECTRA OF SELECTED MILLIMETER WAVE KLYSTRONS\*

53.4

G.W. Rosenberg\*\*, R.W. McMillan and V.T. Brady

Georgia Institute of Technology  
Engineering Experiment Station  
Atlanta, Georgia 30332

## Abstract

During a program whose objective is to measure millimeter wave atmospheric turbulence effects, the phase noise spectra of phase-locked klystron oscillators operating at 116, 140, and 173 GHz were measured. This paper describes the results obtained.

## Introduction

This paper describes the measurements of phase noise spectra of three Varian/Canada millimeter wave klystrons, phase-locked at frequencies of 116.3, 140 and 173 GHz. The phase-lock system is similar to that designed by Henry [1], and uses a discriminator for coarse frequency corrections and a phase-lock system for precise phase control.

## Description of Phase-Lock System

Figure 1 is a block diagram of the phase-lock system used for these measurements. A nominally 100 MHz reference oscillator is used to lock an X-band phase-locked solid state source with an output in the 8.0-8.5 GHz range. This signal acts as the local oscillator for a harmonic mixer which downconverts the klystron output to an intermediate frequency of 700 MHz. The amplified IF signal is split into two equal signals, one of which drives the discriminator resulting in an error signal output proportional to the frequency difference between the IF and a 700 MHz reference signal, and the other gives an error signal proportional to the phase difference between these two signals. The 100 MHz reference oscillator used in these experiments was a Hewlett-Packard 8640B tunable cavity oscillator which allows for tuning of the klystron output. For some of the measurements a Hewlett-Packard 105A quartz frequency standard together with a multiplying chain was used to generate the 100 MHz reference for comparison to the results obtained with the tunable oscillator.

## Results of Measurements

Measurements of phase noise were made on the 700 MHz IF signal by using a Systron Donner 0.01-18 GHz spectrum analyzer for the spectral range greater than 10 kHz from the carrier and a Hewlett-Packard 3580 audio spectrum analyzer to observe the near-carrier spectrum. For these latter measurements

the 700 MHz IF was downconverted to 30 kHz. In determining the phase noise, it is assumed that the AM noise of the klystron is small compared to the FM noise.

Figure 2 shows the phase noise spectrum of the 116.3 GHz klystron. The solid curve was measured by using the HP 105A reference and the dashed curve with the 8640B reference. The spectra of the 140 and 173 GHz sources were measured only with the 8640B and showed little difference from the corresponding 116.3 GHz spectrum. These spectra do not show spurs at 60 and 120 Hz due to the power line; these spurs are about 20 dB above the background level.

Figure 2 shows that the phase noise of the 116.3 GHz klystron locked to the 8640B is significantly better than one would expect by adding a factor  $20 \log N$  ( $N$  is the multiplication factor) to the published phase noise of the 8640B. Hewlett-Packard advises that this is because the oscillator has been significantly improved since the specifications were published, and that the specifications are very conservatively given. Locking the klystrons to a tunable oscillator provides significant advantages in source tunability and phase-locked modulation capability.

Photographs of the klystron spectra are shown in Figures 3 and 4 which show the broadband spectrum of the 173 GHz source and the near-carrier spectrum of the 116 GHz source, respectively. The slight asymmetry in the near-carrier spectrum is thought to be caused by a slight relative drift between the HP 105A and the audio spectrum analyzer local oscillator.

## Conclusions

The results of this paper show that it is possible to phase-lock millimeter wave klystrons so that spectral line widths are less than 1 Hz if a high quality reference source is used. Alternatively, the klystron may be locked to a tunable cavity oscillator to add tuning and frequency modulation capability, with slightly degraded near-carrier phase noise.



# A MILLIMETER WAVE RADIO FREQUENCY SYSTEM FOR ATMOSPHERIC TURBULENCE MEASUREMENTS\*

R.W. McMillan, V.T. Brady, G.W. Rosenberg\*\*,  
and G.F. Kirkman

Georgia Institute of Technology  
Engineering Experiment Station  
Atlanta, Georgia 30332

## Abstract

This paper describes a millimeter wave atmospheric transmission link operating at 116, 140 and 173 GHz designed to measure the mutual coherence function (MCF) for transmission through atmospheric turbulence. The transmitter and receiver local oscillator are phase-locked, and the receiver mixers are second harmonic types in the cross-guide configuration. The receiver uses double conversion, with intermediate frequencies of 930 and 30 MHz. A 30 MHz signal combining network uses phase shifters and video detectors to determine voltages proportional to the parameters required for determination of the MCF.

## Introduction

Atmospheric turbulence is known to have deleterious effects on the propagation of visible and near infrared radiation through the atmosphere. At longer wavelengths, one would not expect the effects to be as significant because of the dependence of the log amplitude variance of intensity fluctuations on  $\nu^{7/6}$  where  $\nu$  is frequency. At frequencies for which atmospheric moisture has a significant effect on propagation, however, the absolute humidity structure parameter  $C_Q^2$  as well as the temperature structure parameter  $C_T^2$  and their cross-correlation  $C_{TQ}^2$  contribute to the magnitude of the index of refraction structure parameter  $C_n^2$ , where for visible and near infrared radiation only  $C_n^2$  contributes [1]. These moisture contributions make millimeter wave turbulence effects significant, and fluctuations in intensity of 1-3 dB and angle-of-arrival of 300  $\mu$ rad peak over a 1 km path may be expected.

## Parameters Measured

The apparatus used to measure the effects of millimeter wave atmospheric turbulence consists of a transmitter separated from a four-receiver array by a distance of 1.3 km. The four receivers are separated by 1.4, 2.8, and 5.6 m, so that six possible pairs of receivers separated by distances varying from 1.4 to 10 m are used for the measurements [2].

To determine the MCF, consider the antenna pair shown in Figure 1.  $V_1$  and  $V_2$  are the voltages measured at each individual antenna. The phase shift  $\alpha_n$  takes on

sequential values of 0,  $\pi/2$ ,  $\pi$ , and  $3\pi/2$  and the voltage output of the receiver  $V_n$  corresponds to each of these values. Under these conditions, it is possible to show that  $V_n$  is given by [3]

$$|V_n|^2 = |V_1|^2 + |V_2|^2 + 2|V_1||V_2|\rho(r)\cos[\alpha_n - \beta(r)] \quad (1)$$

where the mutual coherence function for atmospheric propagation is given by

$$\text{MCF} = \rho(r)e^{i\beta(r)} \quad (2)$$

By varying  $\alpha_n$  through the indicated sequence, it is possible to solve for  $\rho(r)$  and  $\beta(r)$  as follows:

$$\beta(r) = \tan^{-1} \frac{|V_{90}|^2 - |V_{270}|^2}{|V_0|^2 - |V_{180}|^2} \quad (3)$$

$$[\rho(r)]^2 = \frac{(|V_0|^2 - |V_{180}|^2)^2 + (|V_{90}|^2 - |V_{270}|^2)^2}{16|V_1|^2|V_2|^2} \quad (4)$$

The millimeter wave radio frequency system is designed to measure the parameters  $V_n^2$  required for calculation of  $\rho(r)$  and  $\beta(r)$ .

## Millimeter Wave Link

The transmitter and receiver local oscillator are phase-locked to allow for a narrow receiver bandwidth and resulting improvement in signal-to-noise ratio. Klystrons locked to solid state X-band sources which were in turn locked to stable oscillators were used for both transmitter and receiver. Phase-locking is not necessary to determine the parameters of Equations (3) and (4) but was found necessary for calibration in addition to giving the improved noise performance indicated above.

The transmitted frequencies were 116, 140 and 173 GHz, and the receiver local oscillator frequencies were one-half of these values since X2 harmonic mixers were used. These mixers have conversion losses of about 20 dB in this cross-guide harmonic configuration. Double conversion has been used, with IFs of 930 and 30 MHz. Figure 2 is a block diagram of one channel of the receiver, showing the variable attenuator and phase shifter used for calibration.

Instead, a series of relay lenses, termed a lens beam waveguide [4], was chosen to distribute the LO signal, as illustrated in Fig. 3. Twenty-one lenses, 152 mm in diameter and made of high-density polyethylene were used, but the longest run between the klystron and a receiver involved fifteen. Corrugated conical horns couple the LO signal into and out of the beam waveguide and produce a beam with a Gaussian-shaped field profile [4].

The lenses have a curvature and spacing (737 mm) such that they are confocal [4]. The horn feeds were designed such that a beam waist occurs, for a frequency of 55 GHz, half way between the lenses as shown in Fig. 3. At a higher frequency, the feed pattern changes and the beam waist shifts, but at every odd numbered lens in a series, the beam returns to the size that couples efficiently to the output horns. Since all legs of the beam waveguide have an odd number of lenses, it works well over a wide frequency range.

The splitting of LO power between the paths to the various receivers is accomplished by stretched electroformed nickel meshes. Selections were made of meshes of different reflectance to balance the power to all receivers at crucial frequencies. It is calculated, from measured lens and mesh parameters that about ten percent of the klystron power launched into the beam waveguide is delivered to each receiver. Satisfactory mixer performance has been obtained with this system.

### Conclusion

The first field tests, described elsewhere in these proceedings [1], have demonstrated the success of the designs presented in this paper. A notable achievement is the lens beam waveguide LO distribution system with its wide frequency range.

**Acknowledgement:** This work was supported by the U.S. Army Research Office under Contract DAAG29-81-K-0173. The assistance of our research collaborators at the National Oceanic and Atmospheric Administration is gratefully acknowledged.

### References

- [1] R. A. Bohlander et al. and S. F. Clifford et al., these proceedings.
- [2] R. W. McMillan et al., these proceedings.
- [3] R.W.McMillan, R.A. Bohlander, G. R. Ochs, R. J. Hill, and S. F. Clifford, *Optical Engineering* 22, 32-39 (1983).
- [4] G. Goubau in *Millimetre and Submillimetre Waves*, F. A. Benson, ed., London: Iliffe Books (1969).

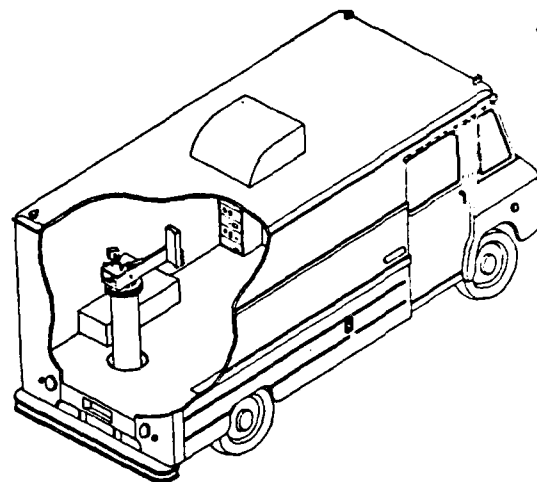


Fig. 1 Cutaway of transmitter van showing transmitting antenna mounted on a pedestal.

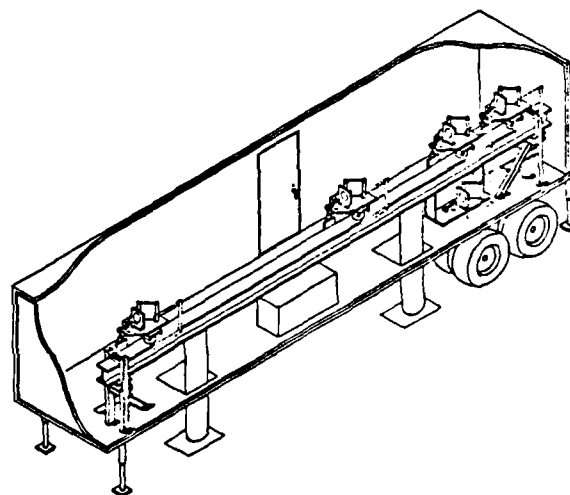


Fig. 2 Receiver array showing four antennas above the I-beam support and one below.

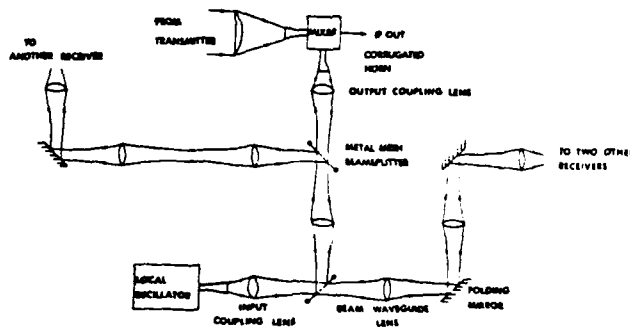


Fig. 3 A representative portion of the lens beam waveguide LO distribution system.

# A Quasi-Optical Millimeter Wave Transmitter and Receiver Array for Measurements of Angular Scintillation

W6..

R. A. Bohlander, V. T. Brady, A. McSweeney, G. F. Kirkman,  
J. M. Newton, A. Davis, and O. A. Simpson\*

Georgia Institute of Technology  
Engineering Experiment Station  
Atlanta, Georgia 30332

## Abstract

This system, used to measure the effects of atmospheric turbulence at frequencies between 116 and 173 GHz, comprises a front-fed, off-axis parabola transmitting antenna located 1.4 km from a receiver array. The five antennas in the latter receive local oscillator power from a phase-locked klystron source via a low-loss lens beam waveguide distribution system.

## Introduction

A key part in the Georgia Tech and National Oceanic and Atmospheric Administration study of millimeter wave atmospheric turbulence effects [1-3] has been the development of an appropriate antenna system. The equipment may be transported to sites of interest and has been used at a specially selected site [1] near Flatville, Illinois. The use of an array of receivers allows phase differences in the wavefront, and hence angle of arrival scintillation, to be measured. The method used is described elsewhere in these proceedings [1-2].

## Transmitter

Three objectives met in the design of the transmitter antenna are: (1) it fills the receiver array for propagation distances of 1 km or more; (2) it avoids overfilling the receiver array and has minimal sidelobes; and (3) it gives far field conditions at the receiver. A picture of the design solution is shown in Fig. 1.

The primary antenna is an off-axis, rectangular (610 X 152 mm) section of a paraboloid reflector. As a result of the unequal height and width, the antenna pattern is spread out horizontally and is narrow vertically, efficiently filling the receiver array which is 1.5 m in vertical extent and 10 m in horizontal. The mirror was copy-turned from solid aluminum.

The primary is front fed by an E-plane corrugated rectangular horn, without obscuration. The corrugations have been included to minimize sidelobes in the feed pattern, and further reduction is effected by application of an absorbing foam to the periphery of the mirror.

As shown in Fig. 1, the antenna is mounted on a pedestal which goes through the floor of the surrounding van, down to a concrete pad which provides stability in pointing the antenna. The van and antenna have been sited on a berm such that the transmitter is at the same height above the plain as the receiver array (namely 3.5m).

## Receiver Array

Each receiving antenna in the array comprises a conical corrugated horn feed, a 305 mm diameter polyethylene lens and a large, optical quality diagonal mirror for beam steering, as may be seen in Fig. 2. All are mounted on a large I-beam that rests on two pillars anchored to concrete ground pads for stability and isolation from the surrounding semi-trailer van.

The array may be termed non-redundant, since any combination of two antennas, gives a unique spacing for which the relative phases of the signals can be measured. The six intervals in the horizontal direction are 1.43, 2.86, 4.29, 5.71, 8.57 and 10 meters, intervals that are not only unique, but nearly uniformly distributed. Preliminary results [1] indicate transverse coherence lengths in the propagated radiation that are within the dimensions of the array. Thus the array size is well matched to the measurement requirement. One antenna shown in Fig. 2 is 1.43 m below the horizontal row of antennas. This allows differences in vertical and horizontal scintillation to be measured.

## Lens Beam Waveguide LO Distribution

Provided that all receivers use the same LO, it is possible to measure meaningful phase differences. The mixers in the receivers are of the harmonic type so the LO frequencies are in the range 58 to 87 GHz. The LO sources are klystrons with available powers of a few hundred milliwatts. The waveguide size used for LO components throughout this range is WR-12.

The combination of the limited power available and the large array size over which the LO signal must be distributed makes it important to have high efficiency in the LO transmission medium. However, the losses in long runs of WR-12 waveguide may be shown to be too high.

\*Present address: Emory University  
Department of Physics Atlanta, Georgia 30322

clude that the system is capable of imaging over the seven-element area used.

A calculation of the receptor spacing required for diffraction-limited resolution yields a value of 3.0 mm. We feel that we can decrease our spacing to maybe 5 mm without affecting the beam patterns, and thus get within a factor of less than two from diffraction-limited resolution. It should be observed that the LTSA samples the image considerably more efficiently than any wave-guide-type feed, or a broad-side planar antenna, since these are all basically aperture antennas, whereas the LTSA achieves its narrow beam primarily due to a traveling-wave mechanism. The conical horn which matches our Cassegrain reflector, for example, could not be stacked closer than 14 mm. A comparison of realizable feed patterns for multi-beam antennas was recently published by Rahmat-Samii et al. [7]. This paper assumes a beam-shape which is proportional to  $(\cos \theta)^q$ , and estimates the value of  $q$  for arrays of feed elements, and different element spacings. We have replotted their data in Figure 7, and included our own measured data for the LTSA array, and this graph clearly shows the superiority of the LTSA in terms of ability to be stacked closely.

Another demonstration of the capabilities of the imaging system was carried out by constructing a 2x2 array of LTSA's on two parallel substrates. A program was written for the HP-85, which enabled the system to track the source. If deliberately pointed off the source, the system was able to correct its pointing and return to the target within one step of the stepping motors, an angular distance of 0.06 degrees.

#### Acknowledgements

We gratefully acknowledge support for the near millimeter imaging program at the University of Massachusetts from the NASA Langley Research Center, Hampton, Virginia, on grant NAS 1-279. We also appreciate the assistance of Peter Sullivan and Doug Bezio in carrying out the experiments.

#### References

- [1] J. W. Goodman, "Introduction to Fourier Optics", McGraw-Hill, New York (1968).
- [2] Rutledge, D.B., Neikirk, D.P., and Kasilingam, D.P., "Infrared and Millimeter Waves" (K.J. Button, ed.), Vol. 10, Academic Press, New York (1983).
- [3] Parrish, P.T., et al. SPIE Proc. Millimeter Wave Technology, 337, 49-52 (1982).
- [4] Kollberg, E.L., Thungren, T., and Yngvesson, K.S., 6th Int. Conf. Infr. Millimeter Waves (1981).
- [5] Thungren, T., Kollberg, E.L., and Yngvesson, K.S., 12th Eur. Microw. Conf., Helsinki, 1982 (p. 361).
- [6] Yngvesson, K.S. et al., SPIE Proc. Millimeter Wave Technology, Vol. 337 (1982) (p. 42-48).
- [7] Rahmat-Samii, Y., Cramer, P. Jr., Woo, K., and Lee, S.W., IEEE Trans. Antennas Propag. AP-29, 961 (1981).

Conical horns  
restrict to 14 mm resol.  
2x worse

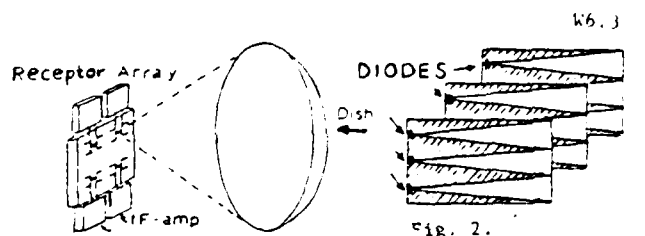


Fig. 1. A typical near millimeter imaging system

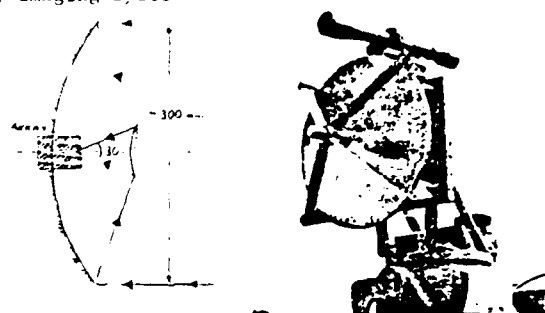


Fig. 3. Optics of the Cassegrain imaging system.

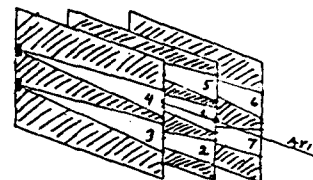


Fig. 4. The seven-element LTSA array implemented for the imaging system. The receptors have been numbered starting at the center. Receptor vertical spacing and spacing between substrates are both 7.9 mm.

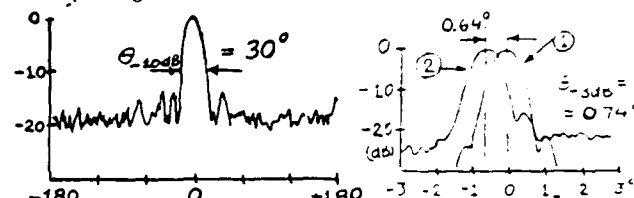


Fig. 5. H-plane pattern for receptor #1 (see Fig. 4). E-plane pattern is similar using receptors #1 and #2 with  $\theta_{-10dB} = 24.2^\circ$ .

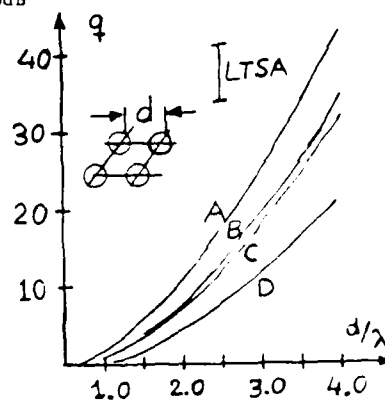


Fig. 7. Plot of  $q$  versus normalized spacing of array-elements. A=Circ antenna; B=Rect. Wave.; C=Circ Wave.; D=pyram. horn [7].

**Observations of Amplitude and Angle of Arrival Scintillation in  
Millimeter Wave Propagation Caused by Turbulence in Clear Air Near the Ground**

R. A. Bohlander, R. W. McMillan, V. T. Brady, G. F. Kirkman,  
M. J. Sinclair, J. W. Larsen, M. L. Blyler, R. P. Lilly, and D. O. Gallentine

Georgia Institute of Technology  
Engineering Experiment Station  
Atlanta, Georgia 30332

S. F. Clifford, J. T. Priestley, R. J. Hill, R. E. Cupp, N. L. Abshire,  
R. B. Fritz, W. Cartwright, G. R. Ochs, R. J. Latatis, J. J. Wilson, and G. M. Walford

National Oceanic and Atmospheric Administration  
ERL/Wave Propagation Laboratory  
Boulder, Colorado 80303

**Abstract**

Observations were conducted over uniform, exceptionally flat farm land in Illinois during clear weather in July, 1983. Scintillation data were obtained at 116.30 and 172.91 GHz for a path 1.4 km long. Rigorous micrometeorological measurements, some of them path averaging, were made along the path. The results of these tests will be described.

**Introduction**

A recently started systematic study of the effects of atmospheric turbulence on millimeter wave propagation will be described here. In the frequency range covered, there have been few previous studies [1] and little if any attention has been given to angular scintillation. The present study includes observations of both amplitude and angular scintillation, measurements of micrometeorological parameters and near infrared wavelength scintillation, and improvements in the theoretical description of millimeter wave scintillation. The millimeter wave regime is interesting because the wavelengths are similar in size to the smallest eddy sizes in the atmosphere, and secondly because transmission can be studied in relatively clear regions of the spectrum as well as in regions of resonant absorption by oxygen and water molecules. In general, millimeter wave turbulence effects differ from those at shorter wavelengths by depending significantly on the microstructure of water vapor in the atmosphere.

**Observation Site**

The propagation path, near Flatville, Illinois, is 1.4 km long and crosses uniform soybean vegetation on ground that is exceptionally flat (one foot or less height variation). The path is about 3.5 m above the ground. There are no raised objects to disturb the wind for at least 400 m on either side of the path, with the exception of the meteorological instruments which are placed to the lee of the propagation path for the prevailing west winds. This exceptionally uniform environment makes theoretical descriptions of the experiment tractable. The site also offers a full range of temperate zone weather for further research.

**Meteorological Facilities**

The overall layout is shown in Fig. 1. Both *in situ* and path averaging meteorological instrumentation (listed in Table 1) has been provided. Data collection is coordinated through two stations located at 400 and 800 m from the receiver van. Near each, a rotatable tower places most of the *in situ* instruments at the same height as the propagation path. It is emphasized that fluctuations of humidity, temperature, and wind velocity can be measured in small volumes and at speeds of at least 100 samples/sec. The path-averaging optical  $C_n^2$  and cross-wind instrumentation [3] is a near infrared scintillometer that provides a measure of the atmospheric temperature (or density) structure and mean crosswind speed. The laser rain gauge [4] will be used in later phases of the research. Presently 32 channels of meteorological data are logged (along with 28 channels of millimeter wave data) on a central computer in the receiver van. Communication from the meteorological stations is via a special purpose buried fiber optic data link.

**Millimeter Wave Facilities**

These consist of klystron transmitters directed over the propagation path to a receiver array with nonredundant antenna separations ranging from 1.4 to 10 m. The transmitter and receiver are separately phase-locked for low noise. A signal combining network facilitates interferometric measurements from which both amplitude and relative phase (or angular) scintillation can be determined. Details are given elsewhere [5, 6].

**Results**

The first measurement series was conducted during a period July 12-20, 1983 when there was clear, mostly sunny weather every day. A second measurement series planned for Nov.-Dec. should also have been carried out by conference time.

The analysis of the data is now at a preliminary stage. Data for midday periods, when convective turbulence was well-developed, show typical amplitude standard deviations of about 9 percent at 116.30 GHz and 11 percent at 172.91 GHz. These were determined under approximately the same conditions of temperature and humidity fluctuations and show the expected dependence on electromagnetic frequency [1]. Near midnight, when the atmosphere is

exceptionally stable, fluctuations as much as thirty times smaller were seen, demonstrating the low noise qualities of the instrumentation.

Typical midday, relative-phase standard deviations for the minimum antenna spacing (1.43 m) were .175 and .20 radians, respectively for the above frequencies. These correspond to apparent angle-of-arrival standard deviations of about 50  $\mu$ rad. The variance of relative phase increases with antenna separation to the 5/3 power in accord with the Kolmogorov model of turbulence [2, 7] for small antenna spacings, and increases less rapidly at larger spacings in a way attributable to the effects of the outer scale of turbulence [7].

At similar times, the path-average millimeter wave structure parameter  $C_n^2$  may be determined to be  $2 \times 10^{-12} \text{ m}^{-2/3}$ , much larger than the infrared value  $8 \times 10^{-14} \text{ m}^{-2/3}$ . This is not unexpected due to the effects of water vapor, but the calculations necessary to make a quantitative comparison with theory [8] remain to be carried through.

#### Conclusions -Future Work

An experimental program has begun that promises to yield a wealth of information on millimeter wave turbulence effects. In turn, it is foreseen that millimeter waves can be developed as a probe of meteorological fluctuations that will complement infrared probes. In the near future it is planned to add new frequencies and to study precipitation and fog effects.

**Acknowledgments:** The work reported has been supported by the U.S. Army Research Office under Contract DAAG29-81-K-0173 and Grant ARO 21-82, and by the National Oceanic and Atmospheric Administration. The authors thank Mr. Leon Harms and his colleagues for providing the place for the measurements, and Mr. John Vogel of the Illinois State Water Survey for assistance with the site and for providing weighing bucket rain gauges.

#### References

- [1] R. W. McMillan, R. A. Bohlander, G. R. Ochs, R.J. Hill and S. F. Clifford, *Optical Engineering* **22**, 32 (1983).
- [2] R. L. Fante, *Proc. IEEE* **63**, 1669 (1975).
- [3] Ting-i Wang, G.R. Ochs and S.F. Clifford, *J. Opt. Soc. Am.* **68**, 334 (1978).
- [4] Ting-i Wang & S. F. Clifford, *J. Opt. Soc. Am.* **47**, 927 (1975) and *J. Appl. Meteor.* **21** 1747 (1982)
- [5] R. W. McMillan et al., these proceedings.
- [6] R. A. Bohlander, V. T. Brady et al., these proceedings.
- [7] S. F. Clifford, G. M. B. Bouricius, G. R. Ochs, M. H. Ackley, *J. Opt. Soc. Am.* **61**, (1971).
- [8] R. J. Hill and S. F. Clifford, *Radio Science* **16**, 77 (1981).

Table 1. Meteorological Instruments

#### In Situ

Lyman alpha humidity gauges  
Fine wire temperature probes  
Three-axis sonic anemometers  
Wet and dry bulb psychrometers  
Vaisalla humidity gauges  
Barometer  
Propeller anemometer  
Wind vane  
Pyronometer  
Weighing bucket raingauges

#### Path Averaging

Optical  $C_n^2$   
Optical crosswind  
Optical rain gauge  
Optical distrometer

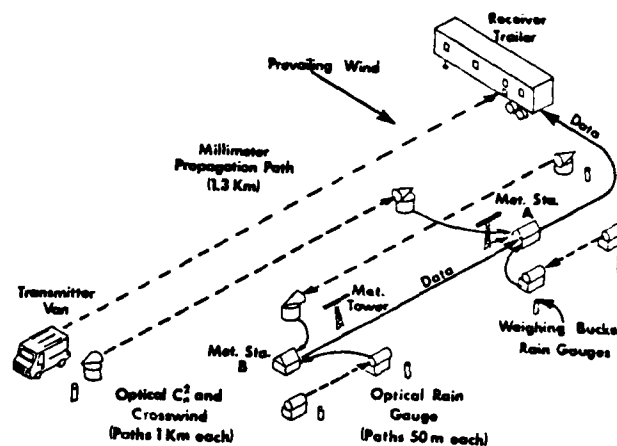


Fig.1 Layout of Millimeter Wave scintillation experiment and associated meteorological instrumentation.

TH6.5

FIELD ATTENUATION MEASUREMENTS AT 0.89 mm

TH6.5  
TH6.6

A.J. Gasiewski, F.L. Merat, Case Western Reserve University,  
Cleveland, OHIO 44106.

Field measurements of clear atmosphere attenuation have been made at a wavelength of 0.89 mm, using an optically pumped far infrared laser as a source. Absolute measurements of attenuation indicated 4 to 14 dB/km above values calculated by absorption line compilations. Attenuation sensitivity measurements yielded values 1.5 to 2.0 times greater than the slopes predicted by monomer theory. Reasonable agreement is obtained with previously measured data by Tanton and by Ryadov and Furashov.

TH6.6

SPECKLE PHENOMENA AT 10 um WAVELENGTH

D.L. Jordan, R.C. Hollins, and E. Jakeman  
Royal Signals and Radar Establishment  
St. Andrews Road  
Great Malvern  
Worcestershire WR14 3PS  
United Kingdom

Scattering of radar and infra-red waves is strongly influenced by the multi-scale (fractal) nature of naturally-occurring surfaces. Measurements using CO<sub>2</sub> laser radiation illustrate striking differences between scattering by fractal and smoothly-varying surfaces. The influence of speckle in coherent laser radar will be discussed.

Zero crossing  
vs. frequency

F-3-2

1984 IR & MM WAVES. TAKARAZUKA

# MILLIMETER WAVE ATMOSPHERIC TURBULENCE MEASUREMENTS\*

Look at frequency  
as function of  
MMW frequency

R. W. McMillan, R. A. Bohlander, D. M. Guillory,  
R. H. Platt, and J. M. Cotton, Jr.

Georgia Institute of Technology  
Engineering Experiment Station  
Atlanta, Georgia 30332 USA

S. P. Clifford, J. T. Priestley, R. J. Hill,  
and R. E. Cupp

National Oceanic and Atmospheric Administration  
Wave Propagation Laboratory  
Boulder, Colorado 80303 USA



## 1.0 Introduction

This paper describes measurements of millimeter wave atmospheric turbulence effects made jointly by Georgia Tech and NOAA at a site near Champaign-Urbana Illinois, chosen for its exceptional flatness and absence of trees, hills or other obstructions which might perturb the atmospheric fields. The measurements were made at frequencies of 116.3, 118.75, 120.75, 142.00, and 173.00 GHz; and under atmospheric conditions of clear air, rain, fog, and snow. The millimeter wave measurements were supported by extensive meteorological instrumentation.

## 2.0 Approach

The turbulence measurement system consists of transmitter and receiver systems separated by a distance of 1.4 km traversing a field planted in soybeans in summer and covered by stubble in other seasons. The transmitter is a phase-locked klystron oscillator feeding an offset paraboloid antenna. The receiver is a 5-element array consisting of 4 elements with non-redundant spacing in the horizontal plane with a 5th element placed immediately below one of the horizontal elements. Each of these array elements is a superheterodyne receiver, and all are pumped by a common phase-locked klystron local oscillator which is distributed to the individual receivers by a beam-waveguide system. This arrangement provides means for measuring both amplitude and phase fluctuations, thus leading to a good approximation for the MMW atmospheric mutual coherence function. This measurement system has been described in more detail elsewhere [1,2,3].

## 3.0 Results of Clear Air Measurements

We have found that the largest fluctuations in both intensity and phase occur under clear air summertime conditions during which the atmosphere is hot and humid. Fluctuations are

especially large when the sun comes out after a rainfall, or when the soybeans are large enough to give up large amounts of water vapor by transpiration. Figure 1 is a copy of a chart recorder trace showing intensity fluctuations of a 142 GHz signal measured on a clear morning after a light rainfall (~3mm) occurred the night before. Figure 2 shows the corresponding phase fluctuations measured between the pair of antennas with a spacing of 10m. Large fluctuations of this nature were common in the summer but did not occur in the winter despite the fact that winter weather was generally more violent. Smaller wintertime variations are ascribed to much lower absolute humidity.

## 4.0 Rain, Fog, and Snow Results

Some of the more interesting results have been observed during rainfall. The MMW attenuation generally closely follows the variations of the path-averaging rain gauge except for the fact that immediately after the rain, the received signal remains lower than at the beginning, presumably because the humidity remains high. These effects are illustrated by the chart recorder traces shown in Figure 3, which show receiver channels 1 and 2 measured at 173 GHz during a heavy rain. Because of its proximity to the strong water vapor absorption at 183 GHz, this frequency is especially sensitive to higher absolute humidity. There is some indication also from preliminary studies of the data that the fluctuation spectrum contains higher frequency fluctuations during precipitation events as expected [4].

A very interesting phenomenon occurs in heavy fog. Figure 4 shows chart recorder traces made at 142 GHz during a fog for which the visibility was estimated to be 200 m. Note the extreme quietness of the traces. Measurements of phase fluctuations made during this fog showed a similar quietness.

A series of measurements at 116 GHz was made during a snowstorm that lasted intermittently for two days and left an accumulation of about 30 cm on the ground. Weather during this storm was fairly violent, with winds gusting to 20 m/s and with accompanying ground blizzards. As stated earlier, the intensity fluctuations are smaller for this case than for the summertime conditions represented by Figure 1.

### 5.0 Conclusions

We have made measurements of MMW turbulence effects at several frequencies of interest under widely varying atmospheric conditions. These measurements are supported by extensive meteorological instrumentation. It is concluded that turbulence effects are more pronounced under hot, humid summertime conditions. Fluctuations measured in winter are smaller because of lower absolute humidity.

### References

1. R. W. McMillan, R. A. Bohlander, G. R. Ochs, R. J. Hill, and S. P. Clifford, *Optical Engineering* 22, 32, (1983).
  2. R. A. Bohlander, et al., Eighth Int. Conf. on Infrared and Millimeter Waves, Miami Beach, FL, (1983).
  3. McMillan, et al. *ibid.*
  4. H. T. Yura, K. G. Barthel and W. Buchtemann, *J. Opt. Soc. Am.*, 73, 11, P.1574, (Nov. 1983).
- \* This work is supported by the U.S. Army Research Office under Contract DAAG29-81-K-0173.

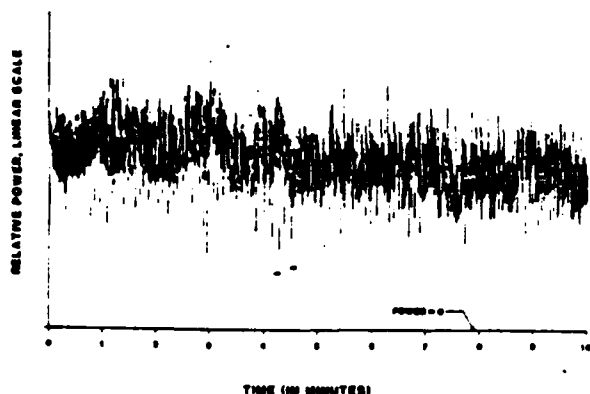


Figure 1. Intensity fluctuations of a 142 GHz signal measured on a hot, humid day.

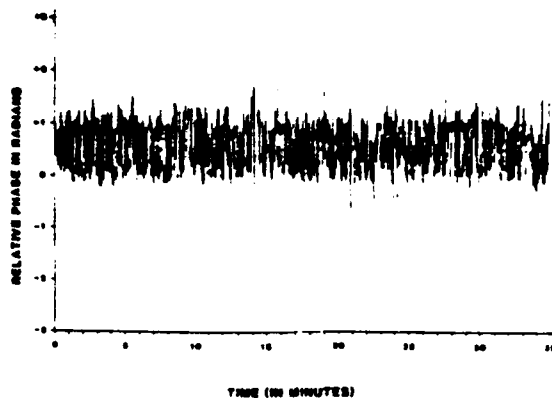


Figure 2. Phase fluctuations measured under the same conditions as Figure 1.

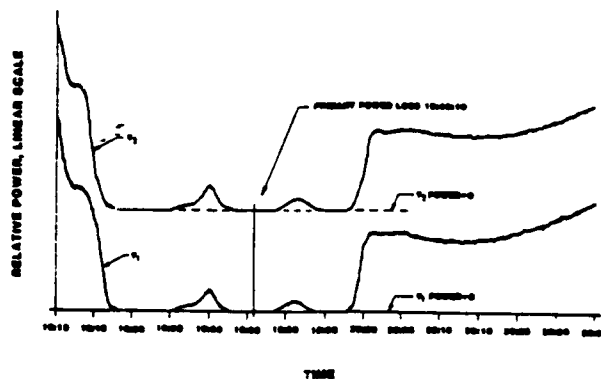


Figure 3. Intensity changes measured at 173 GHz during a heavy rain.

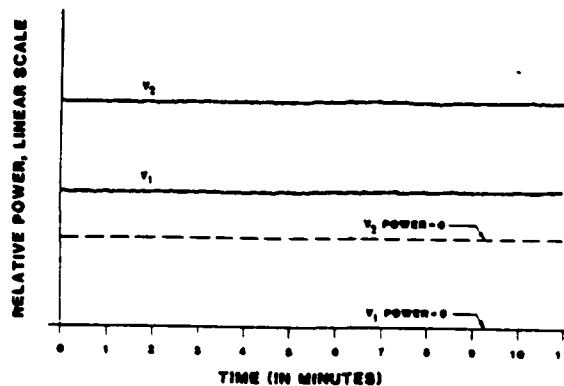


Figure 4. Intensity fluctuations measured during a heavy fog at 142 GHz.

# MILLIMETER WAVE TRANSMISSION FLUCTUATIONS DUE TO SNOW

R. A. Bohlander      Georgia Institute of Technology  
R. W. McMillan      Engineering Experiment Station  
D. M. Guillory      Atlanta, GA 30332  
R. H. Platt

R. J. Hill            National Oceanic and Atmospheric  
S. F. Clifford      Administration  
J. T. Priestley      Wave Propagation Laboratory  
R. E. Cupp           Boulder, CO 80303

R. Olsen            U.S. Army Atmospheric Sciences Laboratory  
White Sands Missile Range, NM 88002

B. E. Rishel        Physical Sciences Laboratory  
R. Okrasinski      New Mexico State University  
Las Cruces, NM 88001

## ABSTRACT

Measurements were made of the effects of falling snow on millimeter wave transmission during November and December 1983 and February 1984 at a specially selected and instrumented site in Illinois. These show intensity fluctuations as well as angle-of-arrival fluctuations for frequencies of 116 and 173 GHz. Transmitter and receiver sub-systems are separated by a distance of 1.4 km over exceptionally flat terrain. Detailed meteorological measurements have been made of normal variables, micrometeorological quantities and particulate parameters. Analyses of results during snow are compared with results when the fluctuations are due only to turbulence in clear air.

## INTRODUCTION

For a full picture of the limitations imposed by the atmosphere on millimeter wave

system performance, it is necessary to have an understanding of the fluctuations caused by turbulence and by hydrometeorite turbidity. The work which will be reported here is part of a systematic study of fluctuations in both intensity and angle of arrival in the frequency range 116-173 GHz and in a wide variety of weather conditions in all seasons of the year. At these frequencies, which are high in the millimeter band, high precision tracking or image formation may be achievable with antennas of moderate size, and thus it is particularly of interest to know whether fluctuations in angle of arrival may show up as significant. There have been few studies which have addressed this question previously [1,2], and generally in these, characterization of meteorological parameters has been scant. In the present study an effort has been made to measure not only the standard meteorological parameters but also ones which characterize the turbulence and particulates

present in a propagation path. For comparison and additional information about atmospheric conditions, infrared scintillation has also been measured. In clear air, the millimeter wave regime is interesting because the wavelengths are similar in size to the smallest turbulent eddy sizes in the atmosphere, and secondly because transmission can be studied in relatively clear regions of the spectrum as well as near regions of resonant absorption by oxygen and water molecules. Turbulence effects on millimeter wave signals are distinguished from those at visible or near infrared wavelengths by the strong dependence on the refractivity and density microstructure of water vapor in the atmosphere.

Although clear air problems are of considerable interest, it is recognized that the development of millimeter wave systems is presently motivated largely by their capabilities in adverse weather. Therefore, it is essential also to cover turbidity effects in a comprehensive study, and among these are the important effects of falling snow. Wintertime measurements have been conducted in the periods November 11 to December 6, 1983 and February 11 to March 6, 1984 at a specially selected site in Illinois which will be described below. During this time, a number of snow fall measurements were obtained as well as data on clear air, fog and rain. Due to the considerable quantity of data recorded to date in the program, there has been time to take only a very preliminary look at the results. The objectives of the present paper then are to acquaint the reader with the measurement techniques employed and to show how the level of fluctuations caused by snow fall compares with levels in other types of winter weather and with clear air turbulence in the summer.

#### OBSERVATION SITE

The site of the measurements near Champaign-Urbana, Illinois

was chosen for its exceptional flatness and general absence of trees, hills or other obstructions. The propagation path is 1.374 km long and crosses a field which is entirely planted in soybeans in the summer and has stuble on otherwise bare ground in the winter. The height of the propagation path above ground is 3.5 meters with a variation of about 0.3 meters. There are no raised objects to disturb the wind for 400 meters or more on either side of the propagation path except meteorological towers which are placed in the lee of the path for the prevailing west winds. There are farm buildings near the ends of the path, and on those occasions when the wind is out of northerly or southerly directions, some inhomogeneity over the path can be seen. The exceptionally uniform conditions usually found, however, are essential to make possible comparisons with theoretical models of fluctuation phenomena. The overall layout of experimental apparatus is diagrammed in Fig. 1 and shown in an aerial photograph in Fig. 2.

#### METEOROLOGICAL FACILITIES

Both *in situ* and path averaging types of meteorological instrumentation are utilized at this site, as listed in Table 1. Two data collection stations have been located by NOAA at sites near the propagation path and 400 and 800 meters from the receiver van. These are connected by a fiber optic link to a computer network that records 32-39 channels of meteorological data as well as the data from 28 channels of millimeter wavelength signals. A third station emphasizing particle measurements was erected by ASL near the receiver trailer during each field test in 1984. Data from this instrumentation has been logged independently and only rough time synchronization has been required.

All of the key *in situ* instruments have been placed on towers, such as the one pictured in Fig. 3, at the same height

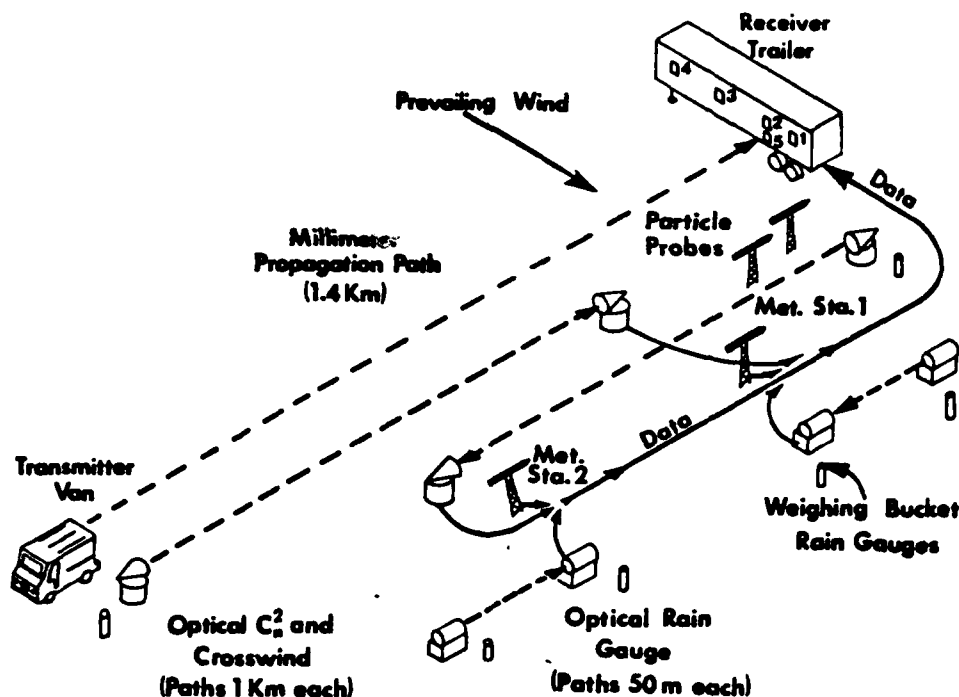


Fig. 1 Instrument Layout

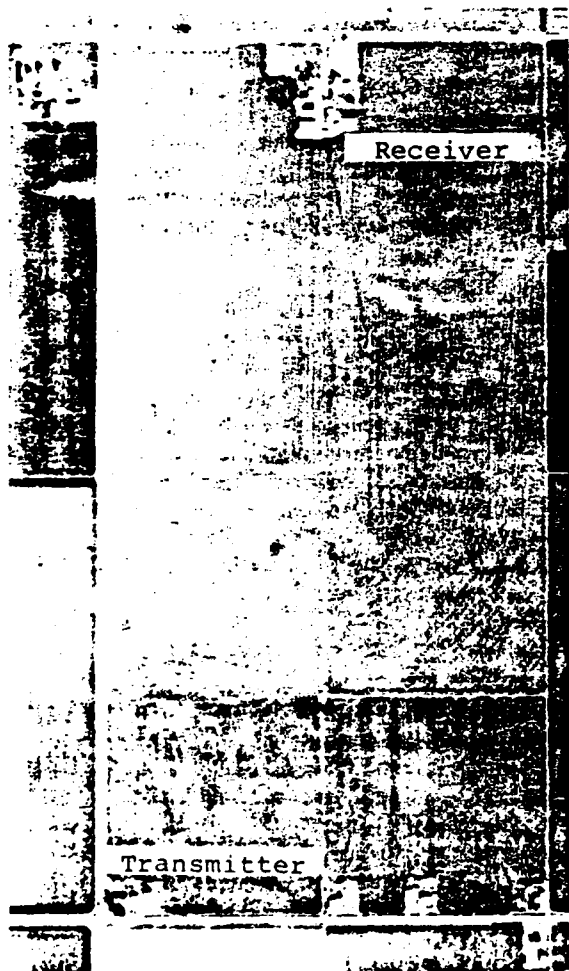


Fig. 2 Aerial View of Site

Table 1.

#### Meteorological Instruments

##### In Situ

Lyman alpha humidity gauges  
 Fine wire temperature probes  
 Three-axis sonic anemometers  
 Wet and dry bulb psychrometers  
 Vaisalla humidity gauges  
 Barometer  
 Propeller anemometer  
 Wind Vane  
 Pyronometer  
 Weighing bucket raingauges  
 Particle Scattering probes  
 (PMS-GBPP and Glassical Scattering)  
 Particle Shadowgraph probes  
 (PMS 2D Optical Ray Spectrometer Probes, OAP-2D-P,C)  
 Visiometer (EG&G type 207 forward scatter meter)

##### Path Averaging

Optical  $C_n^2$   
 Optical crosswind  
 Optical rainauge  
 Optical disdrometer

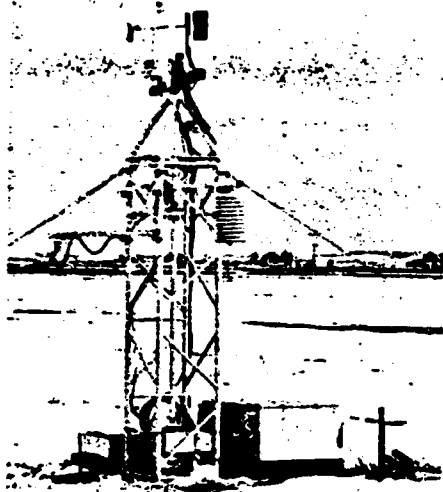


Figure 3. Meteorological Tower

above ground as the propagating millimeter wavelength beam. Those probes which must be oriented in a particular way with respect to the wind are mounted on rotatable booms or stands. Fluctuations of temperature, humidity and wind velocity can be measured in small volumes of air at rates of 25-100 times per second and can be used to derive the microstructure of clear air. The temperature probes are positioned in the same small volumes as those sensed by the high speed humidity and wind probes, and thus important cross-correlations of temperature with these quantities can be derived. Unfortunately, during precipitation occurrences, the high speed humidity and temperature gauges must be disabled for their protection. Precipitation and other particulate counts and spectra are obtained from probes that monitor scattered light in small volumes [3], from shadowgraphs [3] and from path-averaging laser rain gauges [4]. Results from the scattering probes can be obtained as often as once every second. This may make it possible in future investigations to derive a rough microstructure of particulates.

Although precautions have been taken to obtain a homogeneous path which can be characterized by a relatively small number of meteorological stations, it is important to be able to check on the relationship of these sites to conditions over long paths. The path averaging instrumentation shown in Fig. 1 affords opportunities for such comparisons. In addition to the laser rain monitors mentioned above, near infrared scintillometers have been configured as path-averaging optical  $C_n^2$  and cross-wind systems [5]. They provide an alternative measure of the atmospheric temperature (or density) structure and mean cross-wind speed.

#### MILLIMETER WAVE FACILITIES

The transmitter and receiver subsystems were housed in vans so that they could be built and tested at Georgia Tech and then transported to the selected site. Once there, semi-permanent installations were made at concrete placements which gave optically stable configurations of the antennas. The reader may refer to [6-9] for further details.

##### Transmitter

The transmitter comprises a phase-locked klystron tube feeding a specially designed antenna. Several tubes have been obtained in order to conduct measurements at frequencies of 116.3, 118.75, 120.75, 142 and 173 GHz. There is no provision for simultaneous measurements at multiple frequencies, and at least half a day is required to change the frequency of the overall system. Comparisons of results at different frequencies have been possible, given the availability of detailed meteorological data through which similar atmospheric conditions can be identified. However, some types of weather have been sufficiently infrequent that, for example, different types of snow have been seen at the various klystron frequencies.

The transmitter antenna is an off-axis rectangular section (610

x 152 mm) of a paraboloid reflector, front-fed by an E-plane corrugated rectangular horn. The shape of the antenna causes the millimeter wave beam to be spread out horizontally and to be narrow vertically. This efficiently fills the receiver array which is 10 meters in horizontal extent and 1.43 meters in vertical. Low side-lobe levels have been achieved by the use of corrugations in the feed and absorbing material on the periphery of the large reflector. A fixed horizontal (E-plane) polarization is transmitted for compatibility with the receiver where there was a slight design preference for this polarization. Consideration is currently being given to the addition of polarization versatility through the use of optical waveplates for future measurements. This would enable measurements to be made of differences in the millimeter wave fluctuations for a few types of polarization, differences which might be expected particularly during falling snow.

As shown in Fig. 4, the antenna is mounted on a pedestal which goes through the floor of

the surrounding van, down to a concrete pad which provides stability in pointing the antenna. Not shown are the boresighted gunsight and He Ne laser used for initial aiming, nor the high density polyethylene window on the rear of the van through which transmissions are normally made.

#### Receiver Array

Since it is desired to measure not only intensity fluctuations but also fluctuations in angle of arrival, it is necessary to employ an array of receiver antennas. Then by measuring the fluctuating relative phase of signals from the antennas, angle of arrival variations can be determined.

Each antenna in the array is a 305 mm diameter high density polyethylene lens fed by a conical corrugated horn. Beam widths in the frequency range covered are between 7 and 10 mrad. The aim point of the antennas is steered by large optical quality diagonal mirrors, and stable pointing is achieved by the support structure that comprises a large I-beam

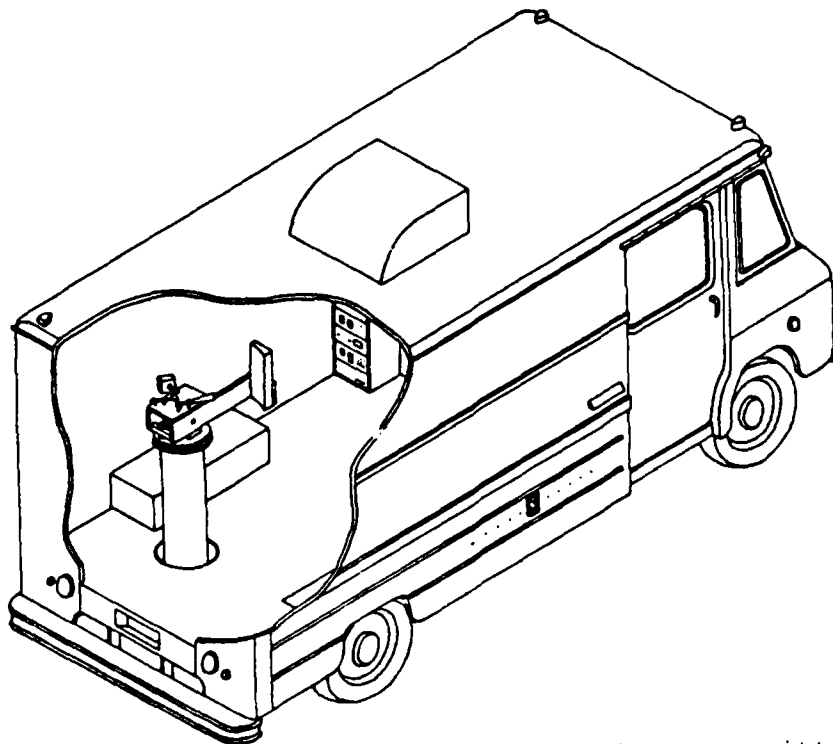


Figure 4. Transmitter Van

resting on two pillars anchored to concrete pads, as illustrated in Fig. 5. Alignment with the transmitter was achieved in two steps. First, each polyethylene lens was replaced with a smaller clear lens of the same focal length and a preliminary visual alignment made. Then the polyethylene lenses were replaced and the millimeter wave signal levels maximized.

The array may be termed nonredundant, since any pair of antennas has a unique spacing for which the relative phase of signals can be measured. The six intervals in the horizontal direction are 1.43, 2.86, 4.29, 5.71, 8.57 and 10 meters, intervals which are also nearly uniformly distributed. Results have shown that these array dimensions span the range of transverse coherence lengths observed in conditions of moderate to strong turbulence. As may be seen in Fig. 5, one antenna is located 1.43 meters below the others and has been used to make a limited number of measurements of vertical angle of arrival fluctuations for comparison with the more detailed study of horizontal fluctuations.

#### Lens Beam Waveguide LO Distribution

Phase measurements are accomplished with superheterodyne receivers at each antenna which share a common local oscillator signal. Post-mixer signal processing will be described in a later section. The mixers used are of the harmonic type and klystrons at half the frequency of the transmitter produce the local oscillator signals. The combination of the limited power available and the large array size over which the LO must be distributed makes a high efficiency distribution system essential. Losses in long runs of conventional waveguide may be shown to be too high.

Instead, a series of relay lenses, termed a lens beam waveguide [10], was chosen to distribute the LO. Corrugated conical horns couple the LO into and out of the beam waveguide and produce a beam with a Gaussian-shaped field profile. The run between the source and the most distant antenna involves fifteen lenses, and along such a run, electroformed mesh beamsplitters split off LO power for intermediate antennas.

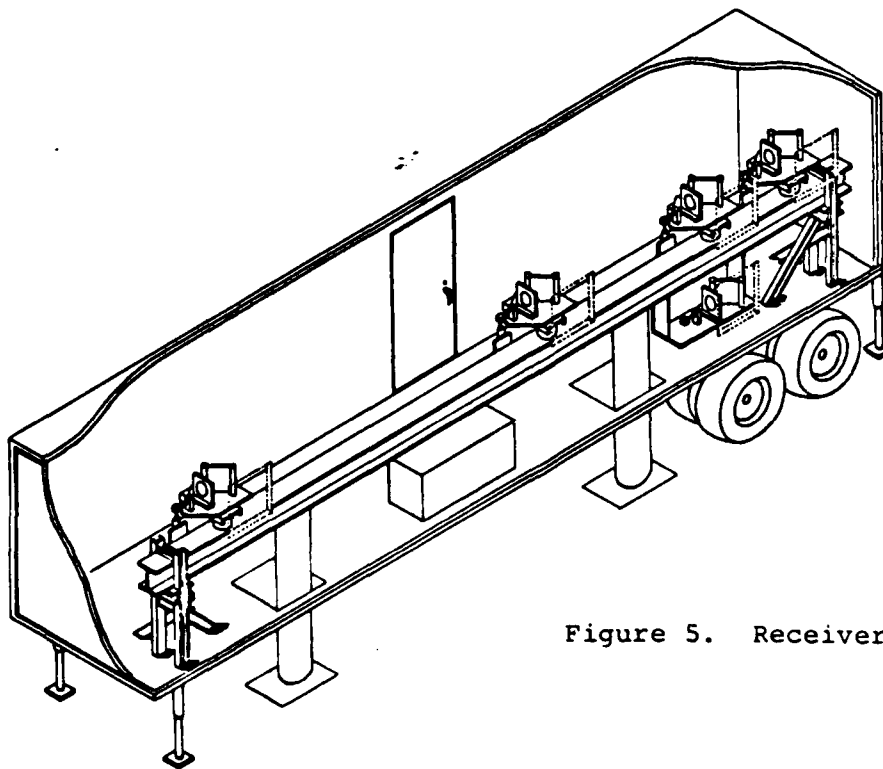


Figure 5. Receiver Van

## Signal Combining

In both the transmitter and receiver, the klystron tubes were phase-locked to permit the use of a narrow receiver bandwidth that improves the signal to noise ratio of reception. The klystrons were locked to solid state X-band sources which were in turn locked to stable oscillators [11,12]. A lock of the transmitter and receiver together has not been implemented so only relative phases between antennas may be determined. Double superheterodyne conversion has been used with IFs of 930 and 30 MHz and a bandwidth of 3 MHz. Fig. 6 is a block diagram of one channel of the receiver array, showing also a variable attenuator and phase shifter used for initial trimming of the array and calibration.

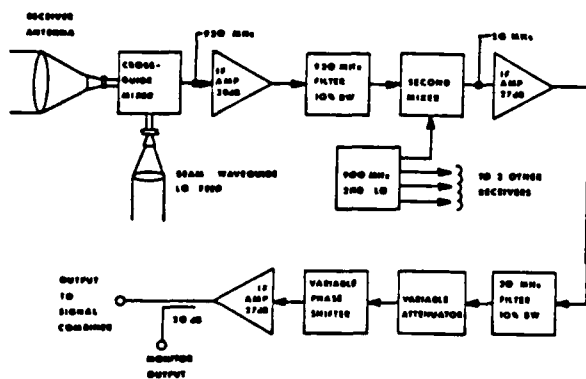


Figure 6. Block Diagram of Receiver System

To get a measure of the phase difference in the signals arriving at two antennas, the signals are mixed in a 2-way signal combiner from which the combined output power (or intensity) is given by

$$I_n = I_1 + I_2 + 2\sqrt{I_1 I_2} \rho(r) \cos[a_n - \beta(r)]$$

where  $I_1$  and  $I_2$  are the intensities at antennas 1 and 2 alone,  $\rho$  is the degree of coherence and is equal to unity to good approximation,  $r$  is the separation of the antennas, and  $a_n - \beta(r)$  is the phase difference between the signals. In this last quantity,  $\beta$  is the part introduced by the atmosphere and  $a$  that due to phase differences caused by the instrumentation. Four different combinations of the signals from two antennas are made with  $a$  set to give 0, 90, 180 and 270 degree shifts, denoted by the subscript  $n$  in the above equation. Then the atmospheric phase shift  $\beta$  can be found from

$$\beta = \tan^{-1}[(I_{90} - I_{270}) / (I_0 - I_{180})]$$

Fig. 7 shows a section of the network where the signals from antennas 1 and 2 are combined. The phases of each receiver input are shifted through 0, 90, 180 and 270 degrees by quadriple network

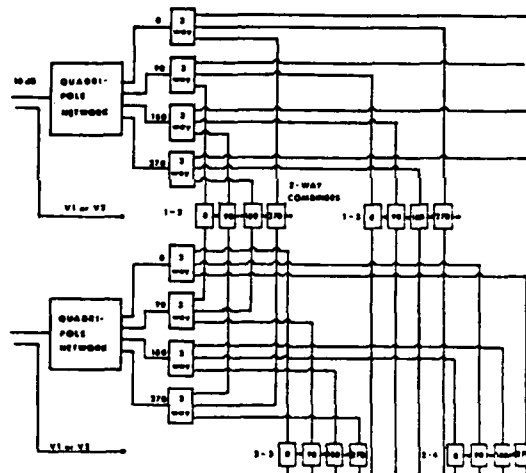


Figure 7. Signal Combining Network

modules. Each of these outputs in turn passes into a 3-way power splitter whose outputs are combined with the proper ones from the other receivers in the 2-way combiners. This gives a total of 24 mixed signals, corresponding to 4 possible phase combinations for each of 6 possible antenna pairs. The 4 signal intensities  $I_1$ ,  $I_2$ , etc., are also monitored. All intensities are detected by ordinary video detectors followed by signal conditioners, amplifiers and analog to digital conversion. The resulting 28 millimeter wave measurements are recorded at a rate of 100 sets per second by a microcomputer and stored on magnetic tape along with meteorological data from the fiber optic link. A parallel processor on the computer network calculates  $\beta$  in real time for output to chart recorders.

## RESULTS

### Snow

Snow fall occurred during field tests on the occasions briefly described in Table 2. The storm in the period February 27-28, 1984 was the most severe and is the only one for which sufficient data analysis has been done to permit discussion here. The frequency used at that time was 116.3 GHz. It is believed to be representative of the largest effects seen so far.

Table 2.

#### Snow Dates During Fluctuation Measurements

Dates	No Hours of Measurements	Frequency (GHz)
11/13/83	1	116.3
12/02/83	2	116.3
12/06/83	3	173.0
2/27-28/84	7	116.3

The storm began at approximately 0730 on the morning of the 27th and continued through the night until the following

morning. Total snow fall was 200-300 mm, as recorded by a weighing bucket rain gauge modified to collect snow and corrected for the known wind velocity. The wind was approximately out of the north at a mean speed of 15 m/s, with gusts to 20 m/s, during the first day. Temperatures were in the range -3 to -6 degrees Celsius, and thus the snow was dry. Early in the storm the snow took the form of moderate sized flakes of a few millimeters in diameter, but as the storm progressed, more and more snow was added in the form of smaller crystals from ground blizzards. Fig. 8 shows particle spectra obtained from the "ground-based precipitation probe" [3] at a time when the storm was well-developed on the 27th and another from the 28th when the snow had subsided to mainly ground blizzards. Due to the high wind speed it is difficult to interpret the shadowgraphs from the 2D particle probes and thus hard data on mean particle orientations are not as yet available. However, visual observations at the time suggested that the gusty winds were producing fairly random orientations of the flakes with respect to the millimeter wave polarization. The high winds also posed another problem; namely, that it was approximately aligned with the propagation path. Such alignment not only leads to some inhomogeneity over the path but also to some difficulties in theoretical interpretation, since the disturbances causing fluctuations are not carried into and out of the beam during their lifetime, as they would be when there is a cross wind. This is not believed to be a significant consideration for the semi-qualitative results to be discussed here. At the time of writing, much remains to be done concerning detailed analysis of both meteorological data and millimeter wave data. As mentioned earlier some meteorological data, such as humidity and temperature fluctuations, are not currently possible to obtain during storms. As it happens, when the wind is high, it is also not possible to measure wind fluctuations at high data rates.

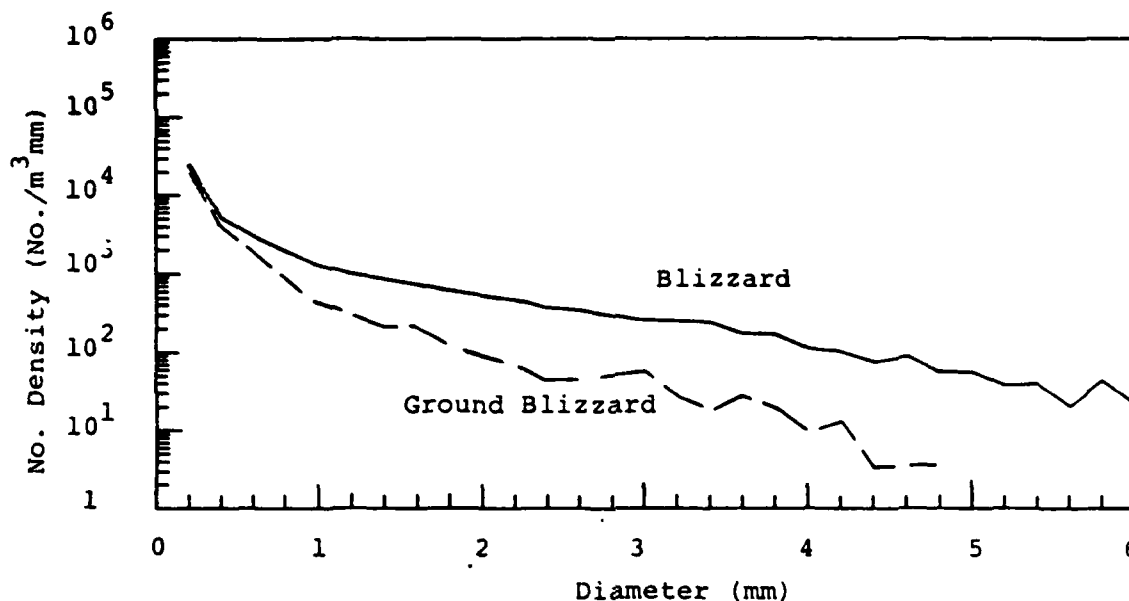


Figure 8. Snow Flake and Ice Crystal Size Spectra.

Representative records of the intensity fluctuations seen on two of the antennas are shown in Fig. 9. Relative phase fluctuations as a function of the antenna separation are shown in Fig. 10 for different portions of the storm and relative intensity fluctuation levels are given in Table 3. Curve 1 corresponds to the time when the snow was just beginning and for curve 2, the storm had significantly intensified (specific snowfall rates are unavailable at the present time). Curve 3 obtained from data on the 28th shows results in ground blizzard conditions and the fluctuation levels are lower. The vertically displaced antenna 5 rather than 4 (see Fig. 1) was operational during these operations thus limiting somewhat the range of antenna separations available. Generally fluctuations associated with antenna 5 were larger, as expected, due to its closer proximity to the ground where, for example, the snow density is larger. The fluctuations levels presented for falling snow conditions were at least a factor of two higher than those found in clear air preceding the storm. Without data on temperature and humidity fluctuations, however, it cannot be said that

Table 3.

Typical Fluctuation Levels In Millimeter Wave Propagation

Condition	Standard Deviations	
	Intensity (Per Cent)	Angle of Arrival (urad)
Summer Daytime		
Clear Air	7.4	38
Snow		
-Near Start	1.9	4.8
-Blizzard	2.4	8.4
-Ground		
Blizzard	1.4	4.4
Winter Rain	1.0	3.8
Winter Fog	0.2	1.1

Based on 20-second slices of data; i.e., 2000 data points.

the observed increase in fluctuations during snow storms are due to the snow or to the accompanying air. However, snow flakes may be expected to make a contribution, by analogy with rain models [13].

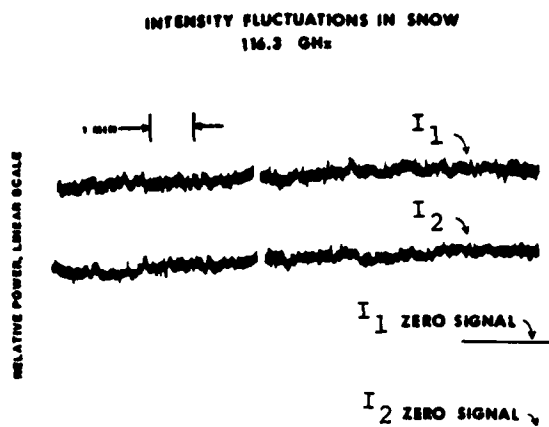


Figure 9. Observed Intensity Fluctuations in Snow.

In the days following the snow storm, the air remained generally below the freezing point, except for one brief period of melting followed by refreezing. This produced a layer of ice on top of the snow about 5-10 mm thick, and shortly thereafter, contributions to the level of fluctuations due to multipath propagation were observed. (It happened that a change was made to a frequency of 142 GHz at this juncture.) Since the wind during the storm had been out of the north and blowing past the receiver trailer, large areas of soil were left bare in its lee out as far as 300 meters. This resulted in some variation in the ground cover seen by the different antennas in the array, and the multipath effects were then spotted as they showed up in some antennas more than others. Fluctuations levels sometimes differed by factors of two. The existence of multipath propagation was confirmed by moving absorbers around near the ground where the antenna patterns were strongest and by noting the resulting variations in signal. Since it was not clear how to characterize the multipath, it was subsequently defeated by erecting three multipath fences made from plywood. During the recent exercises in the summer of 1984, tests for multipath were again made when the soybean crop was a few weeks old and both soil and

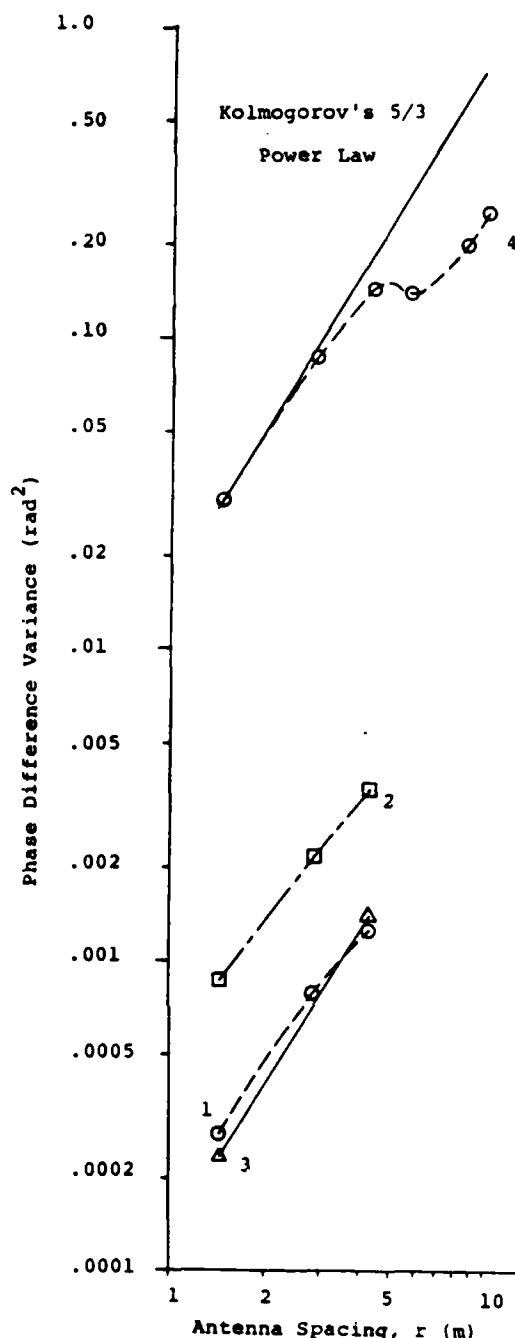


Figure 10. Observed Phase Difference Fluctuations at 116.3 GHz as a Function of Antenna Separation. Curve 1 - early in snow storm. Curve 2 - storm well-developed. Curve 3 - storm reduced to ground blizzards. Curve 4 - summer clear air for comparison.

leaves were visible. As expected, no indicators of multipath effects were found.

#### Clear Air

It is important to try to put the snow results in the context of their relation to findings for clear air. It has been found that the largest fluctuations in both intensity and phase occur in the summer when the atmosphere is hot and humid. Fluctuations are especially large when the sun comes out after a rainfall or when the soybean plants are large enough to give up large amounts of water vapor by transpiration. Fig. 11 shows intensity fluctuations at 142 GHz measured on a clear morning after a light rainfall (~3 mm) the previous night, and Fig. 12 shows the corresponding phase fluctuations measured between the antennas with the largest spacing. Large fluctuations of this kind were common in the summer, and even larger ones were occasionally found with peak to peak phase swings of two  $\pi$ . However, during dry periods such as part of June 1984, humidity fluctuations and millimeter wave transmission fluctuations were significantly lower, despite exceptionally large fluctuations in temperature (as much as 8 degrees peak to peak in periods of a few seconds). This qualitatively demonstrates the expected [14] key role of water vapor in determining the size of millimeter wave effects.

Since in the winter the absolute humidity and its fluctuations are generally much smaller than in the summer, clear air turbulence causes correspondingly smaller millimeter wave effects.

Preliminary studies at SNOW-ONE [1] and in Illinois in the summer of 1983 when clear air was present appear to confirm the expectation that intensity fluctuations in millimeter wave signals depend on frequency to the 7/6 power.

The array of antennas affords an additional capability besides

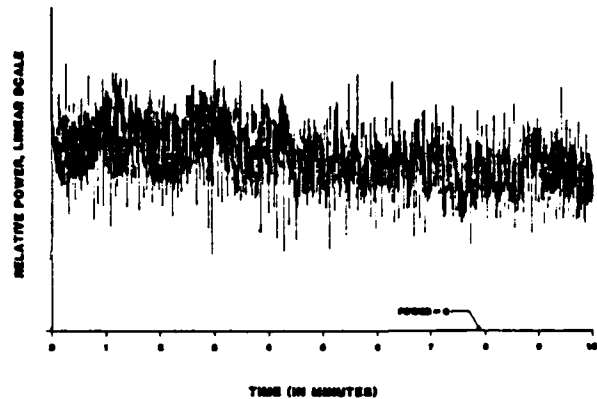


Figure 11. Intensity Fluctuations of a 142 GHz signal measured on a hot, humid day.

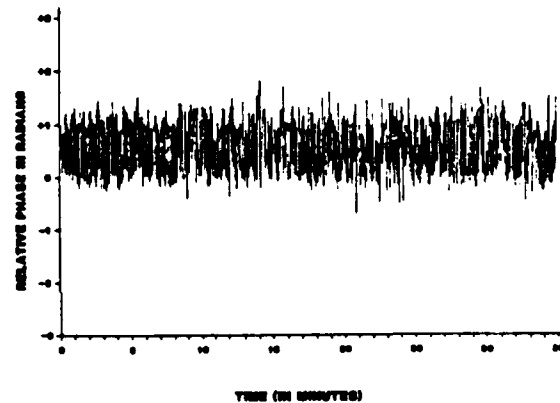


Figure 12. Phase Fluctuations measured under the same conditions as Figure 11.

that of relative phase measurements. It is well-established at visible and near-infrared wavelengths that cross winds may be measured by cross-correlating the intensity fluctuations seen by a pair of receivers [5]. The wind carries the turbulent eddies across the beam and the time for this traversal shows up as the time delay for which the correlation of intensity fluctuations is maximum. This general technique is the basis of the near infrared scintillation cross wind sensors

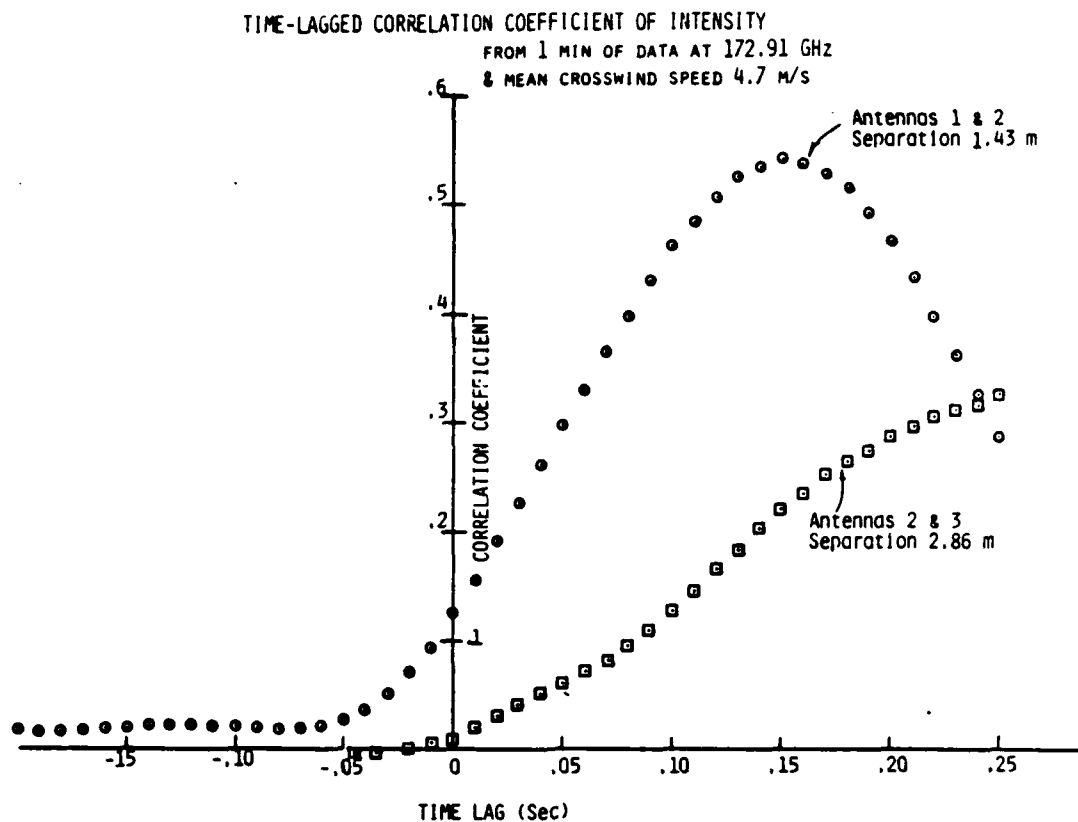


Figure 13. Cross correlation of millimeter wave intensity fluctuations gives a measure of cross-wind speed.

which are operated on the site and which were mentioned earlier. Fig. 13 demonstrates this same sort of analysis applied to the millimeter wave signals seen at antennas 1 and 2 and 1 and 3. A clear maximum is found and the mean cross wind speed  $v_c$  can be calculated from

$$v_c = .5r/\tau$$

where  $\tau$  is the lag time of the maximum correlation. A value of 4.7 m/sec is found, in excellent agreement with that obtained from the average data from the prop and vane sensors at the two meteorological stations along the path. Further development of this concept is underway to apply it also in adverse weather when infrared systems are shut down by atmospheric opacity. It is anticipated that in precipitating conditions, some correlation may also be found between vertically separated antennas giving some measure of fall rates.

#### Fog and Rain

These will be treated only briefly to complete a contextual picture for the snow data. The types of fog observed so far in Illinois have been set not surprisingly in very quiet atmospheric conditions. This is born out by the intensity fluctuations shown in Fig. 14 and by the data in Table 3. The visibility during this period was approximately 200 m based on the visibility of objects at known distances from the receiver trailer.

A preliminary look at data on rain has also been taken as illustrated by the intensity traces in Fig. 15. This shows a relatively brief shower which had a peak rain rate of about 60 mm/hr. Under these circumstances the signals were below the threshold of detection. It was noted in rain events similar to this that intensity fluctuations would increase in level and frequency at the start of a shower

and in many cases would remain higher after the storm than before. One would presume that the change in the level of fluctuations is due to increased humidity fluctuations, but further analysis will be necessary to confirm this. The increase in the frequency of fluctuations is expected from models of precipitation effects [13] as well as from normal increases in wind speed that often occur at the onset of a shower. The fluctuation levels quoted in Table 3 for rain pertain to a steady rain period in the winter; good values for rain rate have not as yet been derived for this particular data, but would probably be in the ballpark of several mm/hr..

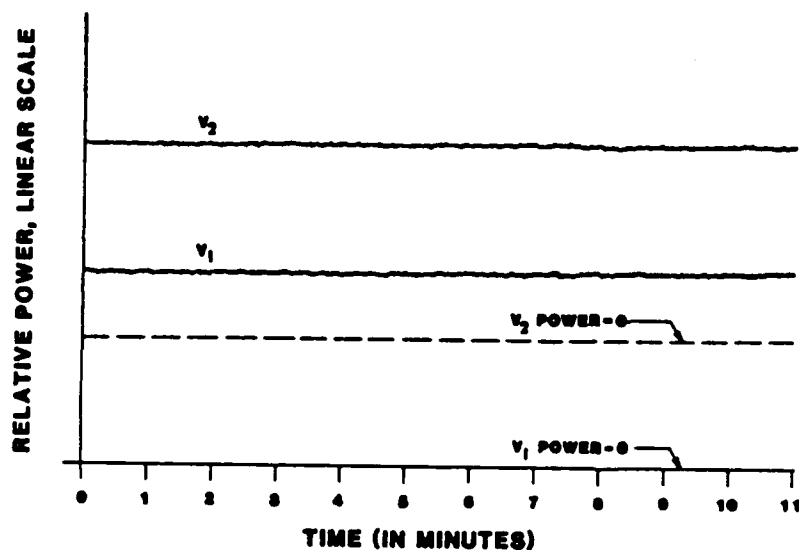


Figure 14. Intensity Fluctuations measured during a heavy fog at 142 GHz.

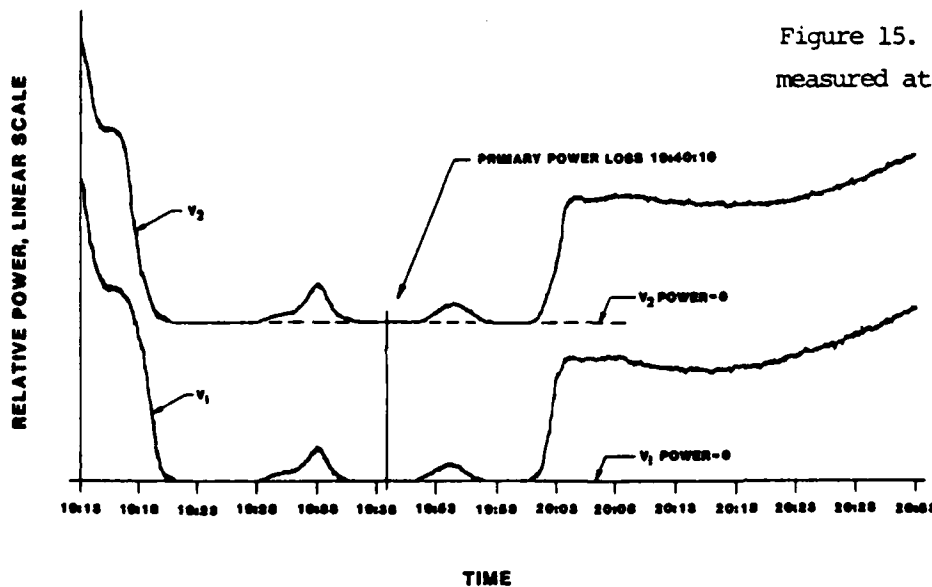


Figure 15. Intensity changes measured at 173 GHz during a heavy rain.

## DISCUSSION AND CONCLUSIONS

The relative importance of various atmospheric conditions as regards typical levels of fluctuations in millimeter wave propagation is borne out by the entries of Table 3. This suggests, interestingly enough, that the aiming precision of millimeter wave systems will be most effected by what goes on in hot, humid climates. The largest angle of arrival fluctuations which have been seen so far (at 142 GHz) have been about 400 microradians peak to peak and the corresponding intensity fluctuations represent changes in signal of 45 percent peak to peak. Smaller fluctuations in the winter are found, due presumably to there being less water vapor present. What is perhaps more significant for millimeter wave system applications is that in adverse weather, fluctuation levels are also moderate, and indeed in fog, they are generally very small.

There are a few caveats to this as regards precipitation, however. One must remember that the fluctuation frequencies are expected to be higher when it is raining or snowing than otherwise and this may effect some millimeter wave systems involving servo-controls differently than the slower clear air case. One must be reminded also that it has not yet been possible to observe a heavy snow with a good cross-wind nor a wet snow fall, and such a cases may have larger fluctuations. Moreover, the relative sensitivities to polarization remain to be demonstrated as regards fluctuation level.

Much work also remains in relating the details of the meteorological data to the millimeter results, and in making comparisons with theory [14]. It may be hoped in the future that millimeter systems may take a place alongside infrared systems for remote probing of mean atmospheric conditions over long paths. Millimeter waves would be complementary in a key way on account of their sensitivity to water vapor and their relatively lower susceptibility to blockage by fog.

## ACKNOWLEDGMENTS

The work reported has been supported by the U. S. Army Research Office under Contract DAAG29-81-K-0173 and Grant ARC 21-82. The authors thank J. M. Cotton, Jr., V. T. Brady, G. F. Kirkman, M. J. Sinclair, J. W. Larsen, M. L. Blyler, R. P. Lilly, D. O. Gallentine, N. L. Abshire, R. B. Fritz, W. Cartwright, G. R. Ochs, R. J. Lataitis, J. J. Wilson, G. M. Walford, R. Valdez, T. Chavez, and G. Alvarez for assistance with preparations, measurements and data analysis. Thanks is given also to Mr. Leon Harms and his colleagues for providing the place for the measurements and to Mr. John Vogel of the Illinois State Water Survey for assistance with the site and for providing weighing bucket rain and snow gauges.

## REFERENCES

1. R. W. McMillan, R. A. Bohlander, G. R. Ochs, R. J. Hill and S. F. Clifford, "Millimeter Wave Atmospheric Turbulence Measurements" *Optical Engineering*, **22**, 32 (1983).
2. G. A. Andreyev, V. A. Golunov, A. T. Ismailov, A. A. Parshikov, B. A. Rozanov, and A. A. Tanyigin, "Intensity and Angle of Arrival Fluctuations of Millimetric Radiowave in Turbulent Atmosphere", *Proc. of Anglo-Soviet Seminar on Atmospheric Propagation at Millimetre and Submillimetre Wavelengths*, Moscow (28 November-3 December, 1977).
3. R. Olsen, B. Rischel, and R. Okrasinsky, "Particle Size and Optical Turbulence Measurements in a Snow Environment", these proceedings.
4. Ting-i Wang and S. F. Clifford, *J. Opt. Soc. Am.* **47**, 927 (1975) and *J. Appl. Meteor.* **21** 1747 (1982).
5. Ting-i Wang, G. R. Ochs and S. F. Clifford, *J. Opt. Soc. Am.* **68**, 334 (1978).

6. R. W. McMillan, V. T. Brady, G. W. Rosenberg, and G. F. Kirkman, "A Millimeter Wave Radio Frequency System for Atmospheric Turbulence Measurements", Proc. 8th Intl. Conf. on Infrared and Millimeter Waves, Miami (12-17 December 1983).
7. R. A. Bohlander, V. T. Brady, A. McSweeney, G. F. Kirkman, J. M. Newton, A. Davis and O. A. Simpson, "A Quasi-Optical Millimeter Wave Transmitter and Receiver Array for Measurements of Angular Scintillation", Proc. 8th Intl. Conf. on Infrared and Millimeter Waves, Miami (12-17 December 1983).
8. R. A. Bohlander, R. W. McMillan, et al. and S. F. Clifford, J. T. Priestley, R. J. Hill, R. E. Cupp et al., "Observations of Amplitude and Angle of Arrival Scintillation in Millimeter Wave Propagation Caused by Turbulence in Clear Air Near the Ground", Proc. 8th Intl. Conf. on Infrared and Millimeter Waves, Miami (12-17 December 1983).
9. R. W. McMillan, R. A. Bohlander, D. M. Guillory, R. H. Platt, J. M. Cotton, Jr., S. F. Clifford, J. T. Priestley, R. J. Hill, and R. E. Cupp, "Millimeter Wave Atmospheric Turbulence Measurements", Proc. 9th Intl. Conf. on Infrared and Millimeter Waves, Osaka (October 1984).
10. G. Goubau in Millimetre and Submillimetre Waves, F. A. Benson, ed., London: Iliffe Books (1969).
11. P. S. Henry, "Frequency-Agile Millimeter-Wave Phase Lock System", Rev. Sci. Instrum. 47, 1020 (1976).
12. H. M. Pickett, "Locking Millimeter Wavelength Klystrons with a Digital Phase Frequency Detector", Rev. Sci. Instrum. 48, 706 (1977).
13. H. T. Yura, K. G. Barthel and W. Buchtemann, "Rainfall Induced Optical Phase Fluctuations in the Atmosphere", J. Opt. Soc. Am. 73, 1574 (1983).
14. R. J. Hill and S. F. Clifford, "Contribution of Water Vapor Resonances to Fluctuations of Refraction and Absorption for Submillimeter through Centimeter Wavelengths", Radio Science 16, 77 (1981).

R. A. Bohlander  
R. W. McMillan  
D. M. Guillory

R. J. Hill  
J. T. Priestley  
S. F. Clifford

R. Olsen

Georgia Tech Research Institute  
Georgia Institute of Technology  
Atlanta, Georgia 30332

National Oceanic & Atmospheric  
Administration  
Wave Propagation Laboratory  
Boulder, Colorado 80302

U. S. Army Atmospheric  
Sciences Laboratory  
White Sands Missile Range  
New Mexico 88002

## Introduction

Since 1983, Georgia Tech, NOAA and the U.S. Army Atmospheric Sciences Laboratory have been engaged in a program whose purpose is to measure fluctuations in millimeter wave signals due to atmospheric turbulence, precipitation and fog [1,2]. Five measurement sessions have been conducted that have sampled atmospheric conditions in a variety of seasons. Frequencies of particular interest for their potential uses in higher precision imaging systems have been studied; namely, 116, 118, 142, 173 and 230 GHz. These span a range of situations including windows between lines and regions near line centers. The measurements have been made over a 1.4 km path at a site near Urbana, Illinois, chosen for its exceptional flatness. It is important that the path and surrounding terrain be flat, homogeneous, and free of trees or other obstructions, so that the turbulence will not be perturbed by such irregularities. During this series of experiments, rigorous meteorological measurements have also been obtained.

At a previous conference in this series, the equipment used and preliminary results were described [3,4]. The following sections briefly review the experimental arrangements and focus on subsequent significant improvements in the experiment and on progress in analyzing the data.

## Transmitter System

Phase-locked reflex klystrons are used as both transmitters and receiver local-oscillators, with the exception of the recently added 230 GHz system which uses a phase-locked cw extended interaction oscillator as the transmitter. Phase locking of the sources is necessary for three reasons: 1) it improves amplitude stability of the source so that the transmitter power variations are less than the smallest atmospherically induced fluctuations, 2) it narrows the bandwidth and therefore improves the detection signal-to-noise ratio, and 3) it aids in system calibration because the receiver second intermediate frequency (IF) output is a very stable sine wave. Recent improvements in this system are described elsewhere in this conference [5].

The primary transmitter antenna is an offset paraboloid with an elliptical aperture. This gives a fan beam filling the receiver array (which is much wider horizontally than vertically). The transmitter is mounted on a pedestal secured to a concrete pad in the ground and is housed in a small step-van truck. This in turn was located on a berm that brought the transmitter height up to 3.5m, the same as the center of the receiver array. The transmitter was aimed through a high density polyethylene window in the rear door, protected by an awning.

## Receiver System

The receiver comprises four apertures with individual mixers and with separations varying from 1.4 to 10 meters so that a wide range of atmospheric scale sizes can be considered in the determination of fluctuation effects. Local oscillator power at nearly half the signal frequency is distributed to the harmonic mixers via a low-loss optical beam waveguide system. The receivers use double down-conversion, and the second IF signals from the six possible pairs of receivers in the array are combined in such a way that the mutual coherence function can be measured. Both amplitude and angle of arrival fluctuations are therefore determined. These measurements are stored on magnetic tape at a rate of 100 per second along with readings from meteorological instruments by the data acquisition computer. In recent work, the ability to vary the polarization of the transmitted and received radiation has been added, of possible interest during observations of falling snow.

The receiver antennas are high density polyethylene lenses aimed by gimbaled diagonal mirrors through high density polyethylene windows. The four receivers and the optical beam waveguide are mounted to a large I-beam secured to concrete pads in the ground by two pillars. The entire receiver system is housed in a semitrailer that is insulated, heated and air conditioned for all-weather operation. The mounting to the ground, rather than to the floor of the trailer, was intended to give the sensitive array isolation from

vibrations. However, in recent analyses, some oscillations in the phase between antennas characteristic of vibrations in the ground have been identified.

#### Meteorological Instrumentation

The parameters measured simultaneously with the millimeter wave data have been temperature, humidity, 3-dimensional wind velocity, temperature and humidity structure, and particle size spectra. These have been sampled at or near the same height as the millimeter wave beam and at three locations along the path. In addition, near infrared optical fluctuations were observed from which structure functions and path averaged wind values were determined. Most of this data has been relayed to the computer in the receiver trailer by a fiber optic link. The results are being used to facilitate comparisons between the millimeter wave measurements and theory [1].

#### Results

Analysis of the massive amounts of propagation and meteorological data is still underway but several significant results can be reported. Intensity fluctuation range from near zero in fog to about 50% (peak to peak) of the nominal signal intensity on a hot day with moist ground. Short term fluctuations in rain and snow fall somewhere in between these two extremes.

Phase fluctuations between the most widely spaced antennas have been observed up as high as plus and minus  $\pi$  radians on warm, humid days, corresponding to angle of arrival fluctuations of about 200 microradians peak to peak.

It appears that the log amplitude variance of the fluctuations increases with frequency as the  $7/6$  power, as predicted by theory. No striking changes in this have yet been noted at frequencies near absorption line centers. The distribution of intensity fluctuations appears to be log-normal, and that of phase fluctuations, normal, also predicted by theory.

It has been verified that water vapor in the atmosphere has a strong effect, frequently causing the millimeter wave index of refraction structure parameters to be a few orders of magnitude larger than those in the visible and infrared. Some preliminary comparisons between the observed millimeter wave structure and that predicted from the meteorological measurements and theory will be discussed in the presentation. Comparisons will also be made between the phase and amplitude fluctuations in clear air and precipitation.

#### Conclusions

In any program of measurements of atmospheric effects on propagation, the question must be asked whether system performance is seriously affected by what is observed. On the basis of the results obtained thus far, it may be concluded that turbulence induced fluctuations and short term fluctuations due to precipitation are probably not very serious. Intensity fluctuations affect signal detection probability, but only at near maximum ranges where detection may be marginal in any case. Angle of arrival fluctuations cause angular errors, but this effect is most severe in clear weather where sighting methods other than millimeter wave systems could be used. Nevertheless, system designers will want to consider the results of this study to verify whether fluctuations can be neglected. Of interest for the future is the possible use of millimeter wave beams in probing atmospheric structure. Their sensitivity to water vapor will be complementary to studies with infrared or visible light which are more sensitive to the temperature structure.

#### Acknowledgments

The authors wish to thank many colleagues who have contributed to the success of this program. This work has been supported in part by the U.S. Army Research Office under contract DAAG29-81-K-0173.

#### References

1. R. J. Hill, S. F. Clifford and R. S. Lawrence, *JOSA* **70**, 1192 (1980)
2. R. W. McMillan, R. A. Bohlander, G. R. Ochs, R. J. Hill and S. F. Clifford, *Opt. Eng.* **22**, 32 (1983)
3. R. A. Bohlander et al. 8th Int. Conf. on IR and MMW, Miami Beach, FL (1983)
4. R. W. McMillan et al., 8th Int. Conf. on IR and MMW, Miami Beach, FL (1983)
5. D. M. Guillory and R. W. McMillan, "Phase and Frequency Control of MMW Sources", this conference.

D. M. Guillory and R. W. McMillan

Georgia Institute of Technology  
Georgia Tech Research Institute  
Atlanta, Georgia 30332

## Introduction

As the use of the millimeter wave (MMW) bands increases, the need for better spectral control of sources also increases because of widening application of this spectrum to Doppler radar, communication, and measurement systems. As the millimeter bands become more crowded, better frequency control will become necessary to avoid interference. There is also a real advantage to be gained in source power stability by phase-locking; locked sources typically exhibit output power stabilities of a few tenths of one percent. Phase locking of MMW sources to a frequency standard also provides the basis for frequency measurements which are perhaps the most accurate measurements of any physical quantity ever made, with accuracies of  $1 \times 10^{-12}$  being attainable. Phase-Lock circuits using both linear and digital techniques are available to the MMW system designer, and both types are discussed in this paper along with some typical results obtained.

## Linear Phase-Lock Circuits

Linear phase-lock circuits use a mixer for phase detection. Even though the mixer is a nonlinear device, its output as a phase detector is a voltage proportional to the sine or cosine of the phase difference between two signals, hence it is considered linear. The phase error voltage output is amplified by an operational amplifier with some desired compensation function and applied to the frequency control electrode of the voltage controlled oscillator (VCO) to be locked, thus closing the phase-lock loop and locking the VCO.

One of the most successful linear phase-locking circuits available is that devised by P. S. Henry<sup>1</sup>, who combined a discriminator loop with a phase control loop to give the circuit a wide frequency capture range. The discriminator is a frequency control loop, and as such does not give spectral purity as good as that attainable with phase control. The phase loop gives excellent spectral purity, but generally has a narrow frequency capture range. Henry's circuit combines these two functions, so that the phase locking system has the broad capture range of the discriminator and the spectral purity of the phase loop. The circuit is designed so that the phase loop is disabled when the discriminator operates and vice versa.

## Digital Phase-Lock Techniques

A technique employing digital circuits<sup>2</sup> was first used for MMW phase-locking by Pickett<sup>3</sup>, and has recently been extensively used at Georgia Tech. Figure 1 is a block diagram of this phase-lock circuit. The front end of this circuit is an emitter-coupled logic (ECL) limiter/prescaler that divides the frequency of the incoming IF signal, which is typically several hundred MHz. Following this stage is an ECL counter which further divides the frequency to the operating range of the digital phase/frequency detector, generally about 10 MHz. This detector compares the phase and frequency of the divided IF signal to that of a crystal reference oscillator and outputs two pulse width modulated signals whose duty cycle is proportional to the phase error. These signals are fed into a differential integrator which serves as an active filter for loop compensation in addition to smoothing the phase detector output. The phase-frequency detector also serves as a discriminator, since its output will be at a maximum duty-cycle limit if the source is unlocked, and the sense of this limit is determined by whether the frequency error is positive or negative.

This digital phase-locking technique has several advantages over the older analog techniques, namely: (1) since a limiter is used, the gain of the phase detector is independent of source (IF) power within the dynamic range of the limiter, typically 25 dB, (2) the digital system is easier to compensate, and (3) a convenient lower frequency crystal reference is used in the digital lock.

## Interfacing to High Frequency Tubes

The frequency control grid of most MMW tubes is at high potential. Some means must be used to sum the phase lock signal with the high voltage from the tube power supply. An optoisolator or a signal transformer are the usual techniques employed.

Using a linear optoisolator with the output floating at high voltage, the phase error signal can be superimposed on the control grid. The frequency response of the optoisolator usually must be taken into account in the loop compensation.



# THE SPECTRA OF AMPLITUDE AND PHASE DIFFERENCE FLUCTUATIONS OF MILLIMETER WAVES PROPAGATING IN CLEAR AIR

S. F. Clifford, R. J. Hill, and J. T. Priestley  
NOAA/ERL/Wave Propagation Laboratory  
325 Broadway  
Boulder, CO 80303

R. A. Bohlander, and R. W. McMillan  
Georgia Institute of Technology  
Atlanta, GA 30332

## ABSTRACT

We report on the initial results of the Flatville experiment where several millimeter wave frequencies in the range 116 to 230 GHz were propagated over a 1.4 km path. Extensive documentation of the site meteorology allowed simultaneous, detailed comparisons of the propagation phenomena with the state of the atmosphere. The theory for amplitude and phase difference in the single scatter approximation is used to explain the observed spectra. The agreement with observations is very close.

## INTRODUCTION

Over the past four years a team of scientists from the National Oceanic and Atmospheric Administration and the Georgia Institute of Technology conducted an extensive set of millimeter-wave propagation measurements. In five, thirty-day sessions, chosen for the widest variety of weather conditions, we propagated millimeter wave frequencies from 116 to 230 GHz over our 1.4 km horizontal path in Flatville, Illinois. Simultaneous,

extensive measurements of the meteorology allowed detailed comparisons of the propagation effects with the state of the atmosphere.

The details of the experiment layout and data processing are contained in Reference 1. Figure 1 illustrates the propagation geometry. The beam propagated 1.4 km - 4 meters above an extremely flat terrain, chosen for its uniform fetch in all wind directions. The intensity fluctuations were measured at each of the four horizontally spaced antennas and phase differences were measured among all possible antenna pairs with spacings from 1.43 m to a 10 m maximum. A fifth antenna was used intermittently to test the isotropy of the different wave parameter fluctuations. The phase-difference and amplitude spectra described below were taken at 142 GHz during the Summer of 1984. Other data being analyzed were taken during two winter and one fall sessions. This afforded us data during rain, fog, snow, and ground blizzards.

## PHASE AND AMPLITUDE SPECTRA

Using the spherical-wave theory for propagation through refractive turbulence, Clifford<sup>2</sup>

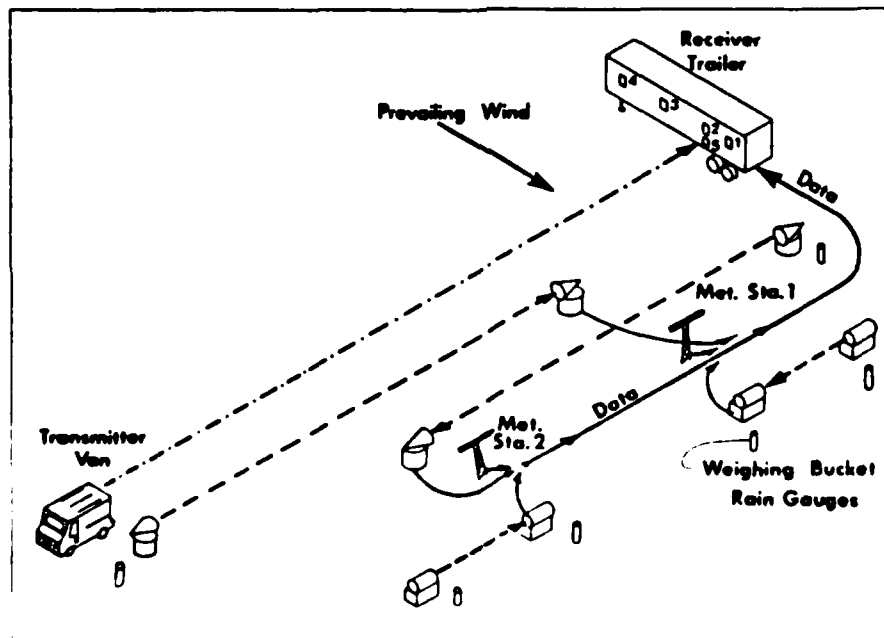


Figure 1. The instrument positions at the experiment site. The dashed and dotted line denotes mm-wave propagation path (1.4 km).

shows that the temporal power spectrum of log-amplitude fluctuations in the single scattering or weak turbulence limit has the form shown labeled "theory" in Fig. 2. In addition Fig. 2 contains a log-log plot of  $(f/f_0)$  times the log-amplitude spectrum  $W$  versus normalized frequency  $(f/f_0)$ . The spectrum  $W$  is normalized to the log-amplitude variance such that the area under the curve is unity. The frequency  $f_0 = v/(2\pi\lambda L)$ , where  $v$  is the cross-path component of windspeed,  $\lambda$  is the wavelength, and  $L = 1.4$  km is the millimeter-wave path length. The dotted (solid) fluctuating curve represents the low (high) frequency Fourier transform of 35 min of log-amplitude data taken at 142 GHz. The solid "theory" curve fits the data quite well until the high frequency tail beyond  $\log(f/f_0) = 1$ , where aperture averaging effects are important. The dashed curve is a plot of the theory including aperture averaging effects; overall, the fit to the data is excellent. Deviation at low frequencies above the "theory" curve are most likely due to receiver amplifier drift. It is possible from the theory to estimate the cross-path velocity from the location of the peak. The peak is predicted at  $\log(f/f_0) \sim 0.43$ . In the case shown the cross-path velocity estimate from the millimeter wave scintillations agrees with the propeller vane to within a few percent. (Note, the data were plotted with  $f$  calculated from propeller vane-measured crosswind.)

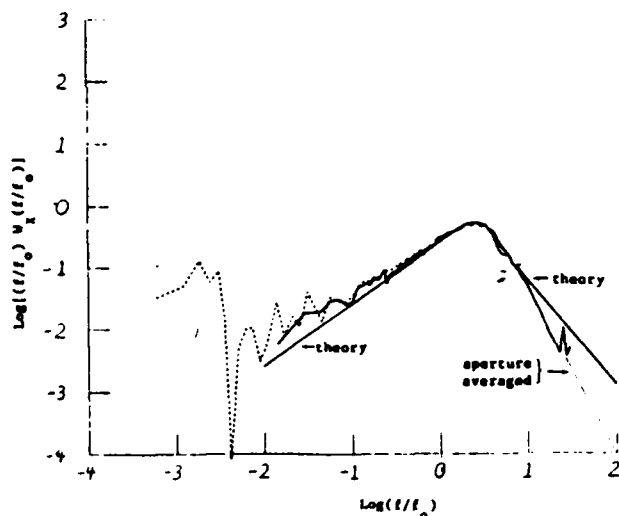


Figure 2. Theoretical and experimental power spectra of amplitude fluctuations.

Figure 3 illustrates the theoretical spectra for phase difference fluctuations. In contrast to the log-amplitude result phase-difference is very sensitive to the "outer scale"  $L_0$  of the refractive index fluctuations. Consequently, we have a family of curves for different values of the spacing  $\rho$  normalized to  $L_0$ . ( $L_0$  is the size of the largest eddy for which the assumption of isotropy holds, so  $L_0$  is the order of the height above the ground). The theoretical curves are plotted versus normalized frequency  $f/f_1$ , where  $f_1 = v/\rho$  and  $v$  is the cross-path wind component.

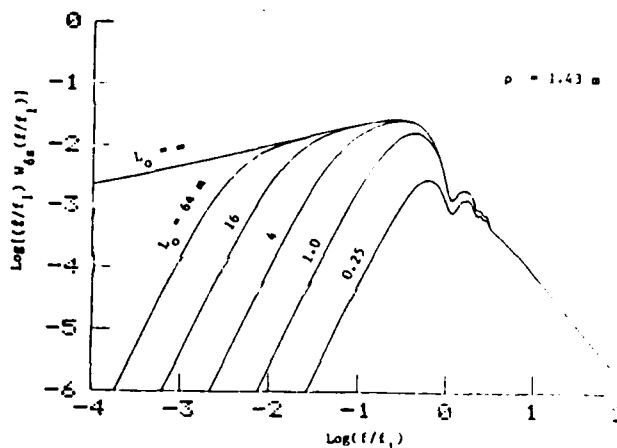


Figure 3. Theoretical power spectra of phase difference fluctuations as a function of the ratio of spacing to the outer scale  $\rho/L_0$  and characteristic frequency  $f_1 = v/\rho$  where  $v$  is the cross-path wind.

From our knowledge of the wind speed and the dependence of the spectra on  $\rho/L_0$ , we can estimate  $L_0$  from a spectrum measured at a known separation, e.g.,  $\rho_{12} = 1.43$  m, and use that derived value  $L_0 \sim 2.8$  m for all further comparisons.

Figures 4 and 5 show the theoretical curves superimposed over the phase-difference spectra from the data for antenna pairs (1,2) separated by  $\rho_{12} = 1.43$  m and antenna pair (1,4) separated by  $\rho_{14} = 10$  m. We used the value  $L_0 \sim 2.8$  m and selected our curves from Fig. 3 to fit the data based on the ratios  $\rho_{12}/L_0 = 0.51$  and  $\rho_{14}/L_0 = 3.5$  appropriate to each antenna pair. The resulting fit is quite good. We could also estimate crosswind from the peak of the spectrum if we knew the accurate  $L_0$  from other independent measurements.

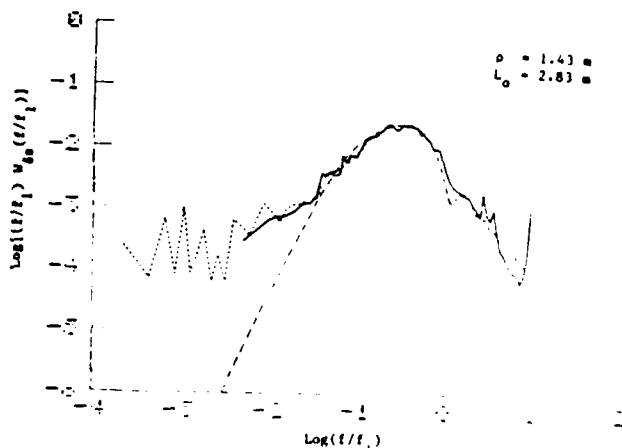


Figure 4. Comparison of theoretical and measured spectra of phase difference for spacing  $\rho_{12} = 1.43$  m.

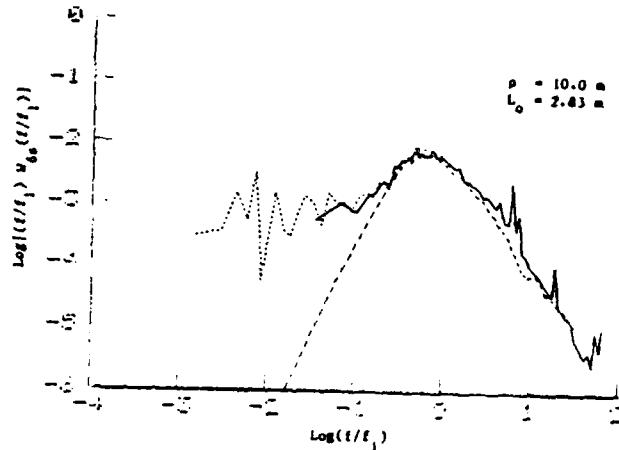


Figure 5. Comparison of theoretical and measured spectra of phase difference for spacing  $p_{14} = 10$  m.

#### CONCLUSIONS

Initial processing of the Flatville data set has yielded results that agree quite closely with clear-air single scatter propagation theory for the turbulent atmosphere. We intend to make much more extensive comparisons in the future. We will also analyze severe weather data and compare with existing theories of mm wave propagation in snow, fog and rain.

ACKNOWLEDGMENT—This work was supported by the Army Research Office under MIPR 122-85.

#### REFERENCES

1. Hill, R.J., W.P. Schoenfeld, J.P. Riley, J.T. Priestley, S.F. Clifford, S.P. Eckes, R.A. Bohlander, R.W. McMillan, NOAA Technical Report, ERL 429-WPL 60, U.S. Government Printing Office, Washington, D.C., (August, 1985).
2. Clifford, S.F., J. Opt. Soc. Am., 61, 1285, (1971).

# INSTRUMENTATION, DATA VALIDATION AND ANALYSIS, AND RESULTS OF THE NOAA-GIT MILLIMETER-WAVE PROPAGATION EXPERIMENT

R. J. Hill, J. T. Priestley and S. F. Clifford  
NOAA/ERL/Wave Propagation Laboratory  
325 Broadway  
Boulder, Colorado 80303

W. P. Schoenfeld  
CIRES/University of Colorado  
Boulder, Colorado 80302

R. W. McMillan and R. A. Bohlander  
Georgia Institute of Technology  
Atlanta, Georgia 30332

## Introduction

We describe the micrometeorological instrumentation and optical scintillation instrumentation deployed during the NOAA-GIT Experiment in Flatville, Illinois. We describe the data validation procedures and data processing techniques for the micromet, optical, and mm-wave data. Results of the data reduction are shown. The body of the paper consists of graphs with self-explanatory captions. The experiment set-up is shown in the first figure of the companion paper by Clifford et al. in this volume. The mm-wave instrumentation has been discussed elsewhere.<sup>1-4</sup> Details of the data reduction, the micromet instruments, and quantities calculated are available.<sup>5</sup>

The two overlapping optical propagation paths are 1 km each; these give the path-averaged optical refractive-index structure parameter ( $C_n^2$ ) as well as the cross-path component of the wind. Two instrumented towers were positioned at one-third and two-thirds the distance between the mm-wave receivers and transmitter. Each tower has a prop-vane, a three-axis sonic anemometer, a Lyman- $\alpha$  hygrometer and two platinum, resistance-wire thermometers, one of which is in the Lyman- $\alpha$  gap and the other is in the center of the sonic anemometer. All the instruments were at a height of 3.6 m on a boom that could be rotated into the wind.

The sonic measures the three fluctuating components of the wind, thus we obtain the variances of these components, and correlation of the fluctuations of the streamwise-component with those of the vertical component which gives the vertical flux of horizontal momentum. The time series from the resistance wire and Lyman- $\alpha$  give us such statistics as temperature and humidity variance and cross correlation, the structure parameters of temperature and humidity ( $C_T$  and  $C_Q$ ) and the temperature-humidity cross-structure parameter ( $C_{TQ}$ ). In addition, correlating the temperature with the vertical velocity fluctuations gives the upward flux of heat, and a similar correlation of the humidity fluctuations with those of vertical velocity gives the humidity flux. Each met. station had an aspirated psychrometer at a height of 3.6 m for mean and long-term fluctuations of temperature and humidity. Station 2 had a barometer for total pressure and an all-sky pyranometer for solar flux.

We graph every datum. This allows us to remove any instrument failures, even those consisting of a single bad datum in the time series, from subsequent analysis. Data averaged to 20 s bins is also graphed over the roughly 38 min duration of our data tapes so that trends can be identified.

The data processing scheme is shown in Fig. 1. PLATCOPY makes a Cyber-compatible data tape, extracts all quantities sampled at 2.56 s rate to a disk file, and writes the location of any gaps in the data to the PEDIGREE FILE. Graphs of the 2.56-s data base are made to check the performance of the instruments; Figs. 5 to 7 show a few of these graphs. METAPE extracts all the 100 Hz and 25 Hz micromet data, calibrates it in engineering units and writes it to the MET TAPE. The strip-chart programs graph the full time series over the duration of each data tape; times of bad data, such as phase-lock-loss, are then entered into the PARAMETERS FILE using MODPARM so that subsequent programs can skip over bad data. The stripcharts are illustrated in Figs. 2 to 4. The METFFT and MILFFT programs produce power and cross spectra which are graphed and also entered in the ANSWERS FILE. The MILDRV program skips bad data, low-pass and high-pass filters the mm-wave data to compensate for HF noise and instrumental drift, and writes 25.6-s statistics to MILSUMS. METDRV does a similar task for the micromet data, but filtering is unnecessary. The 25.6 s mm-wave and micromet statistics are graphed over the 2400 s extent of each data tape so that data quality and stationarity are checked; Fig. 8 shows examples of 25.6-s micromet statistics. METRDR and MILRDR then accumulate the statistics of a chosen stationary interval and enter the results in the ANSWER FILE.

The research was supported by the U.S. Army Research Office under Contracts DAAG29-81-K-0173, DAAG29-77-C-0026 and MIPR 122-A5.

1-3. McMillan, R.W., et al. *Opt. Eng.* 22, 1983; and *Proc. 9th Int'l. Conf. on Infrared and Millimeter Waves*, 463, 1984; and *SPIE Tech. Symp. East '85*, 1985.

4. Bohlander, R.A., et al. *Proc. of 8th Int'l. Conf. on Infrared and Millimeter Waves* 1983.

5. Hill, R.J., et al. NOAA Tech. Rep. ERL 429-WP260, 1985. Available from the authors.

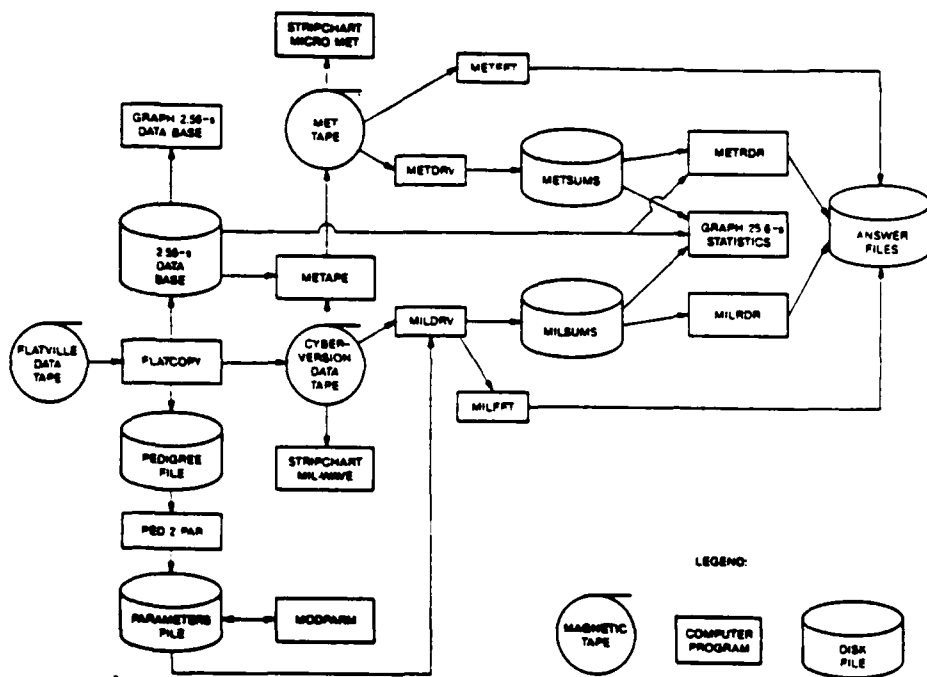


Fig. 1. This data processing scheme is discussed in the introduction.

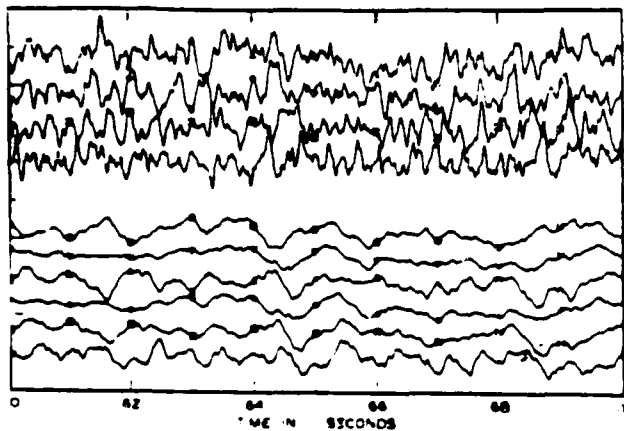


Fig. 2. Ten seconds of 100 Hz mm-wave data from Tape 24 of Session 1. From bottom to top the traces are the six phase differences from antenna pair 1 & 2, 1 & 3, 1 & 4, 2 & 3, 2 & 4, 3 & 4, followed by the intensities at antennas 1, 2, 3, and 4, respectively.

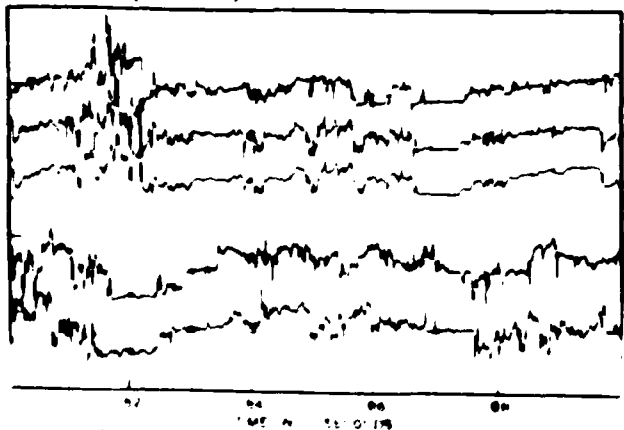


Fig. 3. Twenty seconds of 25 Hz sonic and propvane anemometer data from Tape 24 of Session 1. The bottom and top set of five curves are from met. sta. 1 and 2, respectively. From bottom to top within each set, the traces are from the two horizontal arms of the sonic with the smoother propvane-derived components overplotted; the vertical component from the sonic is the uppermost of each set.

Fig. 4. Ten seconds of 100 Hz resistance-wire temperatures and Lyman- $\alpha$  humidity from Tape 24 of Session 1. The top three curves are from met. sta. 2; the temperature within the sonic is the uppermost followed by the temperature within the Lyman- $\alpha$ ; the humidity is third from the top. The two bottom traces are from the wire thermometers at met. sta. 1; the humidity trace is missing because the Lyman- $\alpha$  was inoperative.

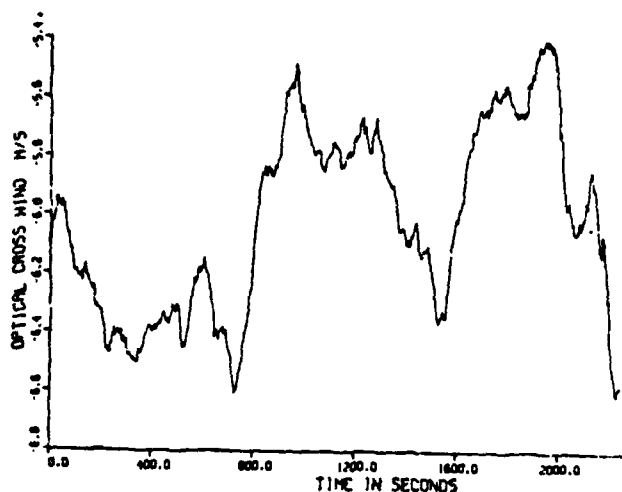


Fig. 5. The cross-path wind component from the 1 km optical path nearest the transmitter. The negative values mean that the wind is from the west. Data are from the entirety of Tape 24 of Session 1. The data is sampled every 2.56 s.

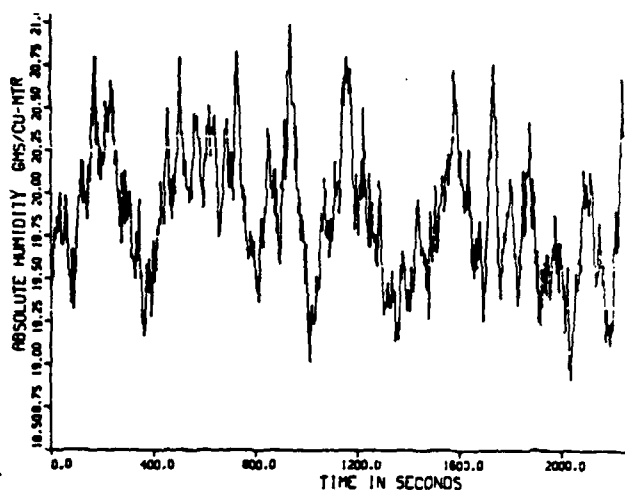


Fig. 7. The absolute humidity in  $\text{g/m}^3$  obtained from the aspirated psychrometer at met. sta. 1 for all of Tape 24 of Session 1. Sample rate was 2.56 s.

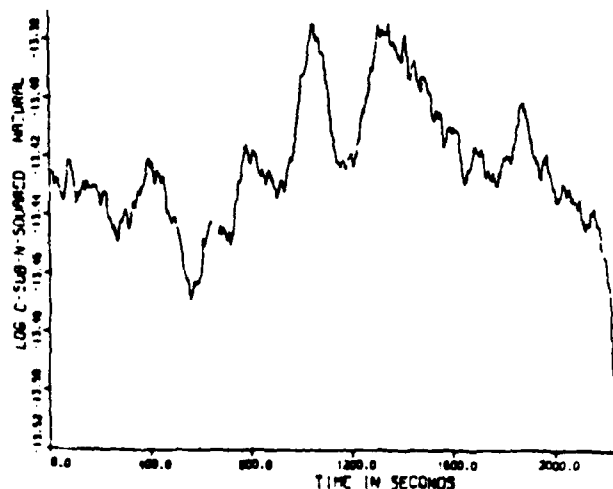


Fig. 6. The optical  $C_n^2$ , sampled every 2.56 s, from the 1 km optical propagation path nearest the receiver. The value of  $\log_{10} C_n^2$  in units  $\text{m}^{-2/3}$  is shown. Data are from all of Tape 24 of Session 1.

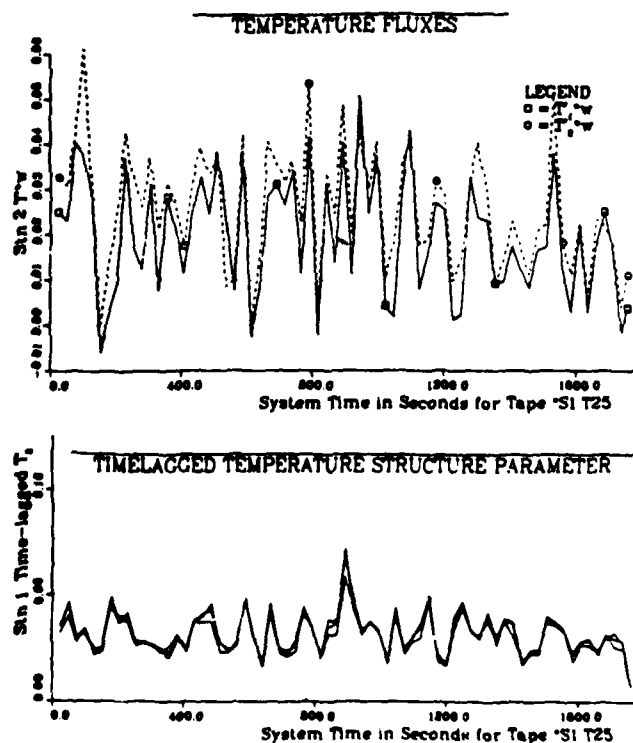


Fig. 8. 25.6-s averages of the temperature flux  $\langle T'w \rangle$  and the time-lagged temperature structure parameter; both are from met. sta. 1 for all of Tape 25 of Session 1. One  $\langle T'w \rangle$  is obtained from the resistance wire within the sonic while the other  $\langle T'w \rangle$  is from the wire in the Lyman- $\alpha$  gap. Three  $C_n^2$  are plotted corresponding to three different time lags; their agreement demonstrates inertial-range turbulence.

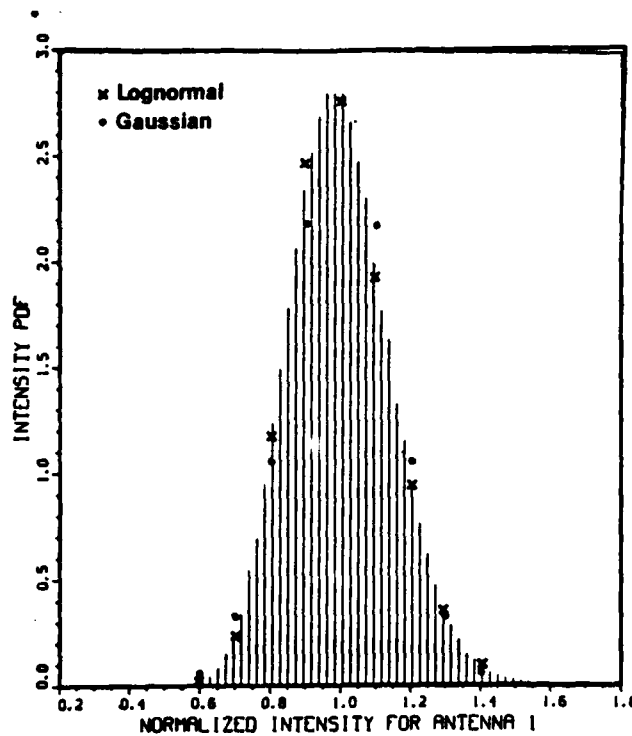


Fig. 9. Probability density function of intensity for antenna 1, Session 1, Tape 24, July 1983. Gaussian and lognormal PDFs are also shown. Normalized intensity is scaled to unit mean value. The PDF is normalized to unit area under the histogram.

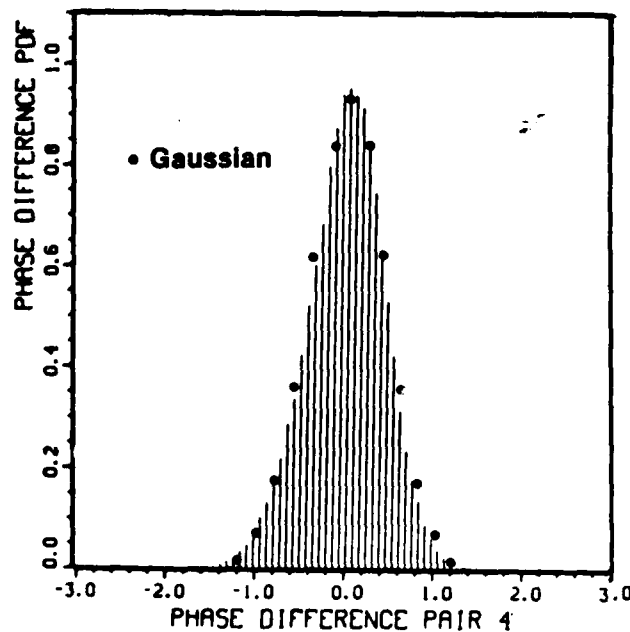


Fig. 10. Probability density of phase difference in radians for antenna pair 4, Session 1, Tape 24, July 1983. A Gaussian PDF is also shown. This PDF is normalized to unit area under the histogram.

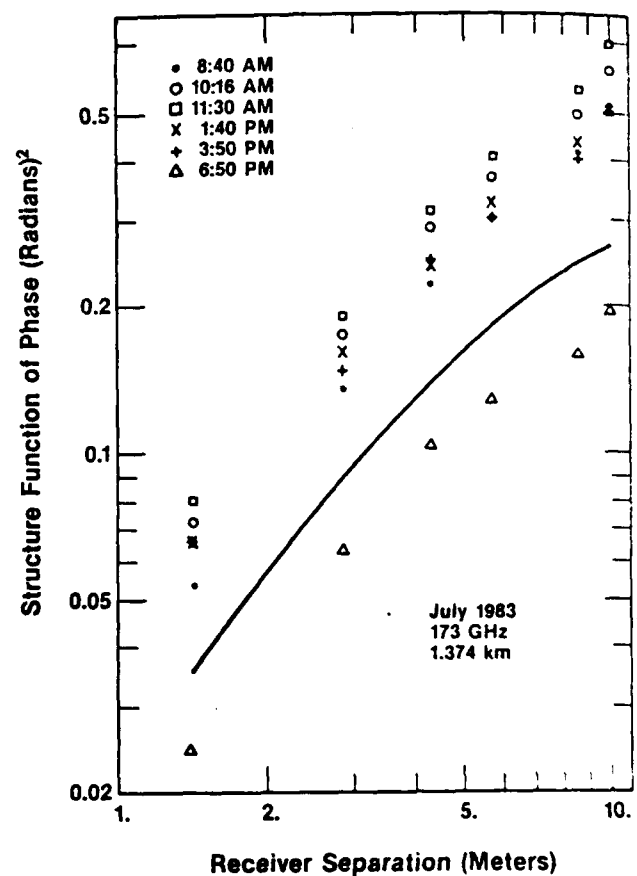


Fig. 11. The structure function of phase. The solid line represents a theoretical prediction for the 6:50 p.m. data, assuming a 2.2-m horizontal outer scale.

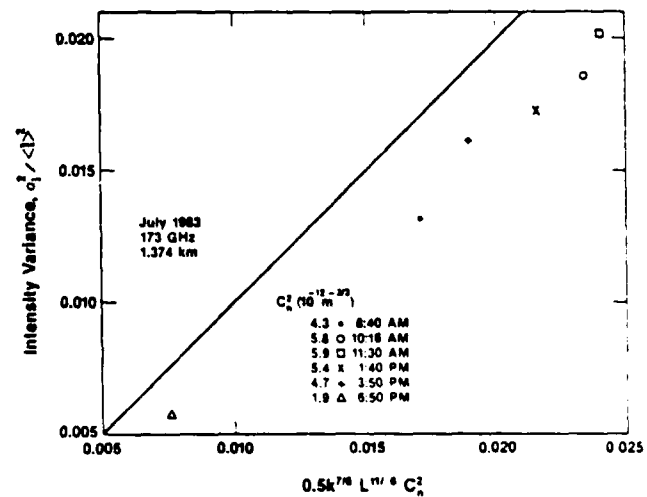


Fig. 12. The normalized variance of intensity versus its inertial-range formula. The straight line shows theoretical calculations.

# **Spectral Density and Distributions of Intensity and Phase of Millimeter Wave Signals Propagated through Rain, Fog, and Snow**

E. M. Patterson, R. A. Bohlander, R. W. McMillan, and R. L. Mandock  
Georgia Tech Research Institute, Georgia Institute of Technology  
Atlanta, GA 30332

R. J. Hill, J. T. Priestley, and S. F. Clifford  
National Oceanic and Atmospheric Administration, Wave Propagation Laboratory  
Boulder, CO 80303

B. E. Rishel  
Physical Sciences Laboratory, New Mexico State University  
Las Cruces, NM 88001

R. Olsen  
Atmospheric Sciences Laboratory  
White Sands Missile Range, NM 88002

## **ABSTRACT**

Spectral densities, structure functions, and distributions of intensity and phase fluctuations of millimeter-wave signals propagated through rain, fog, and snow have been calculated. These calculations are based on a series of millimeter-wave measurements made in the frequency range 116-230 GHz over a 1.4 km path near Flatville, Illinois, during several measurement sessions conducted during the period 1983-1985.

An extensive array of meteorological instrumentation and particle size spectrometers were used to characterize the atmospheric transmission path in these experiments, and this data is available to aid in the interpretation of the millimeter-wave data. The fluctuation spectra will be studied carefully to investigate differences between the clear air spectra and those affected by precipitation and to determine which features are uniquely related to the presence of rain, snow, and fog.

## **INTRODUCTION**

Clear air problems in the propagation of millimeter-waves are of considerable interest, but for a full understanding of the limitations imposed by the atmosphere on millimeter-wave system performance, it is necessary to have an understanding of the fluctuations caused by turbulence and by hydrometeor turbidity. The series of millimeter-wave measurements at Flatville, Illinois between 1983 and 1985 provided the opportunity for measurements of millimeter wave transmission in a wide variety of weather conditions that included rain, snow, and fog. Supporting meteorological data and particle microphysical data were also available to characterize the atmospheric transmission path.

## **MEASUREMENT AND ANALYSIS PROCEDURES**

The millimeter-wave data consists of intensity and phase data in the frequency range of 116 to 230 GHz across a propagation length of 1.4 km. Only one frequency was used at a time, and so not all atmospheric conditions were studied at all frequencies. MMW data were sampled at a rate of 100 Hz. For each data run, MMW data were collected for each of four antennas, designated by a number from 1 to 4, and for 6 antenna pairs, each with different spacing. These data were used to determine phase difference statistics for the different antenna pairs, intensity statistics for each antenna, mixed intensity and phase difference statistics, moments of the field, probability distribution functions for intensities and phase differences, and Fourier transforms of the temporal data for intensities and phase differences.

The power spectra are calculated for each of the four intensities and six phase differences. The computer programs also allow the calculation of cross spectra between two quantities. The power spectra are calculated by means of a fast Fourier transform algorithm on a 4096-point time series, corresponding to 40.96 seconds of data. A number of these transforms (10 to 20) are averaged together to increase the statistical reliability. The resulting transforms are combined to produce the power and cross-spectra, which are averaged to 36 spectral values in 36 approximately logarithmically spaced frequency bins.

Fourier components of lower frequency are obtained by block averaging the time series to 4096 points per data tape (or time stationary interval during which conditions were roughly uniform). The data tapes are roughly 2400 s in duration, so averages of roughly 0.6 sec suffice. These block averaged Fourier

transforms are also averaged to 36 logarithmically spaced frequency bins in a lower frequency range than the first set described.

NOAA micrometeorological data were obtained at two locations along the transmission path, whereas US Army Atmospheric Sciences Laboratory (ASL) particle data were obtained at one location. A complete description of the data analysis for the millimeter-wave data and the micrometeorological data is given in [1]; the results of the ASL analysis are given in a series of reports [2].

#### MEASUREMENT RESULTS

Although turbulence in clear air in humid conditions can produce the largest fluctuations yet observed, we have previously commented [3] that precipitation induced fluctuations in millimeter-wave signals can be significant. Fog, because it occurs when the atmosphere is very quiet, produces the least fluctuations of all.

The data collected during precipitation events is still in an early stage of analysis. We will concentrate here on a consideration of power spectra determined from millimeter-wave data measured on February 10 and 11, 1985 in the Tape 9 to 15 data runs of Session 5. (For this data set the Tape or T numbers refer to particular data runs). During this time there was a range of precipitation encountered that included mixed drizzle and snow, snow, and blowing snow.

Two examples of intensity power spectra calculated from the millimeter-wave data of this time period are shown in Figures 1 and 2. Figure 1, T9 data, shows the power spectrum for 230 GHz transmission calculated for antenna 3 using the individual data points (solid line) and the block averaged data (dashed line). The two lines diverge at lower frequencies, but the dashed line makes use of more of the data and is more significant statistically. The statistical significance of each increases with increasing frequency, and the two curves do converge.

T14 data are shown in Figure 2. As before the two curves represent individual (solid line) and block averaged (dashed line) data. The T14 data differs from the T9 data in that there is significantly more power associated with the high frequency fluctuations in T14 than in T9.

For comparison, T9 and T14 ASL particle size data are shown in Figures 3 and 4. The particle size spectra showed little variation during the individual data runs, and so the data shown in these figures are representative of the entire data periods. These particle size spectra, measured with the Ground Based Precipitation Probe, show that there were

significantly more large particles present during the T14 data run than during the T9 period. Although there is some uncertainty in the T9 particle size data, this uncertainty is not expected to alter the basic conclusions of the size differences in the data. It does appear in this preliminary analysis that the larger particles are associated with the greater power in the higher fluctuation frequencies.

We are aware that models of fluctuations in millimeter wave signals due to rain [4] have a similar shape to that which we observed in the T14 data. We will be working on modifying the rain models to model the fluctuations expected for snow conditions. We will also continue the analysis to determine the spectrum of phase fluctuations, structure functions and distributions of intensity and phase for the data considered above and for other millimeter-wave data.

#### REFERENCES

1. R. J. Hill, W. P. Schoenfeld, J. P. Riley, J. T. Priestley, S. F. Clifford, S. P. Eckes, R. A. Bohlander, and R. W. McMillan, "Data Analysis of the NOAA-GIT Millimeter-Wave Propagation Experiment near Flatville, Illinois", NOAA Technical Report ERL 429-WPL, 60, August, 1985.
2. R. O. Olsen, R. Okrasinski, B. Rishel, R. Valdez, and T. Chavez, "ARO MMW Field Program Flatville Particle Data", Vol 1-5, Unpublished report U. S. Army Atmospheric Sciences Laboratory, 1985.
3. R. A. Bohlander, R. W. McMillan, D. M. Guillory, R. H. Platt, R. J. Hill, S. F. Clifford, J. T. Priestley, R. E. Cupp, R. Olsen, B. E. Rishel, and R. Okrasinski, "Millimeter wave transmission fluctuations due to snow." Proceedings of Snow Symposium IV, U. S. Army Corps of Engineers, CRREL Special Report 84-35, December, 1984.
4. H. T. Yura, K. G. Barthel, and W. Buchtemann, "Rainfall induced Optical Phase Fluctuations in the Atmosphere", J. Opt. Soc. Am., 73, 1574-1580, 1983.

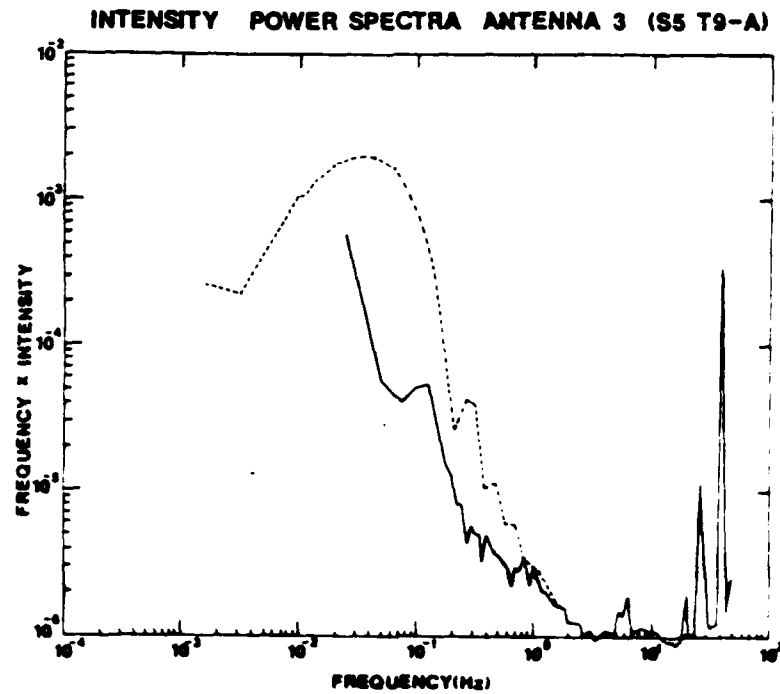


Figure 1. Intensity power spectra determined for Session 5 T9 230 GHz transmission data.

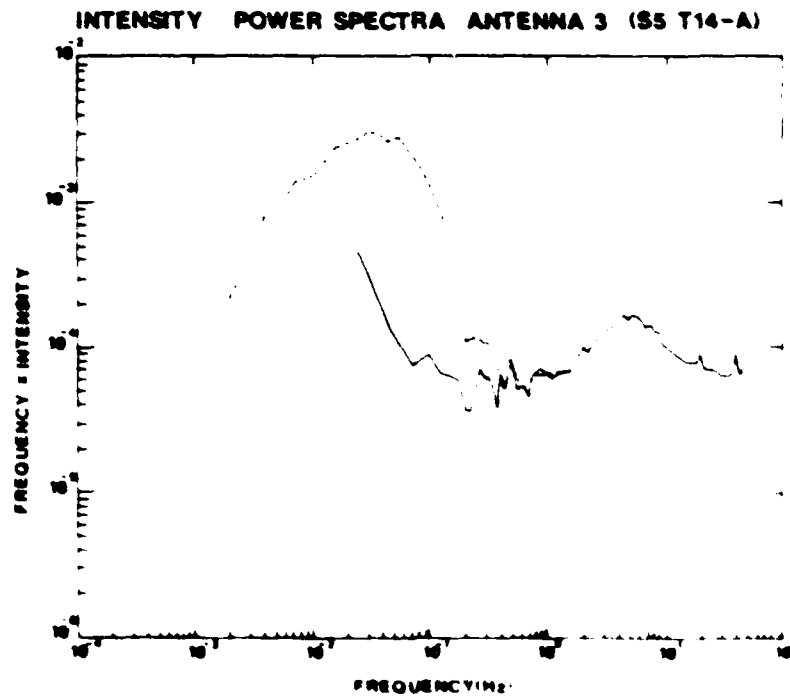


Figure 2. Intensity power spectra determined for Session 5 T14 230 GHz transmission data.

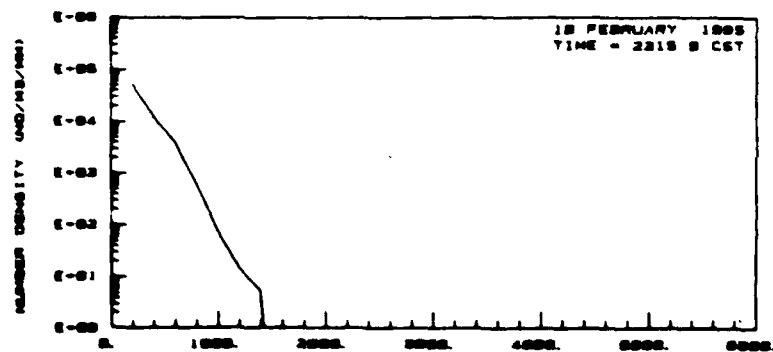


Figure 3. Particle size spectra determined from ASL Ground Based Precipitation Probe data for Session 5 T9.

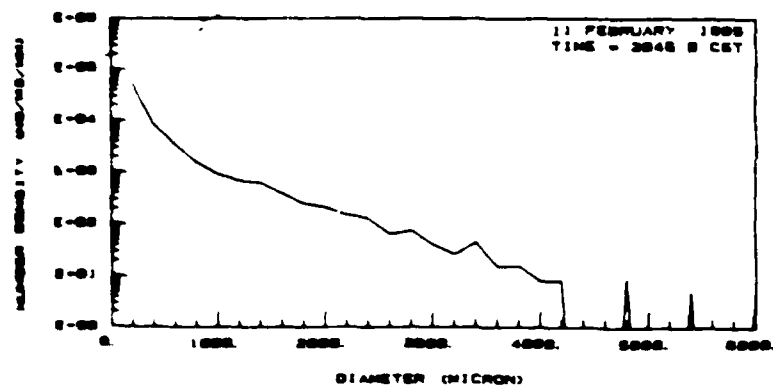


Figure 4. Particle size spectra determined from ASL Ground Based Precipitation Probe data for Session 5 T14.

# Correlation of the Attenuation of Millimeter Wave Signals with Rain Rate

E. M. Patterson, R. L. Mandock, R. W. McMillan,  
and R. A. Bohlander

Georgia Tech Research Institute  
Georgia Institute of Technology  
Atlanta, GA 30332

R. J. Hill, J. T. Priestley  
National Oceanic and Atmospheric Administration  
Wave Propagation Laboratory  
Boulder, CO 80303

B. E. Rishel  
Physical Sciences Laboratory  
New Mexico State University  
Las Cruces, NM 88001

R. Olsen  
Atmospheric Sciences Laboratory  
White Sands Missile Range, NM 88002

## ABSTRACT

Measurements were made of the attenuation of millimeter-wave (MMW) signals by hydrometeors during an extensive study of atmospheric MMW transmission properties between 1983 and 1985 at an instrumented site near Flatville, IL. Data collected during this study showed a marked correlation between the attenuation of MMW signals and the rain rate. The purpose of this report is to discuss quantitatively the relation between the attenuation of MMW signals and the rainfall parameters, including rain rate, volume mixing ratios and precipitation particle size distributions.

## INTRODUCTION

Although clear air problems are of considerable interest, it is recognized that the development of millimeter wave (MMW) systems is presently motivated largely by their capabilities in adverse weather. It is essential, then to have a quantitative understanding of the effects of precipitation on the MMW signal. This will include an understanding of the fluctuations caused by the hydrometeor turbidity as well as an understanding of the attenuation of the MMW signal due to the presence of the hydrometeors. A study of the attenuation of MMW signals by rain and snow was not an original goal of the Flatville experiments. In particular, the calibration of the instrumentation was not stable over long periods making it unsuitable for measuring long term precipitation changes. However, precipitation events were often short in duration that the relative contribution due to the hydrometeors

could be determined. This attenuation could then be related to measured precipitation parameters, including rain rate data, determined by in situ and by gravimetric techniques, and particle concentration data.

## ATTENUATION DUE TO PRECIPITATION IN RELATION TO PRECIPITATION PARAMETERS

The attenuation or extinction coefficient  $\sigma_e$  is related to the particle size distribution by the equation

$$\sigma_e = \int \pi r^2 Q_e(r) N(r) dr$$

with  $r$  the particle radius,  $N(r)$  the number concentration of the particles as a function of radius, and  $Q_e$  the efficiency factor for extinction.  $Q_e$  is determined by Mie scattering theory and is dependent on the ratio of particle size to incident wavelength and the complex refractive index of the particles. A similar equation may be used to describe the extinction of snow particles, but snow is not composed of spherical particles and so the Mie calculations will be only approximately correct. A more exact treatment must consider the effects of the shape of the snow particles as well as of refractive indices that differ from those of pure ice.

The volume concentration of the water in the precipitation is given by the equation

$$\text{Vol} = \int \frac{4}{3} \pi r^3 N(r) dr$$

The volume concentration may be expressed as the mixing ratio of the volume of the hydrometeors in a given volume of air. Multiplication by the density of water or the effective density of the snow will give the mass of precipitation per volume of air. The rain rate,  $R$ , expressed in terms of millimeters of water per hour or some other convenient length units, is proportional to

$$\int \frac{4}{3} \pi r^3 N(r) C_s(r) dr$$

with  $C_s(r)$  the settling velocity of the hydrometeors.

If the size distribution is constant, the MMW attenuation will be proportional to both the volume concentration of the water and the rainfall rate. The ratio of MMW attenuation to rainfall rate or to the volume concentration will also change with changes in the particle size distribution.

In order to estimate the magnitude of the effects of varying hydrometeor size on MMW transmission at 230 GHz, we have calculated the expected attenuation for several representative monodisperse particle sizes. The results of these calculations are shown as the solid lines in Figures 1 and 2. Figure 1 shows the expected extinction at 230 GHz as a function of the volume concentration of water ( $\text{cm}^3$  of water/ $\text{cm}^3$  of air) for droplet sizes of 0.5 mm, 1 mm, 2 mm and 4 mm diameter; Figure 2 shows the comparable MMW attenuation as a function of rain rate (expressed in mm/h rain) for the same droplet sizes. For comparison, the comparable calculations for 35 GHz are also shown. While there are significant differences in the slopes of the lines for the smaller droplets, there appears to be much less difference in the calculated slopes for particles in the 2 to 4 mm diameter range. Similar calculations for integrated size distributions such as the Marshall-Palmer distribution are, of course, planned as part of future efforts.

#### MEASUREMENTS AT FLATVILLE

The measurement program for the Flatville experiments included millimeter wave propagation measurements in the frequency range 116-230 GHz over a path length of 1.4 km, as well as measurements of a variety of micrometeorological parameters and of particle size spectra for aerosols and for hydrometeors. Since the data did allow the determination of the attenuation due to hydrometeors, one of the goals of our analysis is the comparison of observed values with ones

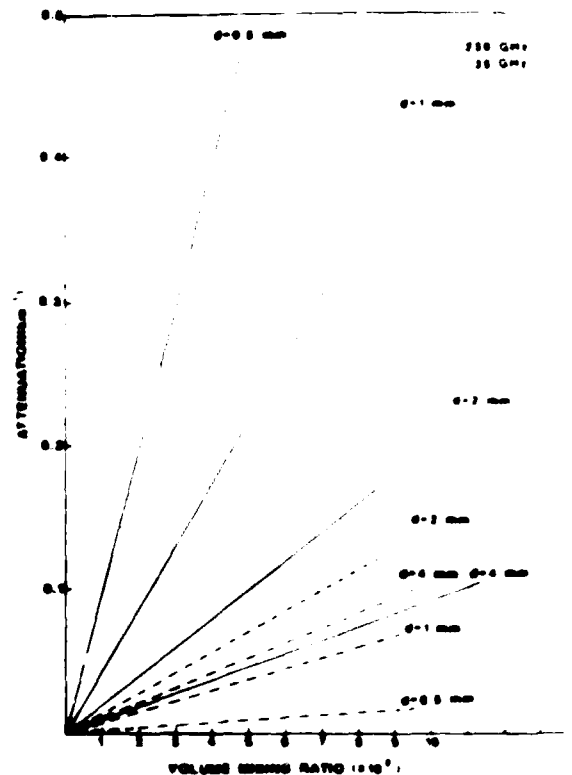


Figure 1. Attenuation coefficient calculated for monodisperse rain particles of 0.5, 1, 2, and 4 mm plotted against the volume mixing ratio for rain water in air. Lines are plotted for 230 GHz (solid line) and 35 GHz (dashed line).

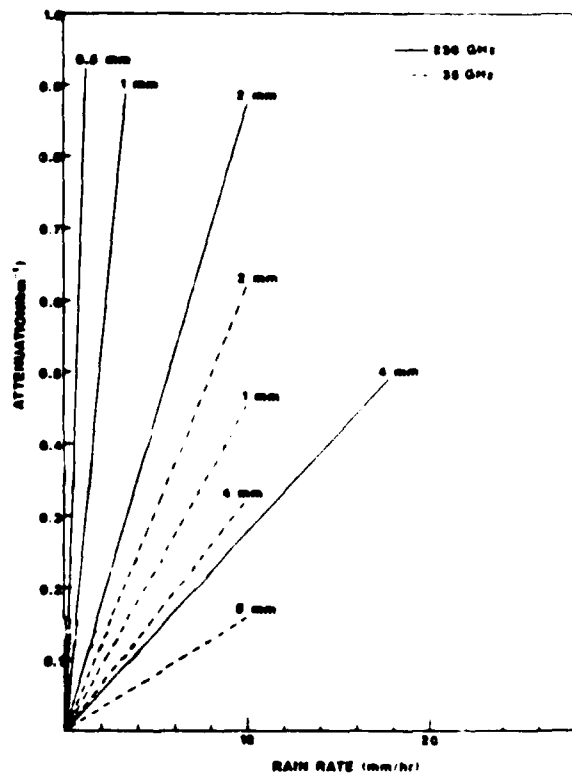


Figure 2. Attenuation coefficient calculated for monodisperse rain particles of 0.5, 1, 2, and 4 mm plotted against rain rate. Lines are plotted for 230 GHz (solid line) and 35 GHz (dashed line).

calculated from models of rain effects [1]. Of particular interest are the high MMW frequency range, for which there are few previous measurements, and the availability of detailed hydrometeor characterizations. More complete discussions of the experimental measurements are given in Hill et al. [2] and Bohlander et al. [3].

Rain rate was measured in two independent sets of measurements. Weighing buckets were set up to collect the precipitation and to record the increase in weight on a chart record. Rain rate was also measured by means of a laser rain gauge in which the sizes and fall rates of the particles are determined *in situ*, with the rain rate determined from these data. For our initial analysis, data from a single weighing bucket as used. There is always a question of the representativeness of the data when any one precipitation gauge is used, and so additional data from the laser probes and additional rain bucket data will be used in subsequent analyses.

Particle sizes were measured by U.S. Army Atmospheric Sciences Laboratory personnel using several different Particle Measurement Systems probes, including a CSASP probe for aerosol particles, a 2D-C probe for sizing particles up to .64 mm diameter, and a Ground-Based Precipitation Probe and a 2D-P Array Spectrometer for sizing particles up to 6.4 mm diameter. The data output from these probes is in the form of particle counts per meter per size interval from which total particle volume and volume mixing ratios can be calculated. Given hydrometeor fall velocities as a function of size, the rainfall rate can also be determined from the data. In addition, the attenuation properties of the hydrometeors can be calculated by means of Mie theory as discussed above, given appropriate optical constants.

#### DISCUSSION OF RESULTS

There were several cases during Measurement Series 3, 4, and 5 in which a variation in the intensity of the transmitted millimeter waves was observed that could be related to variation in the rate of the precipitation or the size characteristics of the hydrometeors. The analysis is still in progress, so we will not present final data. We will present some preliminary data relating MMW attenuation to rain rate and to the volume mixing ratios and will indicate planned future work.

An example of the relation of the MMW attenuation to the rain data is shown in Figure 3. In this figure the attenuation coefficient is plotted against the rain rate for Session 5 T9,

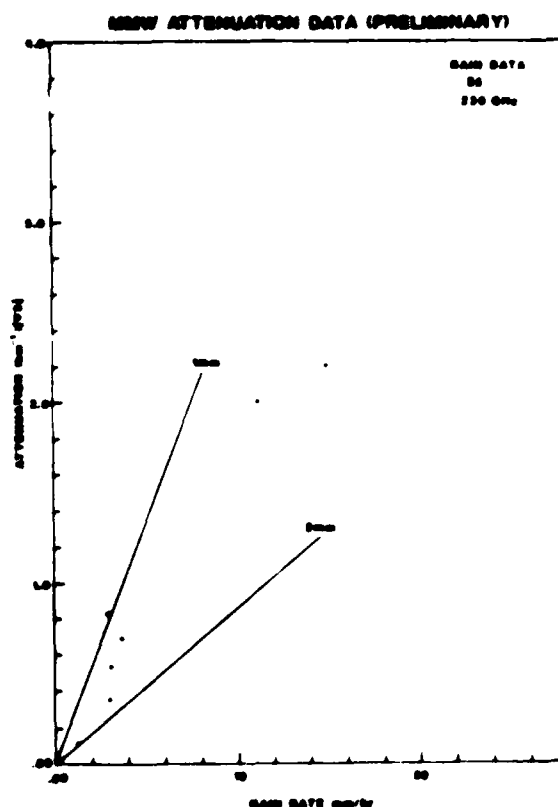


Figure 3. Preliminary MMW attenuation data for Session 5 plotted against rain rate data. Lines of the attenuation expected for 1 and 2 mm diameter droplets are also shown in the figure.

T11, T51, and T52 and Session 4 T76 data. (Tape or T numbers designate individual data runs.) It appears from this admittedly small sample that, while there is some scatter in the data, there is also a reasonable correlation between the attenuation coefficient and the rain rate. We have also included in the figure, lines that show the relations expected for monodisperse 1 and 2 mm particles, indicating that the observed variation is consistent with that expected for 1 to 2 mm particles.

An example of the particle size data is shown in Figure 4 in which Ground-Based Precipitation Probe data from the T9 period of Session 5 are plotted. Attenuation coefficients calculated from the MMW data for this period are plotted against volume mixing ratios calculated from the particle data in Figure 5. For comparison, the line expected for monodisperse 1 mm particles is also shown on the figure. Again, we can say that the data are consistent with expectations.

At the present point in our analysis we can say that the attenuation coefficients are correlated with both rainfall rate and with volume mixing ratios and that the variation in attenuation is consistent with that expected on the basis of the particle size distributions. In future efforts

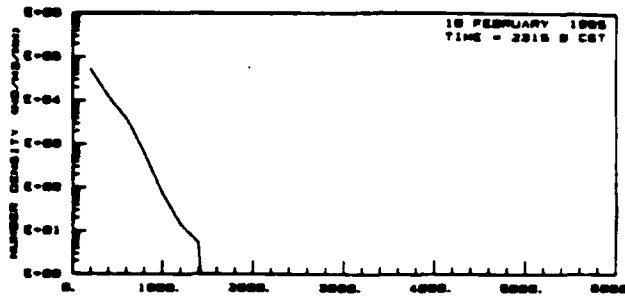


Figure 4. A hydrometeor size distribution determined from Ground-Based Precipitation Probe data collected during the T9 period of Session 5.

we plan to look at the MMW data in relation to data from the laser rain gauge which has higher time resolution. We will also examine the variation of MMW attenuation with variation in rain rate and in hydrometeor volume ratios. We will use Mie theory to calculate the expected attenuation from the measured size distributions as well as standard distributions and will use this data to attempt to account for variations in the observed attenuations. We will also attempt to relate the attenuation measured during snow episodes to snow microphysical parameters and differences between the liquid droplet data and the snow data in terms of the differing properties of the snow and the liquid precipitation.

#### References

1. T. Oguchi, "Electromagnetic Wave Propagation and Scattering in Rain and Other hydrometeors, Proc. IEEE, 71, 1029-1078, 1983.
2. R. J. Hill, W. P. Schoenfield, J. P. Riley, J. T. Priestley, S. F. Clifford, S. P. Eckes, R.A. Bohlander and R.W. McMillan, "Data Analysis of the NOAA-GIT Millimeter-Wave Propagation Experiment near Flatville, Illinois", NOAA Technical Report ERL 429-WPL, 60, August 1985.
3. R. A. Bohlander, R. W. McMillan, D. M. Guillory, R. H. Platt, R. J. Hill, S. F. Clifford, J. T. Priestley, R. E. Cupp, R. Olson, B. E. Rishel, and R. Okrasinski, "Millimeter wave transmission fluctuations due to snow." Proceedings of Snow Symposium IV, U.S. Army Corps of Engineers, CRREL Special Report 84-35, December 1984.

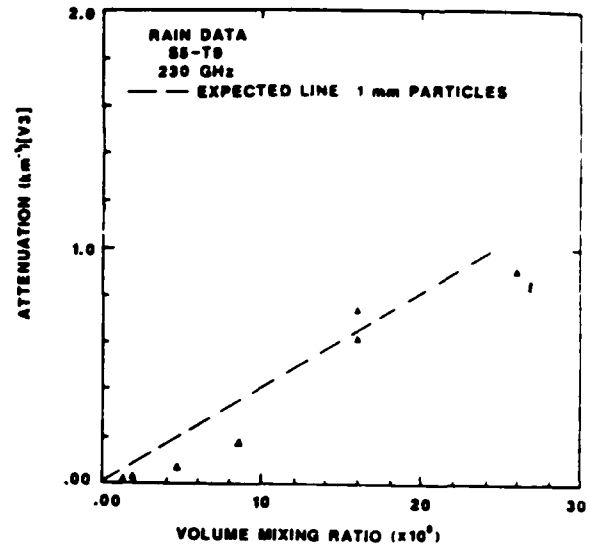


Figure 5. MMW Attenuation data at 230 GHz measured during Session 5 plotted against the volume mixing ratio determined from the Ground-Based Precipitation Probe data. The attenuation expected for 1 mm diameter particles as also shown as a dashed line.

# LINE-OF-SIGHT MILLIMETER WAVE PROPAGATION CHARACTERISTICS

S.F. Clifford, R.J. Hill, and R.B. Fritz  
NOAA/ERL/Wave Propagation Laboratory  
325 Broadway  
Boulder, Colorado 80303

R.A. Bohlander and R.W. McMillan  
Georgia Institute of Technology  
Atlanta, Georgia 30332

## ABSTRACT

From 1983 to 1985 a team of scientists from NOAA's Wave Propagation Laboratory and Georgia Institute of Technology conducted an extensive set of millimeter wave propagation measurements. In five, thirty-day sessions, chosen for the widest variety of weather conditions, we propagated millimeter wave frequencies from 116 to 230 GHz over a 1.4 km horizontal path in Flatville, Illinois. Simultaneous, extensive measurements of the meteorology allowed a detailed comparison of the propagation characteristics with the current state of the atmosphere. We report on the observations of millimeter wave propagation characteristics during clear air and severe weather. Amplitude and phase spectra for propagation in clear air are compared with theory derived using the weak refractive turbulence approximation. Excellent agreement is found. Further, probability density functions appear to be; respectively, lognormal (amplitude) and Gaussian (phase difference), as expected from application of the central limit theorem. Interesting meteorological observations and their millimeter wave signatures will also be presented.

## INTRODUCTION

Over the past five years a team of scientists from the National Oceanic and Atmospheric Administration and the Georgia Institute of Technology conducted an extensive set of millimeter-wave propagation measurements. In five, thirty-day sessions, chosen for the widest variety of weather conditions, we propagated millimeter wave frequencies from 116 to 230 GHz over our 1.4 km horizontal path in Flatville, Illinois. Simultaneous, extensive measurements of the meteorology allowed detailed comparisons of the propagation effects with the state of the atmosphere.

The details of the experiment layout and data processing are contained in Reference 1. (Table 1 and Figs. 1-6 of this paper are extracted from Reference 1.) Figure 1 illustrates the propagation geometry. The beam propagated 1.4 km - 4 meters above an extremely flat terrain, chosen for its outstanding fetch in all wind directions. This enabled us to characterize the site micrometeorology with two instrumented towers using Monin-Obukov surface-layer similarity theory. The intensity fluctuations were measured at each of the four horizontally spaced antennas and phase differences were measured among all possible antenna pairs with spacings from 1.43 to a 10 m maximum. The fifth antenna was used in a limited way to test the isotropy of the different wave parameter fluctuations.

A variety of meteorological measurements were obtained simultaneously with the millimeter-wave data. Figure 1 shows the optical propagation paths which give optical refractive-index structure parameter  $C_n^2$  as well as the cross-path component of the wind. Figure 1 also shows the optical rain gauge, optical drop size disdrometers, and the weighing bucket rain gauges. Two micrometeorological stations are shown on Fig. 1; these are 4 m high instrumented towers. At these stations the mean temperature and humidity were recorded, a prop-vane gave wind speed and direction, a three-axis sonic anemometer gave the fluctuating components of the wind vector, platinum resistance-wire thermometers gave the fluctuating temperature, and Lyman- $\alpha$  hygrometers recorded the humidity fluctuations. The millimeter-wave signals, resistance-wire temperature, and Lyman- $\alpha$  humidity were digitized at 100 Hz. The sonic anemometers were digitized at 25 Hz. The other instrument's signals were digitized at 0.39 Hz. Table 1 shows the great variety of clear-air micrometeorological statistics available from our instrumentation.

Figure 2 shows a probability density function (PDF) of the measured intensity; it is compared with lognormal and Gaussian PDFs. At such small intensity variances (0.02) there is little difference between lognormal and Gaussian PDFs, but the data definitely favors the lognormal PDF. Figure 3 shows the PDF of phase difference obtained from antennas 2 and 3, which have a separation of 2.9 m. This PDF is clearly Gaussian. In addition, we find that intensity and phase difference are uncorrelated.

Figure 4 shows the structure function of phase for each of our antenna pairs (separations). The structure function is definitely less steep than the slope of 5/3 that would be predicted by a Kolmogorov inertial-subrange model. This is caused by the outer scale. A very simple prediction that includes the effects of the outer scale is shown as a solid curve for a horizontal outer scale of 2.2 m. The mutual coherence function (second moment of the field) is shown in Fig. 5. Since the log-intensity and phase difference are both Gaussian and uncorrelated it follows from the weak turbulence

theory that the mutual coherence function should be equal to  $\exp[-.5(D_A + D_S)]$  where  $D_A$  and  $D_S$  are the log-amplitude and phase structure functions. We find that this formula predicts the values in Fig. 5 to within 0.5%.

In Fig. 6 we show the normalized variance of intensity versus the inertial range prediction for a spherical wave. Here the radio  $C_n^2$  is obtained from the micrometeorological data. We see that the intensity variance is somewhat underestimated by the inertial-range prediction but consistent with the phase structure function shown in Fig. 4. This discrepancy is most probably because of difficulties in calibrating the hygrometer.

#### PHASE AND AMPLITUDE SPECTRA

Using the spherical-wave theory for propagation through refractive turbulence, Clifford shows that the temporal power spectrum of log-amplitude fluctuations in the single scattering or weak turbulence limit has the form shown labeled "theory" in Fig. 7. In addition Fig. 7 contains a log-log plot of  $(f/f_0)$  times the log-amplitude spectrum  $W_x$  versus normalized frequency  $(f/f_0)$ . The spectrum  $W_x$  is normalized to the log-amplitude variance such that the area under the curve is unity. The frequency  $f_0 = v/2\pi L$ , where  $v$  is the cross-path component of windspeed,  $\lambda$  is the wavelength, and  $L = 1.4$  km is the millimeter-wave path length. The dotted (solid) fluctuating curve represents the low (high) frequency Fourier transform of 35 min of log-amplitude data taken at 142 GHz. The solid "theory" curve fits the data quite well until the high frequency tail beyond  $\log(f/f_0) = 1$ , where aperture averaging effects are important. The dashed curve is a plot of the theory including aperture averaging effects; overall, the fit to the data is excellent. Deviations at low frequencies above the "theory" curve are most likely due to receiver antenna drift. It is possible from the theory to estimate the cross-path velocity from the location of the peak. The peak is predicted at  $\log(f/f_0) \sim 0.43$ . In the case shown the cross-path velocity estimate from the millimeter wave scintillations agrees with the prop vane to within a few percent. (Note, the data were plotted with  $f_0$  calculated from prop vane-measured crosswind.)

Figure 8 illustrates the theoretical spectra for phase difference fluctuations. In contrast to the log-amplitude result phase-difference is very sensitive to the "outer scale"  $L_0$  of the refractive index fluctuations. Consequently, we have a family of curves for different values of the spacing  $\rho$  normalized to  $L_0$ . ( $L_0$  is the size of the largest eddy for which the assumption of isotropy holds, so  $L_0$  is the order of the height above the ground). The theoretical curves are plotted versus normalized frequency  $f/f_1$  where  $f_1 = v/\rho$  and  $v$  is the cross-path wind component. From our knowledge of the wind speed and the dependence of the spectra on  $\rho/L_0$ , we can estimate  $L_0$  from a spectrum measured at a known separation, e.g.,  $\rho_{12} = 1.43$  m, and use that derived value  $L_0 \sim 2.8$  m for all further comparisons.

Figures 9 and 10 show the theoretical curves superimposed over the phase-difference spectra from the data for antenna pairs (1,2) separated by  $\rho_{12} = 1.43$  m and antenna pair (1,4) separated by  $\rho_{14} = 10$  m. We used the value  $L_0 \sim 2.8$  m and selected our curves from Fig. 8 to fit the data based on the ratios  $\rho_{12}/L_0 = 0.51$  and  $\rho_{14}/L_0 = 3.5$  appropriate to each antenna pair. The resulting fit is quite good. We could also estimate crosswind from the peak of the spectrum if we knew the accurate  $L_0$  from other independent measurement.

#### MILLIMETER PROPAGATION THROUGH RAIN

Figures 11 and 12 illustrate a unique measurement of a rain event where the effects of oscillations in rain rate were observed simultaneously by the millimeter wave link and two laser-beam rain gauges, deployed as shown in Fig. 1. An oscillating rain rate, probably caused by a convective instability in the cloud cover, could explain the observed temporal pattern of the rain. In Fig. 12 the rain fluctuations are compared with the simultaneously measured attenuation fluctuations. As expected, a very high correlation between the two is observed. The lowest curve in Fig. 12, illustrates a simulated attenuation time curve that would result by assuming a sinusoidal convective disturbance propagating along the millimeter path. A more detailed description is available in Reference 3.

#### CONCLUSIONS

The Flatville data set has been analyzed to show the effects of clear air and rain on millimeter wave systems. We have reported only a minute amount of the available data and show that the results agree quite closely with the clear-air single-scatter theory for propagation in the turbulent atmosphere. We intend to make much more extensive comparisons in the future for propagation in clear air, rain, fog, and snow. We made a deliberate choice to forgo analysis of other segments of the data in order to complete a readily accessible data base for study by both NOAA/GIT and other researchers. The completed data base should be available for study in 1987.

#### ACKNOWLEDGMENT

1. Mill, R.J., W.P. Schoenfeld, J.P. Riley, J.T. Priestley, S.P. Clifford, S.P. Eches, R.A. Bohlander, and R.W. McMillan, "Data analysis of the NOAA/GIT millimeter wave propagation experiment near Flatville, Illinois." NOAA Technical Report. ERL 429-WPL 60, U.S. Government Printing Office, Washington, D.C., (August, 1985).
2. Clifford, S.P., "Temporal-frequency spectra for a spherical wave propagating through atmospheric turbulence." J. Opt. Soc. Am., 61, 1285, (1971).
3. Frits, R.B., R.J. Mill, J.T. Priestley, and W.P. Schoenfeld. "Evidence for oscillatory rain rate in a midwestern winter rain." (To appear in Climate and Applied Meteorology).

Table 1.--Summary of micrometeorological data from tape 24,  
taken at 11:30 MDT July 1983

Average Values	
Humidity	19 g/m <sup>3</sup>
Temperature	32°C
Wind speed	5.3 m/s
Wind angle	10°
Pressure	993 mb
Solar flux	94% of full sun
Wind stress	-0.14 (m/s) <sup>2</sup>
Humidity flux	0.1 (g/m <sup>2</sup> )/s
Temperature flux	0.03°C m/s
Stability	-0.03
Square Roots of Variances	
Humidity	0.72 g/m <sup>3</sup>
Temperature	0.35°C
Wind speed	1.2 m/s
Wind angle	11°
Streamwise wind component	1.1 m/s
Cross-stream wind component	1.0 m/s
Vertical wind component	0.54 m/s
Structure Parameters	
$C_n^2$ from optical scintillometers	$2 \times 10^{-13} \text{ m}^{-2/3}$
$C_T^2$ from optical $C_n^2$	$0.03^\circ\text{C}^2 \text{ m}^{-2/3}$
$C_T^2$ from resistance wires	$0.03^\circ\text{C}^2 \text{ m}^{-2/3}$
$C_q^2$ from Lyman- $\alpha$ hygrometers	$0.2 (\text{g/m}^3)^2 \text{ m}^{-2/3}$
$C_{Tq}$ from resistance wires and Lyman- $\alpha$ hygrometers	$0.075^\circ\text{C} (\text{g/m}^3) \text{ m}^{-2/3}$
$C_n^2$ for radio frequencies*	$5.9 \times 10^{-12} \text{ m}^{-2/3}$

\*Obtained from Eq. (79) of Ref. 1, using  $C_T^2$ ,  $C_q^2$ , and  $C_{Tq}$  from the resistance wire thermometer and Lyman- $\alpha$  hygrometer with  $A_T^q$  and  $A_q$  obtained from the radio refractive-index equation.

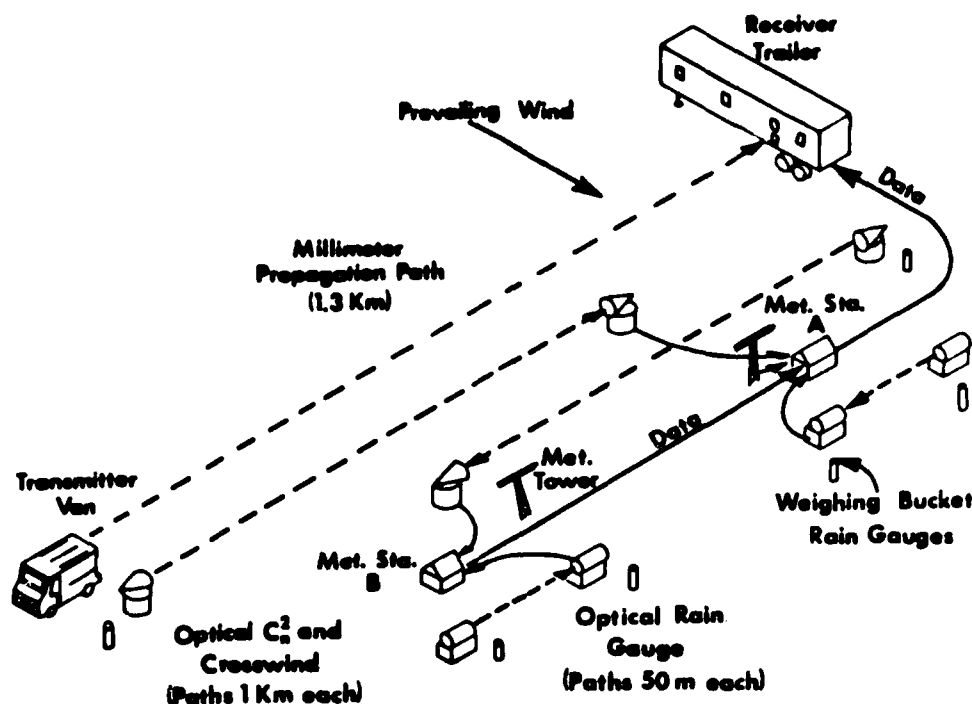


Figure 1. The instrument positions at the experiment site. The dashed and dotted line denotes mm-wave propagation path (1.4 km); the long-dashed lines, the optical propagation paths (1 km each); and the short-dashed lines, the optical rain gauge paths (50 m each). Solid lines show the flow of micrometeorological data to the data acquisition system in the receiver trailer. Antennas are numbered 1 to 5 in the receiver trailer.

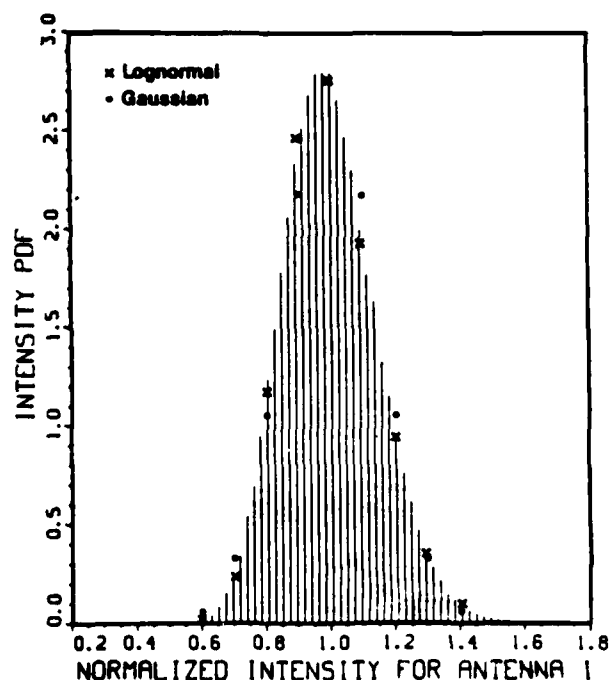


Figure 2. Probability distribution function of intensity for antenna 1. Normalized intensity is scaled to unit mean value.

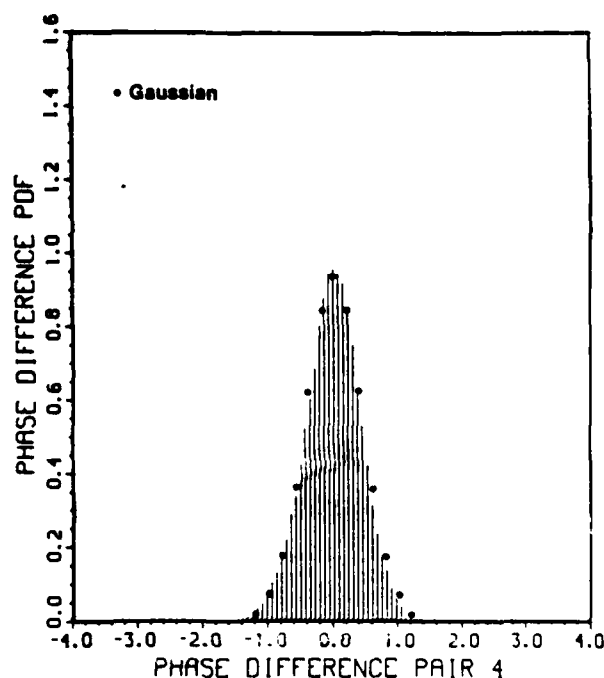


Figure 3. Probability distribution of phase difference in radians.

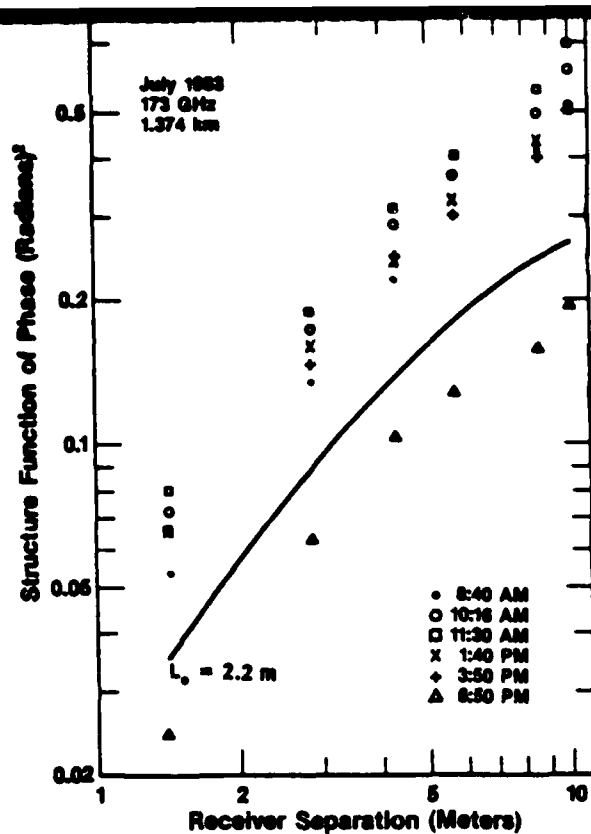


Figure 4. The structure function of phase. The solid line represents a theoretical prediction for the 6:50 p.m. data.

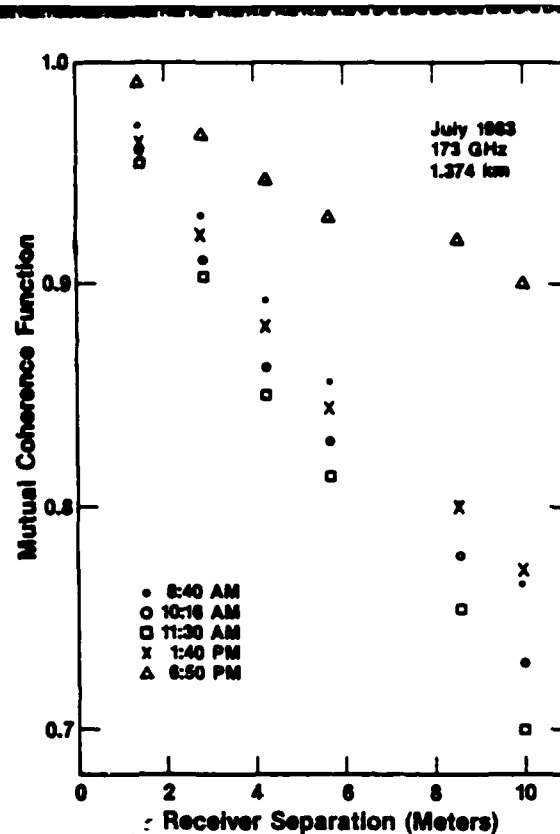


Figure 5. The modulus of the mutual coherence function.

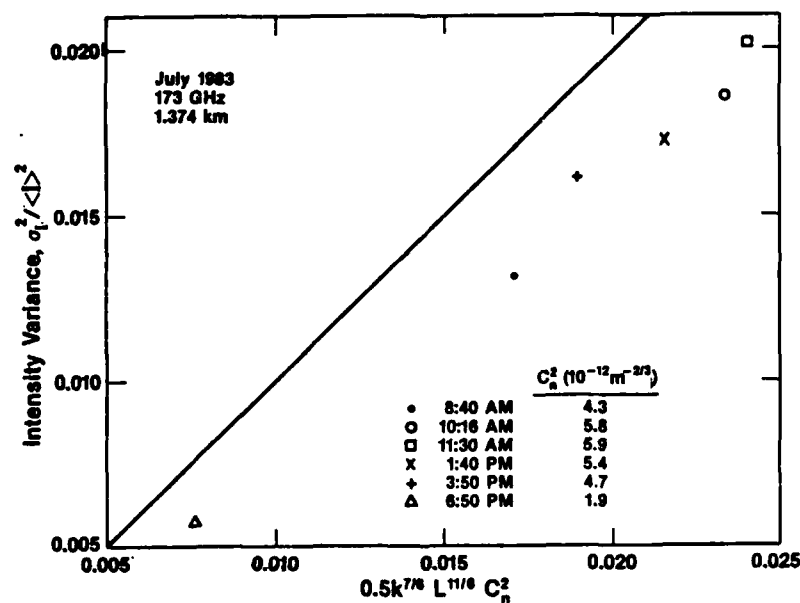


Figure 6. The normalized variance of intensity versus its inertial-range formula. The straight line shows theoretical calculations.

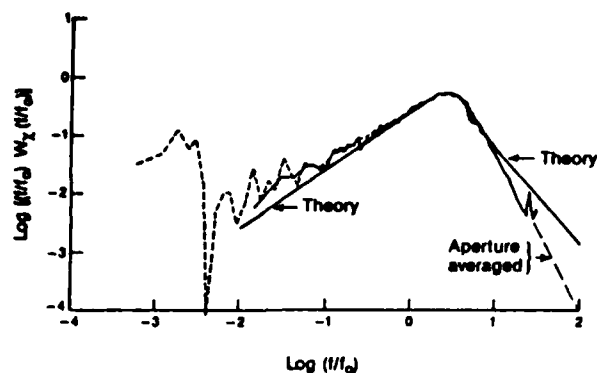


Figure 7. Theoretical and experimental power spectra of amplitude fluctuations.

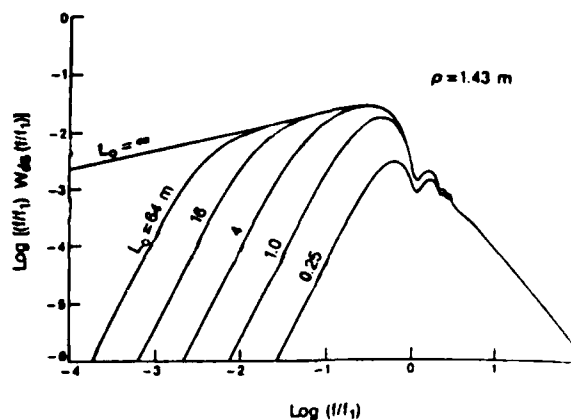


Figure 8. Theoretical power spectra or phase difference fluctuations as a function of the ratio or spacing to the outer scale  $\rho/L_0$  and characteristic frequency  $f_1 = v/\rho$  where  $v$  is the cross-path wind.

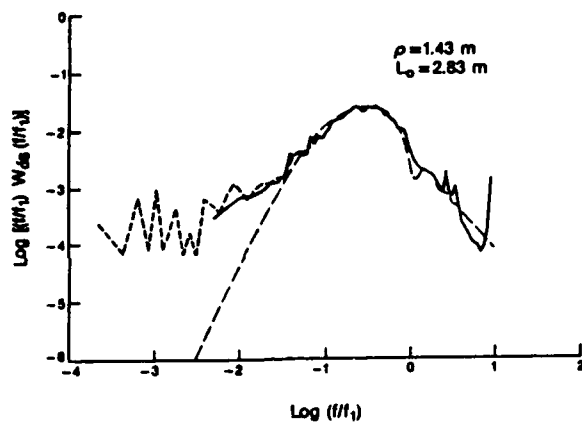


Figure 9. Comparison of theoretical and measured spectra of phase difference for spacing  $\rho_{12} = 1.43$  m.

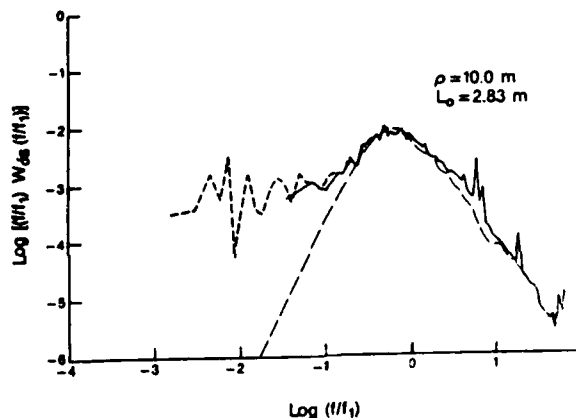


Figure 10. Comparison of theoretical and measured spectra of phase difference for spacing  $\rho_{14} = 10$  m.

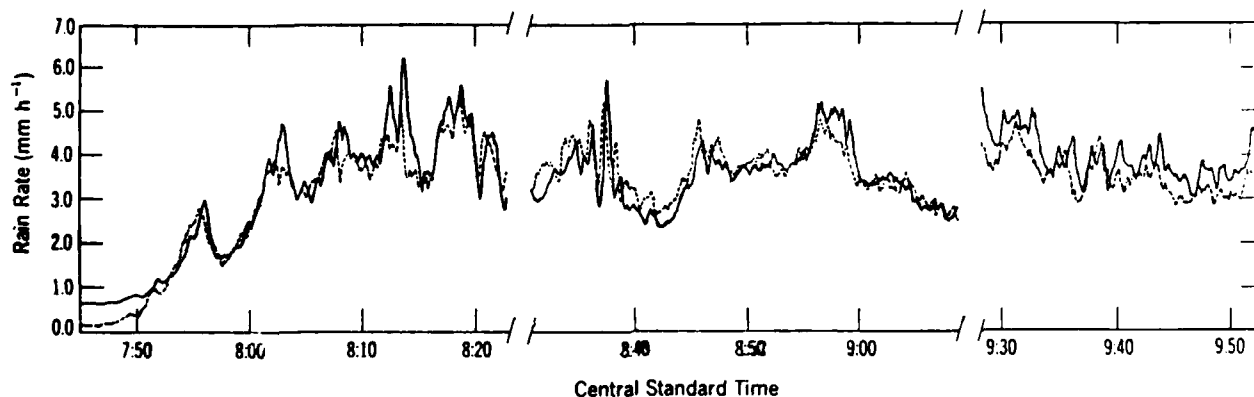


Figure 11. Time series of rain rates measured by path-averaging optical rain gauges. Note oscillatory feature at approximately 0837 CST.

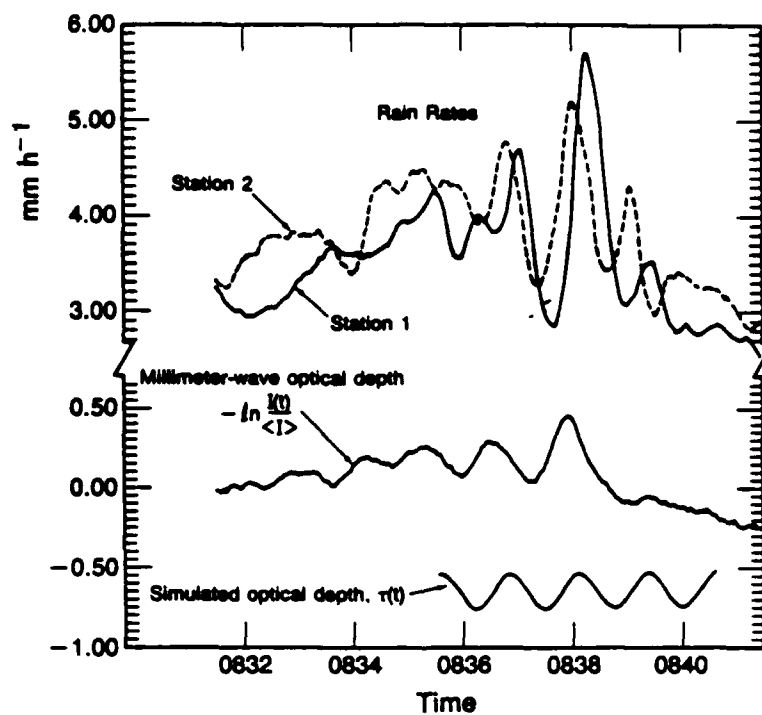


Figure 12. Detail of rain rates and millimeter-wave attenuation, 0832-0841 CST. Bottom trace is the simulated millimeter-wave path optical depth.

## Effects of Turbulence and Inclement Weather on Millimeter Wave Propagation

R. W. McMillan, R. A. Bohlander, and E. M. Patterson  
Georgia Institute of Technology  
Georgia Tech Research Institute  
Atlanta, Georgia 30332

R. J. Hill and S. F. Clifford  
National Oceanic and Atmospheric Administration  
Wave Propagation Laboratory  
Boulder, Colorado 80303

### ABSTRACT

The effects of atmospheric turbulence on the propagation of millimeter wave (MMW) radiation have been less well quantified than corresponding effects on the propagation of radiation at visible and near-infrared wavelengths, although the general theory of propagation of electromagnetic radiation through turbulence is well understood. The basic difference between MMW and IR/visible radiation with regard to propagation through turbulence is caused by the effects of water vapor on the longer wavelengths. Otherwise, turbulence would cause minimal degradation of MMW system performance.

This paper presents some of the results of a series of experiments designed to characterize the atmosphere from the point of view of MMW propagation, with emphasis on turbulence effects and the comparison of these effects to experiment. These experiments used MMW frequencies in four different bands and were conducted in all types of weather. Although the emphasis is on propagation through turbulence, much data were also obtained on propagation through inclement weather. These results are of special interest because they were obtained at the higher MMW frequencies, in the range 116-230 GHz. The results of analyzing early data from these experiments indicate that agreement with the turbulence theory is good; the inclement weather data also agree well in those areas where appropriate propagation theory is available.

### 1. Introduction

During the period 1983-1985, Georgia Tech and NOAA have been engaged in a joint program which has as its purpose the measurement of the effects of atmospheric turbulence on the propagation of millimeter-wave radiation. A series of experiments have been conducted at a site near Urbana, Illinois, chosen for its exceptional flatness and resultant freedom from effects which might perturb the atmospheric effects to be observed. The choice of such a site enables the designers of the meteorological instrumentation part of the experiment to effectively characterize the atmosphere with minimal instrumentation. During the five different measurement sessions conducted for this program, results have been obtained in clear air, rain, fog, and snow, at frequencies of 116, 118, 142, 173, and 230 GHz; although not all frequencies were used under all conditions. These frequencies were chosen for the purpose of characterizing propagation on all of the atmospheric features of interest in the range 116-230 GHz, including the 94 GHz window, the 118.7 GHz oxygen line, the 140 GHz window, the 183 GHz water line, and the 230 GHz window.

The next section of this paper briefly reviews the experimental

arrangement, and Section 3 gives representative results obtained under various types of weather conditions. Section 4 gives some brief conclusions and recommends the design of a system for the measurement of MMW turbulence similar to that used for determination of the visible-wavelength turbulence.

## 2. Experiment

The apparatus used for making the MMW turbulence measurements described in this paper comprise transmitter, receiver, data collection and processing system, and meteorological instrumentation. Figure 1 shows the layout of the propagation path, including the locations of the subsystems mentioned above and the direction of the prevailing wind. More details of the experimental arrangement has been published elsewhere (McMillan, et al., 1983, 1985; Bohlander, et al., 1983).

Phase-locked reflex klystron oscillators were used as both transmitter sources and as receiver local oscillators, with the exception of the 115 GHz measurement system which used a phase-locked extended interaction oscillator transmitter source. Phase locking was necessary because it provided amplitude stability for better resolution of turbulence effects, and frequency stability for narrow-band operation and ease of calibration. The transmitter antenna was an offset paraboloid with an elliptical shape designed to approximately spread the beam over the extent of the receiver trailer with minimum spill over in both horizontal and vertical directions. The transmitter was mounted on a steel pedestal set on a concrete pad, independent of the suspension system of the truck in which it was housed.

The receiver has four apertures, each of which is pumped by the same local oscillator through an arrangement of beam waveguides. The receiver spacings vary from 1.4 to 10 meters to account for different atmospheric scale sizes. Harmonic mixers are used, so that the local oscillator operates at approximately one-half of the signal frequency, resulting in a local oscillator range of about 58-115 GHz. The beam waveguide LC distribution system was found to work very well over this range. Receiver lenses were made of high-density polyethylene, and their aperture was chosen to be 30 cm. The receivers were double-conversion types, with the first intermediate frequency at 930 MHz and the second at 30 MHz. This latter frequency was chosen because of the good availability of signal processing components such as phase shifters and attenuators, and because it can be easily observed on a high-frequency oscilloscope for calibration purposes.

Initial data processing is done in the signal combiner at a frequency of 30 MHz, where each of the four antenna returns is split into 0, 90, 180, and 270 degree phase components, and combined in such a way that the real and imaginary parts of the mutual coherence function result when the proper combinations of them are made (McMillan, et al., 1983). These signals are collected and stored by the data processing computer, which also collects and stores data from each of the meteorological instrumentation channels. This computer also has the capability of performing limited data reduction functions, both on- and off-line, and of supplying real-time information to chart recorders which are used to monitor system performance during data runs.

The propagation range was well characterized by meteorological instrumentation, including devices for measuring temperature, humidity, wind speed and direction, solar flux, rain rate, and particle size distribution. Turbulence related instrumentation included optical  $C_n^2$  measuring devices,  $C_T^2$  probes, and Lyman-Alpha hygrometers for determination of the humidity structure parameter  $C_Q^2$ . All of these met

parameters were recorded simultaneously with MMW data on magnetic tape by the computer system.

### 3. Results

As mentioned earlier, results have been obtained under all weather conditions of interest for most of the frequencies for which measurements have been made during this experiment. It is generally true that results for a given frequency can be applied to any other frequency that is reasonably close by using the scaling law which states that the log amplitude variance for turbulence fluctuations varies as  $v^{7/6}$ . This relationship has been shown to be true for clear-air fluctuations, (McMillan, et al., 1983) but may not be true for fluctuations in inclement weather. This section presents some of the results obtained, including those obtained under both clear-air and inclement weather conditions.

Perhaps the most interesting results obtained during this series of measurements have been obtained under clear air conditions, because fluctuations are, perhaps surprisingly, largest in clear air. Furthermore, the results obtained agree well with theory, whereas the theory of fluctuations under turbid weather conditions is not well developed. Figure 2 shows a typical result obtained in clear air under hot, humid conditions at a frequency of 173 GHz. An examination of the distribution of power in such a trace shows that it is log-normal, with a standard deviation of about 10% of the mean. At the time that these measurements were made, the temperature was 32°C, and the absolute humidity was 19 g/m<sup>3</sup>.

Fluctuations in intensity observed in rain, fog, and snow were smaller than those observed in clear air. When hydrometeors are present in the atmosphere, it is not possible to distinguish intensity fluctuations due to changes in the index of refraction from those due to changes in the density of these hydrometeors. Fluctuations observed in fog are of interest because they are very small - almost undistinguishable from instrumental variations, although different types of fog may give different results. Figure 3 is a copy of a recorder trace obtained in fog at a frequency of 142 GHz.

Intensity fluctuations observed in rain are primarily due to changes in rain rate over the propagation path, although small-scale variations in intensity may be caused by refractive index changes. Figure 4 shows signals received from two of the four receivers during a heavy rainfall, measured at a frequency of 173 GHz. During the heaviest part of this storm, the rainfall rate was 60 mm/hr. Attempts have been made to correlate the attenuation of MMW signals with rain rate (Patterson, et al., 1986).

Figure 5 shows the fluctuations in intensity observed during a snowstorm at a frequency of 116 GHz. The storm during which these observations were made was fairly violent, and much of the snow in the air during its latter part was due to ground blizzards. It is interesting to compare this figure to Figure 2, obtained for clear air. Despite the large amount of snow in the air during the storm, and the fact that the density of snow particles was obviously fluctuating, the MMW signal fluctuates much less in clear air. If one considers that MMW fluctuations are due mainly to humidity changes, it is reasonable to expect that fluctuations would be greater during conditions of high temperature and corresponding high humidity. Similarly, large signal variations have been observed propagating over a field in which water from melting snow was present, even though the temperature was much lower for these measurements.

The spectra of MMW fluctuations under various atmospheric conditions

NO-A184 837

AN INVESTIGATION OF MILLIMETER WAVE PROPAGATION IN THE  
ATMOSPHERE: MEASUR. (U) GEORGIA TECH RESEARCH INST  
ATLANTA R W MCHILLAN ET AL. 17 JUN 87 ARO-18457.12-05  
DARG29-81-K-0173

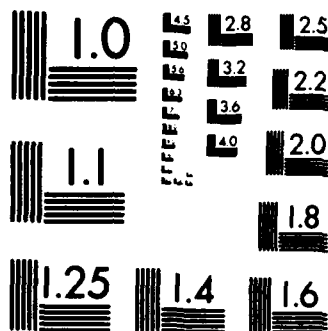
3/3

UNCLASSIFIED

F/G 20/14

NL





MICROCOPY RESOLUTION TEST CHART  
NATIONAL BUREAU OF STANDARDS 1963-A

are also of great interest. It is generally true that the MMW spectra observed do not agree as well with theory as the corresponding spectra observed at visible and near-infrared wavelengths, and the reasons for this discrepancy are not well understood. One expected feature that does not appear in the spectra measured in rain and snow is a small bump at high frequencies that one might expect from small scale fluctuations in the density of these hydrometeors. Figure 6 is a spectrum computed from measurements made at 230 GHz during a snowfall. The two curves are a result of different methods of low-pass filtering the results.

#### 4. Conclusions

Perhaps the most important conclusion that can be reached as a result of these measurements is that the clear-air turbulence theory agrees well with experimental results. It is also interesting to observe that the magnitudes of variations observed under turbid weather conditions are smaller than those observed under hot, humid summertime conditions. Fluctuations measured in fog are especially small for the fog conditions observed during this series of measurements, while rain and snow variations fall between these two extremes. The main effect of rain is to attenuate MMW radiation, and the degree of attenuation appears to be well correlated with the rain rate. Attenuation is of less importance under other atmospheric conditions than in rain, a conclusion that seems to be verified by the data obtained during these measurements. The results of this series of measurements also seem to verify that MMW systems should perform well in inclement weather, although rain attenuation appears to be significant. It will be recalled that rain attenuation is essentially constant with frequency over a wide range beginning at about 100 GHz in accordance with Mie scattering theory.

The largest value of the MMW index of refraction structure parameter  $C_n^2$  observed during this series of measurements was  $5.9 \times 10^{-12} \text{ m}^{-2/3}$ , an observation made under hot, humid summer time conditions. Under these conditions, the fluctuations in intensity and phase observed were about 1 dB and 1 radian, respectively, levels which probably would marginally affect the performance of MMW systems. It is interesting to question whether or not larger values of  $C_n^2$  than those observed in Illinois exist under other atmospheric conditions, and how prevalent are these elevated levels. If the levels of  $C_n^2$  observed in Illinois cause marginal degradation of system performance, then higher levels might cause significant degradation to the extent of making such systems useless under certain conditions. To assess the prevalence of high levels of  $C_n^2$ , a system for measuring this parameter that is similar to a system already developed for the visible wavelength range is proposed. Such an instrument would comprise transmitter, receiver, and data processor, and could be configured for automatic operation. In this way, values of  $C_n^2$  could be measured in places which may be of interest to the MMW system designer, but at which this parameter might not ordinarily be measured, such as in the tropics, desert, or Arctic regions. Such measurements, when combined with other atmospheric studies, would also add to our understanding of the atmosphere.

#### REFERENCES

1. R.A. Bohlander, V.T. Brady, A. McSweeney, G.F. Kirkman, J.M. Newton, A. Davis, O.A. Simpson, "A Quasi-Optical Millimeter Wave Transmitter and Receiver Array for Measurements of Angular Scintillation," Eighth

International Conference on Infrared and Millimeter Waves, Miami Beach, FL, Dec., 1983.

2. R.W. McMillan, R.A. Bohlander, G.R. Ochs, R.J. Hill, "Millimeter Wave Atmospheric Turbulence Measurements: Preliminary Results and Instrumentation for Future Measurements," Optical Engineering, Vol. 22, No. 1, Jan/Feb, 1983, pp. 32-39.

3. R.W. McMillan, R.A. Bohlander, R.H. Platt, D.M. Guillory, J.T. Priestley, R.J. Hill, S.F. Clifford, R.E. Cupp, J. Wilson, "Atmospheric Turbulence Measurement System," SPIE Technical Symposium East, Arlington, VA, April, 1985.

4. E.M. Patterson, R.L. Mandock, R.W. McMillan, R.A. Bohlander, R.J. Hill, J.T. Priestley, B.E. Rishel, R. Olsen, "Correlation of the Attenuation of Millimeter Wave Signals with Rain Rate," URSI Commission F Open Symposium, University of New Hampshire, July, 1986.

#### ACKNOWLEDGEMENT

This work was supported by the U.S. Army Research Office under Contract DAAG29-81-K-0173.

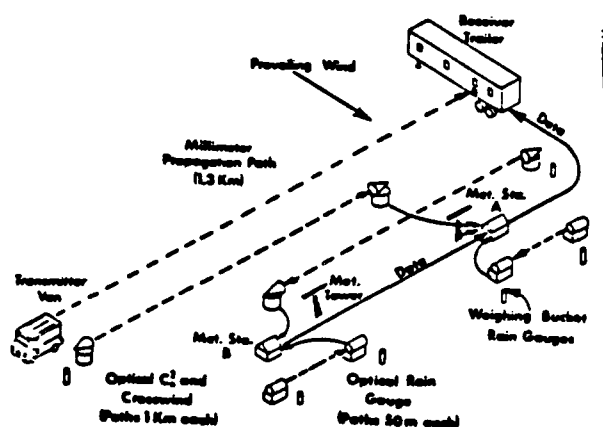


Fig. 1. Layout of experiment showing transmitter, receiver, and meteorological instrumentation stations.

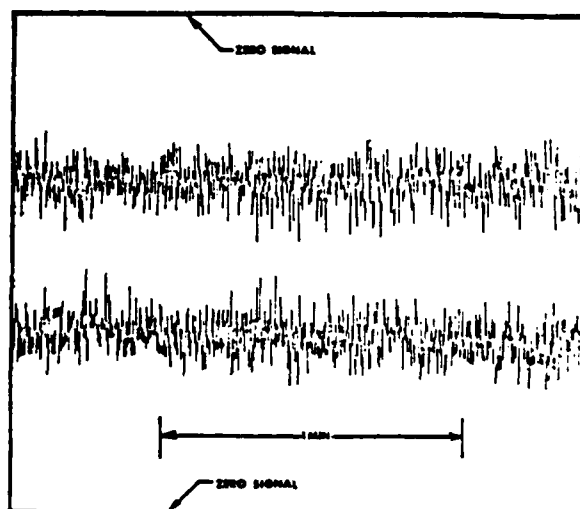


Fig. 2. Intensity fluctuations observed on a hot, humid summer day at 173 GHz.

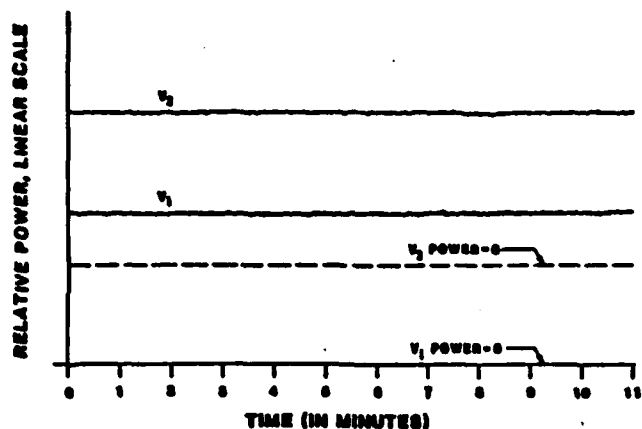


Fig. 3. Intensity fluctuations measured during a heavy fog at 142 GHz.

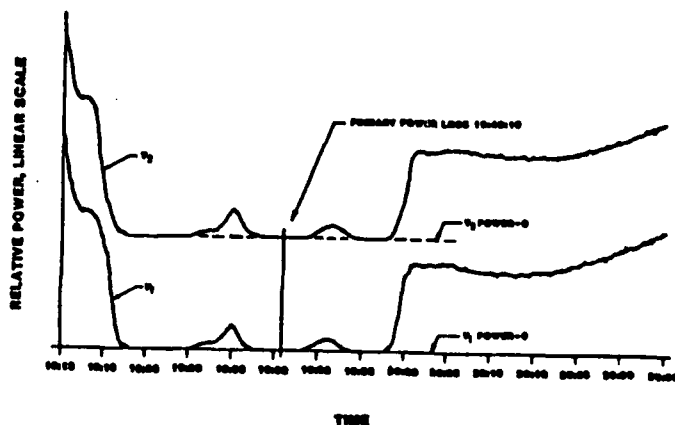


Fig. 4. Intensity changes measured at 173 GHz during a heavy rain.

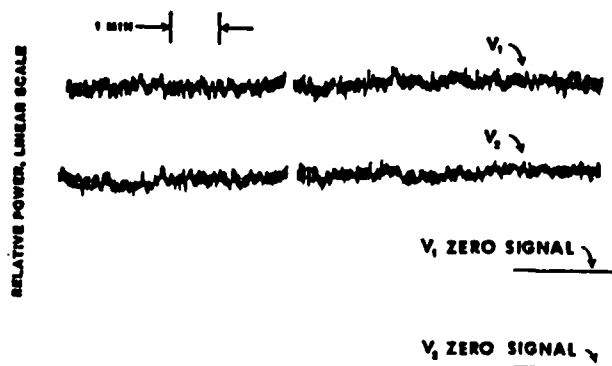


Fig. 5. Intensity fluctuations measured in snow at a frequency of 116.3 GHz

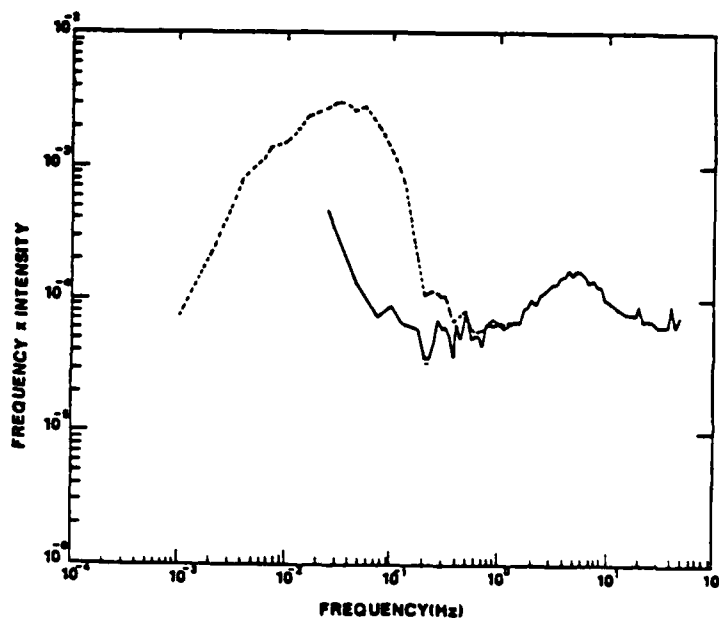


Fig. 6. Intensity power spectra in snow for a frequency of 230 GHz.

END

11-87

DTIC